SCUOLA
NORMALE
SUPERIORE

Classe di Scienze

Corso di perfezionamento in

Fisica

XXXV ciclo

Charting Dark Matter interactions

FIS/02 - Fisica Teorica, Modelli E Metodi Matematici

Candidato

dr. Marco COSTA

Relatore

Prof. Dario BUTTAZZO

Supervisore

Prof. Enrico TRINCHERINI

Contents

Chapter 1

Introduction

One of the biggest puzzles of Fundamental Physics is Dark Matter (DM). Since the first observations by Zwicky in 1933 of velocity dispersion of galaxies, a wealth of other evidence has been collected to foster the idea that the majority of the energy budget of the universe is unexplained by matter predicted in the Standard Model (SM) of particle physics. See [1] for a review and [2] for a more historical perspective on the problem.

While the original observations point to the need to introduce some new physics to correct the motion of visible matter at small, galactic scale ($\lesssim 0.01$ Mpc) (see for example Fig. 1.1), among the best observations so far of the DM phenomenon we mention the spectacular observation of angular anisotropies of the temperature of the Cosmic Microwave Background (CMB) (Fig. 1.2), the distribution of clustering galaxies in Large Scale Structures (LSS) [3, 4], lensing effects [5].

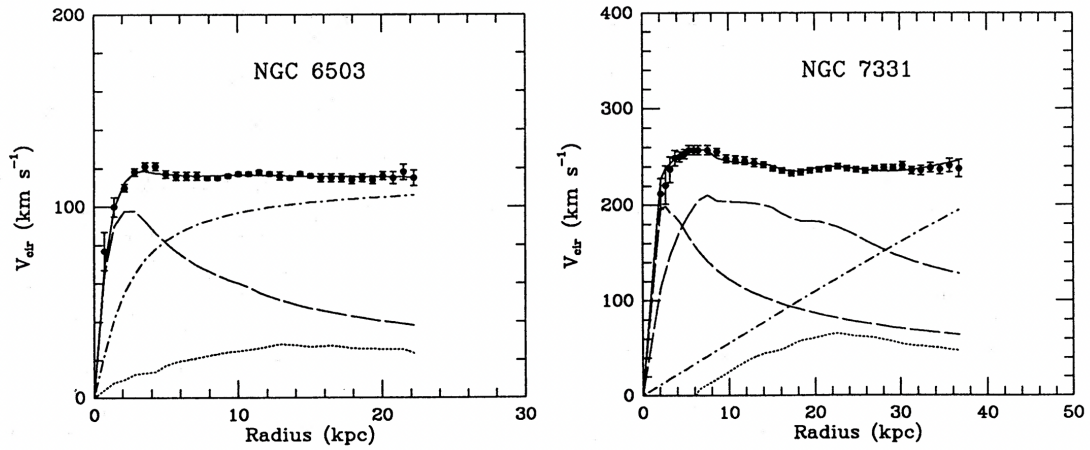

Figure 1.1: *Galaxy rotation curves for two sample galaxies: velocity as a function of the distance from the galactic center. The solid black line is obtained by fitting the data points with a three parameters dark halo fit. The rotation curves of individual components are also shown: dashed for the visible component, dotted for gas and dash-dotted for the dark halo. Taken from [6].*

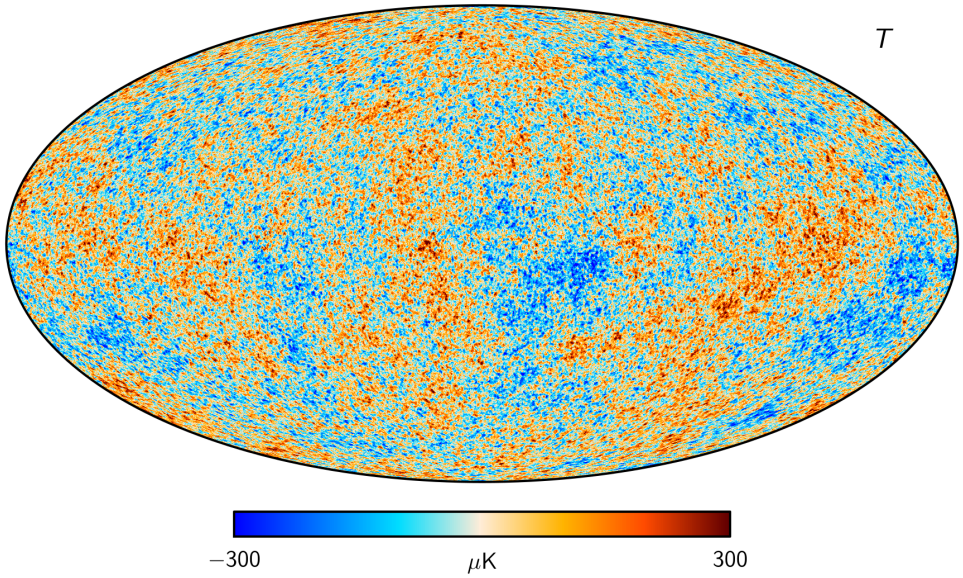

Figure 1.2: *Planck2018 SMICA CMB Temperature Map. Taken from [7].*

These instead call for a modification of physics at larger scales (> 0.01 Mpc). A simple explanation that has been put forward to explain both aspects of these gravitational anomalies is *Cold Dark Matter* (CDM): extra matter that during the cosmological history of the universe has energy content redshifting as non-relativistic particles. Some examples of good DM candidates are new heavy particles (non-relativistic when structures start to gravitationally form) produced in thermal equilibrium (see [8, 9] for reviews) or outside [10, 11], coherent oscillations of a scalar field near the minimum of its quadratic potential [12], like axions [13, 14, 15] or more generically Ultralight DM [16], or even macroscopic objects like Primordial Black Holes [17].

The goal of the Thesis is to explore the nature of DM, however in order to have a complete picture of the cosmological history of the Universe we need to introduce extra ingredients. Indeed the observation of the accelerated expansion of the universe today via local measurements like from SuperNovae (SN) [18] cannot be explained by particle DM, needing instead a fluid exerting negative pressure, dubbed *dark energy* (DE), that would constitute approximately 70% of the total energy budget of the Universe. The presence of DE is also inferred indirectly from CMB measurements, but there is a discrepancy between the two classes of results [19] (the so-called Hubble tension [20, 21]).

The third piece of the puzzle is the existence of an initial stage in the history of the universe called *inflation* [22], in which the universe underwent a very fast accelerated expansion. This is needed to source very smooth initial conditions for the matter density inhomogeneities. Inflation, Dark Matter and Dark energy are the pillars of the Standard Model of Cosmology, called *Concordance Model* or for short ΛCDM from the name of its constituents.

This picture of Cosmology allows to make precise predictions on the distribution of matter at large scale. Indeed, it is possible by using General Relativity (GR) equa-

tions to solve for the evolution of the matter inhomogeneities, to make quantitative predictions on its distribution and compare this with data.

The addition of DE and DM gives results in excellent agreement with the matter distribution on the large scales. Typically, the abundance of DM is expressed in terms of the quantity $\Omega_{\rm DM}h^2 \equiv M_{\rm DM}n_{\rm DM}/\rho_0$, where $M_{\rm DM}$ is the DM mass, $n_{\rm DM}$ its number density and ρ_0 today's critical energy density. Measurements of the CMB from the Planck experiment indicates that the energy budget $\Omega_{\rm DM}h^2$ stored in the DM fluid is [23]:

$$\Omega_{\rm DM}h^2 = 0.1186 \pm 0.0020 \,, \tag{1.1}$$

which is roughly 27% of the total energy density of the universe.

To summarize, the results are consistent with the presence of a new fluid, the Dark Matter, which is stable on cosmological timescales, collisionless, cold (roughly meaning that it behaves as a non-relativistic particle) and dominated by GR at large distance.

The data unfortunately does not hint at any other property of the Dark Matter, nor about the existence of other particles in the so called *Dark Sector* (DS) interacting with it. This fact could suggest that trying to model DM interactions is a useless endeavour. On the contrary, we think that there are at least two reasons for why the opposite is true.

The first reason is that current data by itself does not give any insight on where scientists should look for further evidence. Instead, charting a landscape of the possible DM interactions can give indications on the experiments needed to test the various hypothesis. This is due to both the fact that the interactions can already tell to which visible particle the DM interacts mostly with, and to the fact that in some cases interactions can specify the production mechanism of DM and in turn its mass. In this Thesis it will be shown that, not surprisingly, different models for different DM interactions are best studied in different environments, for both the reasons outlined above.

The second reason is that it is not completely understood if the picture of DM at the very small scales (galactic) is fully consistent with a pure ΛCDM model, in which the DM is truly collisionless. Indeed there have been several claims in the literature of the failure of the vanilla ΛCDM model to properly capture some properties of galactic dynamics [24, 25, 26], such as the radial density profile of DM (observationally less cuspy than expected [27]), the lack of satellites around galaxies [28, 29], and the fact that satellites are more likely to be found in less massive subhalos than predicted (*Too-Big-to-Fail problem*) [30]. Additionally, galaxies exhibit regular dynamical properties [31] that suggests scaling relations between the baryonic and dark matter components that need non-trivial explanations from a purely ΛCDM perspective (and that can look fine-tuned). Examples are the tight correlation between total baryonic mass and radial acceleration (the *baryonic Tully-Fisher relation*) [32], and the strong correlation between total observed acceleration and the one predicted from the baryonic distribution (the *Radial Acceleration Relation*) [33]. Despite the fact that galactic observations were the first to suggest the

existence of DM, in light of these discrepancies they are now the subject of debate whether or not the DM paradigm is the right one, or rather if they call for modifications of gravity, as postulated for example by *Modified Newtonian Dynamics* theories (MOND) [34, 35, 36]. For example, MOND has the advantage of explaining almost by construction the correlations between baryonic matter and features in the galaxy rotation curves. Predictions at the very small scales in ΛCDM are intractable analytically and need expensive large N-body simulations. The predicted DM profiles of these computations can be strongly affected by effects that are hard to model, such as baryonic feedback from Supernovae (see [37] for a proposed mechanism, and references therein), so there is no total consensus on the real nature of these small scales problems. If these discrepancies are to be taken seriously, they call for some physics beyond (or maybe different) from ΛCDM. It has been put forward the idea that the departure from the collionless hypothesis and the introduction of DM self-interaction can ameliorate these small scale problems in DM models (see [38] and [39] for a review). Under this circumstance, studying other possible consequences of DM interactions can help in providing further tests that could be independent from numerical simulations, and pinpoint more precisely the ballpark of the self-interaction.

With these observations in mind, the goal of the Thesis is to chart the landscape of the possible DM interactions (both with itself and with ordinary SM particles) and how to test the several hypothesis that will be put forward. Since Physics is not Mathematics, achieving a description that leaves no loophole open is impossible. Indeed the the possibilities are virtually endless, with plethora of models that can explain the current data and make fancy predictions. If we want to learn something more about the nature of DM, we must ask robust questions about the interactions and try to give systematic answers.

As a starting point to discuss possible interactions, a good strategy is to see what the interactions of visible matter are, and try to understand if the idea behind their modelization can be of any help in our goal.

It is well known that in the SM the interactions between matter and vector force carriers is described via *gauge interactions*. The SM gauge group is

$$G_{\rm SM} = {\rm SU}(3)_c \times {\rm SU}(2)_{\rm L} \times {\rm U}(1)_{\rm Y} \ , \tag{1.2}$$

where the first factor describes the strong nuclear forces while the others the electroweak (EW) ones. If a field (and hence the particles it excites) lies in a given representation of a gauge group, it will interact with the respective gauge bosons with a strength dictated by the dimensionality of the representation and the (universal) gauge coupling. Intuitively, the larger the representation, the stronger the coupling.

The very first question that comes to mind regarding the nature of DM interactions is whether or not DM can exchange forces with SM matter through the SM force carriers. As explained above, this is equivalent to ask if the DM lies in a non-trivial representation of $G_{\rm SM}$. This is the first question that we will try to answer.

We mention that it is also possible to have interactions of matter with a scalar field, like the Higgs in the SM, through so-called *Yukawa* interactions. We will consider them later, both in the context of Yukawa with the SM Higgs and also with new dark scalars.

The second question arises if the answer to the first one is negative: if the DM does not carry any non-trivial SM charges, what are its possible iteractions with the SM? In this case, the DM is a SM singlet. Therefore it can only interact via lagrangian operators, called *portals*, that are made by the product of some DS singlet field that can excite the DM, and some SM singlet field. These portal operators arise for example whenever a heavy mediator charged under both $G_{\rm SM}$ and some symmetry in the DS gets integrated out. For a given dimension of the lagrangian operator there are only a finite number of them, and therefore the scenario can be studied systematically, provided we find observables that do not depend too much on the precise nature of the portal. Our second task therefore will be to study suitable model independent observables and to put generic bounds on portal interactions, following the footsteps of previous works.

The third possibility is that the DM itself interacts only gravitationally with the SM (or the other non-gravitational interactions are simply negligible). Naively this lack of interactions seems like an insurmountable obstacle to our goal to further characterize the DM fluid. However some of the self-interactions in the Dark Sector might qualitatively change how DM inhomogeneities cluster together. Since baryons track the DM inhomogeneities, the DM self-interactions can in principle leave an indirect imprint in the distribution of baryonic inhomogeneities. There are further examples of how other properties of the the DS, such as phase transitions, can be inferred via gravitational interactions (like for example emission of gravitational waves due to bubble collisions [40]), but as a first step in this endeavour we will only consider the modifications of the clustering properties of the DM as a probe of its self-interactions.

To summarize, the questions that we are trying to answer are going to be the following:

i) Does DM interact with ordinary matter via SM gauge forces?

ii) Does DM interact with ordinary matter via SM-singlet operators?

iii) If the non-gravitational interactions are absent or negligibly small, to which extent is it possible to infer informations about DM self-interactions?

Our approach is purely phenomenological: we are surveying the possibile DM interactions and comparing them with data. We are not using any theoretical insight on how a DM model might look like. For example, stability of the DM can be in conflict with certain conjectured properties of quantum gravity (see [41] and references therein), unless the DM is protected by some gauge symmetries (either in the SM or new ones). This concept, called *Accidental Stability*, has been a useful guidance for model building [42, 43]. This suggests that our phenomenological analysis can be complemented by theoretical insights. We will sketch in Chapter 5 how we applied the Accidental Stability of the composite models introduced in [42] to their asym-

metric DM version (see [45, 46] for reviews). Not suprisingly, the combined request of accidental stability and asymmetry generation limits the field content options.

1.1 Interactions through SM forces

Intutive arguments imply that the DM particles cannot interact too much with SM particles, therefore they cannot carry non-trivial $SU(3)_c$ and electric charges. This leaves open the possibility for the DM to have weak interactions, that we explored in [47, 48]. This means that it is a n-plet of $SU(2)_L$ with hypercharge Y, with the lightest stable compenent satisfying $T_3 + Y = 0$ where T_3 is the diagonal generator of $SU(2)_L$ (in the basis we have chosen). We will refer to this charge assignment for the DM with the notation n_Y. Interestingly, once both n, Y are set, the size of the interaction with the SM is essentially fixed[1]. In particular, the size is such that in the early universe the DM multiplet was in thermal equilibrium with the SM plasma, until temperatures of order $M_{\rm DM}/25$. The equation for the number density (and hence energy density given the non-relativistic nature of Cold DM), is given by:

$$\frac{z}{Y_{\rm eq}}\frac{{\rm d}Y}{{\rm d}z} = -\frac{n_{\rm DM,eq}\langle\sigma|v|\rangle}{H}\left(\frac{Y^2}{Y_{\rm eq}^2} - 1\right) , \tag{1.3}$$

where $Y = n_{\rm DM}/s$ is the DM yield (ratio between DM number density and entropy density s), z is the temperature in unit of the DM mass, H the Hubble rate, and $\langle\sigma|v|\rangle$ the thermally averaged annihilation cross section of DM into SM particles. Solving the equation allows to find the DM energy density as a function of the cross section. The latter is, at fixed EW charges, only a function of the DM mass. Therefore the relation completely fix the mass and hence the model (at least in its cosmologically relevant aspects). In order to get a reliable result non-perturbative effects such as Sommerfeld Enhancement (SE) [49, 50] and Bound State Formation (BSF) [51] must be included. It turns out that the masses of fermionic candidates range from 1.1 TeV for $2_{1/2}$ to > 50 TeV for $n > 7$.

This scenario, called *Minimal Dark Matter* (MDM) has been explored in detail in [43, 50, 52]. In such works, some of the n_Y possibilities were not studied in detail because the authors were focusing on models satisfying several extra assumpion: accidental stability and the absence of sub-Planckian Landau poles. Since our approach is focused on understanding if the DM can interact electroweakly, we will drop these more theoretically-driven assumptions. Our only request will be to ask for *calculability*: the prediction for the mass must be reliable in perturbation theory. We will refer to these models with the historical name of *Weakly Interacting Massive Particle* (WIMP), given to a DM candidate with mass set by the freeze-out of a weak interaction: in our case "weakly" truly refers to the SM weak interaction.

Once the value of the mass is known, we develop a strategy to test the hypothesis. The low n candidates ($n = 2, 3, 4$) are suited to be studied at a future high energy lepton collider with center of mass energy $\sqrt{s}$ of few TeV [53]. Higher n candidates

[1]For scalar DM, in principle there are quartic coupling to the Higgs which we anticipate are disfavored by Direct Detection experiments.

are heavier and therefore in order to probe them at collider experiments unrealistically high $\sqrt{s}$ are needed. However in this case large exposure Direct Detection (DD) experiments like DARWIN [54] can exclude at the 2σ level the hypothesis. Residual annihilation of WIMPs into SM particles in Indirect Detection (ID) experiments is also a potentially promising signature, especially with next generation telescopes [55]. However it suffers mostly from the uncertainty in the mass computation and in the peak of the annihilation cross-section in the non-relativistic regime. Other indirect probes that we study are Electroweak Precision Tests (EWPT) [56, 57] and electron dipole moment measurements [58].

We mention that to be precise, the possibility for DM to interact with the strong nuclear force is not completely ruled out, although it appears to be a rather exotic possibility. For details see [59, 60]. We will not further consider this scenario. The strategy that we outline should give a clear answer to the possible SM charges of the DM candidate.

1.2 Interactions via singlet operators

If the DM is a SM singlet, how can it interact with the SM? Such an interaction is modeled by a lagrangian operator that is of the form $\mathcal{O}_{\rm SM}\mathcal{O}_{\rm DS}$ where the $\mathcal{O}$ are singlet operators built as product of SM and DS fields. Interestingly enough, at the renormalizable level only 3 operators can be written:

$$F^{\mu\nu}F'_{\mu\nu}\ , \quad H^\dagger H S^2\ , \quad H^c\bar{L}N\ , \tag{1.4}$$

provided the existence in the DS of a dark photon A'_μ [61, 62, 63], a dark scalar S [64, 65, 66] and a heavy neutral lepton N [67, 68, 69] respectively. These portals are known as the kinetic mixing portal, the Higgs portal[2] and the neutrino portal. In particular, these portals can be responsible for the thermal freeze-out of DM, if its mass is in the MeV [70, 71] range, and thus can be studied via a combination of high intensIty experiments and astrophysical bounds. These scenarios has been thoroughly studied in the literature, given their motivation stemming from an Effective Field Theory (EFT) point of view.

In general, given a UV model for the DS, there is no reason to expect the portal operators at the renormalizable level. Consider for example a theory with *dark quarks* $\mathcal{Q}$ charged under a new confining interaction, dubbed *dark color*. If at some UV scale $\Lambda_{\rm UV}$ a heavy mediator (carrying both dark color and suitable SM charges) connects the two sectors, once it gets integrated out by gauge invariance the first available operators are the following 5D and 6D:

$$\frac{k_S}{\Lambda_{\rm UV}}H^\dagger H\bar{\mathcal{Q}}\mathcal{Q}\ , \quad \frac{k_J}{\Lambda^2_{\rm UV}}J^{\rm SM}_\mu\bar{\mathcal{Q}}\gamma^\mu\mathcal{Q}\ , \tag{1.5}$$

with $J^{\rm SM}_\mu$ a conserved SM current. Models of this kind are for example found in [72, 73, 74, 75]. A less exotic scenario in which the leading portal between some secluded

[2]There is also the super-renormalizable term $H^\dagger H S$.

sector is non-renormalizable appears in the SM itself. Indeed the neutrinos can be seen as "singlet" particle of the $\mathrm{U}(1)_{\mathrm{em}}$ electromagnetic gauge group below the ElectroWeak Symmetry Breaking (EWSB) scale. The mediator in this case can be thought to be the Z boson[3]. We will in general consider non-renormalizable operators of the form:

$$\frac{k_{\mathcal{O}}}{\Lambda_{\mathrm{UV}}^{D-4}}\mathcal{O}_{\mathrm{SM}}\mathcal{O}_{\mathrm{DS}} \ , \tag{1.6}$$

where $D = [\mathcal{O}_{\mathrm{SM}}] + [\mathcal{O}_{\mathrm{DS}}]$ is the sum of the dimensionality of the SM and DS operators. This scenario is less constrained than the EW DM case, due to the fact that the couplings size is not completely fixed by gauge invariance. Also, the constituents field of $\mathcal{O}_{\mathrm{DS}}$ will in general contain not only the DM, but possibly other DS fields. It is not obvious to get robust conclusions in this scenario, both on the cosmological history of the model and on the potential signatures at terrestrial experiments such as beam dumps and colliders. Following the formalism introduced in [76], in [77] we found that it is possible to set constraints on a very broad class of models at current and future neutrino and beam dump experiments. The idea is that for very light dark sectors (lighter than the typical energy of the beam of the experiments for example), the inclusive production cross section of DS excitations depends only on the coupling size and the number of internal degrees of freedom of the DS in a very simple way, as suggested by a very naive application of dimensional analysis. Indeed for non-renormalizable portals of Eq.1.6, the inclusive production cross-section of DS particles σ_{DS} can be estimated as:

$$\sigma_{\mathrm{DS}} \sim \frac{\sqrt{\hat{s}}^{2D-10}}{\Lambda_{\mathrm{UV}}^{2D-8}} \ , \tag{1.7}$$

where $\sqrt{\hat{s}}$ is the relevant energy of the production process (for example the center of mass energy of a collider experiment). Remarkably, for the non-renormalizable operators that we are set to study, the production cross section is dominated by the UV energies. Therefore it is insensitive to the specific details of the DS, like for example the various mass thresholds and mass splittings[4].

In [76] this observation was used to compute missing energy signals at collider experiments, in which DS is produced and escapes detection. We expand their results considering also the case in which some DS particle is unstable and decays back to the SM via one of the portals. This scenario can be tested using high intensity experiments such as beam dumps and neutrino experiments: the DS excitations are produced when the beam impinges on a target, and then one of the produced DS particles decays back to visible particles in the detector placed $\mathcal{O}$(km) downstream. If the DS contains an unstable particle of mass up to few GeV, and if the portal scale is lower than a few TeV, a handful of such particles will decay visibly inside the detectors, leading to exclusion bounds.

[3]The example is not completely fitting due to the existence of the W boson, but we think it still give the corrrect picture.

[4]We are tacitly assuming that $\mathcal{O}_{\mathrm{DS}}$ can excite DS states with different invariant mass p^2_{DS}. Intuitively this means that $\mathcal{O}_{\mathrm{DS}}$ excites multiparticle states. An example of a non-renormalizable portal in which instead p_{DS} is fixed to a given value is the *axion* portal $aF_{\mu\nu}\tilde{F}^{\mu\nu}$, where $\mathcal{O}_{\mathrm{DS}} = a$ excites only axion 1-particle states with $p^2_{\mathrm{DS}} = m_a^2$. Our formalism does not apply to such operators.

Thanks to the approach outlined above, we only need to make a few assumptions on the nature of the event, while the rest of the discussion is kept model independent. We find that for $D = 6$ portals made by the product of a SM and DS currents the leading projected constraints come from the future DUNE multipurpose neutrino detector at FermiLab [78].

It is tempting to ask if it is possible to use a model independent approach to study also the cosmological history of models with non-renormalizable portals. Indeed the presence of a very weakly coupled portal allows for DM to be produced via *freeze-in*, without having to specify the DS self-interactions. As discussed above, non-renormalizable portals are dominated by UV physics, so the freeze-in abundance is set by the highest available temperature of the universe, which is the reheating temperature $T_{\rm RH}$. Therefore the abundance strongly depends on an extra assumption on the initial conditions of the universe. Additionally, the mechanism is viable only if the temperature of the DS is always below $\Lambda_{\rm UV}$ to guarantee the validity of the EFT description. Under this extra assumption, the correct relic abundance is reproduced only for extremely high cutoffs (for example $\Lambda_{\rm UV} > 10^8$ GeV for $T_{\rm RH} = 10^6$ GeV), that are essentially inaccessible at terrestrial experiments. We will not pursue this attempt, altough we mention that it has been studied in [79, 80].

1.3 Gravitational interactions only

If the portal interaction is negligibly small, or if it is completely absent, there is only the gravitational force that allows to peek inside the Dark Sector. In this scenario, can we say something about the self-interactions of the DM itself? A good example in which gravitational observations can put limits on the strength of self interactions is the famous galaxy merging event known as Bullet Cluster. In such event, shown in Fig. 1.3 the dark matter constituents (visible through lensing techniques) can be seen passing through each other, not experiencing any kind of lag due to extra interactions. Therefore this data can be used to put an upper bound on the (elastic) self-interaction cross section of the DM $\sigma_{\rm SI}/M_{\rm DM} \lesssim 1\,{\rm cm}^2/\,{\rm g}$ [82]. We would like to replicate this idea, but instead of using galactic scales, using large scales, in which it is still possible to somewhat retain analytic predictions for the matter distribution. In order to do so, we must first understand which kind of models can be studied in this way. The simplest scenario is to consider a real scalar DM particle, having self-interactions mediated by a real light scalar ϕ ($m_\phi \lesssim H_0$) (e.g. a Yukawa-type interaction). The reason for this choice is that, unlike what happens for vector mediators, the interaction does not suffer from screening effects and it is always attractive. Moreover, the lightness allows essentially to have Coulombian-like interactions inside the cosmological horizon. Such a light field will not undergo oscillations: the role of the scalar at this stage of the work is to only mediate the force. We are planning to study in the future the oscillating scalar scenario, given that it has potentially interesting phenomenological implications. The bounds that are going to apply come from the CMB and from the galaxy matter power spectrum P_g, defined in Fourier space as:

$$\langle \delta_g(\vec{k}_1)\delta_g(\vec{k}_2)\rangle \equiv (2\pi)^3\,\delta_D^{(3)}(\vec{k}_1+\vec{k}_2)P_g(\vec{k}_1)\,, \tag{1.8}$$

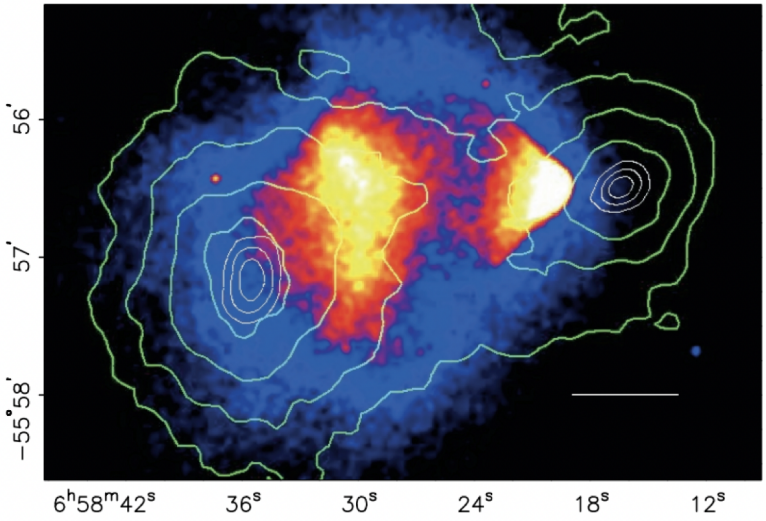

Figure 1.3: *Bullet Cluster event. The colored map represents an X-ray image taken with Chandra telescope. Green lines indicates the reconstructed lensing signal. The white bar corresponds to 200 kpc. Taken from [81].*

where $\delta_g = (n_g - \bar{n}_g)/\bar{n}_g$ are galaxies number overdensities with respect to the homogeneous background $\bar{n}_g$. Bounds from linear cosmology (CMB and BAO) on this scenario were considered in [83]. These bounds constrain the strength of the self-interaction to be 5×10^{-3} weaker than the gravitational force. We extend this work by including Large Scale Structure (LSS) data, like the galaxy power spectrum measured by BOSS [3]. We will also consider projections coming from future galaxy surveys like Euclid [84].

Since the theory of cosmological perturbations is expressed in terms of "fundamental" fields like the number density of DM particle χ and baryons, in order to describe the galaxy density we employ the formalism of *bias parameters*. This framework allows to express the "composite" δ_g as a power series in terms of the "fundamental" fields δ_χ, δ_b, where each of the expansion coefficients is a to-be-fitted *bias parameter* [85, 86, 87].

Due to the relatively small scale of $k \sim 0.3\,h/\text{Mpc}$, we need to include non-linearities in the peturbation evolution using the 1-loop formalism. In order to improve the control of perturbative corrections, we employ the *Effective Field Theory of Large Scale Structure* (EFTofLSS) [88, 89]. We will also include other corrections such as *redshift space distortion* (RSD) [90] and the *Alcock-Paczynski* (AP) effect [91].

The presence of a long range force can be seen as a violation of the Equivalence Principle (EP) in the Dark Sector: indeed after a field redefinition it is possible to show that the theory with the DM interacting with a long range scalar field is equivalent to a theory in which non-interacting DM particles couple to a different metric with respect to the SM. A consequence of this is that in principle objects with different compositions of ordinary matter and DM will fall toward a given matter clump at different rates. This is not too different from the idea behind torsion

balance experiments that test the EP in the laboratory [92, 93].

In our case, what we want to do is to use the whole visible Universe as a scale to test the infall of different matter inhomogeneities. This precise idea is mathematically translated in the Fourier Transform of the 3-point correlator, or equivalently the *galaxy bispectrum* B_g:

$$\langle \delta_g^A(\vec{k}_1)\delta_g^B(\vec{k}_2)\delta_g^C(\vec{k}_3)\rangle \equiv (2\pi)^3\,\delta_D^{(3)}(\vec{k}_1+\vec{k}_2+\vec{k}_3)B_g^{ABC}(\vec{k}_1,\vec{k}_2)\ , \tag{1.9}$$

where A, B, C stand in principle for the different kind of tracers (galaxies) observed. Different types will in general have different DM-SM particle content, and therefore in presence of the new long range force will experience different attractions toward each other. As a first step, we will consider only a single tracer. It will be interesting in the future to study the multi-tracer case since it has a peculiar pole of B_g in momentum space that signals a violation of EP [94]. We will comment on how B_g can help in further constrain the bounds coming from the CMB and LSS surveys.

This Thesis is structured as follows. In Chapter 2 we discuss the possibility of DM interacting with SM forces, in particular the electroweak interaction, discussing in detail the prospects of future detections. In Chapter 3 we consider instead the possibility that DM is a SM singlet, and the interactions with SM particles are described by non-renormalizable effective portals that are overall made by the product of SM and DS total singlet operators. We will put emphasis on a model independent strategy that can be employed to study these scenarios. In Chapter 4 we discuss the last possibility: what if the DM interactions with the SM are only gravitational (or so weak to be impossible to detect)? We will study how long range interactions within the DS sector itself can be imprinted in the distribution of ordinary matter via gravitational interactions. In Chapter 5 we briefly sketch how the theoretical constrain of Accidental Stability can be applied to the composite ADM scenario and constrain the model building possibilities. In Chapter 6 we summarize the results and give details on how this program can be ampliated.

Chapter 2

DM as an EW multiplet

In this section we will explore the possibility that the DM interacts with the SM gauge bosons.

In this scenario, the DM is thermally produced in the early Universe and its abundance is determined by the freeze-out of $2 \to 2$ annihilations into SM states, As remarked in Chapter 1, the elusive nature of DM implies that it cannot interact with the strong nuclear force or with the photon.

Therefore the possibility we will explore, because of its minimality and predictive power, is that the DM is the lightest neutral component of one EW multiplet.

We recall here the logic of our classification as described in [47, 48] (see also [43, 50, 52, 95, 96] for previous work on the subject).

Requiring the neutral DM component to be embedded in a representation of the EW group imposes that its electric charge $Q = T_3 + Y$, where $T_3 = \text{diag}\left(\frac{n+1}{2} - i\right)$ with $i = 1, \ldots, n$ is the diagonal generator of $\text{SU}(2)_\text{L}$, and Y is the hypercharge. At this level, we can distinguish two classes of WIMPs: i) real EW representations with $Y = 0$ and odd n; ii) complex EW representations with arbitrary n and $Y = \pm\left(\frac{n+1}{2} - i\right)$ for $i = 1, \ldots, n$. Class i) models automatically avoid strong constraints from direct detection searches due to the absence of tre level coupling to the Z boson, and will be taken here as a minimal realization of the EW WIMP scenario. The lightest particle in any such representation can be made stable by enforcing a symmetry acting on the DM only (for multiplets with $n \geq 5$ such a symmetry arises accidentally in the renormalizable Lagrangian). However, we shall see that in general this can require additional assumptions about the completion of the theory at some high UV scale. Within class ii), we can further distinguish two subclasses of complex WIMPs: a) complex representations with $Y = 0$ and odd n; b) complex representations with $Y \neq 0$ with even n (odd n) for half-integer Y (integer Y). The subclass a) is a straightforward generalization of the class i) models (analyzed in [47]) where the stability of the DM is guaranteed by an unbroken dark fermion number which can be gauged as was first done in Ref. [96]. For completeness, we give the freeze-out prediction of these scenarios in App. E. The subclass b) is *non-minimal*: the neutral particle is a Dirac (Complex) particle in the fermionic (scalar) case respectively,

and in general it has a non-zero coupling to the Z boson. To avoid direct detection bounds, these neutral degrees of freedom must mix, so that in the physical mass basis there are two Majorana (real) fermionic (scalar) particles with a non-zero mass splitting. In this way, the scattering mediated by the Z is inelastic: if the mass gap between the two neutral particles is large enough, the scattering of DM with the detectors nuclei is kinematically suppressed. In this non-minimal realization, the fact that the neutral particle is the lightest is not guaranteed, and such condition must be enforced with the help of non-renormalizable operators (which represents the mixing with states heavier than the cutoff of these operators).

The main purpose of this Chapter is to study how to experimentally exclude all the possible EW charge assignments, indicated with the symbol n_Y. In order to do so, it is pivotal to accurately compute the DM thermal mass.

For any given n_Y-plet, computing the EW annihilation cross-section in the early Universe allows to infer the WIMP cosmological abundance, and therefore its mass. By requiring it to match the measured value of the DM abundance today, $\Omega_{\rm DM}h^2 = 0.11933 \pm 0.00091$ [23], the mass of the n-plet can be univocally determined. These mass predictions are an essential input to assess if and how the future experimental program will be able to fully test the EW WIMP scenario. In contrast to previous papers on the subject [43, 50, 52, 95, 96], our approach here is to minimize the theory assumptions and fully classify the *calculable* freeze-out predictions. Because of its infrared-dominated nature, the calculability of freeze-out depends purely on the partial wave unitarity of the total annihilation cross-section [97], which we re-analyze here for EW n-plets. All in all, demanding perturbative unitarity requires $n \leq 13$ for both bosonic and fermionic DM. Approaching this boundary the theory uncertainty on the mass prediction grows as shown in Fig. 2.1. Stronger constraints on n can be imposed by demanding the EW interactions to remain perturbative up to scales well above the thermal DM mass.

The effects of Sommerfeld enhancement (SE) and of bound state formation (BSF) are known to significantly affect the freeze-out predictions and need to be included. The first effect has long been recognized to lead to an enhancement of the annihilation cross-section at small relative velocities [49, 98, 99, 100]. The effects of BSF for WIMP freeze-out have been first computed in Ref. [51] for the $n = 5, Y = 0$ fermionic multiplet (see Ref.s [101, 102] for earlier computations in other contexts). Here we extend their treatment to fermionic and scalar representations of arbitrary high n, up to the break-down of perturbative unitarity. At growing n, we find that bound states (BS) are more tightly bound, with their ionization rate being exponentially suppressed. At the same time, the multiplicity of accessible BS channels grows significantly. These two effects result in an increase of the annihilation cross-section compared to the estimates of Ref. [103].

The freeze-out mass predictions are summarized in Table 2.1, Table 2.2 and Fig. 2.1 for the real and complex n-plets considered here. With masses ranging from several TeV to tens or hundreds of TeV, most of the EW WIMP candidates are still out of reach of present experiments, but could be tested in the future, thanks to the forthcoming progress in collider physics and DM detection experiments. With the

mass predictions at hand, we thus commence a systematic survey of the WIMP phenomenology: *i*) at very high energy lepton colliders up to 30 TeV center of mass energy [53, 104, 105, 106, 107]; *ii*) at direct detection experiments with 100 tons/year of exposure like DARWIN [54, 108]; These two methods of detection can in the future be able to exclude the WIMP paradigm. We comment in Sec. 2.7.1 the possibility to study heavier WIMPs at high-energy γ-ray telescopes like CTA [55, 109, 110, 111].

We first examine the reach of a hypothetical future muon collider, studying in detail for which values of center-of-mass energy and integrated luminosity the candidates with $n \leq 5$ can be fully probed through direct production.

We instead find direct production of the EW multiplets with $n > 5$ to be beyond the reach of any realistic future machine (this is in contrast with the results of the recent study [112] due to the increase of the thermal mass of higher n-plets with the inclusion of BSF effects). These larger n-plets are possibly within the reach of large exposure direct detection experiments, and will probably be tested more easily with future high energy γ-ray telescopes. A careful study of the expected signals in indirect detection is left for future works, given the large theoretical uncertainties.

This Chapter is organized as follows. In Sec. 2.1, Sec. 2.2 we summarize the EW WIMP paradigm, discussing the real and complex case respectively. in Sec. 2.3 we illustrate the main features of our freeze-out computations. We discuss them only for the real candidates for clarity purposes, leaving the complex case to App. C. These sections provide a full explanation on the results of Table 2.1, Table 2.2 and Fig. 2.1. In Sec. 2.4 we discuss the implications of our study for a future muon collider, while in Sec. 2.5 and Sec. 2.7 we briefly re-examine the reach of direct detection experiments and other indirect probes respectively in light of our findings.

2.1 Which Real WIMP?

At the renormalizable level, the extensions of the SM that we consider are

$$\mathscr{L}_{\rm s} = \frac{1}{2}\left(D_\mu \chi\right)^2 - \frac{1}{2}M_\chi^2 \chi^2 - \frac{\lambda_H}{2}\chi^2|H|^2 - \frac{\lambda_\chi}{4}\chi^4\,, \tag{2.1}$$

$$\mathscr{L}_{\rm f} = \frac{1}{2}\chi\left(i\bar{\sigma}^\mu D_\mu - M_\chi\right)\chi\,, \tag{2.2}$$

for scalars and fermions, respectively, where $D_\mu = \partial_\mu - i g_2 W_\mu^a T_\chi^a$ is the covariant derivative, and T_χ^a are generators in the n-th representation of $\mathrm{SU}(2)_{\rm L}$. The Lagrangian for the real scalar in Eq. (2.1) also admits quartic self-coupling and Higgs-portal interactions at the renormalizable level. The latter is bounded from above by direct detection constraints (see Fig. 2.16 right) and gives a negligible contribution to the annihilation cross-section.[1]

The neutral component and the component with charge Q of the EW multiplet are splitted by radiative contributions from gauge boson loops. In the limit $m_W \ll M_{\rm DM}$

[1] No other quartic coupling is allowed since $\chi T_\chi^a \chi$ identically vanishes. Indeed, $(T_\chi^a)_{ij}$ is antisymmetric in i, j, being the adjoint combination of two real representations, while $\chi_i \chi_j$ is symmetric.

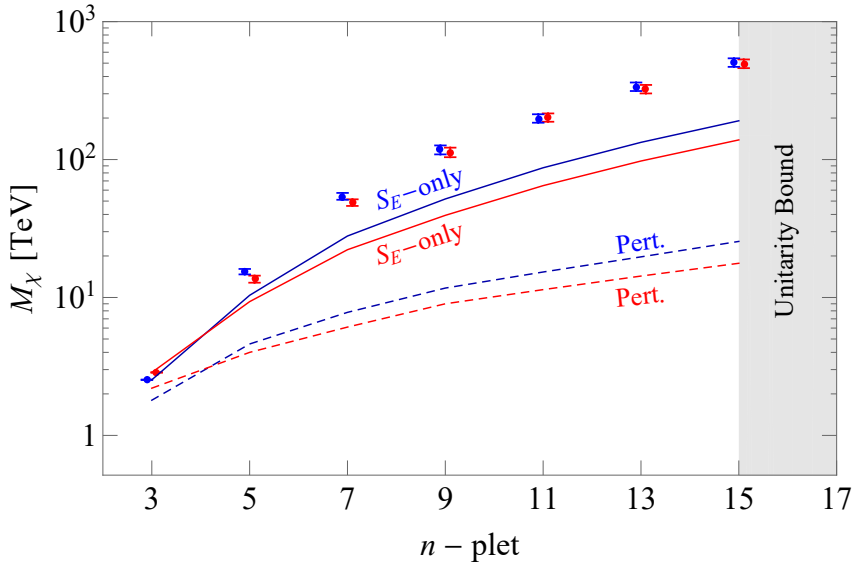

Figure 2.1: *Summary of the thermal masses for Majorana fermion (red) and real scalar WIMPs (blue) including both Sommerfeld enhancement (SE) and bound state formation (BSF). The solid lines are the thermal masses with SE. The dashed lines are the thermal masses for the hard annhilation cross-section. The gray shaded region is excluded by s-wave perturbative unitarity including BSF.*

these contributions are non-zero and independent on M_χ. This fact can be understood by computing the Coulomb energy of a charged state at distance $r \gtrsim 1/m_W$ or the IR mismatch (regulated by m_W) between the self-energies of the charged and neutral states. The latter can be easily computed at 1-loop [115, 116, 117],

$$M_Q - M_0 \simeq \frac{Q^2 \alpha_{\rm em} m_W}{2(1+\cos\theta_W)} = Q^2 \times (167 \pm 4)\ \text{MeV}\ , \tag{2.3}$$

with the uncertainty dominated by 2-loop contributions proportional to $\alpha_2^2 m_t/16\pi$. These have been explicitly computed in Ref.s [118, 119] giving a precise prediction for the lifetime of the singly-charged component, which decays to the neutral one mainly by emitting a charged pion with

$$c\tau_{\chi^+} \simeq \frac{120\ \text{mm}}{T(T+1)}\ , \tag{2.4}$$

where $2T+1 = n$. The suppression of the lifetime with the size of the EW multiplet can be understood in the $M_\chi \gg m_W$ limit where the mass splitting between the charged and neutral components is independent of n while the coupling to W is controlled by $\sqrt{T(T+1)/2}$. As we will discuss in Sec. 2.4.2, the production of a singly charged DM component at colliders gives the unique opportunity of probing EW multiplets with $n = 3$ and $n = 5$ through disappearing tracks [43, 112, 120, 121, 122].

Interestingly, the IR generated splitting from gauge boson loops is not modified substantially by UV contributions. The latter are generated only by dimension 7

DM spin	EW n-plet	M_χ (TeV)	$(\sigma v)^{J=0}_{\rm tot}/(\sigma v)^{J=0}_{\rm max}$	$\Lambda_{\rm Landau}/M_{\rm DM}$	$\Lambda_{\rm UV}/M_{\rm DM}$
Majorana fermion	3	2.86 ± 0.01	–	2.4×10^{37}	$2 \times 10^{12*}$
	5	13.6 ± 0.8	0.003	5.5×10^{17}	3×10^{12}
	7	48.8 ± 3.3	0.019	1.2×10^{4}	1×10^{8}
	9	113 ± 15	0.07	41	1×10^{8}
	11	202 ± 43	0.2	6	1×10^{8}
	13	324.6 ± 94	0.5	2.6	1×10^{8}
Real scalar	3	2.53 ± 0.01	–	2.4×10^{37}	$4 \times 10^{24*}$
	5	15.4 ± 0.7	0.002	7×10^{36}	3×10^{24}
	7	54.2 ± 3.1	0.022	7.8×10^{16}	2×10^{24}
	9	117.8 ± 15.4	0.088	3×10^{4}	2×10^{24}
	11	199 ± 42	0.25	62	1×10^{24}
	13	338 ± 102	0.6	7.2	2×10^{24}

Table 2.1: *Freeze-out mass predictions for WIMP DM in real EW multiplets with $Y = 0$. The annihilation cross-section includes both the contribution of SE and BSF. We provide a measure of how close the DM annihilation cross-section is to the unitarity bound for s-wave annihilation $(\sigma v)^{J=0}_{max} = 4\pi/M^2_{DM} v$. Approaching the unitarity bound, the error on the WIMP mass grows proportionally to the enhancement of the next-to-leading order (NLO) contributions estimated in Eq. (D.4). We derive the scale where EW gauge coupling will develop a Landau pole by integrating-in the WIMP multiplet at its freeze-out mass. The stability of both scalar and fermionic DM can always be enforced by requiring a $\mathbb{Z}_2$ symmetry in the DM sector to forbid DM decays. This symmetry forbids the scalar and fermionic 3-plets decay at renormalizable level as indicated by the *. The value of the UV cut-off Λ_{UV} gives an idea of the required* quality *for this symmetry to make DM stable and avoid stringent bounds on decaying DM ($\tau_{DM} > 10^{28} sec$) [113]: a new physics scale lower than Λ_{UV} would require a $\mathbb{Z}_2$ to explain DM stability, while a cut-off higher than Λ_{UV} would make DM stability purely accidental.*

(dimension 6) operators if the DM is a Majorana fermion (real scalar) and can be written as

$$\Delta\mathscr{L}_I \supset \frac{c_I}{\Lambda^{n_I}_{\rm UV}} \chi^a \chi^b (H^\dagger T^a H)(H^\dagger T^b H) \ , \tag{2.5}$$

with $n_I = 3, 2$ for $I = f, s$. This corresponds to a splitting $\Delta M_I \simeq c_I v^4/\Lambda^{n_I}_{\rm UV} M_\chi^{3-n_I}$ which is always negligible with respect to the residual error on the 2-loop splitting for $\Lambda_{\rm UV} \gtrsim 100$ TeV and $c_I \sim \mathcal{O}(1)$. This is different from the complex WIMP, in which the charged states lifetimes are free parameters.

Requiring perturbativity of the EW gauge coupling above the WIMP thermal mass can provide an upper bound on the dimension of the $\mathrm{SU(2)_L}$ representation. Indeed, large $\mathrm{SU(2)_L}$ n-plets will make the EW gauge coupling run faster in the UV, eventually leading to a Landau pole. In Table 2.1 we provide the value of the scale $\Lambda_{\rm Landau}$ such that $g_2(\Lambda_{\rm Landau}) = 4\pi$. We integrate the RGE equations for the SM gauge couplings at 2-loops and integrate-in the n-plet at the WIMP thermal mass.[2] Comparing $\Lambda_{\rm Landau}$ and $\Lambda_{\rm UV}$, we see that the stability of the fermionic n-plets with $n \leq 5$ only depends on physics in a regime where the EW coupling is still perturbative. Instead, the stability of n_0-plets with $n > 5$ requires specifying a UV completion

[2]Our results are compatible with the ones found in Ref. [123] (where χ is integrated-in at M_Z) given that $\Lambda_{\rm Landau}/M_{\rm DM}$ is approximately independent on $M_{\rm DM}$.

DM spin	n_Y	$M_{\rm DM}$ (TeV)	$\Lambda_{\rm Landau}/M_{\rm DM}$	$(\sigma v)^{J=0}_{\rm tot}(\sigma v)^{J=0}_{\rm max}$	δm_0 [MeV]	$\Lambda^{\rm max}_{\rm UV}/M_{\rm DM}$	δm_{Q_M} [MeV]
DC	$2_{\frac{1}{2}}$	1.08 ± 0.02	$> M_{\rm Pl}$	-	0.22 - $2 \cdot 10^4$	10^7	4.8 - 10^4
	3_1	2.85 ± 0.14	$> M_{\rm Pl}$	-	0.22 - 40	60	312 - 1.6 $\cdot 10^4$
	$4_{\frac{1}{2}}$	4.8 ± 0.3	$\simeq M_{\rm Pl}$	0.001	0.21 - $3 \cdot 10^4$	$5 \cdot 10^6$	20 - 1.9 $\cdot 10^4$
	5_1	9.9 ± 0.7	$3 \cdot 10^6$	0.003	0.21 - 3	25	$10^3 - 2 \cdot 10^3$
	$6_{\frac{1}{2}}$	31.8 ± 5.2	$2 \cdot 10^4$	0.01	0.5 - $2 \cdot 10^4$	$4 \cdot 10^5$	100 - $2 \cdot 10^4$
	$8_{\frac{1}{2}}$	82 ± 8	15	0.05	0.84 - 10^4	10^5	440 - 10^4
	$10_{\frac{1}{2}}$	158 ± 12	3	0.16	1.2 - $8 \cdot 10^3$	$6 \cdot 10^4$	$1.1 \cdot 10^3$ - $9 \cdot 10^3$
	$12_{\frac{1}{2}}$	253 ± 20	2	0.45	1.6 - $6 \cdot 10^3$	$4 \cdot 10^4$	$2.3 \cdot 10^3$ - $7 \cdot 10^3$
CS	$2_{\frac{1}{2}}$	0.58 ± 0.01	$> M_{\rm Pl}$	-	4.9 - $1.4 \cdot 10^4$	-	4.2 - $7 \cdot 10^3$
	3_1	2.1 ± 0.1	$> M_{\rm Pl}$	-	3.7 - 500	120	75 - 1.3 $\cdot 10^4$
	$4_{\frac{1}{2}}$	4.98 ± 0.25	$> M_{\rm Pl}$	0.001	4.9 - $3 \cdot 10^4$	-	17 - 2 $\cdot 10^4$
	5_1	11.5 ± 0.8	$> M_{\rm Pl}$	0.004	3.7 - 10	20	650 - 3 $\cdot 10^3$
	$6_{\frac{1}{2}}$	32.7 ± 5.3	$\simeq 6 \cdot 10^{13}$	0.01	4.9 - $8 \cdot 10^4$	-	50 - $5 \cdot 10^4$
	$8_{\frac{1}{2}}$	84 ± 8	$2 \cdot 10^4$	0.05	4.9 - 6 $\cdot 10^4$	-	150 - $6 \cdot 10^4$
	$10_{\frac{1}{2}}$	162 ± 13	20	0.16	4.9 - $4 \cdot 10^4$	-	430 - $4 \cdot 10^4$
	$12_{\frac{1}{2}}$	263 ± 22	4	0.4	4.9 - $3 \cdot 10^4$	-	10^3 - $3 \cdot 10^4$

Table 2.2: *Thermal masses of complex WIMPs with $Y \neq 0$, obtained including Sommerfeld enhancement and BSF. The upper bound on n for even multiplets comes from the perturbative unitarity bound, as can be seen from the $(\sigma v)^{J=0}_{tot}/(\sigma v)^{J=0}_{max}$, where $(\sigma v)^{J=0}_{max}$ is the maximal allowed annihilation cross section [97]. The loss of perturbativity is also signaled by the Landau pole Λ_{Landau} progressively approaching the DM mass. The upper bound on odd n with $Y = 1$ comes from the perturbativity of the higher dimensional operators generating δm_0 . For multiplets with $n > 5$ the largest UV cutoff Λ^{max}_{UV} required to generate the minimal viable splitting is smaller than $10 M_{DM}$. For each candidate we provide the allowed range for the mass splittings. The lower limit on δm_0 comes from strongest bound between direct detection and BBN as shown in Fig. 2.2. The upper bound from the most stringent condition between DD constraint from PandaX-4T [114] and the perturbativity of the coupling of $\mathcal{O}_0$ in Eq. (2.6). Similarly, the lower limit on δm_{Q_M} comes from the BBN bound on the charged state decay rate, while the upper limit from the strongest limit between DD and the perturbativity of the coupling of $\mathcal{O}_+$ in Eq. (2.6).*

for the EW gauge group that does not give rise to the dangerous operators listed in App. A.1. In this sense, the Majorana 5-plet studied in Ref. [43] is special, because it can be made accidentally stable by raising the scale $\Lambda_{\rm UV}$, without any further assumption on the nature of the UV completion at $\Lambda_{\rm Landau}$.

Requiring $\Lambda_{\rm UV}/M_\chi \gtrsim 10$ to ensure perturbativity of the theory up to well above the WIMP mass would select $n \leq 9$ for fermions, and $n \leq 11$ for scalars. However, requiring a large hierarchy between $\Lambda_{\rm Landau}$ and M_χ is not necessary to ensure the calculability of thermal freeze-out, which depends only on EW processes at energies much below the DM mass. A more robust upper bound on the dimension of the $\mathrm{SU(2)_L}$ n-plets will be derived in App. D, analyzing the s-wave unitarity of the annihilation cross-section. This bound will require $n \leq 13$ for both fermionic and scalar WIMPs. A further study including the NLO effects also on BSF is found in [124].

2.2 Which Complex WIMP?

In this section we focus on complex WIMPs with $Y \neq 0$ whose phenomenology differs substantially from the one with $Y = 0$. We focus here on the fermionic case and leave the discussion about the scalar WIMPs to App. B.2. The minimal Lagrangian for a fermionic complex WIMP with $Y \neq 0$ is:

$$\begin{aligned}
\mathscr{L}_{\rm D} &= \overline{\chi}\left(i\not{\partial} - M_\chi\right)\chi + \frac{y_0}{\Lambda_{\rm UV}^{4Y-1}}\mathcal{O}_0 + \frac{y_+}{\Lambda_{\rm UV}}\mathcal{O}_+ + \text{h.c.}\ , \\
\mathcal{O}_0 &= \frac{1}{2(4Y)!}\left(\overline{\chi}(T^a)^{2Y}\chi^c\right)\left[(H^{c\dagger})\frac{\sigma^a}{2}H\right]^{2Y}\ , \\
\mathcal{O}_+ &= -\overline{\chi}T^a\chi H^\dagger\frac{\sigma^a}{2}H\ ,
\end{aligned} \tag{2.6}$$

where T^a is a $\mathrm{SU}(2)_{\rm L}$ generator in the DM representation. The main difference with respect to real WIMPs is that the renormalizable Lagrangian is no longer sufficient to make the DM model viable. In Eq. (2.6) we write only the minimal amount of UV operators required to make the DM model viable. As we discuss in App. B.1 these operators are also unique and possibly accompanied by their axial counterparts. These are obtained from the ones in Eq. (2.6) by adding a γ_5 inside the DM bilinear. We now illustrate the physical consequence of $\mathcal{O}_0$ and $\mathcal{O}_+$ in turn in Sec. 2.2.1 and Sec. 2.2.2 and derive the implication for the viability of complex WIMPs in Sec. 2.2.3. In general none of the complex WIMPs with $Y \neq 0$ can be accidentally stable in the sense of Minimal Dark Matter [43]. Specific UV completions of the physics generating the inelastic splitting in Eq. (2.8) might allow for DM accidental stability. This question goes beyond the scope of this study. Conversely, complex WIMPs with $Y = 0$ can be accidentally stable thanks to the gauging of the unbroken $U(1)$ flavor symmetry in the DM sector [96]. The freeze-out predictions for these millicharged WIMPs are given in App. E. We comment on DM stability in App. A.

Our results are summarized in Table 2.2, whose logic can be explained as follows. Once the DM mass is fixed from the freeze-out predictions, the phenomenology of complex WIMPs depends essentially on two parameters: i) the "inelastic" splitting between the-next-to lightest neutral component and the DM; ii) the "charged" splitting between the charged components and the DM. In our setup these splittings are generated by its (non-renormalizable) interactions with the SM Higgs (generated by unspecified UV dynamics).

The inelastic splitting δm_0 is bounded from below by DD constraints [125, 126] and BBN constraints on the decay of the next to lightest neutral component. Interestingly, this requirement alone selects a limited number of complex WIMPs: i) scalar and fermionic WIMPs with $Y = 1/2$ and even n up to the unitarity bound of the freeze-out annihilation cross section [97]; ii) scalar and fermionic WIMPs with $Y = 1$ and $n = 3, 5$. Multiplets $Y = 1$ and $n > 5$ or with higher hypercharges are excluded. At the same time, the inelastic splitting is bounded from above by DD constraints on Higgs-mediated nuclear recoils. This leaves a finite window for the inelastic splitting of every multiplet which we report in Table 2.2. This window will be further

probed by large exposure DD experiments such as LZ [127], XENONnT [128], and ultimately by DARWIN/G3 [54, 129].

The natural value of the charged splitting δm_Q is fixed by the radiative EW contributions [115, 116, 117] but (non-renormalizable) interactions with the SM Higgs can induce large deviation from this value. In particular, for all the n-plets with non-maximal hypercharge, these interactions are required to make the DM stable.

The allowed range of the two splittings above controls the hierarchy of the states within the EW multiplet. In this parameter space one can map out the expected signals in a future hypothetical muon collider [130]. Depending on the lifetime of the charged states we can have different signatures at colliders: i) long lived charged tracks; ii) disappearing tracks (DT); iii) missing energy accompanied by an EW bosons. While the first two searches rely on the macroscopic decay length of the charged states, the last is directly related to the DM pair production recoiling against one (or more) EW boson. In general, a future muon collider could complement the large exposure DD experiments in probing complex WIMPs in regions of the parameter space where the DD drops below the neutrino floor of xenon experiments [131].

2.2.1 Inelastic splitting

The non-renormalizable operator $\mathcal{O}_0$ is required to remove the sizeable coupling to the Z boson of the neutral component χ_N of the EW multiplet

$$\mathscr{L}_Z = \frac{ieY}{\sin\theta_W \cos\theta_W} \overline{\chi}_N \not{Z} \chi_N \ . \tag{2.7}$$

This coupling would lead to an elastic cross section with nuclei already excluded by many orders of magnitude by present DD experiments [132]. After the EWSB, $\mathcal{O}_0$ induces a mixing between χ_N and χ_N^c. Replacing the Higgs with its VEV, $(H^{c\dagger})\frac{\sigma^a}{2}H$ is non-zero only if we pick $\sigma^a = \sigma^+$, so that the new (pseudo Dirac) mass term in the Lagrangian reads

$$\begin{aligned} \mathscr{L}_m &= M_\chi \overline{\chi}_N \chi_N + \frac{\delta m_0}{4} \left[\overline{\chi}_N \chi_N^c + \overline{\chi^c}_N \chi_N\right], \\ \delta m_0 &= 4 y_0 c_{nY0} \Lambda_{\rm UV} \left(\frac{v}{\sqrt{2}\Lambda_{\rm UV}}\right)^{4Y} \ . \end{aligned} \tag{2.8}$$

$c_{nYQ} = \frac{1}{2^{Y+1}(4Y)!} \prod_{j=-Y-|Q|}^{Y-1-|Q|} \sqrt{\frac{1}{2}\left(\frac{n+1}{2}+j\right)\left(\frac{n-1}{2}-j\right)}$ contains the normalization of $\mathcal{O}_0$ and the matrix elements of the generators. The mass eigenstates are Majorana fermions, χ_0 and $\chi_{\rm DM}$, with masses $M_0 = M_\chi + \delta m_0/2$ and $M_{\rm DM} = M_\chi - \delta m_0/2$, whose coupling to the Z boson is

$$\mathscr{L}_Z = \frac{ieY}{\sin\theta_W \cos\theta_W} \overline{\chi}_0 \not{Z} \chi_{\rm DM} \ . \tag{2.9}$$

The Z-mediated scattering of DM onto nucleons is no longer elastic and the process is kinematically forbidden if the kinetic energy of the DM-nucleus system in the center-of-mass frame is smaller than the mass splitting

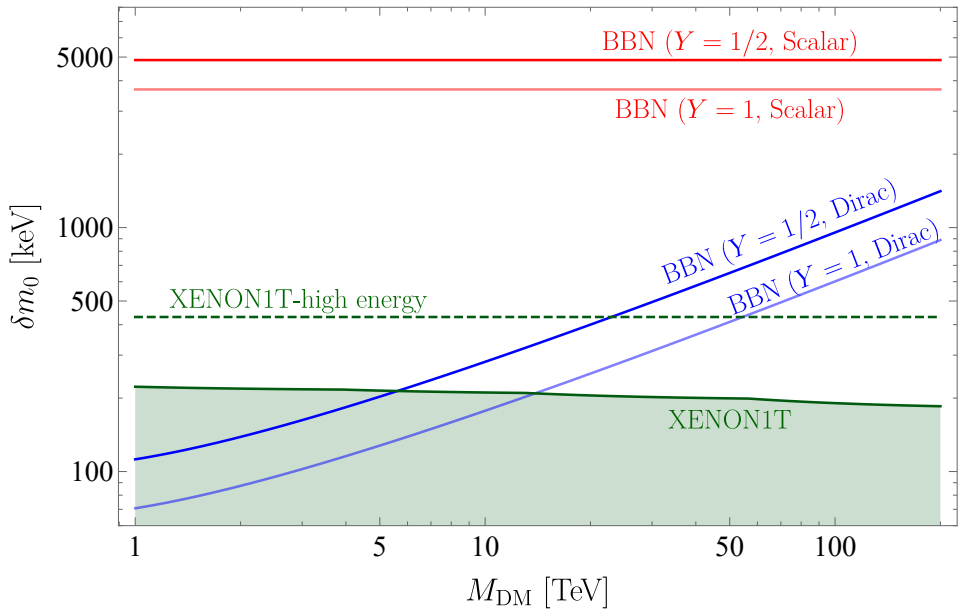

Figure 2.2: *Summary of the lower bounds on the neutral mass splitting. The* **dark green** *shaded region is excluded by tree-level Z-exchange in XENON1T [133] for both scalar and fermionic DM. The* **dashed green** *line shows what XENON1T could probe by analyzing high recoil energy data. The* **blue** *and* **red** *lines are the BBN bounds on the splitting for fermionic and scalar DM respectively.*

$$\frac{1}{2}\mu v_{\rm rel}^2 < \delta m_0 \ , \quad \mu = \frac{M_{\rm DM} m_N}{M_{\rm DM} + m_N} \ , \tag{2.10}$$

where m_N is the mass of the nucleus, μ is the reduced mass and $v_{\rm rel}$ is DM-nucleus relative velocity. In particular, given the upper bound on the relative velocity $v_{\rm rel} < v_{\rm E} + v_{\rm esc}$, where $v_{\rm E} = 240$ km/sec is the Earth's velocity and $v_{\rm esc} = 600$ km/sec is the assumed escape velocity of DM in the Milky Way, the largest testable mass splitting is $\delta m_0^{\rm max} = 1/2\mu(v_{\rm E} + v_{\rm esc})^2$ which for xenon nuclei gives $\delta m_0^{\rm max} \simeq 450$ keV. The splitting for a given recoil energy is

$$\delta m_0(E_R) = \sqrt{2 m_N E_R}(v_{\rm E} + v_{\rm esc}) - E_R \frac{m_N}{\mu} \ , \tag{2.11}$$

which explain why the maximal constrained splitting experimentally is $\delta m_0^{\rm max,exp} \simeq 240$ keV as shown in Fig. 2.2, given that XENON1T [133] analyzed data only for $E_R < 40$ keV. Extending the range of XENON1T to higher recoil energies would be enough to probe splitting up to $\delta m_0^{\rm max}$ as already noticed in Ref. [125, 126].

In principle, larger mass splittings can be reached using heavier recoil targets than xenon such as iodine in PICO-60 [134], tungsten in CRESST-II [135], $CaWO_4$ [136], $PbWO_4$ [137], ^{180}Ta [138], Hf [139] and Os [140]. However, these experiments currently do not have enough exposure to probe EW cross-sections.

A complementary bound on δm_0 comes from requiring that the decay $\chi_0 \to \chi_{\rm DM}$+SM happens well before BBN. The leading decay channels are $\chi_0 \to \chi_{\rm DM}\gamma$, $\chi_0 \to \chi_{\rm DM}\bar{\nu}\nu$

and $\chi_0 \to \chi_{\rm DM} \bar{e} e$ with decay widths

$$\Gamma_\gamma = \left(1 + \frac{1}{2}\log\left(\frac{m_W^2}{M_{\rm DM}^2}\right)\right)^2 \frac{Y^2 \alpha_2^2 \alpha_{\rm em}}{\pi^2} \frac{\delta m_0^3}{M_{\rm DM}^2} \,, \tag{2.12}$$

$$\Gamma_{\bar{\nu}\nu} \simeq 6\Gamma_{\bar{e}e} = \frac{G_F^2 \delta m_0^5 Y^2}{5\pi^3} \,. \tag{2.13}$$

The first process is induced by a dipole operator generated at 1-loop for fermionic DM as computed in [141]. The three body decays are instead induced at tree-level by the EW interactions both for fermionic and scalar DM. For fermionic DM, the dipole-induced decay dominates the width in the mass range of interest. In order for these processes not to spoil BBN, we have to impose the following condition on the decay rate of χ_0:

$$\Gamma_{\chi_0} \equiv \Gamma_{\bar{\nu}\nu} + \Gamma_{\bar{e}e} + \Gamma_\gamma > \tau_{\rm BBN}^{-1} \,, \tag{2.14}$$

where $\tau_{\rm BBN}^{-1} = 6.58 \times 10^{-25}$ GeV. The lower bounds on the neutral mass splitting for fermions are shown in Fig. 2.2 together with those for scalars computed in App. B.2. The main difference between scalars and fermions is that the former are typically more long lived due to the suppression of $\chi_0 \to \chi_{\rm DM}\gamma$. As a consequence the BBN bounds are stronger for scalar WIMPs.

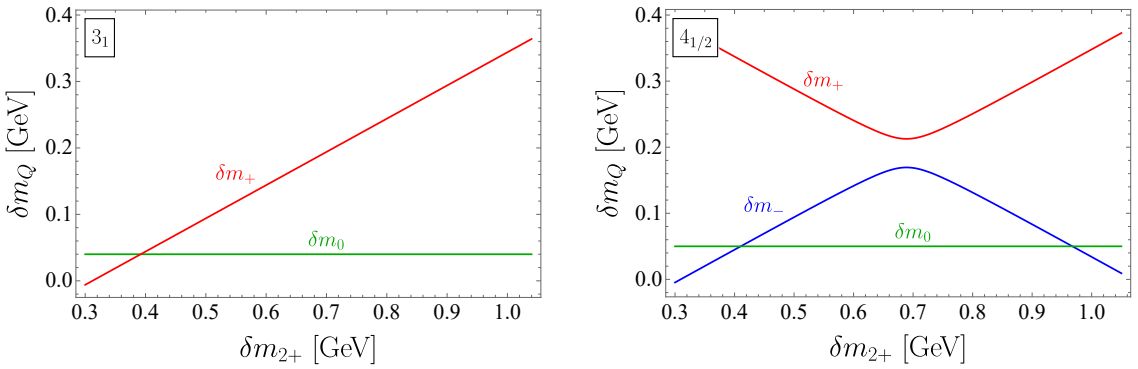

Figure 2.3: *Mass splittings of* 3_1 *(left) and* $4_{1/2}$ *(right) as a function of* δm_{2+}*. In the* 3_1 *case, no mixing between the charged components of the multiplet can occur and* δm_+ *is a monotonic function of* δm_{2+}*. In the* $4_{1/2}$ *case, instead, because of the mixing induced by* $\mathcal{O}_0$*, the positively charged mass eigenstate* χ^+ *is always heavier than* χ^-*. The splitting between* χ^+ *and* χ^- *has a minimum of order* δm_0*, which was taken 50 MeV in this plot for display purposes.*

2.2.2 Charged splitting

The operator $\mathcal{O}_+$ in Eq. (2.6) is necessary to make the DM the lightest state in the EW multiplet for all the n-plets whose hypercharge is not maximal. Indeed, EW interactions induce at 1-loop mass splittings between the charged and the neutral components of the EW multiplet which in the limit $m_W \ll M_\chi$ are [115, 116, 117]

$$\Delta M_Q^{\rm EW} = \delta_g \left(Q^2 + \frac{2YQ}{\cos\theta_W}\right) \,, \tag{2.15}$$

where $\delta_g = (167 \pm 4)$ MeV and $Q = T_3 + Y$. This implies that negatively charged states with $Q = -Y$ are pushed to be lighter than the neutral ones by EW interactions. Notable exceptions are odd-n multiplets with $Y = 0$ where one recovers Eq. (2.3) and all the multiplets with maximal hypercharge $|Y_{\rm max}| = (n-1)/2$ where negatively charged states are not present. For these multiplets, having $y_+ = 0$ would be the minimal and phenomenologically viable choice.

Including the contribution of $\mathcal{O}_+$, the final splittings $\delta m_Q = M_Q - M_{\rm DM}$ between the DM and the charged components read

$$\delta m_Q = \frac{\delta m_0}{2} + \delta_g Q^2 + \mathrm{sgn}(Q)\sqrt{\left(\frac{2Y\delta_g}{\cos\theta_W} - \frac{y_+ v^2}{4\Lambda_{\rm UV}}\right)^2 Q^2 + \frac{\delta m_0^2}{4}\frac{c_{nYQ}^2}{c_{nY0}^2}}\,, \tag{2.16}$$

where $\mathrm{sgn}(Q)$ in Eq. (2.16) accounts for the presence of opposite charge states that are not related by charge conjugation, as implied by to the non-zero hypercharge of our WIMPs. The second term inside the square root comes from the mixing between the charged gauge eigenstates χ_Q and χ^c_{-Q} induced by $\mathcal{O}_0$. This obviously vanishes for $Q > (n-1)/2 - Y$.

The different charged-neutral mass splittings can all be written in terms of two independent splittings, which we choose to be δm_0 and δm_{Q_M}, where $Q_M \equiv Y + (n-1)/2$ is the largest electric charge in the multiplet. Since $c_{nYQ_M} = 0$, δm_{Q_M} is a monotonic function of y_+ and Eq. (2.16) can be inverted. In Fig. 2.3 we show as an example the mass splittings of 3_1 and $4_{1/2}$ as a function of δm_{2+}. In the former case, no mixing occur within the components of the multiplet and δm_+ is a monotonic function of δm_{2+}. For the $4_{1/2}$, instead, the mixing induced by $\mathcal{O}_0$ between the components with $Q = \pm 1$ makes the positively charged mass eigenstate χ^+ heavier than χ^-.

In Sec. 2.5.2 we will explore the parameter space spanned by δm_0 and δm_{Q_M}, fixing the thermal DM mass of every EW multiplet as shown in Table 2.2. Crucially, the operators inducing the splitting in Eq. (2.6) also generate new Higgs-exchange contributions to the spin-independent scattering cross-section of DM on nucleons. Therefore, the current best upper limit on the DM elastic cross section onto nucleons set by PandaX-4T [114] translates into upper bounds on the neutral and charged splittings as reported in Table 2.2.

Charged-neutral splittings smaller than the EW one in Eq. (2.15) require a certain amount of fine-tuning between UV operators and the EW contribution. To quantify this we define the Fine Tuning (F.T.)

$$\text{F.T.} \equiv \max_I \left[\frac{\mathrm{d}\log \delta m_Q}{\mathrm{d}\log \delta m_I}\right]\,, \tag{2.17}$$

where the index I runs over the three contributions in the definition of δm_Q in Eq. (2.16). Large values of F.T. imply a significant amount of cancellation between two or more parameters.

2.2.3 Viable complex WIMPs

The EFT approach used to write Eq. (2.6) is meaningful only if the UV physics generating $\mathcal{O}_+$ and $\mathcal{O}_0$ is sufficiently decoupled from DM. When $\Lambda_{\rm UV}$ approaches the DM mass the cosmological evolution of the DM multiplet cannot be studied in isolation, since the heavy degrees of freedom populates the thermal bath at $T \simeq M_{\rm DM}$ and are likely to modify our freeze-out predictions. To avoid these difficulties we restrict ourselves to $\Lambda_{\rm UV} \geq 10 M_{\rm DM}$. Notice that this choice is conservative since freeze-out happens at $T \ll M_\chi$.

This condition, together with the required inelastic splittings in Fig. 2.2, can be used to select the viable complex WIMPs. Starting from Eq. (2.8) and imposing $\delta m_0 > \delta m_0^{\rm min}$, we derive the viable window for $\Lambda_{\rm UV}$:

$$10 M_{\rm DM} < \Lambda_{\rm UV} \leq \left(\frac{4 y_0 c_{nY0} v^{4Y}}{2^{2Y} \delta m_0^{\rm min}} \right)^{\frac{1}{4Y-1}} . \tag{2.18}$$

We are now interested in estimating for which multiplets the viable window shrinks to zero. Setting $y_0 = (4\pi)^{4Y}$ in Eq. (2.18) that is the largest value allowed by Naive Dimensional Analysis (NDA) we derive the values of n and Y having a non zero cutoff window in Eq. (2.18). These are for both scalar and fermionic WIMPs $n_{1/2}$ multiplets with $n \leq 12$ together with the 3_1 and the 5_1 mupltiplets.

This result can be understood as follows. The upper bounds on n for $Y = 1/2$ multiplets come from the perturbative unitarity of the annihilation cross section as discussed in App. D. The maximal cutoff required to obtain the phenomenologically viable splittings is of order $\sim 10^7$ TeV as shown in the fifth column of Table 2.2. This is many orders of magnitude larger than the DM masses allowed by freeze-out so that Eq. (2.18) results in a wide range of allowed $\Lambda_{\rm UV}$.

For $Y = 1$ multiplets the maximal required cutoff is of order $\sim 10^2$ TeV so that the n-dependence of the allowed window in Eq. (2.18) becomes relevant. Given that the DM mass grows with n as $M_{\rm DM} \sim n^{5/2}$ and the required cutoff stay approximately constant, we expect the allowed window to shrink to zero for large n. Numerically we find that the last allowed multiplet has $n = 5$.

We refer to App. B.2 for a similar argument for scalar WIMPs. These have a slightly different parametric which however results in the same viable EW multiplets of the fermionic case.

We now introduce the *minimal splitting* benchmark: that is when the mass splittings are chosen to be the smallest possible allowed by the requirements of the previous section. For fermions, we set $\delta m_0 = 220$ keV for $n_{1/2}$ WIMPs with $n \leq 4$ as well as for the allowed n_1 WIMPs. For $n_{1/2}$ WIMPs with $n > 4$ the BBN bound in Fig. 2.2 gives the minimal δm_0. For scalars instead, we set $\delta m_0 = 4.9$ MeV for $n_{1/2}$ and $\delta m_0 = 3.7$ MeV for n_1 WIMPs, both coming from BBN.

In this minimal setup, $2_{1/2}$ and 3_1 stand out as the only two multiplets where the DM is automatically the lightest state, with a splitting with the $Q = 1$ state given by the pure EW splitting in Eq. (2.15) that is 354 MeV for $2_{1/2}$ and 542 MeV for 3_1.

For all the other WIMPs a UV generated splitting is needed to make the DM lighter than the negatively charged states. We fix this splitting to the smallest possible value that gives the DM as the lightest state. As can be seen from Eq. (2.16) this requires a UV splitting which is of the order of the EW one.

This is useful to study the complex WIMPs in the minimal setup. We will explore in Sec. 2.6 what happen in the *non-minimal* scenario, in which the splittings are allowed to vary.

2.3 WIMP cosmology

The determination of the DM thermal mass hinges on a careful computation of the DM annihilation cross-section in the non-relativistic regime. This require the inlcusion of non-perturbative effects such as Sommerfeld Enhancement (SE) and Bound State Formation (BSF). To discuss the impact of such effects, we will discuss only the real WIMP scenario: in the complex case they can also arise from the exchange of the weak hypercharge boson, but the qualitative picture does not change, and it will be discussed in App. C. For real WIMPs, the potential is generated by $\mathrm{SU}(2)_\mathrm{L}$ gauge boson exchange between DM pairs. It is attractive for isospins $I \lesssim \sqrt{2}n$, resulting into Bound State Formation (BSF) through the emission of an EW gauge boson in the final state. The energy of the emitted gauge boson is of the order of the Bound State (BS) binding energy $E_{B_I} \simeq \frac{\alpha_{\rm eff}^2 M_\chi}{4n_B^2} - \alpha_{\rm eff} m_W$, where n_B is the BS energy level, $\alpha_{\rm eff}$ is the effective weak coupling defined in Eq. (2.28), and we neglected corrections of order m_W^2/M_χ^2. In the non-relativistic limit, and at leading order in gauge boson emission, the BSF process

$$\chi_i + \chi_j \to \mathrm{BS}_{i'j'} + V^a \tag{2.19}$$

is encoded in the effective dipole Hamiltonian described in Ref. [51, 142] which dictates the BS dynamics.

$$\begin{aligned} \mathscr{H}_I^{\rm LO} = \; & -\frac{g_2}{M_\chi}\left(\vec{A}^a(\vec{x}_1)\cdot\vec{p}_1 T^a_{i'i}\delta_{j'j} + \vec{A}^a(\vec{x}_2)\cdot\vec{p}_2 \overline{T}^a_{j'j}\delta_{i'i}\right) + \\ & + g_2\alpha_2\left(\vec{A}^a(0)\cdot\hat{r}e^{-M_a r}\right) T^b_{i'i}\overline{T}^c_{j'j} f^{abc}\,, \end{aligned} \tag{2.20}$$

where the first to terms are a simple generalization of the standard QED dipole interaction while the last one is a purely non-abelian term which arises from vector boson emission from a vector line.

The BS dynamics relevant for DM freeze-out is well described by the unbroken phase of $\mathrm{SU}(2)_\mathrm{L}$ so that the configuration of the DM pair can be decomposed into eigenstates of the isospin I of the pair

$$|\chi\chi\rangle_{II_z} = \mathcal{C}(II_z|ij)|\chi_i\chi_j\rangle, \;\; I_z \in \left[-\frac{I-1}{2}, \frac{I-1}{2}\right], \tag{2.21}$$

where $\mathcal{C}(II_z|ij)$ are the Clebsch-Gordan coefficients and I is the dimension of the isospin representation. Denoting with L and S the total angular momentum and the spin, the isospin-Lorentz structure of the dipole Hamiltonian enforces the following selection rules: *i)* $\Delta S = 0$ because the dipole Hamiltonian is spin-independent; *ii)* $|\Delta L| = 1$ because the dipole operator transform as a vector under rotations; *iii)* $|\Delta I| = 2$ because a single, G-parity odd weak boson is emitted.

Since we are dealing with real representations, spin-statistics imposes further restrictions on the allowed quantum numbers, depending on the fermionic or scalar nature of the wave function. In particular we have

$$(-1)^{L+S+\frac{I-1}{2}} = 1 \ , \tag{2.22}$$

which implies that for scalars $n_B s$ ($n_B p$) bound states, *i.e.* with $L = 0$ ($L = 1$), can exist only with even (odd) $\frac{I-1}{2}$, while for fermions odd (even) $\frac{I-1}{2}$ states with $L = 0$ are forced to have $S = 1$ ($S = 0$).

We are now ready to describe the system of coupled Boltzmann equations for the evolution of the number densities of DM and BS. Following [51], we will discuss how this coupled system can be reduced to a single equation for the DM number density with an effective annihilation cross-section. The Boltzmann equations for DM and BS read

$$z\frac{\mathrm{d}Y_{\rm DM}}{\mathrm{d}z} = -\frac{2s}{H}\langle\sigma_{\rm ann}v_{\rm rel}\rangle\left[Y_{\rm DM}^2 - (Y_{\rm DM}^{\rm eq})^2\right] - \frac{2s}{Hz}\sum_{B_I}\langle\sigma_{B_I}v_{\rm rel}\rangle\left[Y_{\rm DM}^2 - (Y_{\rm DM}^{\rm eq})^2\frac{Y_{B_I}}{Y_{B_I}^{\rm eq}}\right] \ , \tag{2.23a}$$

$$z\frac{\mathrm{d}Y_{B_I}}{\mathrm{d}z} = Y_{B_I}^{\rm eq}\Bigg\{\frac{\langle\Gamma_{B_I,\rm break}\rangle}{H}\left[\frac{Y_{\rm DM}^2}{(Y_{\rm DM}^{\rm eq})^2} - \frac{Y_{B_I}}{Y_{B_I}^{\rm eq}}\right] + \frac{\langle\Gamma_{B_I,\rm ann}\rangle}{H}\left[1 - \frac{Y_{B_I}}{Y_{B_I}^{\rm eq}}\right] + \\ + \sum_{B_J}\frac{\langle\Gamma_{B_I\to B_J}\rangle}{H}\left[\frac{Y_{B_J}}{Y_{B_J}^{\rm eq}} - \frac{Y_{B_I}}{Y_{B_I}^{\rm eq}}\right]\Bigg\} \ , \tag{2.23b}$$

where $B_{I,J,\ldots}$ labels the different bound states, $z = \frac{M_\chi}{T}$, s is the entropy density and $Y = \frac{n}{s}$ is the number density per co-moving volume.

The dynamics of a given BS B_I in the plasma is described by Eq. (2.23b) and depends on: *i)* its ionization rate $\langle\Gamma_{B_I,\rm break}\rangle$; *ii)* its annihilation rate into SM states $\langle\Gamma_{B_I,\rm ann}\rangle$; *iii)* its decay width into other bound states $\langle\Gamma_{B_I\to B_J}\rangle$. The ionization rate $\langle\Gamma_{B_I,\rm break}\rangle \equiv n_\gamma\langle\sigma_{I,\rm break}v_{\rm rel}\rangle$ encodes the probability of a photons from the plasma to break the BS B_I. Assuming thermal equilibrium, detailed balance relates the cross-section for the BS breaking $\langle\sigma_{I,\rm break}v_{\rm rel}\rangle$ to the BSF cross-section $\langle\sigma_{B_I}v_{\rm rel}\rangle$

$$\langle\Gamma_{B_I,\rm break}\rangle = \frac{g_\chi^2}{g_{B_I}}\frac{(M_\chi T)^{\frac{3}{2}}}{16\pi^{\frac{3}{2}}}e^{-\frac{E_{B_I}}{T}}\langle\sigma_{B_I}v_{\rm rel}\rangle \ , \tag{2.24}$$

where g_{B_I} and g_χ count the number of degrees of freedom of the bound state B_I and of the DM multiplet, respectively. If either the BS decay or the annihilation rate satisfies $\Gamma \gg H$, we can neglect the LHS in Eq. (2.23b), obtaining algebraic relations between the DM and the BS yields.

Plugging these relations into Eq. (2.23a), we arrive at the final form of the DM Boltzmann equation

$$\frac{\mathrm{d}Y_{\rm DM}}{\mathrm{d}z} = -\frac{\langle\sigma_{\rm eff} v_{\rm rel}\rangle s}{Hz}(Y_{\rm DM}^2 - Y_{\rm DM}^{\rm eq,2}) \ , \tag{2.25}$$

where

$$\langle\sigma_{\rm eff} v_{\rm rel}\rangle \equiv S_{\rm ann}(z) + \sum_{B_J} S_{B_J}(z), \tag{2.26}$$

and we defined the effective cross-section as the sum of the direct annihilation processes, $S_{\rm ann}$, and the ones which go through BSF, S_{B_J}. In particular, $S_{\rm ann}$ can be written as

$$S_{\rm ann} = \sum_I \langle S_E^I \sigma_{\rm ann}^I v_{\rm rel}\rangle \ , \tag{2.27}$$

where $\sigma_{\rm ann}^I$ is the hard cross-section for a given isospin channel I, S_E^I is the Sommerfeld enhancement (SE) of the Born cross-section, and $v_{\rm rel}$ is the relative velocity of the two DM particles. In the limit of small relative velocity between the DM particles (but larger than m_W/M_χ), the SE factor can be approximated as

$$S_E^I \approx \frac{2\pi\alpha_{\rm eff}}{v_{\rm rel}} \ , \quad \text{where} \quad \alpha_{\rm eff} \equiv \frac{I^2+1-2n^2}{8}\alpha_2 \ . \tag{2.28}$$

The finite mass effects modify the behavior of the SE at $v_{\rm rel} \lesssim m_W/M_\chi$ and are included in our full computation (see Ref. [100] for explicit formulas). However, Eq. (2.28) will be enough to estimate the behavior of the SE at the temperatures most relevant for freeze-out.

Analogously we can factorize the BSF processes as

$$S_{B_J} = \sum_{I,l} \langle S_E^I S_{B_J}^{I,l}\rangle R_{B_J} \ , \tag{2.29}$$

where $S_{B_J}^{I,l}$ is the "hard" BSF cross-section of the state B_J starting from a free state with angular momentum l and isospin I multiplied by the SE factor of that particular isospin channel as defined in Eq. (2.28). Explicit expressions for this can be found in Ref. [51, 142]. R_{B_J} gives instead the effective annihilation branching ratio into SM states which depends on the detailed BS dynamics (*i.e.* annihilation, ionization and decay). In particular, R_{B_J} approaches 1 once the temperature of the plasma drops below the binding energies of the bound states involved in the decay chains.

In the case of a single BS, R_{B_J} takes a rather intuitive form

$$R_{B_J} = \frac{\langle\Gamma_{\rm ann}\rangle}{\langle\Gamma_{\rm ann}\rangle + \langle\Gamma_{\rm break}\rangle} \ , \tag{2.30}$$

which applies to $1s_I$ and $2s_I$ BS with $I \leq 5$. The latter, once formed, annihilate directly into pairs of SM vectors and fermions, with rates $\Gamma_{\rm ann} \simeq \alpha_{\rm eff}^5/n_B^2 M_\chi$. These BS together make up for more of the 50% of the BSF cross-section.

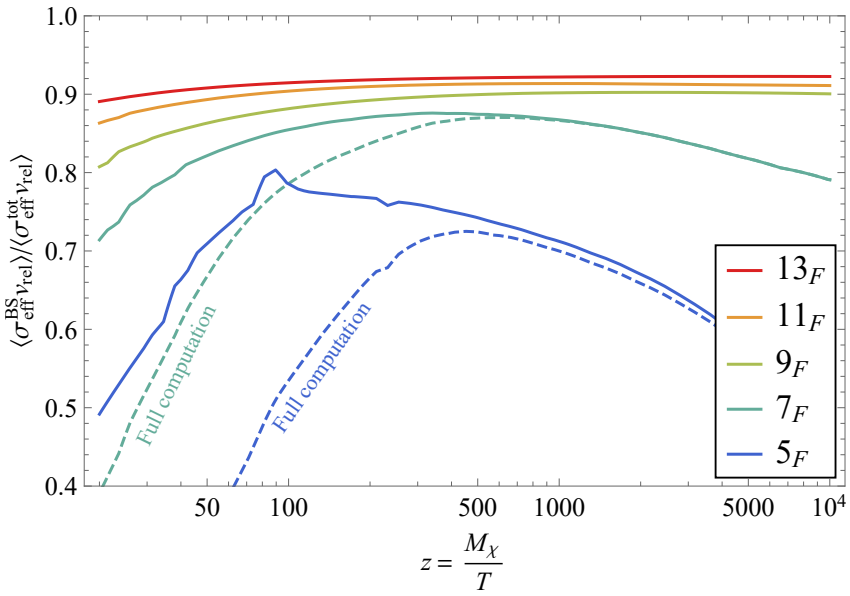

Figure 2.4: *Effective cross-section for BSF normalized over the total annihilation cross-section as a function of $z = M_\chi/T$ assuming vanishing ionization rates, i.e. $R_{BS} = 1$ (see Eq. (2.29) and below). The dashed lines for the fermionic 5-plet (dark blue) and 7-plet (cyan) show the deviation of the real bound state dynamics from the approximation of vanishing ionization rates. For $n > 5$ the error due to the $R_{BS} = 1$ is subdominant compared to the virtual and real effects at NLO in gauge boson emission.*

While the effect of BSF has already been computed for the fermionic 5-plet in Ref. [51], here we include it for the first time for all WIMP candidates. For larger EW multiplets, we find the relative effect of BS dynamics on the total cross-section increases, as can be seen from Fig. 2.4.

This is the consequence of two effects: *i*) the binding energy grows at large n, suppressing the ionization rate with respect to the annihilation one; *ii*) at larger n the number of attractive channels increases and thus the BS multiplicity per energy level grows linearly with n. For example, for $n = 5$ the attractive channels have $I = 1, 3, 5$, for $n = 7$ BS with $I = 7, 9$ can also form. The relevance of these higher isospin channels was not recognized in [103], where only the $I = 1, 3$ channels were included, significantly underestimating the thermal mass already for $n = 7$.

As we increase the dimension of the multiplet, the bound states become more tightly bounded and the effect of the ionization rate becomes smaller. This can be explicitly seen from Eq. (2.24) where the binding energy controls the Boltzmann suppression of the ionization rate. For this reason, we only account for the detailed BS dynamics for $n \leq 7$ while for $n > 7$ we set the annihilation branching ratios to 1. We assume, as explicitly checked for the 7-plet, that the formation cross sections for $4s$ and $3p$ BS are negligible. In fact, the cross sections of BS differing only for their principal quantum number have the same parametric dependence on n, so that the hierarchy between different energy levels is independent on n.

2.4 WIMP at high energy lepton colliders

We now look at the possible detection strategies for *direct production* of WIMPs at collider experiments. From the results in Table 2.1, Table 2.2 one can immediately see that DM masses $\gtrsim 30$ TeV are required to achieve thermal freeze-out for EW multiplets with $n > 5$, . Pair-production of these states would require center-of-mass energies exceeding 60 TeV, which are unlikely to be attained at any realistic future facility. On the other hand, multiplets with $n \leq 5$ have thermal masses in the few (tens) of TeV range, potentially within the reach of present and future colliders.

Direct reach on these dark matter candidates at hadron colliders is limited by the absence of QCD interactions for the DM candidates, which can be produced only via electro-weak interactions. As such the limits at the LHC (see e.g. [143]) are rather far from the interesting thermal mass targets and only a future pp collider may have the reach for some low-n candidates if collisions around 100 TeV can be attained [121, 144, 145]. Low energy e^+e^- colliders tend to have reach mainly through indirect effects, e.g. the modification of the angular distributions in simple $f\bar{f}$ production at center of mass energies below the threshold to produce the DM pair. The reach in this case is up to masses a factor a few above the center of mass energy [146, 147].

A very-high-energy lepton collider, such as a muon collider, would be the perfect machine to hunt for these WIMPs, due to its large center-of-mass energy, relatively clean collision environment, and the capability of pair-producing weakly interacting particles *up to kinematical threshold*. Here we consider in particular a future muon collider with center-of-mass energy of 10 TeV or more and the baseline integrated luminosity of [104]

$$\mathcal{L} \simeq 10 \text{ ab}^{-1} \cdot \left(\frac{\sqrt{s}}{10 \text{ TeV}} \right)^2 . \tag{2.31}$$

While such a machine is currently not feasible, various efforts to overcome the technological challenges are ongoing. Early developments on machine performances [148, 149] found the luminosity Eq. (2.31) to be achievable for $\sqrt{s} \lesssim 10$ TeV, and further development to produce a realistic accelerator design is currently in progress [53, 150].

We implement two possible search strategies: i) Missing Invariant Mass searches (MIM), in which some SM particle recoils against the heavy, undetected DM particle, ii) Disappearing Tracks (DT) searches, in which one of the charged partner of the DM leaves a macroscopic track in the detector before decaying inside it.

We mention a third possible method for testing direct production of WIMPs, which is via resonant production of bound states at colliders [151, 152]. It can be very powerful for specific candidates with the right quantum numbers such as the Majorana 5_0, but not in general and therefore we will not further discuss this channel.

The biggest difference relevant for collider searches between the real and complex candidates is that the lifetime of the real ones is fixed and cannot be significantly modified by UV physics. On the other hand, in the complex WIMP scenario the

splittings $\delta m_0, \delta m_{Q_M}$ determine the lifetime of the charged components of the EW multiplet, which are pivotal to understand the viable collider signatures. When discussing about MIM for complex WIMPs, we will assume that the charged particles promptly decays into the stable neutral DM. To be more systematic, we will fix as a benchmark point the *minimal splitting* case, in which the parameters of the model are chosen to give the minimal mass splitting allowed by phenomenological constraints. Then we discuss the reach in general as a function of the lifetime.

We start by discussing missing energy signatures for real candidates. For $n = 3, 5, Y = 0$ we determine the minimal center-of-mass energy and luminosity required to directly probe the freeze-out predictions. The $n = 7$ candidate is too heavy to be directly tested at thes machines. First, we detail in Sec. 2.4.1 the prospects for the observation of DM as undetected carrier of momentum recoiling against one or more SM objects. We systematically study all the "mono-V" channels, where DM is recoiling against a SM gauge boson $V = \gamma, Z, W$. We also investigate double vector boson production, that we dub "di-V" channels, where requiring a second SM gauge boson in the final state could help ameliorating the sensitivity. After the preliminary study on real WIMPs, we transfer this knowledge to the complex WIMP case. We will only compute the reaches for the mono-γ, mono-W channels in these cases: as it will be shown for the real WIMPs, multiple emissions are effective only for the heavier candidates and in presence of large systematics. The mono-Z channel instead has a lower reach.

Second, in Sec. 2.4.2 we study the reach of disappearing track searches – which are robust predictions of WIMPs in real EW representations as discussed in Sec. 2.1 – recasting the results of [122]. For the complex case we discuss the reach for the minimal splitting benchmark and then in full generality.

Notice that our study is in principle applicable both to high-energy $\mu^+\mu^-$ and e^+e^- colliders, even though soft QED radiation, beam-strahlung, and the presence of beam-induced backgrounds could affect the results in different ways.

The projections for direct production derived here have to be contrasted with similar studies in the context of future high energy proton machines [120, 121] (which are limited by the partial reconstruction of the collision kinematics) or electron-positron machines [153, 154] (which are limited by the moderate center-of-mass energy and hence more effective to hunt for lighter DM candidates).

Complementary studies have also considered indirect probes of WIMPs at future high energy lepton colliders, focusing on the modifications of Drell-Yan processes [147]. Given the freeze-out masses of Table 2.1, EW n-plets with $n > 5$ are beyond the reach of any realistic future collider *directly*. Including *indirect* methods (corrections to fermion production cross sections) can help lowering the required energy for $n = 5, 7$ [155]. In particular, via these methods, the Majorana 7-plet can be excluded at energies of order 30 TeV.

A summary of the capabilities of the several stages of a high energy muon collider is given in Fig. 2.5 under the assumption of luminosity following the scaling of Eq. (2.31). The upshot of these studies is that, as the center of mass energy of the

collider is increased, the higher energy machine gains sensitivity to heavier WIMP candidates. All in all, the list of WIMP candidates that we have described in this Thesis provides a series of targets that can be probed at successive stages of a future high energy muon collider.

2.4.1 WIMPs as missing momentum

We perform a full study of the different channels to observe DM as undetected carrier of momentum. The generic strategy is to measure a hard SM particle or a set of particles X recoiling against a pair of invisible objects,

$$\ell^+\ell^- \to \chi^i\chi^j + X\,. \tag{2.32}$$

Notice that we treat all the components χ^i of the EW multiplet as invisible, assuming the soft decay products of the charged states to be undetected. Additional soft SM radiation is also implicit in Eq. (2.32). The prospects for the "mono-photon" topology at a future muon collider have been already studied in [112]. Here, we want to extend this analysis by enlarging the set of SM objects recoiling against the invisible DM multiplets.

Mono-V. We start by considering "mono-V" scattering processes where V$=\gamma, Z, W$ is a generic EW gauge boson that accompanies the production of χ states from the n-plet,

$$\text{mono-}\gamma\text{:} \qquad \ell^+\ell^- \to \chi^i\chi^{-i} + \gamma\,, \tag{2.33}$$

$$\text{mono-}Z\text{:} \qquad \ell^+\ell^- \to \chi^i\chi^{-i} + Z\,, \tag{2.34}$$

$$\text{mono-}W\text{:} \qquad \ell^+\ell^- \to \chi^i\chi^{-i\mp1} + W^\pm\,. \tag{2.35}$$

The main contribution to all these processes comes from initial- and final-state radiation of a vector boson, which have sizeable rates because of the large weak charge of the DM multiplet and the weak charge of the beams.[3] We sum over all components of the multiplet χ^i, but the dominant signal corresponds to the production of the state with largest electric charge ($i = \pm n$), subsequently decaying into DM plus soft SM particles.

For each of these signals, the corresponding SM background is dominated by a single process,

$$\text{mono-}\gamma\text{ bkg:} \qquad \ell^+\ell^- \to \gamma\nu\bar{\nu}\,, \tag{2.36}$$

$$\text{mono-}Z\text{ bkg:} \qquad \ell^+\ell^- \to Z\nu\bar{\nu}\,, \tag{2.37}$$

$$\text{mono-}W\text{ bkg:} \qquad \ell^+\ell^- \to W^\mp\nu \;+\; \ell^\pm(\text{lost})\,, \tag{2.38}$$

where the missing transverse momentum is carried by neutrinos; the mono-W background also requires a lost charge along the beam.

[3] The mono-Higgs signal has a much lower cross-section due to the suppression of initial- and final-state radiation. Furthermore, final-state radiation is model-dependent for scalar DM.

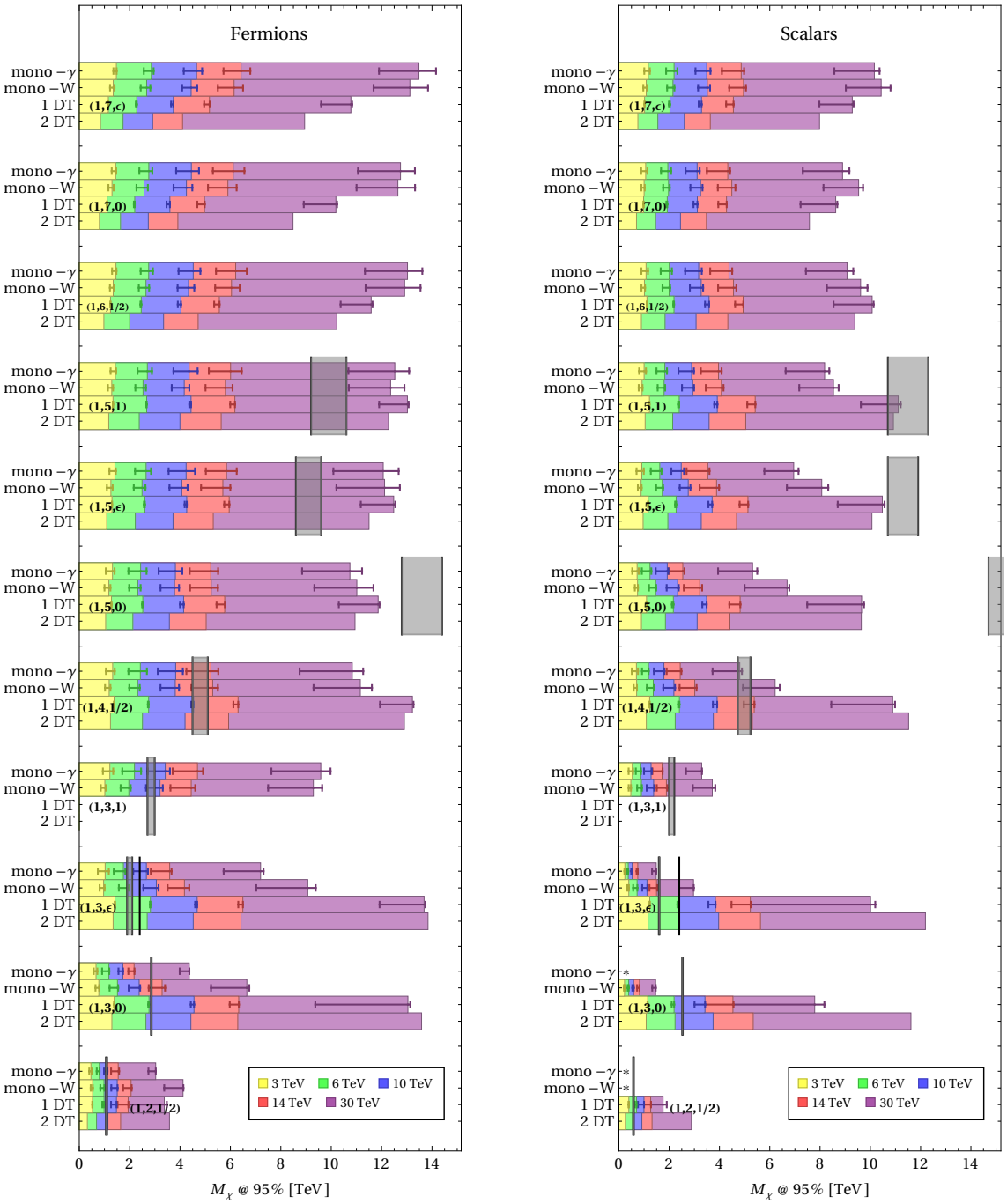

Figure 2.5: *Mass reach in the mono-γ, mono-W and DT channels for fixed luminosity as per Eq. (2.31) at $\sqrt{s}$ 3 TeV (yellow), 6 TeV (green), 10 TeV (light blue), 14 TeV (red), and 30 TeV (purple). In the mono-W and mono-γ searches we show an error bar, which covers the range of possible exclusion as the systematic uncertainties are varied from 0 to 1%. The colored bars are for an intermediate choice of systematics at 0.1%. In the 1 DT search the error bar corresponds to uncertainties from 0 to 10%, and the colored bars to 1%. The 2 DT search is not affected by systematics. Missing bars denoted by an asterisk * correspond to cases where no exclusion can be set in the mass range $M_\chi > 0.1\sqrt{s}$. For such cases it is worth considering VBF production modes at the fixed luminosity Eq. (2.31) or higher luminosity at potentially smaller $\sqrt{s}$ as illustrated in Fig.s 2.9,2.10*

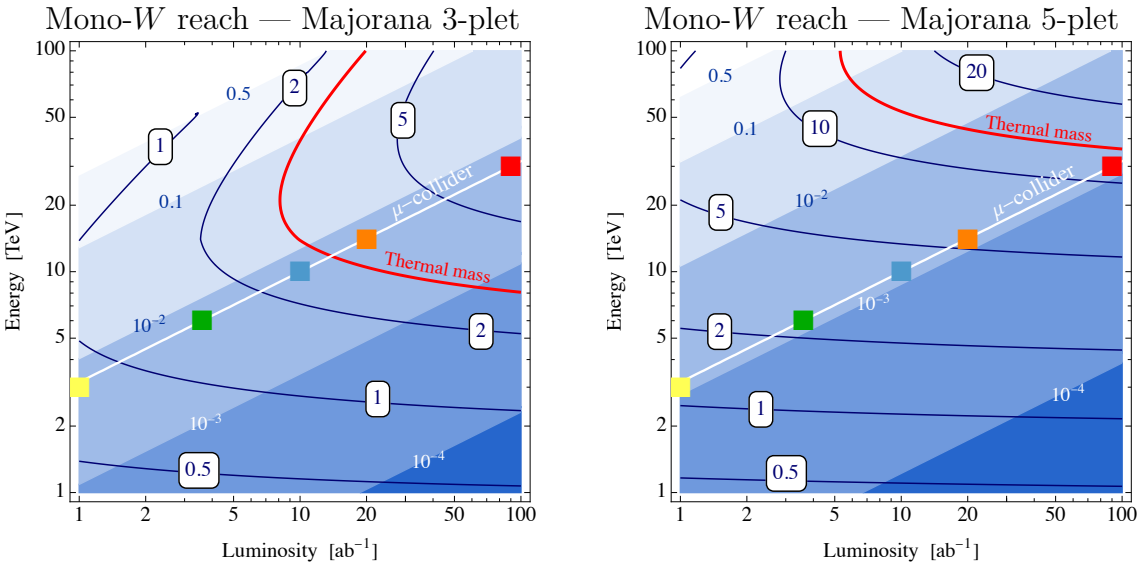

Figure 2.6: *Reach from mono-W searches at a muon collider, as a function of collider center-of-mass energy $\sqrt{s}$ and integrated luminosity $\mathcal{L}$. The blue contours show the 95% C.L. reach on the WIMP mass; the prediction from thermal freeze-out is shown as a red line. The precision of the measurement is shown by the blue shadings. Systematic uncertainties are assumed to be negligible. The white line corresponds to the luminosity scaling Eq. (2.31), with various collider benchmarks shown as colored squares:$\sqrt{s} = 3$ TeV yellow, $\sqrt{s} = 6$ TeV green, $\sqrt{s} = 10$ TeV blue, $\sqrt{s} = 14$ TeV orange and $\sqrt{s} = 30$ TeV red.* **Left:** *Majorana 3-plet.* **Right:** *Majorana 5-plet.*

We simulate signal and background events with MadGraph5_aMC@NLO [156, 157], for different DM mass hypotheses and different collider energies. The W and Z bosons are assumed to be reconstructed from all their visible decay products and are treated as single objects. We impose basic acceptance cuts on the rapidity and transverse momentum of the vectors, requiring $|\eta_V| < 2.5$ and $p_{\mathrm{T},V} > 10$ GeV. Other detector effects are neglected.

We then perform a cut-and-count analysis, estimating the significance of the signal as

$$\text{significance} = \frac{S}{\sqrt{S + B + \epsilon_{\text{sys}}^2 \left(S^2 + B^2\right)}} \,, \tag{2.39}$$

where S, B are the numbers of physical signal and background events, and ϵ_{sys} parametrizes the systematic uncertainties. The signal is isolated from the background employing the kinematics of the visible object, parametrized in terms of its transverse momentum $p_{\mathrm{T},V}$, its pseudo-rapidity η_V, and the missing invariant mass (MIM) which is a function of the energy of the visible particle itself

$$\text{MIM} = \left(s + m_V^2 - 2\sqrt{s} E_V\right)^{1/2} \,. \tag{2.40}$$

We select events with MIM $\geq 2M_\chi$, $p_{\mathrm{T},V} \geq p_{\mathrm{T},V}^{\text{cut}}$, $|\eta_V| \leq \eta_V^{\text{cut}}$, where the p_{T} and η selection cuts are chosen to maximize the significance for each value of M_χ. The precise values of the selection cuts, together with the expected number of events and the reach of the various search channels, are given in Table F.1 in the Appendix.

The background rates for mono-γ and mono-Z are very similar, with fiducial cross-sections of around 3 pb that depend weakly on the collider energy. As already pointed out in [112] for the mono-γ case, the optimal reach on M_χ is obtained for low signal-to-noise ratios – in other words, systematic uncertainties could be important. For this reason, we present results for different values of $\epsilon_{\rm sys} = 0, 1‰, 1\%$. We point out that in presence of larger systematic uncertainties, the optimal selection cuts are stronger (as can be seen in Table F.1) and lead to higher values of S/B.

The mono-W differs from the other two channels. The SM background is dominated by vector boson fusion (VBF) processes, that lead to forward leptons (lost along the beam pipe) and W bosons. The signal is instead made of events where the W is radiated from the initial or final states, leading to a more central distribution. The cut on $p_{{\rm T},W}$ can efficiently suppress the VBF background, with a lesser impact on the signal compared to the mono-γ or mono-Z cases. As a consequence, we find that the mono-W search has the best sensitivity among the various mono-X channels. We comment in App. F.2 on detils of the background computation. The 95% C.L. exclusion reach on M_χ for a Majorana 3-plet and 5-plet is shown in Fig. 2.6 as a function of collider center-of-mass energy $\sqrt{s}$ and luminosity $\mathcal{L}$. We also show the expected values of S/B for the excluded signal in absence of systematic errors, which are rather low also for the mono-W search.

Due to the presence of initial-state radiation, the W boson of the signal has a preference for being emitted in the forward (backward) direction, measured with respect to the flight direction of the ℓ^- beam, if its charge is negative (positive). Since the charge of the W boson is potentially observable for leptonic decays, we can envisage a strategy to isolate the signal from the background using the full distribution in η_W (instead of its absolute value). We thus also perform an analysis of leptonic mono-W events, where we impose the additional cut $\eta_{W^\pm} \lessgtr 0$. We find the reach of this search to be weaker than the one of the inclusive mono-W because of the small leptonic branching ratio. However, the leptonic mono-W search possesses signal-free regions of the η_W distribution which would allow for an *in situ* calibration of the background from the data itself, leading to possible reduction of the systematic uncertainties.

Di-V. We now consider scattering processes with multiple emission of vector bosons. While generally being suppressed by higher powers of the gauge coupling constant, these processes can be enhanced for large center-of-mass energies, and for multiplets with large weak charge. They can therefore provide very useful handles to probe WIMPs in the regimes where the mono-V searches have very low signal-to-noise ratios. Of course, a too large rate for multiple boson radiation would indicate the breakdown of the perturbative expansion, requiring the resummation of large logarithms. We have checked that for the EW 3-plet and 5-plet, and for the energies under consideration here, the fixed-order computations are still accurate.

First, we consider the di-photon process

$$\ell^+\ell^- \to \chi^i\chi^{-i} + \gamma\gamma\,. \tag{2.41}$$

We apply the same acceptance cuts of the mono-γ analysis, and in addition we

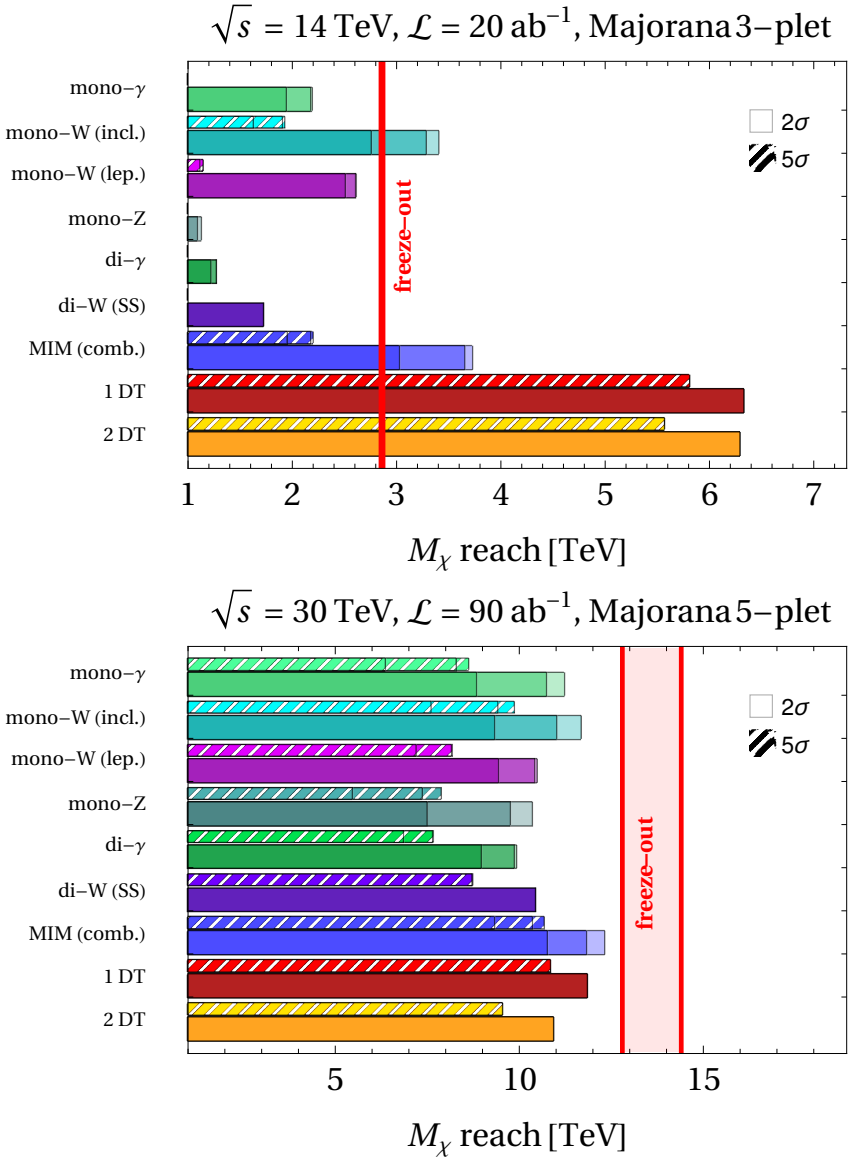

Figure 2.7: *Different bars show the* 2σ *(solid wide) and* 5σ *(hatched thin) reach on the WIMP mass at a muon collider for different search channels. The first seven bars show the channels discussed in Sec. 2.4.1 where DM would appear as missing invariant mass (MIM) recoiling against one or more SM objects: mono-gamma, inclusive mono-W, leptonic mono-W, mono-Z, di-gamma, same sign di-W, and the combination of all these MIM channels (blue). The last two bars show the reach of disappearing tracks as discussed in Sec. 2.4.2, requiring at least 1 disappearing track (red), or at least 2 tracks (orange). All the results are shown assuming systematic uncertainties to be 0 (light), 1‰ (medium), or 1% (dark). The vertical red bands show the freeze-out prediction.* **Above:** *Majorana 3-plet for* $\sqrt{s} = 14\,\text{TeV}$ *and* $\mathcal{L} = 20\,\text{ab}^{-1}$. **Below:** *Majorana 5-plet for* $\sqrt{s} = 30\,\text{TeV}$ *and* $\mathcal{L} = 90\,\text{ab}^{-1}$.

require a separation $\Delta R_{\gamma\gamma} > 0.4$ between the two photons. We employ the same event selection strategy of the mono-γ case, using as variables η_X, $p_{\mathrm{T},X}$, where X is the compound $\gamma\gamma$ system. Moreover, we require each photon to be as central as the $\gamma\gamma$ system itself. For the 5-plet, we find that the di-γ search can be stronger than the mono-γ in presence of large systematic uncertainties, where suppressing the SM background is more important. For the 3-plet, which has a smaller EW charge, the signal yield is too much affected by the requirement of a second emission to be competitive with the mono-V. In both cases, the values of S/B for the excluded di-γ signal are much larger than for the mono-γ signal, and systematic errors thus have a smaller impact. Details of the results are reported in Table F.1 in the Appendix.

Second, we consider the double W emission

$$\ell^+\ell^- \to \chi^i \chi^{-i\mp 2} + W^\pm W^\pm \,, \tag{2.42}$$

which holds a potentially very clean signature due to the two same-sign W bosons. We focus on leptonically decaying W bosons to ensure that their charge can be accurately tracked. A potential SM background consists in events with two lost charged particles, with the leading contribution being

$$\ell^+\ell^- \to W^-W^-W^+W^+ \,, \tag{2.43}$$

where two W bosons of same sign are lost. This background is however negligible, as pairs of W bosons with opposite charge tend to be radiated from the same external leg and to be collinear: requiring only one of two collinear W bosons to be within detector acceptance reduces the rate to negligible levels. The other possible background is given by events with a misidentified charge,

$$\ell^+\ell^- \to W^-W^+(\text{mistag})\ \nu\bar{\nu} \,, \tag{2.44a}$$

$$\ell^+\ell^- \to W^-W^+(\text{mistag})\ \ell^+\ell^- \,, \tag{2.44b}$$

where in the second case the charged final-state leptons are lost along the beam line. Requiring $p_{\mathrm{T},WW} \gtrsim \sqrt{s}/10$ makes the process in Eq. (2.44b) subdominant with respect to the $\nu\bar{\nu}$ background Eq. (2.44a). On top of this p_T cut, we do not apply further selection cuts, and simply require the two W bosons to be within the geometrical acceptance of the detector, $|\eta_W| < 2.5$. As an estimate for the charge misidentification probability we take $\epsilon_{\text{misid}} = 10^{-3}$.

Due to the negligible background contamination, the same-sign di-W signal has a much higher signal-to-noise ratio than the mono-V channels and even than the di-photon signal, reaching up to $S/B \sim \mathcal{O}(1)$. This makes this channel very robust against systematic uncertainties, and particularly effective for large n-plets $n \geq 5$ at higher energies due to their large EW charge. This signature may be one of the most robust and convincing signal of $n = 5$ multiplets at colliders. Further sources of background and a proper characterization of the missing (transverse) momentum in this reaction depend on detector performances, as well as on the knowledge of the initial state of the collision to be used in the computation of kinematic variables.

We summarize the results of all the mono-V and di-V signatures discussed above in Fig. 2.7, where we show the 95% C.L. exclusion on M_χ for real fermion 3-plets and

5-plets, together with the 5σ discovery potential, at two benchmark muon colliders. We also show the combined reach from all these missing mass channels. The bands with different shadings correspond to different systematic uncertainties. One can see that the inclusive mono-W yields the strongest exclusion for both the 3-plet and the 5-plet. The main effect of di-V searches is to reduce the impact of systematic uncertainties. A 14 TeV muon collider with the benchmark luminosity of Eq. (2.31) would be able to probe a thermally-produced Majorana 3-plet WIMP, while a center-of-mass energy of slightly above 30 TeV is needed to probe the thermal freeze-out mass with missing energy searches in the case of the 5-plet.

We repeat the analysis for complex candidates, focusing on the powerful mono-γ and mono-W channels. In order to have MIM signature, the charged partners must decay promptly on collider scales. We take as benchmark for promptness the lifetime of the *Lightest Charged Particle* (LCP) $c\tau_{\rm LCP} < 0.33$ cm . This choice for the threshold value to consider the signal as prompt corresponds to $c\tau/2$ of the charged track for the $2_{1/2}$ WIMP in the minimal splitting scenario (shown in Fig. 2.13), which is a known benchmark where DT reconstruction starts to become challenging. In this case, the LCP WIMP decays promptly on collider scales and gives missing energy signatures such as the mono-W and mono-γ discussed in Sec. 2.4.1. Full details on MIM searches are given in App. F.

We focus on the collider reach for the complex doublet ($2_{1/2}$) and the complex triplet (3_1), that are the lightest WIMPs and have the greater chance to be discoverable at $\sqrt{s} \leq 10$ TeV. Theoretically, these candidates are the most minimal complex WIMPs since they have maximal hypercharge and the neutral component is automatically the lightest one at the renormalizable level. The only required higher dimensional operator is $\mathcal{O}_0$ which generates the inelastic splitting in Eq. (2.8). We have optimized the selection for the fermion $2_{1/2}$ and 3_1 at $\sqrt{s} = 3, 6$ TeV and $\sqrt{s} = 6, 10$ TeV, respectively. As can be seen from Fig. 2.8, the MIM search at $\sqrt{s} = 3$ TeV with the benchmark luminosity $\mathcal{L} = 1$ ab^{-1} is not sensitive to the $2_{1/2}$. A $\sqrt{s} = 6$ TeV collider with benchmark luminosity $\mathcal{L} = 4$ ab^{-1}, instead, is able to probe the doublet WIMP at 2σ C.L. In general the mono-W and mono-γ channels give comparable mass reach for the benchmark luminosity adopted here, full detail is given in Table F.3. The sensitivity of each channel has a specific behavior as a function of the luminosity and for different assumed systematics. The overall combination as function of the total luminosity for fixed thermal mass is shown in Fig. 2.8. We remark that the reach deviates from a pure rescaling by $\sqrt{\mathcal{L}}$ because the selections, hence the result, have been optimized as a function of $\mathcal{L}$ when dealing with $\epsilon_{\rm sys} \neq 0$.

In Fig. 2.8 we show similar results for the 3_1 at its thermal mass, which entails interesting results at 6 and 10 TeV center of mass energy machines. For the 10 TeV collider we find that MIM searches are effective probes of this WIMP candidate and can establish a bound at 95% CL with a small luminosity or give a discovery with the nominal luminosity. Mono-W and mono-γ perform similarly well and their combination is worth being done.

We repeat the results for generic center-of-mass energy and integrated luminosity in

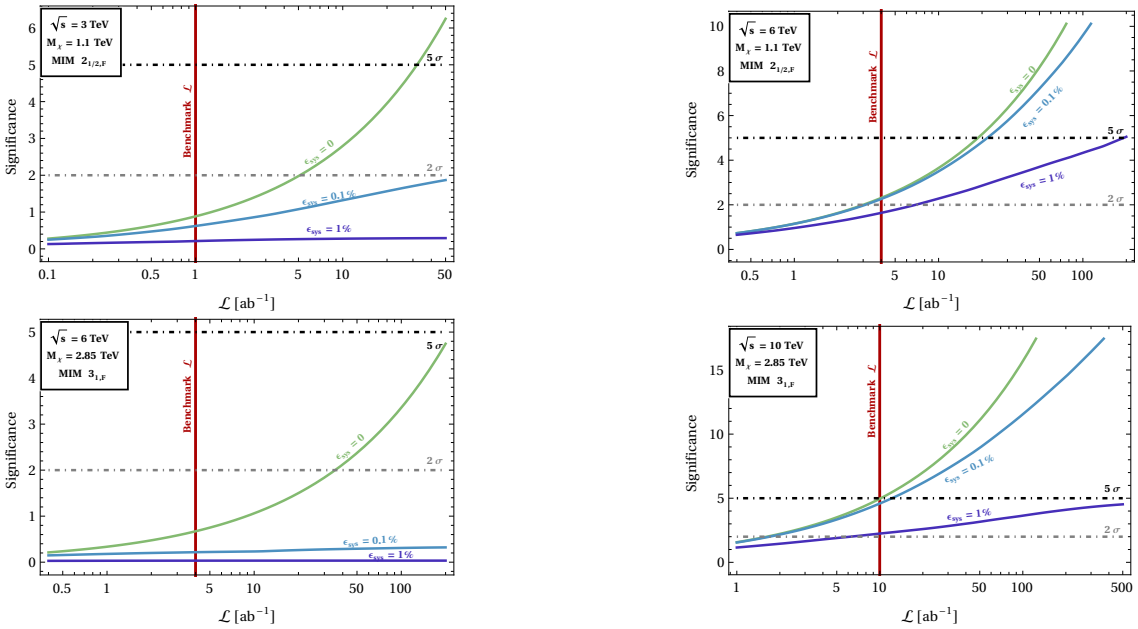

Figure 2.8: *Combined reach for MIM (mono-γ+mono-W) as a function of the luminosity $\mathcal{L}$ for different value of the expected systematic uncertainties parametrized by ϵ_{sys}:* 1% **(purple)**, 0.1% **(cyan)**, *0* **(green)**. *The* **red** *lines show the benchmark luminosity following Eq. (2.31).* **Upper row:** *Collider reach for the $2_{1/2}$ of mass $M_\chi = 1.1$ TeV and $\sqrt{s} = 3$ TeV (left) and $\sqrt{s} = 6$ TeV (right).* **Bottom row***: same as for the top rows, but for the case of the 3_1 of mass $M_\chi = 2.85$ TeV and $\sqrt{s} = 6$ TeV (left) and $\sqrt{s} = 10$ TeV (right).*

Fig.s 2.9, 2.10 for the mono-γ and mono-W channels. We do not show the same for tracks given that for complex WIMP the lifetime is model dependent. The results on these figures have been obtained by rescaling the results at $\sqrt{s} = 3, 6, 10, 14, 30$ TeV, under the assumption that all cross-sections and kinematical cuts scale trivially with collider energy, and neglecting systematic errors.

For the other candidates we used the optimal cuts that we derived from our previous results for real candidates with odd n [47]. For each level of systematics ϵ we have interpolated our previous results as functions of n and $\sqrt{s}$ and we have derived optimal cuts for the new n plets studied in this work. We remark that this procedure is potentially inaccurate as the real odd n-plets contain 2 times fewer degrees of freedom, hence have rates smaller by a factor 2. This can in principle affect the result of the optimization of the selection. We checked that the difference with a dedicated optimization is negligible, thus our event selection should be quite close to the optimal one. We report in Fig. 2.11 the results on the sensitivity for the $2_{1/2}$, 3_1, $4_{1/2}$, 5_1, at colliders with suitable $\sqrt{s}$ that can provide 95% C.L. exclusion. Full results for all benchmark colliders at the nominal luminosity of Eq. (2.31) are given in Tables F.3 and F.4, for the various search channels under consideration. As can be seen, a muon collider of energy $\sqrt{s} = 30$ TeV can test via MIM searches also the complex candidates up to the 5_1 fermion candidate.

Scalar WIMPs have lower production cross-sections. Missing mass searches do not allow to put stringent constraints on their mass, nor to probe the masses required for thermal freeze-out. We provide more details on the collider signatures, and results for real scalars in App. F.1, for both real and complex candidates.

2.4.2 Disappearing tracks

A second handle to tag the production of EW WIMPs at colliders is the detection of tracks from the charged states in the n-plet. We start again by analyzing real WIMPs. As discussed in Sec. 2.1, the decay of $\chi^\pm \to \chi^0 \pi^\pm$ has a lifetime of roughly $c\tau_{\chi^+} \simeq 48 \text{ cm}/(n^2-1)$, which is sufficiently long-lived to give rise to reconstructed tracks of length $\mathcal{O}(\text{cm})$ for $n = 3, 5$ that can be observable at colliders. The resulting tracks from these processes are somewhat too short for regular track reconstruction to work efficiently and they will show up as disappearing tracks (DTs), with missing hits in the outermost layers of the tracker and with little or no activity in the calorimeter and the muon chamber. States with higher electric charge in larger multiplets decay promptly to $\chi^\pm$, and eventually contribute to the number of disappearing tracks.

A full-detector level study has shown that a high energy lepton collider like CLIC at $\sqrt{s} = 3$ TeV can reconstruct them sufficiently well to separate them from other sources of look-alike short tracks [158, 159]. A recent study [122] has attempted a first evaluation of the performance of this type of search at a multi-TeV muon collider. A main source of worry and a main difference with respect to e^+e^- machines is the abundant number of tracker hits from underlying event activity due to the muon beam decay and to the resulting secondary particles from the interactions with the machine and detector materials. These hits can accidentally become a potentially

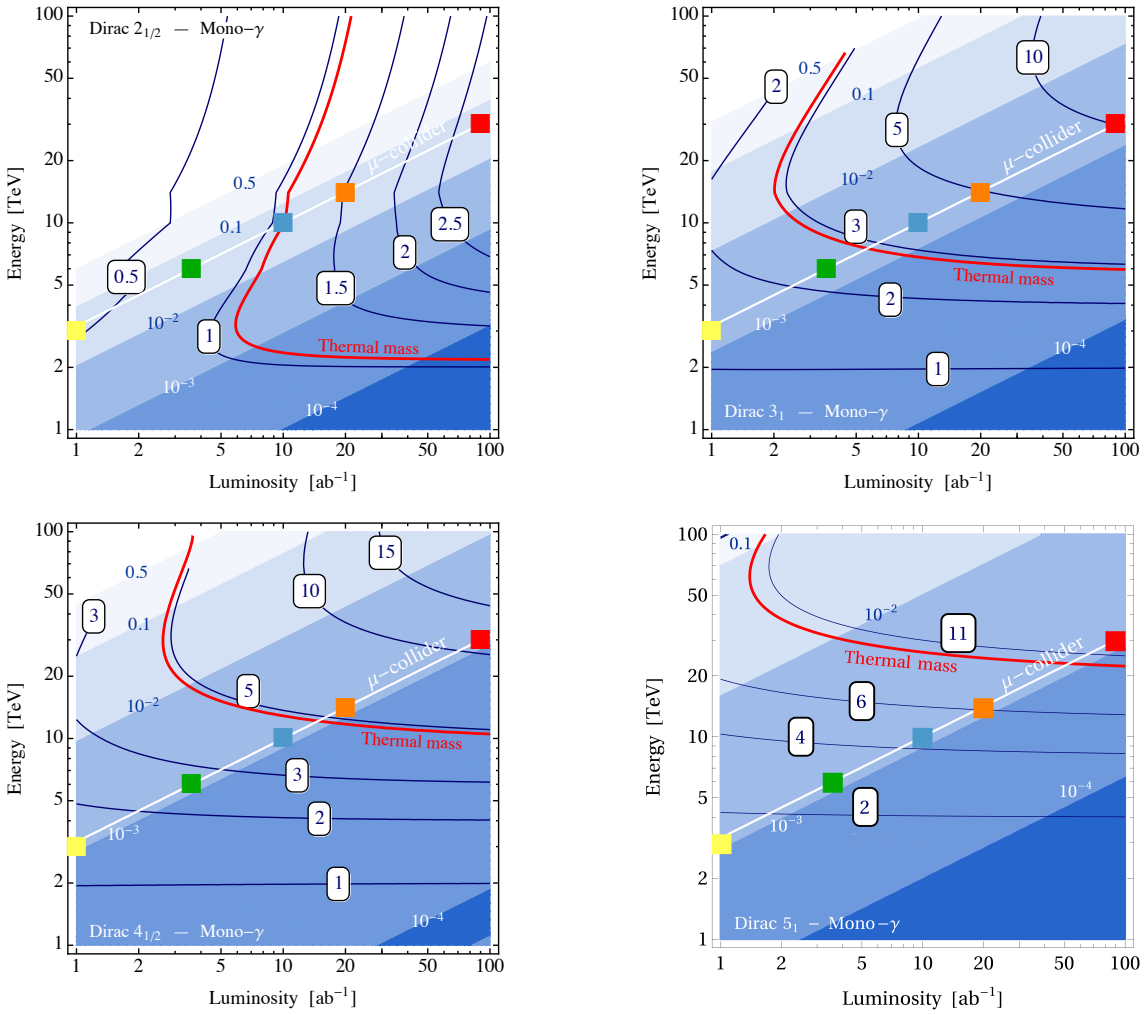

Figure 2.9: *Mass reach (in TeV) in the mono-γ channels as a function of collider center-of-mass energy and luminosity (blue lines). The thermal freeze-out mass is shown in red. Blue shades show the expected values of the ratio of the signal rate over background. Systematic uncertainties are set to zero. The muon collider luminosity Eq. (2.31) is shown as a white line, with the benchmark values of $\sqrt{s}$ highlighted by the colored squares.* ***Top Left:*** *Dirac $2_{1/2}$.* ***Top Right:*** *Dirac 3_1.* ***Bottom Left:*** *Dirac $4_{1/2}$.* ***Bottom Right:*** *Dirac 5_1.*

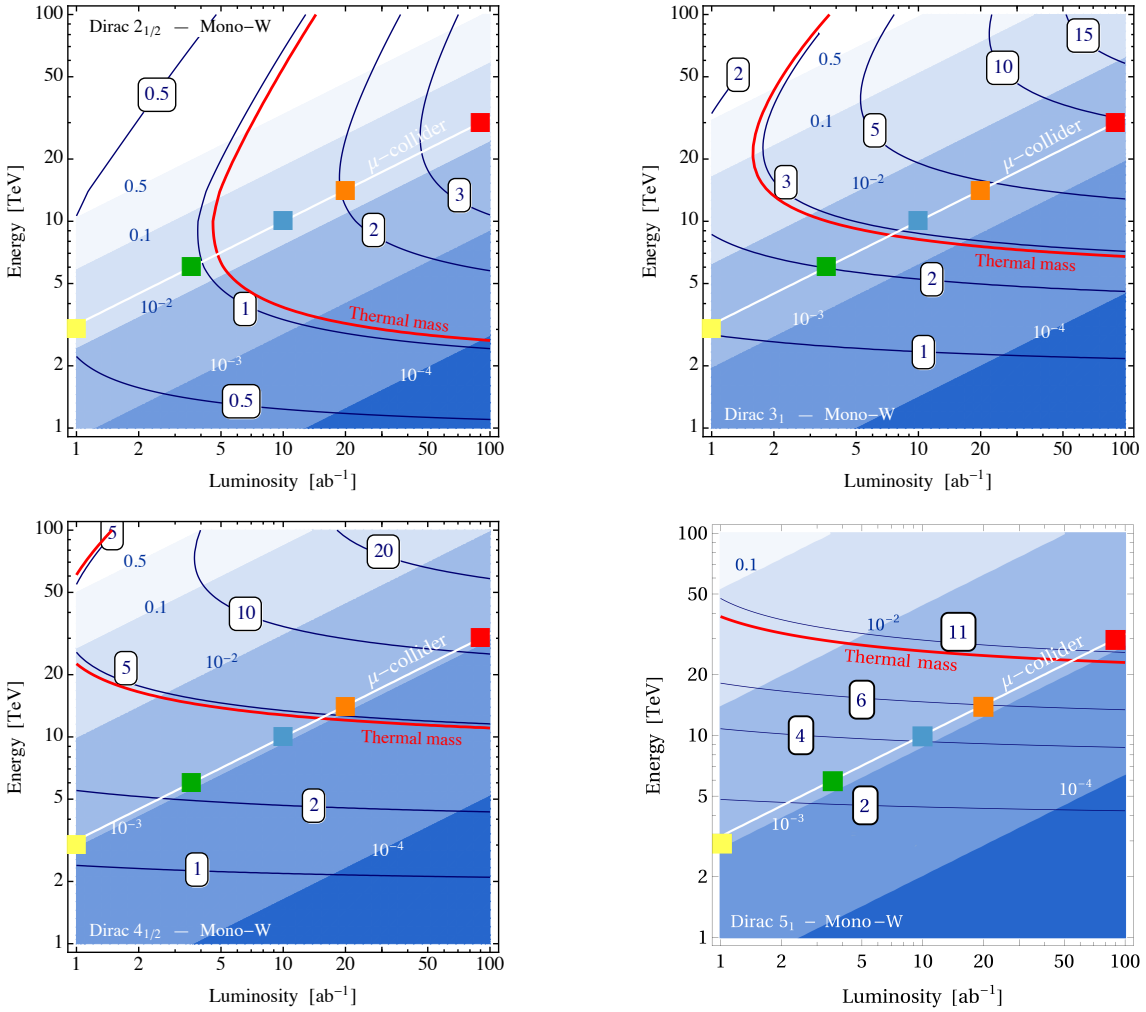

Figure 2.10: *Same as Fig. 2.9, but for the mono-W channel instead.*

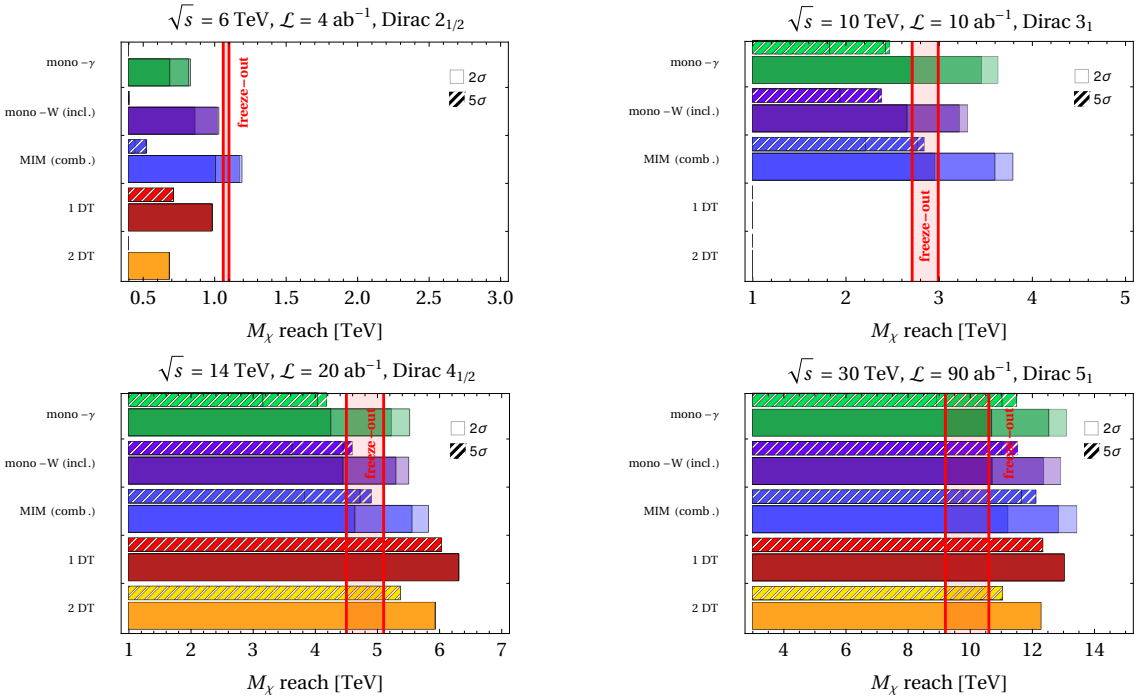

Figure 2.11: *Different bars show the 2 σ (solid wide) and 5σ (hatched thin) reach on the fermionic WIMP mass at a muon collider for different search channels. The first three bars show the channels discussed in Sec. 2.4.1 where DM would appear as missing invariant mass (MIM) recoiling against one or more SM objects: mono-γ, inclusive mono-W, and the combination of all these MIM channels (blue). The mono-Z channel is not reported since it gives results below the minimum mass shown. The last two bars show the reach of disappearing tracks, requiring at least 1 disappearing track (red), or at least 2 tracks (orange). All the results are shown assuming systematic uncertainties to be 0 (light), 1‰ (medium), or 1% (dark) for MIM searches. The vertical red bands show the freeze-out prediction. Tracks have been computed assuming minimally split neutral states, and a charged-neutral splitting δm_+ equal to the gauge contribution for the $2_{1/2}$ and 3_1. For the $4_{1/2}$ and 5_1 the splitting-inducing couplings y_0 and y_+ have been tuned so that $\delta m_+ = \delta m_-$ (up to minimal δm_0 corrections), which represents a least favorable condition for DT searches.* ***Top Left:*** *Dirac $2_{1/2}$ for $\sqrt{s} = 6$ TeV and $\mathcal{L} = 4$ ab^{-1}.* ***Top Right:*** *Dirac 3_1 for $\sqrt{s} = 10$ TeV and $\mathcal{L} = 10$ ab^{-1}.* ***Bottom Left:*** *Dirac $4_{1/2}$ for $\sqrt{s} = 14$ TeV and $\mathcal{L} = 20$ ab^{-1}.* ***Bottom Right:*** *Dirac 5_1 for $\sqrt{s} = 30$ TeV and $\mathcal{L} = 90$ ab^{-1}.*

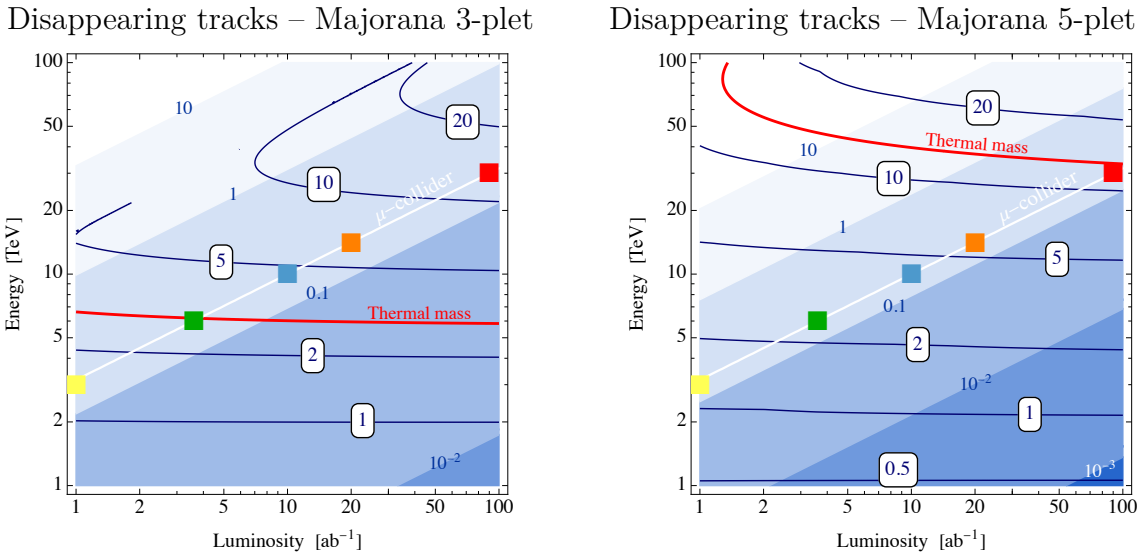

Figure 2.12: *Same as Fig. 2.6, but for disappearing track searches in mono-γ events.* **Left:** *Majorana 3-plet.* **Right:** *Majorana 5-plet.*

severe source of background for searches aimed at highlighting the presence of short tracks of BSM origin. We do not enter in the details of these issues here, and simply follow the analysis of [122], which is based on a simulation of beam-induced background at 1.5 TeV, and recast their results for the EW 3_0-plet and the 5_0-plet. We remind that the background from decaying muons is expected to decrease at higher energies, making our estimate conservative in this sense.

We consider mono-photon events with disappearing tracks, and search for events compatible with a WIMP signal. Following [122], we distinguish two event-selection strategies to hunt for disappearing tracks: i) events with at least a disappearing track with $p_{\rm T} > 300$ GeV and a hard photon with $E_\gamma > 25$ GeV; ii) events with a hard photon, and two disappearing tracks originating from the same point along the beam axis. To estimate the reach we work in the cut-and-count scheme as in Eq. (2.39), and ignore systematic uncertainties. Further details are summarized in App. F.3 for completeness.

The result of our recast is shown in the last two columns of Fig. 2.7 for Majorana 3-plets and 5-plets at two benchmark colliders, and in Fig. 2.12 as a function of collider energy and luminosity. One can see that DTs are especially powerful in the case of the Majorana 3-plet, where the reach goes almost up to the kinematical threshold. In particular, an EW 3-plet WIMP of mass as predicted by thermal freeze-out can be discovered already at a 6 TeV muon collider as suggested in [112, 122]. For higher n-plets DT substantially loose exclusion power because the lifetimes of the $\chi^\pm \to \chi^0\pi^\pm$ decay become shorter. For the 5-plet the DT reach is comparable to the combined reach of the MIM searches.

We remark that for the 3_0 WIMP the double track analysis has a higher exclusion power than the single track analysis, whereas for $n \geq 5$ it has a lower reach. This is due to the shorter life-time $\tau_\chi \propto 1/n^2$ of larger multiplets, that suppresses the exponential decay factor of Eq. (F.1) twice in the double-track rate.

As discussed in more detail in App. F, DT searches are particularly important to probe real scalar WIMPs, since the lower production cross-sections have no significant impact on these almost background-free searches. Disappearing tracks might be the only direct signature of scalar WIMPs at collider experiments.

We now move to study complex WIMPs. For 1 m $> c\tau_{\rm LCP} >$ 0.33 cm the lightest charged WIMP gives a disappearing track signal. The DT searches in general require, at fixed $M_{\rm DM}$, a scan in the $(\delta m_0, \delta m_{Q_M})$ to compute the signal, since the spectrum and the decay width of the particle χ^Q is determined uniquely by the splittings δm_{Q_M}, δm_0.

To get a feel of how powerful DT searches can be, we fix the neutral splitting to a representative value $\delta m_0 \simeq 200$KeV for the fermions. Our results are given in Fig. 2.14 where we display the region of the plane WIMP mass versus $c\tau$ where experiments can probe the several WIMPs considered in each panel of the figure. For this result we consider only χ^+ and its conjugate as candidate long-lived for the $2_{1/2}$. For the 3_1, the $4_{1/2}$ and 5_1 all states with charge greater than 1 are assumed to decay promptly to the candidate charged long lived states at the bottom the spectrum.[4] As we have fixed δm_0 much smaller than the mass splitting between the neutral and charged states, we can effectively consider decays into both χ^0 and $\chi^{\rm DM}$ as if they were degenerate in mass. Considering the possible decay channels χ^- into $e^-\nu_e\chi^{0,\rm DM}$, $\mu^-\nu_\mu\chi^{0,\rm DM}$, $\pi^-\chi^{0,\rm DM}$ and the charge conjugates for χ^+ we get

$$\Gamma\left(\chi^\pm \to \chi^{0,\rm DM} + \text{SM}\right) = \Gamma_{e^\pm} + \Gamma_{\mu^\pm} + \Gamma_{\pi^\pm} \,, \tag{2.45}$$

where the RHS indicates the decay width into neutral states plus the SM states indicated by the subscript. The relevant widths are given by:

$$\begin{aligned}
\Gamma_{e^\pm} &= g\left(n, Y, \pm 1\right) \frac{G_F^2 \delta m_\pm^5}{60\pi^3} \,, \\
\Gamma_{\mu^\pm} &= g\left(n, Y, \pm 1\right) \frac{G_F^2 \delta m_\pm^5}{2\pi^3} \Phi(\delta m_\pm, m_\mu) \,, \\
\Gamma_{\pi^\pm} &= g\left(n, Y, \pm 1\right) \frac{G_F^2 f_\pi^2 |V_{ud}|^2 \delta m_\pm^3}{4\pi} \sqrt{1 - \frac{m_\pi^2}{\delta m_\pm^2}} \,,
\end{aligned} \tag{2.46}$$

where $g\left(n, Y, Q\right)$ accounts for the different strengths of the W boson coupling to each of the χ^Q:

$$g\left(n, Y, Q\right) = n^2 - 1 - 4(Q - Y)(Q - Y - \text{sgn}(Q)) \,, \tag{2.47}$$

with n the dimensionality of the multiplet and Y its hypercharge, G_F is the Fermi constant, $f_\pi = 131$ MeV is the pion decay constant. In the above formula Φ is the dimensionless full phase space of the 3-body decay of a massive particle of mass M into a massless lepton (e.g neutrino), a massive lepton with mass $m_l \ll M$ (e.g.

[4] We keep track in detail of the mixing of the charge ± 1 gauge eigenstates into the suitable charge ± 1 mass eigenstates.

muon), and a heavy particle with a mass $M - \delta$, for splitting $\delta \ll M$:

$$\begin{aligned}\Phi(\delta, m_l) =& \frac{1}{60\delta^5}\sqrt{\delta^2 - m_l^2}\left(2\delta^4 - 9\delta^2 m_l^2 - 8m_l^4\right) + \\ &+ \frac{1}{4\delta^5} m_l^4 \delta \,\mathrm{ArcCoth}\left(\frac{\delta}{\sqrt{\delta^2 - m_l^2}}\right) .\end{aligned} \tag{2.48}$$

The massless limit was employed for the electron since in the regions relevant for DTs the splittings allow to neglect m_e. In principle, for large splittings, also kaon and tau channels should be considered. However, for such large splittings the decays into the other SM particles are so fast that tracks will never be reconstructed.

If we move away from the $\delta m_0 \simeq 0$ points, we have to consider cases in which χ^+ is heavier than some of the particles with $Q > 1$.

We checked that for the 3_1, $4_{1/2}$, 5_1 there are choices of the couplings y_0 and y_+ for which $M_{\chi^{++}} < M_{\chi^+}$. In this case, χ^{++} cannot decay into χ^+, and is forced to decay to the neutral states by emitting twice an off-shell W boson that gives rise to $l^+\nu_l$ or π^+.

This decay rate has been estimated by summing over all possible final states using NDA. With respect to the decay with just one off-shell W emission, we get an extra factor $g(n, Y, 2)G_F f_\pi \delta/(16\pi^2)$ and $g(n, y, 2)G_F\delta^2/(16\pi^2)^2$ for any extra π or $l^+ v_l$ pair, respectively. Decays into negatively charged states are even more suppressed, since they need more extra final states. These configurations can give χ^{++} DT signals as well as *charged tracks* signals, which are potentially interesting for their peculiar detector response.

In Fig. 2.13 we display results for the DT search for the $2_{1/2}$ and 3_1 as a function of the lifetime of the charge +1 state, that is in a 1-to-1 relation with the mass splitting δm_+ (assuming minimal δm_0). We see that a collider of $\sqrt{s} = 6$ TeV can probe the $2_{1/2}$ for charge-neutral splitting generated purely by EW interactions. A collider of $\sqrt{s} = 3$ TeV can probe a large portion of the allowed lifetimes for the charged tracks corresponding to non-zero UV contributions in Eq. (2.16).

The DT search cannot probe the EW splitting for the 3_1, however it can cover a large portion of allowed lifetimes in the non-minimal case in which UV physics is contributing to the charged-neutral splitting.

The sensitivity to disappearing tracks is shown in the plots of Fig. 2.14, for minimal δm_0 imposed by DD and BBN, as a function of the dark matter mass and the lifetime $c\tau$ for each of the considered WIMP candidates.

The results of Fig. 2.14 show that the thermal mass can be excluded over the entire range of lifetimes that give rise to the DT signature. For the $2_{1/2}$ this corresponds to the full parameter space with splitting larger than the EW one. The contours for the $4_{1/2}$ and 5_1 WIMPs deserve some comment. In this case two singly-charged states are present: at least one state is in the DT region, and DT searches for this long-lived state, shown as solid contours, can probe the thermal mass over the full range of possible lifetimes. We also show the DT reach for the state with shorter lifetime,

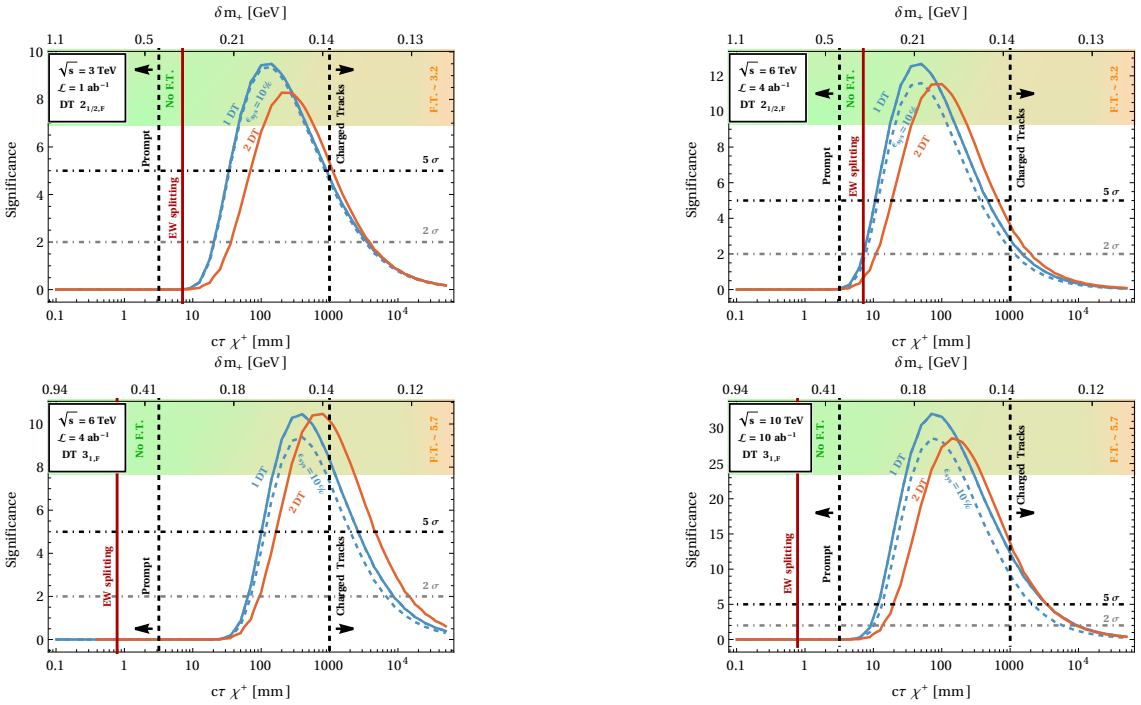

Figure 2.13: *Reach of DT for varying lifetime of the charged track. The* **red** *vertical line shows the benchmark lifetime for EW splitting. The* **blue** *and* **orange** *curves correspond to the reach with 1 and 2 disappearing tracks. For the single track search the solid (dashed) line assumes 0 (10%) systematics on the background. Fine-Tuning values computed on δm_+ following Eq. (2.17) are displayed as color code from green (no fine-tuning) to red (higher fine-tuning).* **Upper row:** *Collider reach for the $2_{1/2}$ of mass $M_\chi = 1.1$ TeV and $\sqrt{s} = 3$ TeV (left) and $\sqrt{s} = 6$ TeV (right).* **Bottom row**: *same as for the top rows, but for the case of the 3_1 of mass $M_\chi = 2.85$ TeV and $\sqrt{s} = 6$ TeV (left) and $\sqrt{s} = 10$ TeV (right).*

which could produce a second observable signal in parts of the parameter space. We show with different colors the two different physical solutions where the long-lived mass eigenstate χ^+ corresponds to the gauge eigenstate χ_+ or χ_-^c (corresponding to the regions of low or high δm_{2+} in Fig. 2.3), which have slightly different production cross-sections.

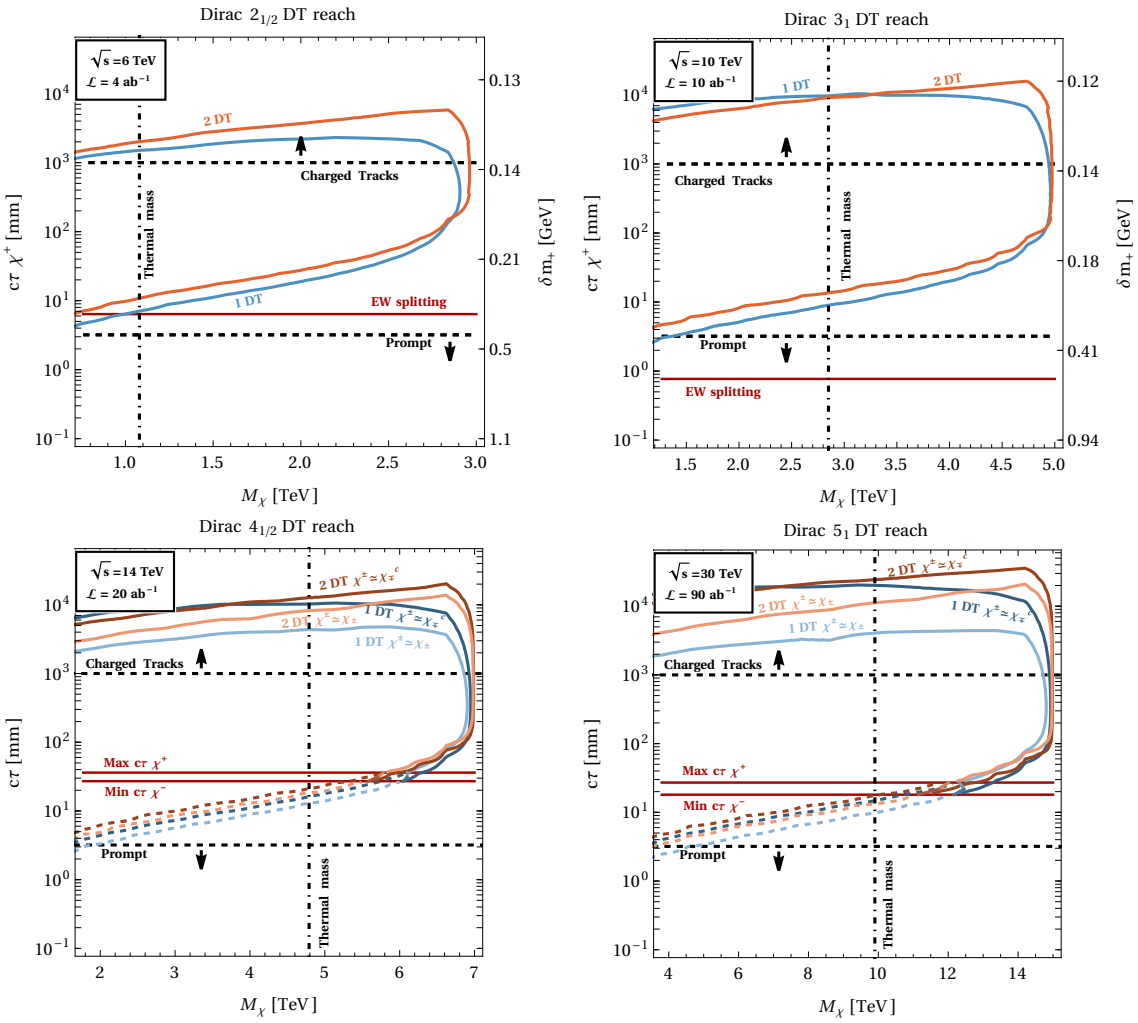

Figure 2.14: *Sensitivity at 95% C.L. from DT searches as a function of M_χ and the proper lifetime of the charged particle χ^+. The mass splitting δm_+ is also shown in the extra vertical axis in two upper panels. In the lower panels, the two different contours for each search channel correspond to the different physical situations where the heavy mass eigenstate corresponds to one of the two gauge eigenstates χ_+ or χ_-^c.* ***Top Left:*** *Dirac $2_{1/2}$ at $\sqrt{s} = 6$ TeV, $\mathcal{L} = 4$ ab^{-1}.* ***Top Right:*** *Dirac 3_1 at $\sqrt{s} = 10$ TeV, $\mathcal{L} = 10$ ab^{-1}.* ***Bottom Left:*** *Dirac $4_{1/2}$ at $\sqrt{s} = 14$ TeV, $\mathcal{L} = 20$ ab^{-1}.* ***Bottom Right:*** *Dirac 5_1 at $\sqrt{s} = 30$ TeV, $\mathcal{L} = 90$ ab^{-1}.*

If the LCP lifetime is even longer, then DT's become inefficient. Indeed for $c\tau_{\rm LCP} >$ 1 m the LCP gives long charged tracks (CT) with an average length roughly corresponding to the middle layer of the outer tracker. The SM background processes for this "long" track with anomalous properties strongly depends on the properties of the detector, therefore its study is outside the scope of this work. We limit ourselves

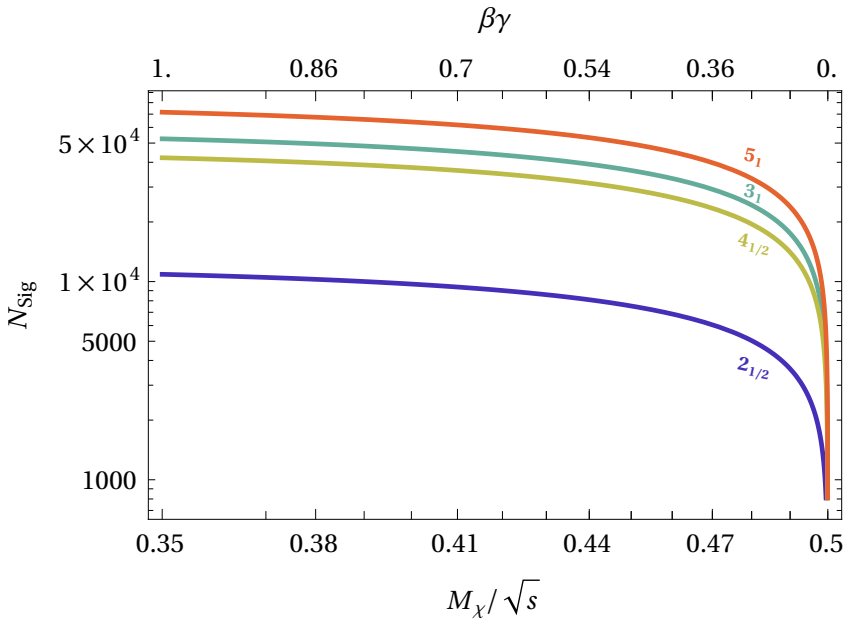

Figure 2.15: *Signal yield of the charged tracks for the* $2_{1/2}$, 3_1, $4_{1/2}$, 5_1. *The plot holds for all* $\sqrt{s}$ *in the tens of TeV range, assuming the luminosity scales as Eq. (2.31). The cuts applied on the produced charged* χ*'s are* $p_T > 200$ *GeV,* $|\eta_\chi| < 2$.

to estimate the number of expected signal events of charged χ pair production at a muon collider, as shown in Fig. 2.15. We highlight that this results approximately hold for generic $\sqrt{s}$ in the domain of tens of TeV, as long as Eq. (2.31) for the luminosity holds. In Fig. 2.15 we show the $\beta\gamma$ of the produced charged particle, which plays a crucial role to disentangle these special tracks from the SM background.

Our estimates for the LCP signature is based on the counting the number of LCP produced. For the LCP we require $p_T > 200$ GeV, $|\eta_\chi| < 2$, inspired by LHC searches [160]. For the $2_{1/2}$ and 3_1 we include in our counting all charged particles production, using the fact that χ^{2+} always promptly decays to the long lived χ^+. For the $4_{1/2}$ and 5_1, which have more complicated spectra, we stick to the minimal splitting scenario for the estimate of the charged tracks yield, which corresponds to the minimal y_+ necessary to lift χ^- above $\chi_{\rm DM}$. In this spectrum configuration χ^- is the most natural and only candidate to make long charged tracks, therefore we only consider this contribution in our result.[5]

2.5 WIMP direct detection

As outlined in Sec. 2.4, it is not possible to test heavy WIMP candidates at realistic future facilities. In this Section we briefly summarize the opportunities of the future Direct Detection experimental program in light of the mass predictions derived in Table 2.1.

[5]We neglect any possible contribution coming from χ^+ decaying into $\chi^{-,c}$, since in the region where mixing is relevant, the charged particles lifetimes are too short and are in the "stub tracks region", as shown in Fig. 2.18.

2.5.1 Real WIMPs

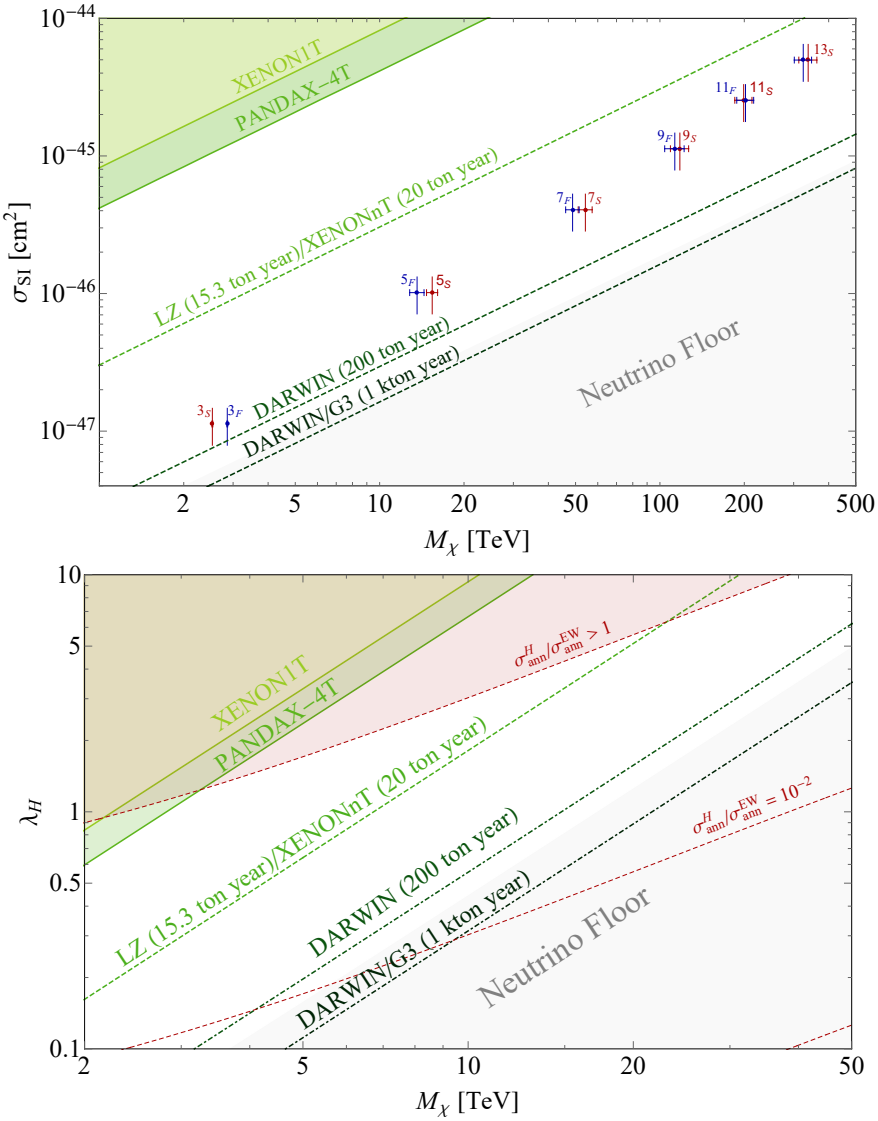

Figure 2.16: *In dark green we show the present contraints from XENON-1T [133] and PandaX-4T [114], the green dashed line shows the reach of LZ [127] and the brown green dot-dashed line the ultimate reach of DARWIN [54]. The light gray region show the neutrino floor for 200 ton/year exposure derived in Ref. [161].* **Above:** *Expected spin independent (SI) direct detection cross-section for Majorana n-plets (red) and for real scalar n-plets (blue) (assuming the Higgs portal coupling $\lambda_H = 0$). The vertical error bands correspond to LQCD uncertainties on the elastic cross-section in Eq. (2.53) while the horizontal error band comes from the theory determination of the WIMP freeze out mass.* **Below:** *Current and future reach on the Higgs portal quartic λ_H defined in Eq. (2.1) for scalar DM. In the shaded dark red region the quartic modifies the freeze-out cross-section by $\mathcal{O}(1)$ or more. The dashed red contours indicate smaller ratios of the Higgs-portal and the EW annihilation cross-sections.*

For $Y = 0$ the elastic scattering of DM with the nuclei is induced by EW loop diagrams first computed in [162, 163]. After EW gauge bosons are integrated out,

the structure of the UV effective Lagrangian describing the DM interactions reads

$$\mathscr{L}_{\rm eff}^{\rm SI} = \bar{\chi}\chi\left(f_q m_q \bar{q}q + f_G G_{\mu\nu}G^{\mu\nu}\right) + \frac{g_q}{M_\chi}\bar{\chi} i\partial^\mu\gamma^\nu\chi\mathcal{O}^q_{\mu\nu}\,,$$

where we focus on the DM spin independent (SI) interactions with quarks and gluons [164]. The quark twist-2 operator is defined as:

$$\mathcal{O}^q_{\mu\nu} \equiv \frac{i}{2}\bar{q}\left(D_\mu\gamma_\nu + D_\nu\gamma_\mu - g_{\mu\nu}\not{D}/2\right)q\,. \tag{2.49}$$

The Wilson coefficients of the operators for general EW n-plets with $Y = 0$ have been computed in Ref. [165] and at the leading order in $M_\chi/m_{W,h} \gg 1$ read

$$f_q^{\rm EW} \simeq \frac{(n^2-1)\pi}{16}\frac{\alpha_2^2}{m_W m_h^2}\,, \tag{2.50}$$

$$f_G^{\rm EW} \simeq -\frac{(n^2-1)}{192}\frac{\alpha_2^2\alpha_s}{m_W}\left(\frac{\sum_q \kappa_q}{m_h^2} + \frac{1}{m_W^2}\right)\,, \tag{2.51}$$

$$g_q^{\rm EW} \simeq -\frac{(n^2-1)\pi}{24}\frac{\alpha_2^2}{m_W^3}\,, \tag{2.52}$$

where $m_h = 125$ GeV is the SM Higgs mass, $q \in (c, b, t)$ and $\kappa_c = 1.32$, $\kappa_b = 1.19$, $\kappa_t = 1$.

Following Ref. [164], starting from the UV DM interactions we derive the IR interaction of DM with the nucleons. All in all, the SI elastic cross-section per nucleon in the limit $M_\chi \gg m_N$ reads

$$\sigma_{\rm SI}^{\rm EW} \simeq \frac{4}{\pi}m_N^4|k_N^{\rm EW}|^2, \tag{2.53}$$

where m_N is the nucleon mass and $k_N^{\rm EW}$ is defined as

$$k_N^{\rm EW} = \sum_q f_q^{\rm EW} f_{Tq} + \frac{3}{4}(q(2)+\bar{q}(2))g_q^{\rm EW} - \frac{8\pi}{9\alpha_s}f_{TG}f_G^{\rm EW}\,.$$

with the dimensionless nucleon form factors defined as $f_{Tq} = \langle N|m_q\bar{q}q|N\rangle/m_N$, $f_{TG} = 1 - \sum_q f_{Tq}$ with $q \in (u, d, s)$ and

$$\langle N(p)|\mathcal{O}^q_{\mu\nu}|N(p)\rangle = \frac{1}{m_N}(p_\mu p_\nu - \frac{1}{4}m_N^2 g_{\mu\nu})(q(2)+\bar{q}(2))\,. \tag{2.54}$$

where $q(2)$ and $\bar{q}(2)$ are the second moments of the parton distribution functions for a quark or antiquark in the nucleon taken from [165]. Notice that we choose a different set of values for the nucleon form factors with respect to previous studies [166] which explain the difference in our results. In particular, we take the FLAG average of the lattice computations in the case of $N_f = 2+1+1$ dynamical quarks [167, 168, 169].

By propagating LQCD uncertainties on the elastic cross-section (Eq. (2.53)), we obtain the vertical uncertainties on the SI cross-section predictions in Fig. 2.16. We find the partial accidental cancellation between the one loop and the two loop

contribution to reduce the elastic cross-section up to 30%. The horizontal bars represent the uncertainties coming from the computation of the thermal masses through the relic abundance. As shown in the plot all the WIMP cross-sections lie above the Xenon neutrino floor as computed in [161], but only a very large exposure experiment like DARWIN [54] would be able to probe the heavy thermal WIMPs.

Spin dependent (SD) interactions of DM with the nuclei are also induced by EW loops

$$\mathscr{L}_{\rm eff}^{\rm SD} = d_q(\bar{\chi}\gamma^\mu\gamma_5\chi)(\bar{q}\gamma_\mu\gamma_5 q), \quad d_q \simeq -\frac{(n^2-1)\alpha_2^2\pi}{24 m_W M_\chi}, \tag{2.55}$$

where the Wilson coefficient was computed in Ref. [165] and we expanded it at zeroth order in $M_\chi/m_h \gg 1$. The corresponding SD cross-section is too small to be probed even at a very large exposure experiment like DARWIN.

We comment on the new opportunities for direct detection that arise for scalar DM. Here, a non-zero Higgs portal quartic in Eq. (2.2) leads to a new contribution to the SI DM scattering cross-section with the nuclei, which again in the $M_\chi \gg m_N$ limit reads

$$\sigma_{\rm SI}^{\rm H} = \frac{4}{\pi} m_N^4 |k_N^{\rm H}|^2 \,, \tag{2.56}$$

where

$$k_N^{\rm H} \simeq \frac{\lambda_H f_N}{4 m_h^2 M_\chi} \,, \tag{2.57}$$

with $f_N \simeq 0.31$ obtained from lattice QCD results (see [170] for a more detailed discussion on the scalar triplet). In the lower panel of Fig. 2.16 we show the regions of parameter-space where the Higgs-portal interaction can be tested in direct detection. The requirement of not significantly affecting the freeze-out dynamics bounds the annihilation cross-section induced by the Higgs portal to be smaller than the EW cross-section, $\sigma_{\rm ann}^H/\sigma_{\rm ann}^{\rm EW} \lesssim 1$, which results in an upper bound on the quartic coupling λ_H shown by the red shading in Fig. 2.16. An estimate for this bound can be obtained by comparing the hard annihilation cross-sections, and reads

$$\lambda_H^2 \lesssim (n^2-3)(n^2-1) g_2^4/8 \,. \tag{2.58}$$

Interestingly, XENON1T and PANDAX-4T already exclude a large part of the region where the Higgs portal induces $\mathcal{O}(1)$ modifications of the freeze-out predictions, while LZ will completely exclude this possibility.

2.5.2 Complex WIMPs

Now we focus on the complex WIMPs. Unlike the real case, UV physics is relevant since it is necessary to produce the inelastic splitting needed to avoid Z scattering. However, the very same oeprators that are responsible for the splitting can also give extra contribution to DD cross-sections. Also, the non-zero hypercharge will change some of the form factors from the real case. Therefore we will analyze the prospects first of the minimal splitting benchmark, then trying to generalize to the other cases.

Minimal Splitting

The spin independent scattering cross-section $\sigma_{\rm SI}$ of DM on nuclei receives two contributions: i) from purely EW loop diagrams ii) from Higgs mediated tree-level diagrams generated by both $\mathcal{O}_0$ and $\mathcal{O}_+$. For minimal splitting Higgs mediated scattering is subdominant and $\sigma_{\rm SI}$ can be computed by considering only EW loop diagrams.

The Lagrangian describing the spin-independent (SI) DM interactions with quarks and gluons is identical to Eq. (2.5.1). The Wilson coefficients are modified by the presence of $Y \neq 0$ [165]

$$
\begin{aligned}
f_q^{\rm EW} &\simeq -\frac{\pi\alpha_2^2}{16 m_h^2 m_W}\left[n^2-1-\left(1.03+22(a_q^{V,2}-a_q^{A,2})\right)Y^2\right], \\
g_q^{\rm EW} &\simeq \frac{\pi\alpha_2^2}{24 m_W^3}\left[n^2-1-\left(4-18.2(a_q^{V,2}+a_q^{A,2})\right)Y^2\right], \\
f_G^{\rm EW} &\simeq \frac{\alpha_s\alpha_2^2}{192 m_h^2 m_W}\left[\left(\sum_{q=c,b,t}\kappa_q+2.6\right)(n^2-1)-\left(1.03\sum_{q=c,b,t}\kappa_q-7.5\right)Y^2\right],
\end{aligned}
\tag{2.59}
$$

where m_h is the mass of the Higgs and $\kappa_c = 1.32$, $\kappa_b = 1.19$, $\kappa_t = 1$. The loop functions $g_{\{H,S,T1,W,Z\}}$ have been evaluated in what follows in the limits

$$
w \equiv \frac{m_W^2}{M_{DM}^2} \to 0, \quad z \equiv \frac{m_Z^2}{M_{DM}^2} \to 0, \quad y \equiv \frac{m_t^2}{M_{DM}^2} \to 0.
$$

Furthermore we have defined $a_q^V = T_{3q}/2 - Q_q s_w^2$, $a_q^A = -T_{3q}/2$ with c_w, s_w being the cosine and the sine of the Weinberg angle, respectively. The terms proportional to Y correspond to the exchange of Z bosons inside the EW loops.

After the IR matching of these interactions at the nucleon scale [164], we can express $\sigma_{\rm SI}$ per nucleon (for $M_{\rm DM} \gg m_N$) exactly as in Eq. (2.53), with same $k_N^{\rm EW}$[6].

The direct detection reach on the different complex multiplets for minimal splitting is summarized in Fig. 2.17. As can be seen by the figure, most of the WIMPs can be probed for minimal splitting by future large exposure direct detection experiments like DARWIN with the notable exception of the $2_{1/2}$ and the 5_1 that we discuss below.

Combining Eq. (2.59) with Eq. (2.53) the parametric expression for $\sigma_{\rm SI}$ is

$$
\sigma_{\rm SI} \approx 10^{-49}\ {\rm cm}^2 (n^2 - 1 - \xi\, Y^2)^2, \tag{2.60}
$$

where $\xi = 16.6 \pm 1.3$ with the error coming from the lattice determination of the nucleon form factors. This formula makes evident that large cancellations with

[6]Notice that since $Y \neq 0$, the up and down quarks can give different contributions to the SI cross section Eq. (2.53). The ETM Collaboration [168] has computed the form factors in the case of degenerate light quarks so we take $f_{Tu} = f_{Td}$, ignoring possible differences between these two form factors.

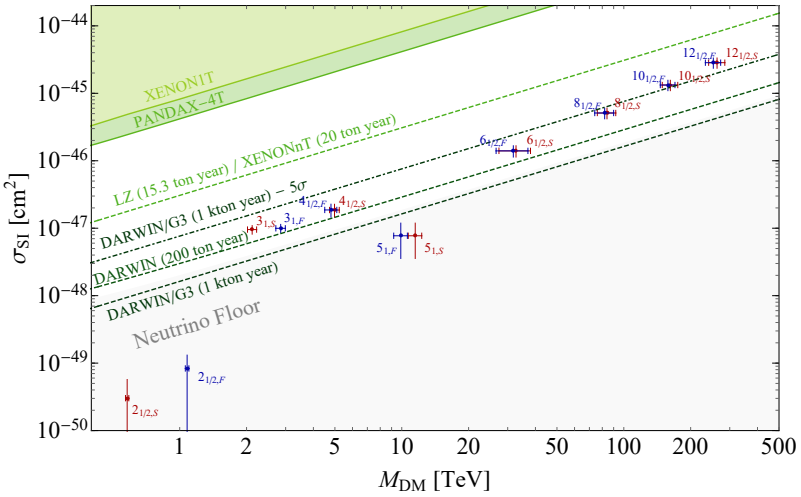

Figure 2.17: *Expected SI cross-sections for different complex WIMPs for minimal splitting as defined in Sec. 2.5.2. The* **blue dots** *correspond to Dirac WIMPs and the* **red dots** *to complex scalar WIMPs. The vertical error bands correspond to the propagation of LQCD uncertainties on the elastic cross-section (Eq. (2.53)), while the horizontal error band comes from the uncertainty in the theory determination of the WIMP freeze out mass in Table 2.2. The* **light green** *shaded region is excluded by the present experimental constraints from XENON1T [133] and PandaX-4T [114], the* **green dashed** *lines shows the expected 95% CL reach of LZ/XENONnT [127, 128] and DARWIN [54, 129].*

respect to the natural size of the elastic cross section can take place when $Y \simeq \sqrt{(n^2-1)/\xi}$. In particular, for $n = 2$ the exact cancellation takes place at $Y \simeq 0.44 \pm 0.02$, which almost matches the exact hypercharge of the doublet leading to the large uncertainty in Fig. 2.17. Similarly, the cancellation happens at $Y \simeq 1.2$ for $n = 5$, which explains why in this case the signal entirely lies below the neutrino floor, while it is within DARWIN reach for their real or millicharged counterparts as shown in Fig. 2.16 and Fig. E.1 respectively.

Spin dependent (SD) interactions of DM with the nuclei are also induced by EW loops and can lead to a larger cross section compared to the SI one [165]. Unfortunately, the predicted SD cross section for all the complex WIMPs lies always well below the neutrino floor and it will be impossible to test even at future direct detection experiments.

Non-minimal splitting

The Higgs portal operators in Eq. (2.6) generate upon EWSB a linear coupling of the DM to the Higgs boson of the form

$$\mathscr{L}_{D,h} = -\frac{\lambda_D v}{2\Lambda_{\rm UV}} \chi^2_{\rm DM} h \,. \tag{2.61}$$

This coupling mediates tree-level SI scattering processes of DM onto nuclei, therefore it can be constrained by direct detection experiments. As the mass splitting δm_0 has to be sufficiently large to suppress the scattering mediated by the Z boson, we find that the allowed parameter space for the non-renormalizable couplings is compact.

Following Ref. [65] we can integrate out the Higgs boson and write the couplings of the DM to the SM

$$\mathscr{L}^{\rm SI}_{\rm eff,h} = \frac{\lambda_D}{2m_h^2\Lambda_{\rm UV}}\chi^2\left(m_q\bar{q}q - \frac{\alpha_s}{4\pi}G^a_{\mu\nu}G^{a\mu\nu}\right), \tag{2.62}$$

so that the matrix elements f_q and f_G required to compute $\sigma_{\rm SI}$ are simply given by

$$f_q = f_q^{\rm EW} + \frac{\lambda_D}{2m_h^2\Lambda_{\rm UV}}, \qquad f_G = f_G^{\rm EW} - \frac{\alpha_s}{8\pi}\frac{\lambda_D}{2m_h^2\Lambda_{\rm UV}},$$

where $f_q^{\rm EW}$ and $f_G^{\rm EW}$ come from EW loops and are given in Eq. (2.59). We can rewrite the coupling λ_D solely in terms of mass splitting as

$$\frac{\lambda_D}{\Lambda_{\rm UV}} = -\frac{2Y}{v^2}(\delta\mu_{Q_M} + n\delta\mu_0), \tag{2.63}$$

where

$$\delta\mu_{Q_M} \equiv \frac{2\delta m_{Q_M} - \delta m_0 - 2\Delta M^{\rm EW}_{Q_M}}{2Q_M}, \qquad \delta\mu_0 \equiv \frac{\delta m_0}{n} \tag{2.64}$$

and $\Delta M^{\rm EW}_{Q_M}$ is the gauge induced mass splitting in Eq. (2.15).

$$\begin{aligned}
&\sigma_{\rm SI} \simeq 1.5\times10^{-49}\ {\rm cm}^2\frac{\left(P(n,Y) + (12+5.7(-1)^{2Y})\delta\mu\right)^2}{\left(2n+(-1)^{2Y}+1\right)^2},\\
&\delta\mu \equiv (2Q_M-1)\delta m_0 + 2\delta m_{Q_M},\\
&P(n,Y) \equiv -2n^3 - \left(2.4+1.5(-1)^{2Y}\right)n^2 + \left(16+7.4(-1)^{2Y}\right)n + 12(-1)^{2Y} + 12\,.
\end{aligned} \tag{2.65}$$

Replacing Eq. (2.63) into Eq. (2.53) allows us to translate the upper bound on $\sigma_{\rm SI}$ into an upper bound on δm_0 and δm_{Q_M}.

Results are shown in the summary plots in Fig. 2.18.

2.6 Parameter space for complex WIMPs

As discussed in the previous sections, for the complex WIMPs the operators responsible for the mass splittings, and hence the lifetimes, contribute non-trivially to Direct Detection cross sections. We now examine in greater detail the parameter space spanned by δm_0 and δm_{Q_M} specifically looking at each of the lightest multiplets of Table E.1 up to the 5_1 WIMP.

The $2_{1/2}$ and 3_1 are special WIMPs because they are the only multiplets with maximal hypercharge compatible with our assumptions. In particular, for $2_{1/2}$ requiring $\delta m_{0,+} > 0$ automatically implies the neutral WIMP candidate is the lightest one. Perturbativity requires $\delta m_0 < 40$ MeV for the $n = 3_1$ WIMP, because of the strong suppression of the 7 dimensional operator generating the neutral splitting. The narrower range of δm_0 for the 3_1 with respect to $2_{1/2}$ was expected from the higher dimensionality of $\mathcal{O}_0$ for $Y = 1$ as compared to $Y = 1/2$.

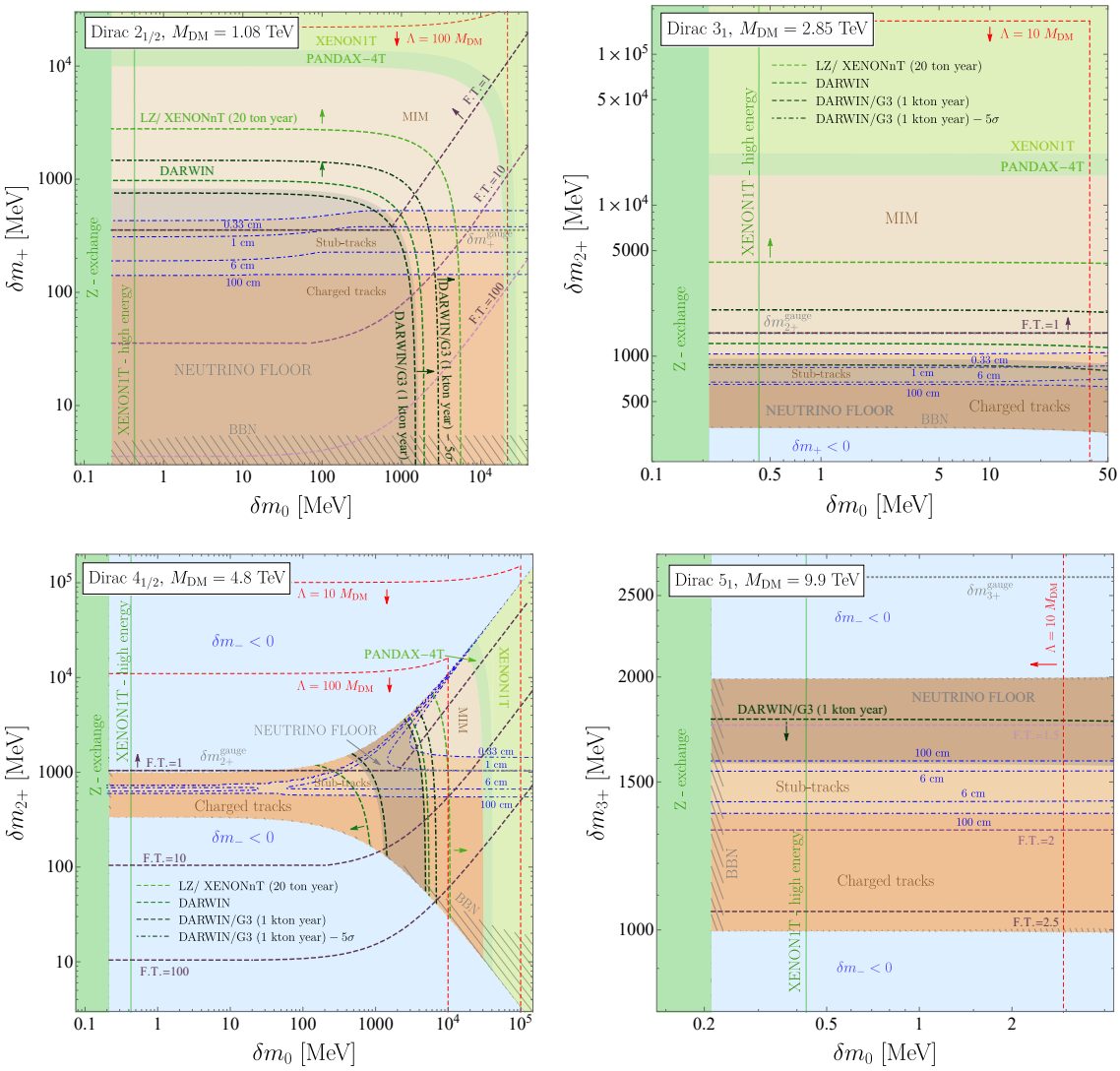

Figure 2.18: *Direct Detection and collider signatures in the plane δm_0 vs. δm_{Q_M} from the $2_{1/2}$ (upper left), 3_1 (upper right) $4_{1/2}$ (lower left) and 5_1 (lower right).* **Green** *shaded regions: excluded by current DD constraints on inelastic DM at small δm_0 and on Higgs-exchange elastic scattering at large splittings.* **Gray hatched** *regions: excluded by BBN constraints on the longest lived unstable particle in the multiplet.* **Red** *dashed lines: range of perturbative mass splitting at fixed Λ_{UV}/M_{DM} ratio.* **Light blue** *shaded patches: excluded because the lightest WIMP in the n-plet is not the neutral one.* **Dashed green** *lines: prospects from future high exposure xenon experiments like LZ, DARWIN and DARWIN/G3 (arrows pointing to the direction of the expected probed region).***Gray shaded** *region: DD signal below the neutrino floor of xenon experiments [129, 131]. The vertical XENON1T-high energy line show the ultimate reach of xenon experiments on inelastic DM (see Fig. 2.2).* **Blue** *dot-dashed lines: different expected lengths of charged tracks. Accordingly, different hues of* **brown** *distinguish regions where different signatures at future colliders are expected, as defined in Sec. 2.4.2. In every panel the DM mass is fixed to its freeze-out value. The precise center-of-mass energy for exclusion/discovery requires a more detailed study (see Sec. 2.4 and App. F).* **Dashed gray** *line: EW value of δm_{Q_M}.* ***Purple*** *dashed lines: fine-tuning contours among the different mass splittings as defined in Eq. (2.17). Mass splittings above the F.T.=1 line are not fine tuned.*

In Fig. 2.18 we show the constraints on the Dirac $2_{1/2}$ and 3_1 in the parameter space spanned by δm_0 and δm_{Q_M} coming from present DD experiments like XENON1T and PANDAX-4T, as well as prospect from future high exposure xenon experiments, *i.e.* LZ, XENONnT, DARWIN and DARWIN/G3. As we can see from Eq. (2.63), these bounds depend solely on the combination

$$\delta\mu \equiv 2\delta m_{Q_M} + (2Q_M - 1)\delta m_0 \ . \tag{2.66}$$

In particular we find

$$\sigma_{\rm SI} \approx 10^{-48}{\rm cm}^2 \begin{cases} \left(0.3 - \dfrac{\delta\mu}{1\ {\rm GeV}}\right)^2, \ [2_{1/2}] \\ \left(0.2 + \dfrac{\delta\mu}{1\ {\rm GeV}}\right)^2, \ [3_1] \end{cases} . \tag{2.67}$$

In the region of low mass splitting for both $2_{1/2}$ and 3_1 the direct detection cross section lies below the neutrino floor. For $2_{1/2}$, Eq. (2.67) shows that large cancellations between EW loops and tree-level Higgs exchange occur around $\delta\mu \simeq 300$ MeV, while for 3_1 the minimum $\sigma_{\rm SI}$ is obtained for $\delta\mu = 0$ and falls below the neutrino floor. To produce a direct detection cross section above the neutrino floor for the $2_{1/2}$ (3_1) we need $\delta\mu > 1.6$ GeV ($\delta\mu > 2.0$ GeV). PANDAX-4T already excludes mass splitting $\delta\mu < 20$ GeV ($\delta\mu < 30$ GeV) for the $2_{1/2}$ (3_1).

All in all, DD still leaves a large portion of parameter space unconstrained between the neutrino floor and the PANDAX-4T constraints. Remarkably, this region corresponds to mass splittings that do not require tuned adjustments of the three contributions to δm_0 and δm_+. The region of large splittings down to $\delta\mu \sim 1$ GeV can be covered by large exposure xenon experiments while the large portion of the parameter space lying below the neutrino floor should be taken as a major motivation for a future muon collider.

For $2_{1/2}$ WIMP the neutrino floor region can be fully probed only via a combination of charged tracks, DT and MIM searches. The different search strategies become relevant depending on the δm_+ value, as shown in Fig. 2.18. For the 3_1 WIMP stub and charged tracks can exclude the entire neutrino floor region, while MIM and DT searches can be complementary to large exposure DD experiments to probe the rest of the parameter space.

While the plot in Fig. 2.18 show the possible regions in which DT can be reconstructed efficiently, they do not show if the reach is large enough to guarantee exclusion (or discovery) of the WIMP candidate. For these two WIMP candidates a detailed discussion was given in Sec. 2.4. The general message is that for $\sqrt{s}$ sufficiently larger than twice the thermal DM mass DT searches will be powerful enough to probe the parameter space.

We now study the $4_{1/2}$ and 5_1, which require non-maximal hypercharge. The constraints coming from DM stability shape the allowed parameter space of the $4_{1/2}$. In particular, we must require δm_- to be positive. This constraint excludes the light blue shaded region in Fig. 2.18 bottom left.

The region where the direct detection cross section lies below the neutrino floor is reduced to a tiny band for 4 GeV $< \delta\mu <$ 15 GeV. This region can be probed by direct searches at a future high energy muon collider with $\sqrt{s} > 10$ TeV because of the thermal mass of the $4_{1/2}$ lies around 4.8 TeV. In particular, stub and charged tracks searches could cover almost the entire neutrino floor region, except for a small portion accessible only to MIM searches. The rest of the viable parameter space for the $4_{1/2}$ can be in principle probed by large exposure direct detection experiments.

We show the parameter space of the 5_1 WIMP in Fig. 2.18 bottom right. The dominant constraint comes from the perturbativity of the operator generating the neutral splitting, which requires $\delta m_0 < 3$ MeV. As a consequence, testing larger splittings for inelastic DM at XENON1T can already probe large portions of the allowed parameter space of the 5_1. DM stability requires 1 GeV $\lesssim \delta m_{3+} \lesssim$ 2 GeV. The parameter space can be fully excluded by charged and stub track searches if a muon collider of $\sqrt{s} > 20$ TeV will be constructed. Besides, all the allowed mass splittings except a small window 1.8 GeV $\lesssim \delta m_{3+} \lesssim$ 2.0 GeV can be probed by DARWIN/G3.

2.7 Other WIMP probes

In this Section we study indirect probes of EW WIMPs. In Sec. 2.7.1 we study the constraint from Indirect Detection: the DM particle can still have residual annihilations into SM particles that can be detected from telescopes. In Sec. 2.7.2 we explore how the presence of extra EW multiplets can modify SM precision observables in the EW sector. These two experimental probes are available to both real and complex WIMPs. In Sec. 2.7.3 we study the possibility that some of the operators needed to have viable complex WIMPs can introduce new sources of CP violation in the SM that can be in principle tested by electron dipole moment (EDM) experiments.

2.7.1 Indirect Detection

The current and upcoming ground-based Cherenkov telescopes are in a very good position to probe heavy WIMP n-plets with $n > 5$, which would be inaccessible otherwise. Indeed, these telescopes are designed to detect very high energy gamma-rays (i.e. $E_\gamma \gtrsim 100$ GeV) coming from different astrophysical objects and they are therefore sensitive to the gamma-ray signal from the annihilations of EW n-plets. The typical spectrum is characterized at very high energy by gamma-ray lines, peaking at the DM mass $E_\gamma \simeq M_\chi$, from the loop-induced annihilations into $\gamma\gamma$ and γZ. The cross-section in this channel is largely boosted by the SE (see e.g. [50, 171, 172]) and can raise above the gamma-ray continuum from the showering, hadronization and decays of the electroweak gauge bosons [173].

From the astrophysical point of view, the reach of high energy gamma lines searches depends very much on which portion of the sky the telescopes will be pointed at. In finding the optimal choice, a balance has to be found between the maximization of photon flux at Earth and the control over the systematical uncertainties. Two very well studied astrophysical targets are the Galactic Center (GC) [55, 174] and the

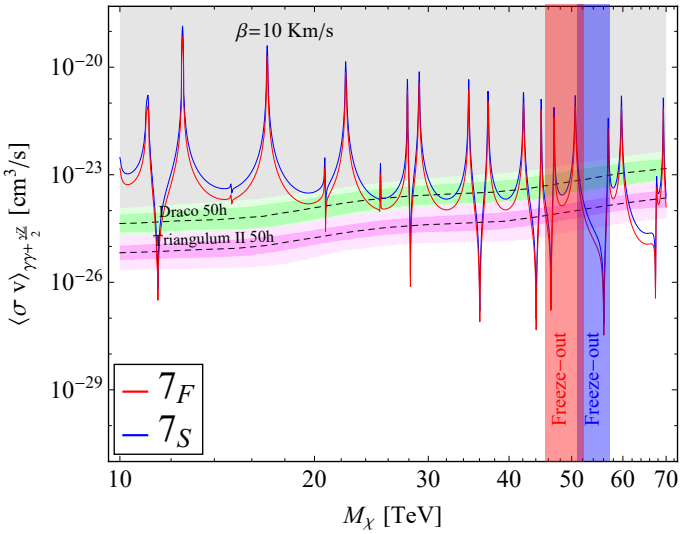

Figure 2.19: *Expected CTA sensitivities (dashed black lines) with 68% and 95% CL intervals derived as in Ref. [55] assuming 50 hours observation time towards Draco (green) and Triangulum II (magenta). We show the SE annihilation cross-section into the channels that contribute to the monocromatic gamma line signal (i.e. $\gamma\gamma$ an γZ) for a scalar 7-plet (blue) and a fermionic 7-plet (red). The vertical bands show the predicted thermal masses for the scalar 7-plet (blue) and the fermionic 7-plet (red), where the theory uncertainty is dominated by the neglected NLO contributions (see Table 2.1).*

Milky Way's dwarf Spheroidal galaxies (dSphs) [55]. In the GC, the uncertainties are dominated by the importance of the baryonic physics in the inner most region of the Milky Way which comes together with the poor knowledge of the DM distribution at the center of the Milky Way [175, 176, 177, 178]. On the contrary, dSphs stands out as very clean environments to search for high energy γ-lines only residually affected by systematics related to the determination of their astrophysical parameters in the presence of limited stellar tracers [179, 180].

Motivated by the above considerations, we show a very preliminary analysis of ID signals coming from annihilations of the WIMP real 7-plet. We focus on the CTA prospects by considering 50h of observations time towards two dSph targets in the northern hemisphere: the classic dSph Draco and the ultra-faint one Triangulum II. Notice that the DM properties of Draco come from hundreds of stellar tracers, while those from Triangulum II are based on just 13 tracers, making the latter more speculative and subject to large systematics in the determination of the geometrical J-factor [181]. Hence, the reach of Draco should be taken as the baseline reach for CTA.

Our analysis is simplified because the signal shape we consider is essentially a single line at $E_\gamma \simeq M_\chi$. Consistently we take the CTA prospects derived in Ref. [55] for a pure line. We ignore the contributions of the continuum spectrum, the extra features of the spectral shape induced by the resummation of EW radiation and the contribution of the BSF to the photon flux. While neglecting BSF is justified if we focus on very high energy photons, a careful computation of the $\gamma + X$ cross-section, where X is any other final state would be needed to precisely assess the experimental

sensitivity [182]. In the last decade, many different groups have investigated the impact of large Sudakov logarithms and large collinear logarithms on the indirect detection reach, focusing mainly on the case of the fermionic 3-plet [183, 184, 185, 186, 187, 187]. The inclusion of these effects has been shown to increase the reach of $\sim 20 \div 30\%$ for the 3-plet [55, 174, 188] and it is expected to be even more important for higher DM masses.

In Fig. 2.19 we overlay the SE annihilation cross-section for the real 7-plets at $v = 10$ km/sec against the CTA experimental reaches. In order to compute the SE in this velocity regime, we took advantage of the parametrization introduced in [172] and used the full expressions for the SE at leading order, including EW breaking effects. The SE saturate already at $v \simeq 10^{-3} \div 10^{-2}$ far away from the resonances. As we can see, both a 50 hour observation of Triangulum II and of Draco have good chances to detect the high energy γ line in the 7-plet annihilation spectrum.

As we see from Fig. 2.19, given the strong mass-dependence of the features of the SE cross-section, a major source of theoretical uncertainty on the reach of indirect detection is still the determination of the real 7-plet thermal mass. Therefore, a full computation of the thermal relic mass including NLO effects is required together with a careful computation of the $\gamma + X$ cross-section along the lines of Ref.s [183, 184, 185, 186, 187, 187] to careful assess the indirect detection reach for the real 7-plet.

Independently on our current inability of making a conclusive statement because of the large theory uncertainties, it is clear that large n-plets are a perfect target for future Cherenkov telescopes which deserves further theoretical study. A complementary open phenomenological question is if the low energies gamma lines at $E_\gamma \simeq E_B$ associated to BSF can be actually disentangled from the continuum (see [51, 189] for preliminary work in this direction). An analogous question can be asked for monochromatic neutrinos from BS annihilations.

2.7.2 Electroweak precision observables

The addition of new EW multiplets to the SM leads to deviations in EW observables which could be tested with LEP data, at the LHC and at future colliders [147, 190]. Since the presence of new EW multiplets affects mainly gauge bosons self energies, their indirect effects can be encoded in the oblique parameters [56, 57]. Here we briefly summarize the main features of these contributions following the notation of Ref. [57]. The most relevant oblique parameters can be related to the SM gauge boson vacuum polarizations

$$\begin{aligned} \hat{Y} &= \frac{g_Y^2 m_W^2}{2} \Pi''_{BB}(0) \quad , \quad \hat{W} = \frac{g_2^2 m_W^2}{2} \Pi''_{33}(0) \ , \\ \hat{S} &= \Pi'_{3B}(0) \quad , \quad \hat{T} = \frac{\Pi_{33}(0) - \Pi_{WW}(0)}{m_W^2} \ , \end{aligned} \tag{2.68}$$

where Π_{ij} appear in the kinetic terms of the EFT describing the SM vectors interactions at energies smaller than the DM mass

$$\mathscr{L}_{\text{oblique}} = -\frac{1}{2} V_i^\mu \Pi_{ij} V_{j,\mu} \ . \tag{2.69}$$

In particular, all the EW multiplets (both real and complex) give a universal contribution to the $\hat{W}$, $\hat{Y}$ as previously found in [43]

$$\hat{W} = \frac{\alpha_{\text{em}} \cot^2\theta_W}{180\pi} \frac{m_Z^2}{M_{\text{DM}}^2} \kappa n(n^2-1) \simeq 3.8\kappa \times 10^{-7} \left(\frac{1\ \text{TeV}}{M_{\text{DM}}}\right)^2 n(n^2-1) \ , \tag{2.70}$$

$$\hat{Y} = \frac{\alpha_{\text{em}}}{15\pi} \frac{m_Z^2}{M_{\text{DM}}^2} \kappa n Y^2 \simeq 3.4\kappa \times 10^{-7} \left(\frac{Y}{1/2}\right)^2 \left(\frac{1\ \text{TeV}}{M_{\text{DM}}}\right)^2 n \ , \tag{2.71}$$

where $\kappa = 1, 1/2, 1/8, 1/16$ for Dirac fermions, real fermions, complex scalars and real scalars respectively. In the numerical estimates we normalized the expected contributions to the fermionic $2_{1/2}$. The rough expectations for heavier WIMPs can be obtained from the equations above by remembering that $M_{\text{DM}} \sim n^{5/2}$. The contribution to $\hat{W}$ scale like as $\sim 1/n^2$ while the one to $\hat{Y}$ as $\sim 1/n^4$.

$\hat{W}$ and $\hat{Y}$ induce effects in SM observables that grow with energy so that LHC searches have already ameliorated the sensitivity on these operators compared to LEP. In particular $\hat{W}$ has been recently bounded by CMS [191] and $\hat{Y}$ is also set to be tested with a similar precision [192]. Even if the current precision is not sufficient to probe the WIMP thermal masses, further improvements are expected in a future high energy muon collider. This could provide interesting indirect tests of EW WIMPs [147, 155, 193]. Given the size of the expected WIMP contributions in Eq. (2.70) and Eq. (2.71) the results of Ref. [155] indicates that a muon collider of $\sqrt{s} = 30$ TeV would be needed to observed these deviations.

As extensively discussed in this thesis, complex WIMPs require contact interactions with the SM Higgs to be phenomenologically viable. These interactions give an additional contributions to the $\hat{S}$ parameter. Moreover, the mass splittings inside the EW multiplet induced by $\mathcal{O}_0$ and $\mathcal{O}_+$ break the custodial symmetry in the Higgs sector. As a consequence, complex WIMPs give irreducible contributions also to the $\hat{T}$ parameter. The explicit formulas for fermionic WIMPs are

$$\begin{aligned}
\hat{S}_F &= -\frac{\alpha_{\text{em}} Y n(n^2-1)}{9\pi s_{2W} M_{\text{DM}}} \delta\mu_{Q_M} \simeq \\
&\simeq -1.6 \times 10^{-6} \left(\frac{Y}{1/2}\right) \left(\frac{1\ \text{TeV}}{M_{\text{DM}}}\right) \left(\frac{\delta\mu_{Q_M}}{10\ \text{GeV}}\right) n(n^2-1) \, , \\
\hat{T}_F &= -\frac{\alpha_{\text{em}}}{18\pi s_{2W}^2} n(n^2-1) \frac{\delta\mu_{Q_M}^2 + \delta\mu_0^2}{m_Z^2} \simeq \\
&\simeq -2.3 \times 10^{-6} \frac{\delta\mu_{Q_M}^2 + \delta\mu_0^2}{100\ \text{GeV}^2} n(n^2-1) \, ,
\end{aligned} \tag{2.72}$$

where $s_{2W}^2 = \sin^2 2\theta_W \simeq 0.83$ while $\delta\mu_{Q_M}$ and $\delta\mu_0$ are defined in Eq. (2.64). The corresponding formulas for scalar WIMPs are easily obtained from the fermionic

ones by replacing $\hat{S}_S = \frac{1}{4}\hat{S}_F$ and $\hat{T}_S = -\hat{T}_F$. Our result for $\hat{T}_S$ is consistent with the result in Ref. [123], first computed in [194].

Both $\hat{S}$ and $\hat{T}$ are currently constrained at the level of 3×10^{-3} by LEP data (where the precise value will of course depend on the correlation between these two parameters [57]). High luminosity colliders further exploring the Z pole like FCC-ee will improve this precision typically by a factor of 10 [195] with the ultimate goal of pushing the precision of EW observables to the level of 10^{-5} [196].

Concerning $\hat{S}$ we conclude that the deviations induced by complex WIMPs are unlikely to be visible unless for light multiplets with the ultimate EW precision. Conversely, at fixed large splitting and increasing size of the multiplet, the deviations on $\hat{T}$ are enhanced to the point that a $12_{1/2}$ multiplet is giving $\hat{T} \simeq 3 \times 10^{-3}$, which is within the reach of current LEP data and could help reducing the tension the m_W mass extracted from the EW fit and the one measured directly by the CDF collaboration [197]. Of course this extreme scenario requires very large couplings at the boundary of perturbativity for the contact operators inducing the splitting in Eq. (2.6).

2.7.3 Electric dipole moment

As mentioned in Chapter 2 and detailed in App. B.1, the operators generating the splittings for complex fermionic WIMPs have in general two different chiral structures and different relative phases. This generically induces operators contributing to the electron EDM at 1-loop [198, 199]. Following the notation of Ref. [198], the leading operator generated by WIMPs loops is

$$\mathscr{L}_{\rm EDM} \supset \frac{c_{WW}}{\Lambda^2_{\rm UV}} |H|^2 W\tilde{W} \ , \tag{2.73}$$

where we neglect for this discussion operators such as $|H|^2 B\tilde{B}$ and $H^\dagger \sigma^a H W\tilde{B}$ that would be suppressed by powers of Y/n with respect to the one with two $\mathrm{SU}(2)_{\rm L}$ field strength insertions.

The Wilson coefficient in Eq. (2.73) is constrained by the recent measurement of the ACME collaboration [200] to be

$$c_{WW} < 4 \times 10^{-3} g_2^2 \left(\frac{\Lambda_{\rm UV}}{10\ \text{TeV}}\right)^2 \frac{d_e}{1.1 \times 10^{-29} \text{e cm}} \ . \tag{2.74}$$

The effective operator in Eq. (2.73), is generated at $4Y$-loops from the $\mathcal{O}_0$ operator and its axial partner and at 2-loop from the $\mathcal{O}_+$ operator and its axial partner. For example the 2-loops Wilson coefficients can be estimated as

$$c_{WW}|_{\rm 2-loop} \simeq \frac{g_2^2 n(n^2-1)^2 \mathcal{I}[y_I y^*_{I,5}]}{32(16\pi^2)^2 \Lambda^2_{\rm UV}} \ , \tag{2.75}$$

where the index y_I controls the contribution from $\mathcal{O}_0$ or $\mathcal{O}_+$ and $y_{I,5}$ the ones from their axial counterpart. If only $\mathcal{O}_0$ is present, like it would be for instance in the

minimal splitting case for the $2_{1/2}$ multiplet, the bound in Eq. (2.74) can be rewritten as an upper bound on the neutral splitting

$$\delta m_0 < 16 \text{ GeV} \left(\frac{2}{n}\right)^{\frac{3}{2}} |\theta_{\rm CP}|^{\frac{1}{2}} \sqrt{\frac{|d_e|}{1.1 \times 10^{-29} \text{e cm}}} \,, \tag{2.76}$$

where we defined $\theta_{\rm CP} = y_I^2/\mathcal{I}[y_I y_{I,5}^*]$. A similar bound is found for δm_{Q_M} in the minimal splitting case, where $\mathcal{O}_0$ can be neglected. Hence, for $\mathcal{O}(1)$ couplings and CP-violating phases, the EDM already gives competitive if not stronger bounds with respect to those shown in Table 2.2. Interestingly, future experimental upgrades are expected to be sensitive to electron EDM as small as $d_e \simeq 10^{-34}$e cm [58] which would provide sensitivity to the WIMP parameter space down to splittings of order ~ 50 MeV for $\mathcal{O}(1)$ couplings and CP-violating phases.

It would be interesting to further explore this direction in models where the $\mathcal{O}(1)$ CP-violating phase is motivated by a mechanism producing the observed baryon asymmetry in the Universe such as WIMP baryogenesis [201, 202].

2.8 Summary

After many years of hard experimental and theoretical work, the possibility that Dark Matter is part of an EW multiplet is still open and deserves theoretical attention in view of the future plans for experimental searches. In [47, 48] we made a first step in sharpening the theoretical predictions computing all the calculable thermal WIMP masses for real and complex EW representations. We included both Sommerfeld enhancement and bound-state-formation effects at LO in gauge boson exchange and emission. Our results are summarized in Table 2.1 and Table 2.2.

We find that the largest $\mathrm{SU}(2)_{\rm L}$ n-plet for which thermal freeze-out is calculable at LO is the 13-plet, which is as heavy as 350 TeV. Stronger requirements about the perturbativity of the EW sector up at high scales can further lower the number of viable candidates.

Given the updated mass predictions from thermal freeze-out, we re-examined various phenomenological probes of WIMP DM, with a focus on collider and Direct Detection experiments. High energy lepton colliders in the $6 \div 30$ TeV range, such as a future muon collider, can directly produce EW multiplets with $n \leq 5$. We summarize our findings in Fig. 2.5.

In order to probe a Majorana fermion with $n = 3$ ($n = 5$) with missing-mass searches, a collider with at least $\sqrt{s} \sim 12$ TeV ($\sqrt{s} \sim 35$ TeV) and the baseline integrated luminosity of Eq. (2.31) would be required. The highest mass reach is obtained by means of an inclusive mono-W search. Interestingly, disappearing tracks originating from the decay of the singly-charged state into the neutral one are robust predictions of real EW multiplets with $Y = 0$, and ameliorate the sensitivity for the 3_0-plet compared to missing-mass searches. For the 5_0-plet we find the expected sensitivity of disappearing tracks to be very similar to the one of missing-mass searches due to the shorter average lifetime of the tracks.

Regarding complex candidates, we find that thanks to combined MIM searches a future muon collider with $\sqrt{s} = 6$ TeV would be able to fully probe the existence of a fermionic complex WIMP doublet at its thermal mass around 1.1 TeV. [7] Instead, a muon collider of $\sqrt{s} = 10$ TeV would be able to make a discovery at the thermal mass for the fermionic 3_1 using a luminosity around 10 ab^{-1}, that is considered as a benchmark for currently discussed project for this type of collider [149, 203].

Scalar WIMPs can not be probed through missing-mass searches, due to their smaller production cross-section. However, disappearing tracks searches are very powerful tests even for scalar multiplets, thanks to their very low background contamination. This signature is therefore a crucial ingredient to fully explore the parameter space of thermally produced WIMP Dark Matter at future colliders.

Finally, large-exposure liquid Xenon experiments like DARWIN can in principle probe all the relevant EW WIMPs through their weak interaction with nuclei. Our main result, summarized in Fig. 2.16 and Fig. 2.18, is that a kiloton exposure xenon experiment would be able to probe most of the complex and the real WIMPs, with the notable exceptions of the complex $2_{1/2}$ and the 5_1, whose cross sections lie naturally well below the neutrino floor. This result for the complex doublet was of course well known from the many previous studies on the SUSY Higgsino [204], but it gets further substantiated in the context of our WIMP classification. The fermionic 5_1 can be discovered at a $\sqrt{s} \lesssim 30$ TeV machine, showing the interplay between DD and collider experiments.

We further study the parameter space of the different complex WIMPs and find regions where the direct detection cross section can drop below the neutrino floor because of accidental cancellations of the EW elastic scattering (like for the 5_1) or at small (mildly tuned) values of the charged-neutral mass splittings (like for the 3_1) or for the destructive interference of EW and Higgs induced scattering (like for the $4_{1/2}$). In all these cases a high energy lepton collider might be again the only way of discovering these WIMPs.

Scalar WIMPs can further be tested through their Higgs-portal quartic interaction. Interestingly, $\mathcal{O}(1)$ modification of the thermal freeze-out masses due to the Higgs portal are already partially excluded by the XENON1T and PANDAX-4T results, and will be completely excluded by LZ.

The list of WIMP candidates we furnished provides a series of targets that can be probed at successive stages of a future machine. Moreover, our analysis shows that future searches for long-lived charged tracks will be crucial to fully probe the WIMP parameter space. This strongly motivates a detailed collider study assessing the expected sensitivity of these searches in a realistic muon collider environment.

[7] Note that our results on the DT differs from the ones in Ref. [122]. This discrepancy can be ascribed to their overestimation of the efficiency for DTs with short lifetimes. We thank the authors for correspondence on this. We believe that our projections on the mono-γ are stronger than the ones derived on Ref. [112] because of our optimization of the kinematical cuts.

Chapter 3

DM as a SM singlet

In Chapter 2 we studied the consequences of DM being charged under the SM gauge group. More precisely, we have considered EW WIMPs. As outlined in the introduction, if the DM has no SM gauge interactions, the interaction between the Dark Sector and SM might happen through contact interaction captured by portal operators made by the product of singlet operators. Our goal is to attempt to study the scenario of a Secluded Dark Sector (DS) in a model-agnostic way. Secluded Dark Sectors with their own particle content and dynamics, that interact with the Standard Model feebly, are well motivated for a variety of reasons. If such sectors contain or interact with dark matter, they are a natural scenario to probe in terrestrial and cosmological studies. Such sectors can also arise naturally from bottom-up BSM considerations motivated to address various issues in SM, as well as in top-down string constructions. The hidden valley scenario [72] initiated various model-building and phenomenological aspects of such DS and this remains a focus of much present research activity to date.

We want to keep the study as general as possible, therefore we want to avoid specifying the precise interaction of DS particles. In general it is hard to fix the cosmology of DS models only specifying the portal (see [79] for an attempt). Therefore we will neglect the cosmology, and try to test the model by studying the lightest excitations that can be produced at experiments.

Dark sectors with sufficiently low production threshold are generally probed by high-intensity experiments with centre-of-mass energies much lower than typical high energy collider machines. Such high-intensity experiments involve a proton or electron beam (or even muon beam, see ref. [205, 206, 207] for future proposals of fixed target experiments with a muon beam) hitting a fixed target, producing a high flux of SM particles alongside a beam of putative DS particles (see ref. [208, 209, 210, 211, 212, 213] for general reviews on the capabilities of high intensity experiments). Due to weak couplings to the SM, lightest DS particles once produced tend to have long lifetimes, allowing them to travel macroscopic distances before decaying back to visible particles. Suitable detectors placed downstream from the fixed target can be used to discriminate a possible DS signal against SM background.

We remark that in this case what is being tested is not really the DM hypothesis, but the presence of some light states, that might be or not be the DM. In particular, since we focus on decaying particles, such excitations cannot be the DM but rather some DS partner that lives in the DS. While this is a non-minimal assumption on the nature of the DS, such particles are expected to exist especially in strongly coupled scenarios.

Short and long-baseline neutrino experiments happen to be placed behind some of the most powerful proton beams up to date. Thus, they provide an ideal and pre-existing infrastructure for probing low scale dark sectors. In fact, neutrinos themselves are a prototype for a DS, so it is not a surprise that a facility for studying them is useful more generally. Further, a rich short-baseline experimental program for neutrinos has been planned at Fermilab (e.g. DUNE, SBNP, see ref. [214, 215, 216] for experiment details, ref. [217, 218, 219] for recent studies on DS search at these experiments). These new proposals will improve upon the current neutrino experiments, using a higher number of protons on target (POT), and better detectors that can help in reducing SM background [220], therefore leading to an increased sensitivity for DS searches.

Apart from neutrino experiments, a natural setup to probe DS is at future experiments proposed for long-lived particle (LLP) searches (e.g. see [221, 222, 223] for a review). These experiments are in the study phase and may require a longer timescale. Existence of current data from neutrino experiments, and a fairly short timescale for future ones to come online make neutrino experiments a powerful and efficient probe of dark sectors.

Any broad enough search for dark sectors must explore all axes of ignorance of such scenarios. The dimensionality D of the portal interaction between the DS and SM is one such axis. While searches for DS interacting with the SM via relevant portals ($D \leq 4$) have been well studied (see refs. [222, 224, 225] and references therein), the case of irrelevant portals ($D > 4$) is equally well motivated. Among these, the *axion* portal ($D = 5$) has been studied the most, especially at the high intensity frontier [226, 227, 228, 229, 230, 231, 232] (see [233] for a study specific to neutrino experiments). Regarding other irrelevant portals ($D \geq 5$) that might connect the DS and SM, some recent progress has been made [75, 76, 234, 235, 236, 237, 238, 239]. In this Chapter, we probe SM-neutral dark sectors which interact via irrelevant portals with the SM at neutrino oscillation experiments. On general principles we are led to $D \sim 5$ and $D \sim 6$ portals. Such dark sectors are in general *very elusive* due to the irrelevant nature of the portal. The results presented here are complementary to the constraints from current high energy terrestrial experiments and astrophysical data, presented in [76], and in specific cases, much stronger, as we point out in the relevant sections.

Here we consider various (inclusive) DS production processes. Depending on the DS 4-momentum $p_{\rm DS}$, a different production process can be relevant: meson decays (for $\sqrt{p_{\rm DS}^2} \lesssim$ M, the parent meson mass), direct partonic production (for $\sqrt{p_{\rm DS}^2} \gtrsim \Lambda_{\rm QCD}$) or dark bremsstrahlung (for $\sqrt{p_{\rm DS}^2} < \Lambda_{\rm QCD}$). We require the DS states to be produced away from any mass thresholds, which allows estimating the rates based on

general principles. DS particles once produced are required to decay to SM particles inside the neutrino near-detectors placed generally $\sim \mathcal{O}(100\text{m})$ downstream from the target[1].

Compared to previous attempts at studying irrelevant portals, our work is more comprehensive, as we point out now. Compared to [230, 235], we study a more complete set of operators, both in production and decay of DS particles. We perform a detailed study of production modes through irrelevant portals, such as dark bremsstrahlung and partonic production, that have either been neglected or only considered partially [235, 236, 237]. We find that the bremsstrahlung mode can be comparable to other modes and is necessary for a complete analysis. Compared to [75, 76] we focus on high intensity experiments, particularly on neutrino and other proton dump experiments that were not considered previously in this framework. We do so by adopting the model agnostic strategy outlined in [76]. More importantly, this allows us to put bounds on *strongly coupled* light dark sectors through irrelevant portals, which as far as we know is not a thoroughly studied scenario at high intensity experiments (except in [76]. See [75, 238, 240, 241] and references therein for searches at collider experiments). Strongly coupled GeV-scale DS are relevant in frameworks containing composite resonances from a new gauge group, such as composite versions of Asymmetric Dark Matter [45, 46, 242], Mirror world models [243, 244], some incarnations of the Twin Higgs paradigm [245] and are a natural realization of the Hidden Valley scenario [72].

The outline of the Chapter is as follows: in Sec. 3.1 we describe the dark sector portals and the relevant model agnostic framework for estimating inclusive rates, lifetime and multiplicity of DS particles, also pointing out the mild model dependent assumptions we have to make to proceed. In Sec. 3.2 we describe various DS production processes relevant at neutrino experiments, while in Sec. 3.3, we give an overview of the neutrino experiments we use to constrain the parameter space, and describe our strategy for estimating signal events from DS decaying inside the neutrino detector. Our results and bounds can be found in Sec. 3.4 with a discussion and summary in Sec. 3.5. In App. G and App. H we explain technical details of the computations.

3.1 A model agnostic strategy (and its limitations)

In this section we discuss the relevant theoretical details for studying dark sectors with irrelevant portal to the SM. The emphasis is towards being as model agnostic as possible, and only allowing for minimal model dependence where necessary. We point out the assumptions we have to make at various stages for this. Our work builds upon the model agnostic approach first undertaken in [76], wherein more details can be found.

Dark sectors with portal interactions to the SM from irrelevant operators can be

[1]Far detectors are less constraining due to a very small angle subtended to the interaction point.

generated in a large class of models, generically by exchange of heavy mediators charged under both the SM and the DS. The general form of such a portal is

$$\frac{\kappa}{\Lambda_{\rm UV}^{D-4}}\mathcal{O}_{\rm SM}\,\mathcal{O}_{\rm DS}\,, \tag{3.1}$$

where $\Lambda_{\rm UV}$ is the mass scale of the heavy mediator, κ is a dimensionless coupling, and $\mathcal{O}_{\rm SM}$ ($\mathcal{O}_{\rm DS}$) are local operators made of SM (DS) degrees of freedom. The dimensionality of portal $D = [\mathcal{O}_{\rm SM}] + [\mathcal{O}_{\rm DS}]$ is greater than 4 for irrelevant portals. States in the DS are further characterized by a mass gap $\Lambda_{\rm IR}$, and the dynamics between the scales $\Lambda_{\rm UV}$ and $\Lambda_{\rm IR}$ is approximately scale invariant. A large hierarchy between these scales is a working assumption of this scenario. In order to avoid strong constraints, we also assume that the portal preserves both CP and flavor symmetries of the SM.

The most constrained portals are expected to be those with lowest dimension D. In concrete examples of such DS, both weakly and strongly coupled, the two lowest dimension DS operators are a scalar operator $\mathcal{O}$ (of dimension $\Delta_{\mathcal{O}} \lesssim 4$) and a conserved current operator $J_\mu^{\rm DS}$ (of dimension 3). While the dimension of a conserved current operator is fixed to be 3 in 4D, the reason to take the scalar operator close to being marginal is to ensure that the condition $\Lambda_{\rm IR}/\Lambda_{\rm UV} \ll 1$ is realized naturally. We will consider $\Delta_{\mathcal{O}} = 3, 4$ in this Chapter. Specific to a given model there can be other operators that generate portals to the SM. However in the absence of a symmetry, their dimension is either unprotected or requires additional assumptions about the DS. We will therefore limit ourselves with only a current and a scalar operator on the DS side. The gauge invariant operators on the SM side that can be used to make a portal operator, with increasing scaling dimension, are $H^\dagger H$ and $J_\mu^{\rm SM} = \bar{f}\gamma_\mu f,\ \bar{f}\gamma_\mu\gamma^5 f,\ f = l, q$ or $J_\mu^{\rm SM} = H^\dagger i\overleftrightarrow{D}_\mu H$ (see Table 1 in ref. [76] for a complete list of scenarios). The lowest dimension Lorentz invariant combinations are then $J_\mu^{\rm DS}\,J_{\rm SM}^\mu$ and $\mathcal{O}\,H^\dagger H$. In the unitary gauge, $H^\dagger i\overleftrightarrow{D}_\mu H \sim Z_\mu$ so that for this portal the interactions with the DS proceed through a Z-boson. We will refer to this as the *Z portal*. At the energy scales relevant at neutrino experiments, Z is never produced on-shell, so we can integrate it out and generate an effective JJ operator where now the SM current is the one that couples to Z. Therefore, considering JJ portals where the SM current is either generic or the one for Z, we cover all possibilities. We will refer to these as the *generic* JJ portal and the *Z-aligned* JJ portal respectively.

Hence the lowest dimension portals that can be formed are

$$\begin{aligned}\mathscr{L}_{\rm portal} &= \frac{\kappa_{\mathcal{O}}}{\Lambda_{\rm UV}^{\Delta_{\mathcal{O}}-2}}\mathcal{O}H^\dagger H + \frac{\kappa_J}{\Lambda_{\rm UV}^2}J_\mu^{\rm DS}J_{\rm SM}^\mu + \frac{\kappa_Z}{\Lambda_{\rm UV}^2}J_\mu^{\rm DS}H^\dagger i\overleftrightarrow{D}^\mu H = \\ &= \frac{\kappa_{\mathcal{O}}}{\Lambda_{\rm UV}^{\Delta_{\mathcal{O}}-2}}\mathcal{O}H^\dagger H + \frac{\kappa_J}{\Lambda_{\rm UV}^2}J_\mu^{\rm DS}J_{\rm SM}^\mu + \frac{\kappa_Z}{\Lambda_{\rm UV}^2}\frac{v}{m_Z}J_\mu^{\rm DS}J_{\rm SM,\,Z}^\mu\,,\end{aligned} \tag{3.2}$$

where $\kappa_{\mathcal{O}}, \kappa_J, \kappa_Z$ are dimensionless coefficients, v is the electroweak VEV and in the second line we have integrated out Z, which couples the DS current to $J_{\rm SM,\,Z}^\mu$, the SM current that couples to Z. The three terms in Eq. (3.2) are the Higgs portal, the generic JJ portal and the Z portal respectively. It is clear that a Z-aligned JJ

portal can be obtained from the Z-portal with a rescaling: $\kappa_J = \kappa_Z(v/m_Z)$. For $\Delta \lesssim 4$, all these portals are of dimension $D \sim 6$. In principle, a DS described by a local QFT also possesses a stress-energy tensor $T^{\mu\nu}_{\rm DS}$ of dimension 4, that can be used to build dimension 8 operators with SM dimension 4 operators. However, given a larger suppression compared to the dimension 6 portals in Eq. (3.2), the bounds on them are too weak to be of any interest.

If the energy $\sqrt{s}$ of an experiment that probes the DS is such that $\Lambda_{\rm IR} \ll \sqrt{s} \ll \Lambda_{\rm UV}$, the DS states are produced directly in the conformal regime. Inclusive DS production rates can be estimated using only the scaling dimension of the DS operator, along with the optical theorem. The optical theorem allows to sum over the DS phase space in an inclusive manner and relates it to the imaginary part of the two point function of the DS operator, which in turn is fixed by the scaling dimension of the operator. In particular, the optical theorem gives

$$\sum_n \int \mathrm{d}\Phi_{\rm DS} \left|\langle\Omega|\, \mathcal{O}_{\rm DS}\, |n\rangle\right|^2 = 2\,\mathrm{Im}\left(i\,\langle\Omega|\, \mathcal{O}_{\rm DS}\mathcal{O}_{\rm DS}\, |\Omega\rangle\right)\,, \tag{3.3}$$

where the DS operator $\mathcal{O}_{\rm DS}$ interpolates a DS state $|n\rangle$ from vacuum $|\Omega\rangle$ and the integration is over the entire dark sector phase space $\mathrm{d}\Phi_{\rm DS}$.

This approach allows calculating the cross section for DS production without specifying the fields that make the composite operator $\mathcal{O}_{\rm DS}$. While for irrelevant portals, the matrix element does not decrease with energy (specific behavior depends on the production mode), this needs to be convolved with the structure functions (e.g. the pdfs/form-factors/splitting functions, depending on the production channel), and this changes where the bulk of events come from. As long as the involved $p_{\rm DS}$ values are away from $\Lambda_{\rm UV}, \Lambda_{\rm IR}$, one can ignore the events near the thresholds in a self-consistent manner. Relatedly, the two point function of $\mathcal{O}_{\rm DS}$ will also depend on the ratio $\Lambda^2_{\rm IR}/p^2_{\rm DS}$ and $p^2_{\rm DS}/\Lambda^2_{\rm UV}$. For self-consistency, we again need both these ratios to be small. In particular, the condition $p^2_{\rm DS}/\Lambda^2_{\rm UV} < 1$ effectively ensures the mediators of mass $\Lambda_{\rm UV}$ are not directly produced and the effective local operator for the portal is a good description. In ref. [76], this was enforced by ensuring that the obtained bound on $\Lambda_{\rm UV}$ always satisfies this condition for the highest $p^2_{\rm DS}$ used in the calculation. In practice, this effectively resulted in a lower limit on the parts of $\Lambda_{\rm UV}$ ruled out, or completely invalidated certain bounds. As we will see, for neutrino experiments, where the involved energy is much smaller than LHC or LEP, this condition is less detrimental. By restricting to $\Lambda_{\rm UV} \gtrsim 50$ GeV, we are able to get useful bounds as well as be consistent with the EFT condition. The condition on $\Lambda_{\rm IR}$ on the other hand needs to be imposed, which we do for each production mode.

After production, the DS states will interact and decay into each other, and eventually all the DS degrees of freedom would decay to the *Lightest Dark Sector Particle* (LDSP), which we denote by ψ. We will take the mass of ψ to be of order $\Lambda_{\rm IR}$ and this can be taken as our definition for the mass gap $\Lambda_{\rm IR}$. In the absence of additional symmetry, ψ will decay back to SM states from the portal interactions itself. Since the portal interactions are weak, the typical time for DS states to decay into each

other is much smaller than the typical lifetime of ψ, and can be safely ignored. Note that the LDSP is not the DM candidate in the scenario under consideration—a DM candidate would need to be much more long lived, and will have a missing energy signal. In this Chapter we will assume that the produced DS particles relax entirely to LDSPs, and leave the question of considering a fraction of events to be missing energy, for future work.

The signatures of ψ depend on its lifetime, and this is the first place where some assumptions have to be made, which bring some model dependence. At high energy colliders, depending on the lifetime of ψ, one can get missing energy events, displaced vertices, or prompt decays, ordered by decreasing lifetimes. Missing energy events, being most inclusive, need minimal information about the underlying dynamics of DS, while displaced vertices and prompt decays being exclusive, need some information. Note that the requirement $\Lambda_{\rm IR}/\Lambda_{\rm UV} \ll 1$ puts us away from the prompt decay regime, since in this limit, the lifetime increases. Focusing on neutrino experiments, since the detectors are placed some distance from the interaction point, we are in the displaced vertex scenario. It is possible to detect the decay of ψ inside the detector, or its scattering against electrons or nucleons of the detector [246, 247, 248, 249, 250, 251, 252, 253]. Both signatures need some knowledge of the IR behaviour of the underlying theory, and are model dependent, however with varying degrees. For these two signatures, the relevant DS matrix elements are:

$$\begin{aligned} \text{Decay}: \ & \langle \Omega | \mathcal{O}_{\rm DS} | \psi \rangle = a\, f\, \Lambda_{\rm IR}^{\Delta_{\mathcal{O}}-2} \,, \\ \text{Scattering}: \ & \langle \psi(p_f) | \mathcal{O}_{\rm DS} | \psi(p_i) \rangle = a\, F(p_i, p_f, \Lambda_{\rm IR}) \,, \end{aligned} \tag{3.4}$$

where $|\Omega\rangle$ is the vacuum, f is a decay constant, F is a form factor and a is an $\mathcal{O}(1)$ number, all of which are model dependent. In this Chapter, we will only focus on the decay mode.

The model dependence that enters in the decay case comes in the combination $a\,f$. Scattering process, on the other hand, requires knowing the form factor which can be a complicated function of the momenta (especially for strongly coupled sectors). The functional dependence also influences who ψ recoils against most efficiently. The spin of ψ does not fix the portal, since one can make multiple total spin states using two ψ. Further, depending on the spectrum, an LDSP might up scatter to a close by state, making the scattering inelastic (similar to what happens in inelastic Dark Matter scenarios [254]), leading to a different parametric dependence for the scattering cross-section. These aspects make it clear that scattering processes require additional model dependent assumptions, and we will not consider them here. A further reason to choose decays over scattering is that they have a larger signal-to-noise ratio, and we will have more to say about it in Sec. 3.3. Note that while there are weakly coupled models in which all the LDSPs are stable under some accidental symmetry, and therefore can only be studied through scatterings in the experiments under scrutiny (and therefore our analysis will not apply to such scenarios), in strongly coupled models unstable resonances are expected generically: all operators not protected by symmetries are expected to be generated with $\mathcal{O}(1)$ coefficients, unlike weakly coupled theories in which these coefficients can be $\ll 1$.

The lifetime of ψ to decay to SM states, via the portal itself, can be estimated in a straightforward manner. However there are differences when the decay is from mixing with a SM state or a direct decay. For a direct decay from a portal of dimension D, the lifetime can be estimated to be

$$\frac{1}{\tau_\psi} \sim \Lambda_{\rm IR} \frac{\kappa^2}{8\pi} \frac{f^2}{\Lambda_{\rm IR}^2} \left(\frac{\Lambda_{\rm IR}^2}{\Lambda_{\rm UV}^2} \right)^{D-4} , \tag{3.5}$$

where the decay constant f is defined by the matrix element $\langle \Omega | \mathcal{O} | \psi \rangle = a\, f\, \Lambda_{\rm IR}^{\Delta_\mathcal{O}-2}$ and a is an $\mathcal{O}(1)$ number taken to be 1. Further, f can be estimated via the optical theorem to be $f = \sqrt{c}\,\Lambda_{\rm IR}/4\pi$, where c is the number of degrees of freedom of the DS. On the other hand, if the LDSP decays through mixing with a SM particle such as Higgs, if the LDSP is spin 0, or Z, if the LDSP is spin 1 (e.g. through $\mathcal{O}H^\dagger H$ or $J_\mu^{\rm DS} H^\dagger i \overleftrightarrow{D}^\mu H$ respectively), the lifetime in the limit $\Lambda_{\rm IR} \ll m_{Z/h}$ is given as

$$\frac{1}{\tau_\psi} = \Gamma_i \sin^2\theta_i \,, \;\; \tan 2\theta_i = \frac{2\delta_i}{m_i^2} \,, \;\; i = Z, h \,, \tag{3.6}$$

where $\Gamma_{Z/h}$ is the decay width of Z/h evaluated at $m_{Z/h} = \Lambda_{\rm IR}$, and the mixing parameter δ_i is

$$\begin{aligned} \delta_h &= \kappa_\mathcal{O}\, v f \left(\frac{\Lambda_{\rm IR}}{\Lambda_{\rm UV}} \right)^{\Delta_\mathcal{O}-2} , \\ \delta_Z &= \kappa_J\, v f \frac{m_Z \Lambda_{\rm IR}}{\Lambda_{\rm UV}^2} \,. \end{aligned} \tag{3.7}$$

To model the hadronic decay of the scalar LDSP (that mixes with the Higgs), we use the spectator quark model for $\Lambda_{\rm IR} > 2$ GeV and the dispersive analysis for $\Lambda_{\rm IR} < 2$ GeV , following [255]. For a spin-1 LDSP (mixing with the Z) we again use the spectator quark model for $\Lambda_{\rm IR} > 2$ GeV , and a data-driven approach for $\Lambda_{\rm IR} < 2$ GeV , following [256, 257] for the vector and axial vector component respectively.

The next model dependent assumption needed in order to evaluate the reach at high intensity experiments is how many LDSPs are produced per DS shell, or equivalently how many are excited by the DS operator acting on the vacuum. We will take two benchmark values, $n_{\rm LDSP} = 2$ for weakly coupled dark sectors and $n_{\rm LDSP} = n(p_{\rm DS}^2)$ a function of the invariant mass squared $p_{\rm DS}^2$ of the DS system, similar to the case of QCD [258]:

$$n(p_{\rm DS}^2) = A\,(\log x)^B \exp\Big\{ C\,(\log x)^D \Big\} \,, \tag{3.8}$$

where $x = p_{\rm DS}^2/\bar{\Lambda}^2$, $\bar{\Lambda} = 0.1\Lambda_{\rm IR}$, $A = 0.06, B = -0.5, C = 1.8, D = 0.5$, and $p_{\rm DS}^2$ is the invariant mass squared of the DS system. Our results are not very sensitive to small changes in $n_{\rm LDSP}$. In particular, as argued in section 3.4, its impact on the exclusion plots will be mostly in regions in which the LDSPs are light and long-lived.

Finally, we need to know the directional distribution of the produced LDSPs, to estimate if they interact with the detector. In the strongly coupled benchmark

where typically $n_{\rm LDSP} > 2$, we assume that the LDSPs have a uniform angular distribution in the rest frame of DS (i.e. the frame in which $p_{\rm DS}$ only has a time component), and we can boost it to the lab frame to know its relevant distribution. A uniform distribution in the rest frame is a simplifying choice, and is well motivated, at least for a certain class of strongly coupled theories (e.g. see ref. [259] for such a scenario). Further, even if the distribution is not uniform per event, it can be uniform when all the events are considered. For light enough LDSPs, which are very boosted in the lab frame, small deviations from this assumption do not change our results significantly.

The weakly coupled case is in principle different, and the angular distribution depends on the production mode, spin of produced DS particles and the specific form of the portal. In general we expect $\mathcal{O}(1)$ differences among the possible LDSP angular distributions in the DS rest frame. For example, in DY production the typical LDSP distribution is either proportional to $\sin^2\theta$ or $1+\cos^2\theta$ for scalar and light fermion LDSPs respectively. The difference between the two distributions is that the scalar distribution is more peaked around the most probable LDSP lab angle $\sim 1/\gamma_{\rm DS}$. However, since the LDSP is produced with a high boost, any differences in the distribution are washed out, and we can assume an isotropic distribution in the DS rest frame as before. We have checked this by an explicit computation.

3.2 Production Modes at Proton Beam based Experiments

Even though at neutrino experiments the primary process is a proton interacting with a nucleus, depending on the energy scale of the process, there are various production modes to consider. In this Chapter, we consider experiments based on 120 and 400 GeV beam energies. For such energies there are three relevant production modes. First of all, the proton nucleus interaction creates mesons, which may decay into lighter mesons and DS states, or completely annihilate into DS states. Denoting the 4-momentum carried by the DS state as $p_{\rm DS}$, this requires $p_{\rm DS}^2 \leq (\mathbf{M}_{\rm heavy} - \mathbf{M}_{\rm light})^2$ for the first scenario and $p_{\rm DS}^2 = \mathbf{M}_{\rm heavy}^2$ for the second. We will refer to these as radiative and annihilation meson decays (MD) respectively. For $p_{\rm DS}^2 \gtrsim \Lambda_{\rm QCD}^2$, the incoming proton is at high enough energies so one has to consider partonic process involving constituents from the incoming proton and the nucleons in the target, and we refer to this as Drell-Yan (DY) production mode. For $p_{\rm DS}^2 \lesssim \Lambda_{\rm QCD}^2$, DS states can be produced from initial state emission, which we will refer to as Dark Bremsstrahlung (DB) mode. For each of these processes, the production cross section has a different differential distribution in $p_{\rm DS}^2$. Fig. 3.1 shows a comparison of the differential DS production cross-section for DY, DB and radiative MD mode, for Z portal, at 120 GeV beam energy. The radiative MD mode is flat in $p_{\rm DS}$, switching off when the phase space for DS production closes, which in turn is set by the parent meson mass. The DB mode switches off around $\Lambda_{\rm QCD}$ beyond which it is not a valid description of the scattering process. The sharp peak in the DB mode is due to meson resonance, as seen in the form factors (see App. G.1). The switch off of DY mode comes from the drop in the PDFs of constituents of the

proton at higher $p^2_{\rm DS}$, given $\sqrt{s}$ of the experiment, and is a slower drop.

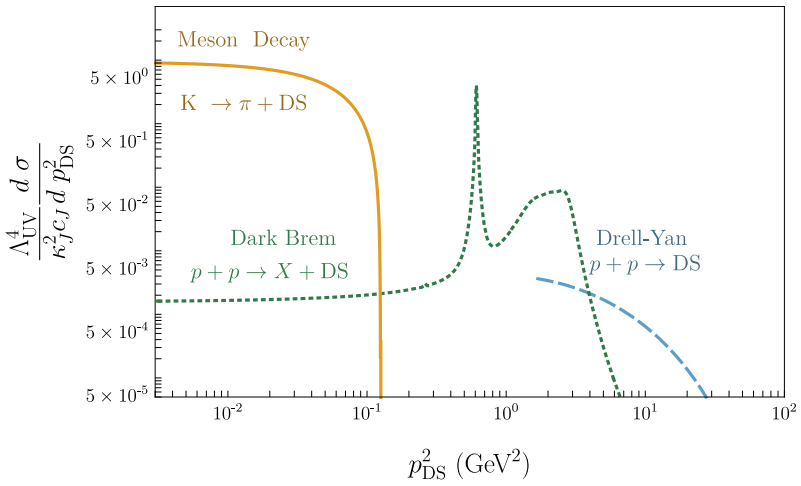

Figure 3.1: *Relative importance of various production modes: the scaled differential cross-section for DS production at DUNE-MPD (E_{beam} = 120 GeV) as a function of p^2_{DS} for various DS production modes (for Z portal). Solid yellow shows meson decay: $K \to \pi +$ DS mo, dotted green line shows dark bremsstrahlung mode ($p + p \to X +$ DS), and dashed blue line shows Drell-Yan mode ($p+p \to$ DS). The reported cross-section is per proton-on-target, and is without the geometric acceptance factor ϵ_{geom} (which at DUNE is approximately 10^{-3} for DY and meson modes and around 10^{-2} for DB mode).*

We remark that dependence of the production cross section on the center of mass energy $\sqrt{s}$ of the experiment is not the one given by naive power counting (*i.e.* $\sigma \sim s^{D-5}/\Lambda_{\rm UV}^{2D-8}$), and is general dependent on the production mode. For MD and DB modes, the typical scale of the process is not set by the center of mass energy of the experiment, but rather by the hadronic resonances. There is a residual dependence on $\sqrt{s}$ in the meson production cross section and in the proton-nucleon cross section respectively, but typically this dependence is much weaker than the expected one above the specific hadronic production threshold. DY production instead is more sensitive on $\sqrt{s}$. These features are easily seen in Fig. 3.1.

Independent of the production mode, we need to estimate the number of DS signal events S produced. This is generically given as

$$S = N_{\rm signal} = N_{\rm DS}\, P_{\rm decay}\, \epsilon_{\rm geo}\ , \tag{3.9}$$

where $P_{\rm decay}$ is the probability for at least one LDSP to decay inside the radial location of the detector, $\epsilon_{\rm geo}$ is the geometric acceptance for the LDSP direction to intersect with the detector and $N_{\rm DS}$ is the number of DS states produced. For more than one production mode, a sum is implied. Note that we have defined a signal event as one in which at least one LDSP decays inside the detector. The case of more than one LDSPs can be accounted for by multiplying the single LDSP probability with the number of LDSPs produced, and it's included in the definition of $P_{\rm decay}$ (see App. H.1 for a detailed discussion of this). As the final step to get the number of signal events S, we have to express $N_{\rm DS}$ in Eq. (3.9) in terms of the

(inclusive) signal cross section $\sigma_{\rm S}$ as

$$N_{\rm DS} = \frac{N_{\rm POT}}{\sigma_{\rm pN}} \sigma_{\rm S} \,, \tag{3.10}$$

where $\sigma_{\rm S}$ is the cross section for DS production, $N_{\rm POT}$ is the total number of proton delivered on target during the duration of the experiment (projected years for future experiments) and $\sigma_{\rm pN}$ is the typical proton-nucleus cross section for the proton beam hitting the target, taken constant for the center of mass energies of the experiments we consider [260]:

$$\sigma_{\rm pN} = A^{0.77}\, 49.2 \text{ mb} \,, \tag{3.11}$$

with A the target nucleus' atomic weight. In Eq. (3.10), we are considering only DS production in the first interaction length of the target (or the dump for beam-dump experiments), neglecting production happening at later lengths with a degraded beam. Our computations are therefore conservative.

Specific to the case of meson decays, for a given meson $\mathbf{M}$ and in a given decay channel C, $N_{\rm DS}$ is given as

$$N_{\rm DS} = N_{\rm POT}\, N_{\rm M} {\rm Br}_{\rm C} \Big(\mathbf{M} \to {\rm DS}\ (+\mathfrak{m}) \Big) \,, \tag{3.12}$$

where $N_{\rm M}$ is the number of mesons produced per collision and ${\rm Br}_{\rm C}$ is the branching ratio of the meson $\mathbf{M}$ to the DS (which may be in association with other mesons $\mathfrak{m}$).

Strictly speaking, the various factors that go into the estimation of the number of signal events $N_{\rm signal}$ depend on the kinematic information, the production mode, and the details of the detector (*e.g.* on- vs off-axis). For example, depending on $p^2_{\rm DS}$, the boost of the DS states and therefore its decay probability is different. Further, depending on whether the DS is produced with a non-zero transverse momentum or not, the angle subtended at the detector can be different. The correct procedure would be to consider differential quantities and integrate over the allowed range.[2] This however can obscure the relation between a given experiment and the probed parameter space. As a way out, we use the average value of boost factor for estimating the probability, and compute the average geometric acceptance. In App. H.3 we compare this procedure, referred to as *factorized* approach, with the exact procedure, called the *full* approach, and show that the difference between the two is small.

This simplified strategy to compute bounds is useful for the following reason. While production quantities such as the cross section depend in a trivial way on $\Lambda_{\rm UV}$ and very weakly on $\Lambda_{\rm IR}$ via the kinematic condition $p^2_{\rm DS} \geq n^2_{\rm LDSP} \Lambda^2_{\rm IR}$, the decay probability depends on both parameters. By using averages in the production quantities allows factorizing them from the decay probability. This procedure therefore allows an analytic understanding of $\Lambda_{\rm UV}$ dependence on the number of signal events. Given the vast array of cases, coming from different experiments, different production channels (which can depend also on extra parameters like the dimension Δ), different

[2]Note that for meson annihilation decay $\mathbf{M} \to {\rm DS}$, $p^2_{\rm DS}$ is fixed to M^2.

decay channels, and the strongly vs weakly coupled scenario, this factorization allows to track the $\Lambda_{\rm UV}$ dependence clearly, and also speeds up the computations.

We next briefly outline the details of the three production modes discussed earlier.

3.2.1 Meson Decays

The considered portals between the SM and the DS can cause mesons to decay into DS states. Once the mesons are produced by the incoming proton hitting the target, they can decay in two ways. The first possibility is a heavier meson $\mathbf{M}$ decaying into a lighter SM state (such as another meson $\mathfrak{m}$) along with DS states. This is to be contrasted with the case when the mesons decay just into the DS states and nothing else. These two are the radiative decay and annihilation decay modes respectively. The differential production cross section for radiative decay, as shown in Fig. 3.1 for the Z portal, is flat in $p_{\rm DS}$ up to kinematic threshold. The decay width for both modes can be approximately estimated, keeping the portal generic:

$$\Gamma(M \to {\rm DS} + X) \sim \kappa^2\, g_{\rm SM}^2\, \Phi(\Delta) \left(\frac{f_M}{M}\right)^a \begin{cases} \frac{v^2}{m_h^4}\, \frac{M^{2\Delta_{\mathcal{O}}-1}}{\Lambda_{\rm UV}^{2\Delta_{\mathcal{O}}-4}}\,, & \mathcal{O}H^\dagger H \text{ portal}, \\ \\ \frac{M^5}{\Lambda_{\rm UV}^4}\,, & JJ \text{ portal}. \end{cases} \tag{3.13}$$

where κ is the portal coupling, M is the mass of the parent meson, f_M is the decay constant, $\Delta_{\mathcal{O}}$ is the dimension of $\mathcal{O}$, $g_{\rm SM}$ is a dimensionless coupling built out of dimensionless SM couplings (like the gauge couplings, loop factors, extra SM particles' phase space, and relevant spurions), and $\Phi(\Delta)$ is the phase space factor coming from the integration over the DS degrees of freedoms (e.g. see Eq. (3.14)). The exponent of the dimensionless ratio (f_M/M) depends on the process, and is -2 for processes coming from the axial anomaly, $+2$ for tree level processes from the chiral Lagrangian and 0 for processes directly proceeding through the portal (without going through the chiral Lagrangian). In this estimate we have ignored the lighter meson mass for radiative decay, and have not included the meson form factors for simplicity. In our full analysis we include all these effect. We next discuss specific details of the radiative and annihilation decays as DS production modes.

Radiative Decays

For the radiative decay of the form $\mathbf{M} \to \mathfrak{m} + {\rm DS}$ proceeding via a flavour violating loop, the DS state is produced either by the quark line, and/or by the internal W loop (which is necessary to change the quark flavor). This depends on the portal operator. For $J_\mu^{\rm SM} J_{\rm DS}^\mu$ portal where $J_\mu^{\rm SM}$ is the quark current, the DS is produced just by the quark lines, whereas for $J_\mu^{\rm SM} = iH^\dagger \overleftrightarrow{\rm D}_\mu H \sim Z_\mu$, the DS states can be produced by attaching a Z to the quarks, or to the W in the loop[3]. The DS states can also be produced by the Higgs portal $\mathcal{O}H^\dagger H$. To understand their relative importance, let's consider the ratio of the branching ratios of the two different portals for DS

[3]We are working in the unitary gauge.

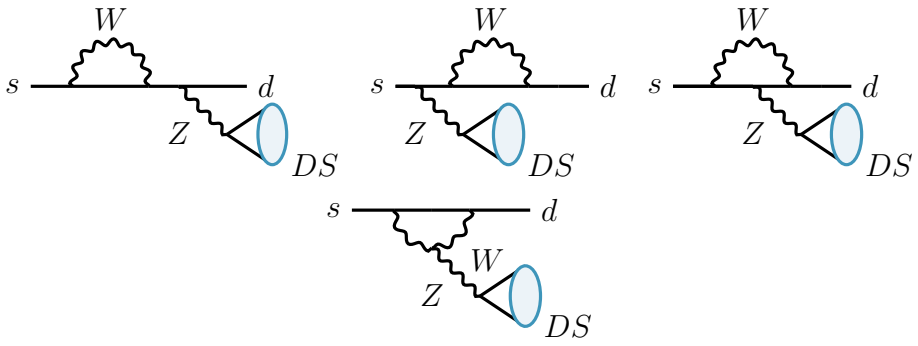

Figure 3.2: *The underlying quark level transition in DS production via Z portal in flavour violating decays such as $K \to \pi + DS$.*

production:

$$\frac{\mathrm{BR}_{OHH}}{\mathrm{BR}_{JHDH}} \sim \frac{3456\ \Gamma(\Delta_{\mathcal{O}} + 1/2)}{\pi^{1/2}\Gamma(2\Delta_{\mathcal{O}})\Gamma(\Delta_{\mathcal{O}} - 1)} \frac{M^2}{m_h^4} \frac{(M-m)^{2\Delta_{\mathcal{O}}-6}}{\Lambda_{\mathrm{UV}}^{2\Delta_{\mathcal{O}}-8}} \tag{3.14}$$

with M (m) being the mass of the heavy (light) meson, $\Delta_{\mathcal{O}}$ the dimensionality of the operator $\mathcal{O}$, where for the higgs portal case we have used the usual effective lagrangian coupling $C_{ij}\bar{d}_L^i d_R^j h$ between the flavour changing quarks and higgs (see [76] for example) and for the Z portal case, we have considered only the top quark contribution in the loop of the $\mathcal{O}(m_t^2/m_W^2)$. It is clear that for $\Delta_{\mathcal{O}} \geq 4$, production through the Higgs portal is suppressed with respect to the Z portal and will give weaker bounds. We discuss this in more detail in Sec. 3.4.4.

For production through a $\Delta_{\mathcal{O}} = 3$ Higgs portal, even though the Λ_{UV} scale probed is higher than Z portal production case (discussed in more detail in Sec. 3.4.4), the bound is still at most only marginally stronger compared to missing energy searches at LHC [76]. In this subsection we will mostly focus only on the Z portal production for mesons, but will make some comments about the Higgs portal case in Sec. 3.4.

Examples of radiative meson decay processes are $K^+ \to \pi^+ + \mathrm{DS}$, $B^+ \to K^+ + \mathrm{DS}$ and $D^+ \to \pi^+ + \mathrm{DS}$, and a prototypical diagram (for $K^+ \to \pi^+ + \mathrm{DS}$) is shown in Fig. 3.2. In general, these processes proceed through insertion of two CKM entries, so that for flavor i going to j, the amplitude approximately scales as $\sum_k V_{ik}^{\mathrm{CKM}} V_{kj}^{\mathrm{CKM}} f(m_k/m_W)$, where m_k is the quark mass of flavor k, m_W is the W mass and $f(x)$ is a loop function [261, 262]. Due to the GIM mechanism the loop function is suppressed for small masses: $f(x) \simeq x + \mathcal{O}(x^2)$. For D mesons, for which the underlying process is $c \to u$, there is no top quark in the loop, as opposed to B, K decays, which makes the D-meson process suppressed. As a result, the D decays are not very constraining—e.g. the large number of D mesons expected at SHiP (enhancement by $\sim 10^4$ compared to B meson production, see ref. [263]) is not enough to overcome the GIM and CKM suppression of $\sim 10^{-12}$.

Due to the abundant number of K mesons produced at neutrino experiments, $K \to \pi + \mathrm{DS}$ decay is an important mode for DS production. For this process, and for the Z portal case, the Feynman diagrams are shown in Fig. 3.2. Note that one

must include penguin diagrams as well as self-energy diagrams [261, 262]. The DS production rates can be obtained from the SM calculation for $s \to d\bar{\nu}\nu$, but with some modifications. We can use the SM results if we keep only the penguin diagrams and omit the box diagrams in the $d\bar{s} \to \bar{\nu}\nu$ process, since the latter are specific to the neutrino coupling (e.g. see [262]). This however must be done in the unitary gauge since the box and the penguin diagrams are needed together to make the result gauge invariant in an arbitrary gauge, but their gauge dependent parts vanish individually in the unitary gauge[4] [262]. Once these subtleties are addressed, we can simply replace the neutrino current coupling to Z, $g_2/2 \cos\theta_W (\bar{\nu}_L \gamma_\mu \nu_L)$, with the DS current coupling to Z, $(\kappa_J v m_Z/\Lambda^2_{\rm UV}) J^{\rm DS}_\mu$. This allows us to write the rate of decay of $K^+ \to \pi^+ + \text{DS}$, using the optical theorem, as:

$$\Gamma_{K^+\to\pi^++\text{DS}} = \frac{1}{2M_K}\left(\frac{G_F}{\sqrt{2}}\frac{g_2\cos\theta_W}{8\pi^2}\right)^2 \frac{m_Z^2 v^2 \kappa_J^2}{\Lambda^4_{\rm UV}}\left(\sum_{j=c,t} V^*_{js}V_{jd}\bar{D}(x_j, x_u=0)\right)^2 \times \int \frac{{\rm d}^3 p_\pi}{(2\pi)^3}\frac{1}{2E_\pi}\mathcal{M}_\mu \mathcal{M}^*_\nu \times 2\ {\rm Im}\,\langle J^\mu_{DS}(p_{\rm DS}) J^\nu_{DS}(p_{\rm DS})\rangle \ , \tag{3.15}$$

where G_F is the Fermi constant, θ_W is the weak mixing angle, g_2 is the SU(2)_L gauge coupling, M_K is the mass of the K meson, v is the Higgs VEV, m_Z is the Z boson mass, $E_\pi = \sqrt{m_\pi^2 + |\vec{p}_\pi^2|}$, $p_{\rm DS} = p_K - p_\pi$, $\mathcal{M}_\mu = \langle \pi^+| \bar{d}\gamma_\mu s |K^+\rangle$ is the SM QCD matrix element (see App. G.2.1 for details), and V_{ij} are CKM matrix elements. The loop functions $\bar{D}(x_j)$, where $x_j = m_j^2/m_W^2$, sum the contributions from various diagrams. The upper limit for p_π integral is fixed by the kinematic requirement $p^2_{\rm DS} \geq n^2_{\rm LDSP}\Lambda^2_{\rm IR}$. We discuss in Sec. 3.4 the bounds from this decay channel by NA62.

Apart from the decay $K^+ \to \pi^+ + \text{DS}$, one can also consider the decays of K^0_L and K^0_S. We can obtain the partial width of K^0_L from that of K^+ using ref. [261] by replacing $|V^*_{js}V_{jd}|^2$ in Eq. (3.15) with $|\text{Im}(V^*_{js}V_{jd})|^2$. The $K^0_S \to \pi^0 + \text{DS}$ decay is less constraining since it has a smaller branching ratio due to the large width of K^0_S (see refs [219, 264]).

We next consider decays of B mesons to DS which is relevant at proton-beam experiments with higher beam energies (e.g. SHiP and CHARM, with $E_{\rm beam} \sim 400$ GeV, $\sqrt{s} \sim 27$ GeV). These high energy proton beam experiments would also have a high K meson production rate but a large number of them get absorbed in the beam dump or target. Unlike B mesons, kaons have a decay length[5] which largely exceeds the hadronic interaction length (l_H) hence they tend to be absorbed in thick targets (for a target length of several l_H s) and only a fraction of them then decay to DS before absorption [255, 265]. For estimating this, we use ref. [265] for SHiP, and ref. [255] for CHARM.

The B meson decays to lighter mesons like K and π take place via Z-penguin diagrams which we already encountered in the case of $K^+ \to \pi^+ + \text{DS}$ (see Fig. 3.2)

[4] If we stayed in arbitrary gauge, the DS would also couple to the longitudinal modes of W and hence the box diagrams would also contribute. In the unitary gauge, $H^\dagger D_\mu H \sim Z_\mu$, the DS does not couple to W, and the box diagrams' contributions vanish.

[5] The decay length of $K^\pm, K^0_L$ is ~ 3 meters $\gg l_H \sim 15.3$ cm for SHiP and CHARM target [255].

except for the appropriate exchange of external quark flavors ($b \to s/d + \text{DS}$ instead of $s \to d + \text{DS}$). Of all the B decay modes, we find that the largest contribution to signal comes from the decays $B \to K + \text{DS}$ and $B \to K^* + \text{DS}$ [266]. For example, even though the partial width for the decay of $B_s \to \rho + \text{DS}$ is twice of $B \to K + \text{DS}$, the number of signal events from B_s decays are suppressed due to smaller number of B_s mesons produced with respect to $B^\pm$ and B_0 mesons at SHiP [263]. The contribution from $B \to \pi + \text{DS}$ is suppressed with respect to $B \to K + \text{DS}$ by a factor ~ 20 coming from $|V_{ts}|^2/|V_{td}|^2$ that enters in the respective decay widths [261]. This same suppression applies when comparing B meson decays to vector mesons: $B \to \rho + \text{DS}$ is suppressed with respect to $B \to K^* + \text{DS}$. We calculate the partial decay widths for these B decays in the same way as in Eq. (3.15) using the appropriate QCD matrix elements from Eq. (G.9) and Eq. (G.11) in App. G.2.1 and App. G.2.2.

We do not consider DS production from radiative decays of pseudoscalar mesons like π, η, η'. Their radiative decay into $\gamma + \text{DS}$ through a generic JJ portal is suppressed by the loop factor from the chiral anomaly triangle diagram, from the electromagnetic coupling and from the lightness of the meson in the π case [235].[6]

Radiative decays of vector mesons like ρ and ω can also produce DS via decay modes like $\rho^0 \to \pi^0 + \text{DS}$, etc. These decays would occur via flavour conserving transitions producing DS either through Z portal or SM vector quark current. The number of DS events from this mode is sub-leading due to the large width of ρ meson with respect to K meson width ($\Gamma_\rho \sim 10^{-1}$ GeV $\gg \Gamma_K \sim 10^{-17}$ GeV). Moreover, the radiative decays of vector mesons $V \to \text{DS} + P$ where P is a generic pseudo scalar are anyway suppressed since the interaction mediating the process come from the same triangle diagram mediating pseudoscalar radiative decays like $\pi^0 \to \gamma + \text{DS}$.

Recently [267] considered three-body leptonic decays of mesons to put bounds on leptophilic ALPs. In our case too, DS can be produced from such leptonic charged meson decays such as from the decay $K^+ \to \mu^+ + \nu + DS$ via Z portal. However we find this mode to be very suppressed with respect to $K \to \pi + \text{DS}$, due to phase space suppression (see also [268]).

Eventually, to calculate the number of DS events from a meson decay, we use Eq. (3.12). It is clear from Eq. (3.12) that the meson decay mode that gives the strongest bound would depend on N_M, the number of parent mesons produced per POT at a given neutrino experiment. In general, this can be estimated as the ratio of production cross section of the meson to the total cross section between proton beam and target: $N_{\text{M}} = \sigma_{pN\to M}/\sigma_{pN}$. We take these numbers for various experiments from ref. [263] (also see references within) for 400 GeV beam energy and from ref. [217] for 120 GeV beam energy, which are obtained using PYTHIA simulations.

[6]For the Z portal case, one external leg of the triangle diagram would produce Z which can couple with DS. This mode can give bounds at LSND due to the huge number of pions ($N_{\pi_0} \sim 10^{22}$), and we find that the Λ_{UV} probed is comparable to CHARM in the Meson Production mode.

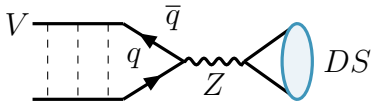

Figure 3.3: *DS produced via Z portal in annihilation decays of vector mesons.*

Annihilation decays

DS states can also be produced via annihilation decays of vector mesons through the JJ portal: $V \to \text{DS}$ where V can be $\rho, \phi, \omega, J/\psi$. We do not consider DS production from the annihilation decay of pseudoscalar mesons from this portal since it will not be model-independent under our approach [76]: the pseudoscalar decay matrix element is proportional to its momentum p_μ, which either vanishes when contracted to a conserved DS current, or gives a term proportional to a new, model dependent scale if the DS current is not conserved (corresponding to the internal DS symmetry breaking scale).

In principle the same topology can happen for the Higgs portal and scalar mesons (the matrix element for the spin 1 annihilation through this portal vanishes). However, given the uncertainties in the details of scalar meson production and their subdominance, we do not consider this possibility here. The leading contribution in this topology for the Higgs portal comes from FCNC CP-violating pseudoscalar annihilation decays such as $K \to \text{DS}$ [269], and we will briefly discuss them together with radiative decays in Sec. 3.4.

For a general V, and for the case of $V \to \text{DS}$ via Z portal, we can compute the decay width as before:

$$\begin{aligned}&\Gamma(V \to \text{DS}) = \\ &\frac{1}{2\,m_V}\frac{1}{3}g_Z^2\frac{\kappa_J^2 v^2}{m_Z^2\Lambda_{\text{UV}}^4}f_V^2 m_V^2 \sum \epsilon_\mu^*(p)\epsilon_\nu(p)\; 2\;\text{Im}\,\langle J^\mu_{\text{DS}}(p) J^\nu_{\text{DS}}(p)\rangle\,|_{p^2=m_V^2} = \\ &= \frac{\kappa_J^2 c_J}{96\pi}\frac{g_Z^2 v^2}{m_Z^2}\frac{m_V^3 f_V^2}{\Lambda_{\text{UV}}^4}\,,\end{aligned} \tag{3.16}$$

where m_V is the mass of the vector meson, f_V is the decay constant defined by $\langle V(p)|\,\bar{q}\gamma_\mu\, q\,|\Omega\rangle = i f_V m_V \epsilon_\mu^*(p)$, $\epsilon_\mu^*(p)$ is the polarization vector for V meson, and g_Z is the coupling of $\bar{q}\gamma_\mu\, q$ to Z boson. Here we have again used the optical theorem to do integration over DS phase space and used the expressions reported in [76] for the imaginary part of the correlators at $m_V \gg \Lambda_{\text{IR}}$. Out of ϕ, ω and J/ψ, the largest branching ratio to DS would be that of J/ψ because of the narrow total width, and a partial width which is enhanced by the mass.

We find that the bounds from $J/\psi \to \text{DS}$ are comparable to those from $B \to K/K^* + \text{DS}$ decays at SHiP. Despite $\text{BR}(J/\psi \to \text{DS})/\text{BR}(B \to K/K^* + \text{DS}) \sim 10^{-2}$, the large number of J/ψ mesons expected at SHiP as compared to B mesons, $N_{J/\psi}/N_B \sim \mathcal{O}(100)$ compensates for this.

For neutrino experiments based on the 120 GeV NuMI beam line, annihilation decays of lighter vector mesons like ρ, ω, ϕ can give contribution to signal events. Out

of the three vector mesons $\rho,\ \omega,\ \phi$, we find that the leading contribution to DS production is via ϕ meson decay to DS. We can compare the branching ratio for ϕ and ω decay to DS via Z portal:

$$\frac{\mathrm{BR}(\phi \to \mathrm{DS})}{\mathrm{BR}(\omega \to \mathrm{DS})} = \frac{\mathrm{BR}(\phi \to e^+e^-)}{\mathrm{BR}(\omega \to e^+e^-)} \frac{m_\phi^4}{m_\omega^4} \frac{\left(-\frac{1}{2} + \frac{2}{3}\sin^2\theta_W\right)^2}{e_s^2\ 4\sin^4\theta_W}\,, \tag{3.17}$$

where $e_s = -1/3$ is the EM charge of strange quark. Using this we expect DS produced in ϕ decay to dominate over ω decay to DS by a factor given by: $N_\phi/N_\omega \times \mathrm{BR}(\phi \to \mathrm{DS})/\mathrm{BR}(\omega \to \mathrm{DS}) \sim 0.007/0.03 \times 50 \sim 10$. Here we have used numbers for ϕ meson production at 80 GeV from ref. [270] and ω meson production at 120 GeV from [235]. A similar estimate shows that the case of ρ is also subleading. Therefore we only focus on the ϕ decay and do not consider ρ and ω. Note that ρ and ω annihilation decays overlap with the (vector) bremsstrahlung production mode when p^2_{DS} hits the resonance peak [252]: not including them avoids over-counting such contributions. We do not consider the annihilation decays of heavier mesons like Υ since its production will be very suppressed at neutrino experiments due to its large mass.

Now we outline how we compute the LDSP boost entering the decay probability and geometric acceptance factors for the meson production mode. More details can be found in App. H.2.1. In order to calculate the decay probability of the LDSP, we use the following estimate for the average boost factor for the LDSP produced from meson decays:

$$\langle\gamma\rangle_{\mathrm{LDSP}} \approx \frac{\left\langle E^{\mathrm{lab}}_{\mathrm{DS}}\right\rangle}{\langle n_{\mathrm{LDSP}}\rangle\, \Lambda_{\mathrm{IR}}}\,, \tag{3.18}$$

where $\left\langle E^{\mathrm{lab}}_{\mathrm{DS}}\right\rangle$ is the average energy of the DS produced from parent meson decay in the lab frame. We have checked that an honest average of $\langle\gamma\rangle_{\mathrm{LDSP}}$ matches this estimate very well. To obtain $\left\langle E^{\mathrm{lab}}_{\mathrm{DS}}\right\rangle$, the strategy is as follows: for radiative decays of the form M $\to$ m + DS, in the parent meson rest frame, the DS 3-momentum $\vec{p}^{\,0}_{\mathrm{DS}} = \{(p^0_{\mathrm{DS}})_T, (p^0_{\mathrm{DS}})_z\}$ can be written using energy conservation as:

$$|\vec{p}^{\,0}_{\mathrm{DS}}| = \sqrt{\frac{(M^2 - m^2 + p^2_{\mathrm{DS}})^2}{4M^2} - p^2_{\mathrm{DS}}}\,, \tag{3.19}$$

and fixes $(p^0_{\mathrm{DS}})_z = |\vec{p}^{\,0}_{\mathrm{DS}}|\cos\theta^0_{\mathrm{DS}}$, where θ^0_{DS} is the angle that the DS makes with the meson flight direction, in its rest frame. For annihilation decays, of the form M $\to$ DS, the DS 3-momentum in the meson rest frame is zero by momentum conservation. We further assume that 3-momentum of the mesons that decay to DS is perfectly aligned along the beam axis i.e. $\theta_{\mathrm{meson}} = 0$.[7]

We next calculate $(E^{\mathrm{lab}}_{\mathrm{DS}}, (p^{\mathrm{lab}}_{\mathrm{DS}})_z)$ from $(E^0_{\mathrm{DS}}, (p^0_{\mathrm{DS}})_z)$ using the boost and the velocity of the parent meson in the lab (which is along the z-axis), obtained from the average

[7] A more refined analysis using [217] shows that the most probable value for the ratio between transverse and longitudinal components of 3-momentum of decaying K mesons $|p^{\mathrm{T}}_{\mathrm{meson}}/p^{\mathrm{z}}_{\mathrm{meson}}| \sim \theta_{\mathrm{meson}} \sim 10^{-2} \ll 1$. Using a non-zero but small value of θ_{meson} does not change our final results.

meson momentum values for various experiments from Table 6 in ref. [235]. From $(p_{\rm DS}^{\rm lab})_z$, we can obtain $\left|\vec{p}_{\rm DS}^{\rm lab}\right|$ by noting that the transverse component is unaffected by the z direction boost, so that everything is a function of $\theta_{\rm DS}^0$ and $p_{\rm DS}^2$. Finally, to get the average value of DS 3-momentum $\left\langle\left|\vec{p}_{\rm DS}^{\rm lab}\right|\right\rangle$, we average over $\cos\theta_{\rm DS}^0$, since DS is isotropic in this variable and set $p_{\rm DS}^2$ to its average value for each radiative meson case. We have again checked that this matches a true average.

To get the final number of signal events as in Eq. (3.9), we also need the geometric acceptance, which we again compute as an average. See App. H.2.1 for details of these computations, and App. H.3 for a comparison between using this average procedure with a more refined analysis. Some typical values of $\langle\gamma\rangle_{\rm LDSP}$ are given in Table 3.1.

$E_{\rm beam}^{\rm lab}$ (GeV)	Z portal production						H portal production					
	$\langle\gamma\rangle_{\rm DS}^{\rm weak}$	$\langle\gamma\rangle_{\rm DS}^{\rm strong}$	$\langle\gamma\rangle_{\rm LDSP}^{\rm weak}$	$\langle\gamma\rangle_{\rm LDSP}^{\rm strong}$	$\langle\epsilon_{\rm geo}\rangle^{\rm weak}$	$\langle\epsilon_{\rm geo}\rangle^{\rm strong}$	$\langle\gamma\rangle_{\rm DS}^{\rm weak}$	$\langle\gamma\rangle_{\rm DS}^{\rm strong}$	$\langle\gamma\rangle_{\rm LDSP}^{\rm weak}$	$\langle\gamma\rangle_{\rm LDSP}^{\rm strong}$	$\langle\epsilon_{\rm geo}\rangle^{\rm weak}$	$\langle\epsilon_{\rm geo}\rangle^{\rm weak}$
Drell-Yan												
120 (DUNE-MPD)	12	12	1490	160	0.004	0.004	9	9	1600	150	0.002	0.002
400 (SHiP)	25	25	4310	400	0.63	0.63	17	17	4830	364	0.54	0.54
Dark Bremsstrahlung												
120 (DUNE-MPD)	80	80	4500	655	0.040	0.040	74	74	4630	650	0.039	0.039
400 (SHiP)	270	270	15000	2200	1	1	250	250	15700	2200	0.96	0.97
Meson Radiative Decay $K \to \pi + \rm DS$												
120 (DUNE-MPD)	31	26	215	48	0.003	0.004	31	26	215	48	0.003	0.004
400 (SHiP)	55	45	375	84	0.79	0.89	55	45	375	84	0.79	0.89
Meson Annihilation Decay $\phi \to \rm DS$												
120 (DUNE-MPD)	8	8	403	61	0.001	0.001	-	-	-	-	-	
400 (SHiP)	14	14	702	107	0.27	0.27	-	-	-	-	-	-

Table 3.1: *Average quantities $\langle\gamma\rangle_{DS} = \langle E_{DS}^{lab}/p_{\rm DS}\rangle$, $\langle\gamma\rangle_{LDSP}$ and $\langle\epsilon_{\rm geo}\rangle$ for Z portal and H portal production, for various production modes, and for weak/strong case. The reported numbers are for fixed $\Lambda_{IR} = 10$ MeV. For Higgs portal, we have taken $\Delta_{\mathcal{O}} = 4$. The shown numbers are for DUNE-MPD (at 120 GeV) and SHiP (at 400 GeV) target materials (which sets the target atomic weight and number A, Z respectively). The average DS boost $\langle\gamma\rangle_{DS}$ depends on weak/strong case through the kinematic condition $\sqrt{p_{\rm DS}^2} \geq n_{LDSP}\Lambda_{IR}$ imposed when calculating the average, and is a weak dependence. Annihilation decays of vector mesons does not proceed through the Higgs portal due to mismatch in quantum numbers.*

3.2.2 Drell-Yan production

If the typical exchanged momentum from the protons to the DS is comparable or larger than $\Lambda_{\rm QCD}$, the process is able to probe the partonic constituents of the nucleon. Given the energy scales involved, the protons are ultra-relativistic, and using the parton distribution functions (PDF) language to model the interaction between the constituents is justified. Notice that in our case, the condition to probe the partonic structure of the nucleon is $p_{\rm DS}^2 \gtrsim 1\ {\rm GeV}^2$, which is a request on the total DS system, and not on the mass $\Lambda_{\rm IR}$ of the DS constituents. This is unlike what happen in models in which the mediator is produced on-shell, such as in light dark photon models. The production cross-section is in general dependent on the portal. A general estimate for the amplitude of DY through a given portal can be obtained on dimensional grounds, by assuming the typical momentum to be $\sqrt{p_{\rm DS}^2}$, and integrating over it to get the cross section. For Higgs portal, the partonic cross-section comes from Higgs exchange and is dominated by gluon initial states, while for Z portal, there is a Z exchange, and the initial states are the quarks. For the

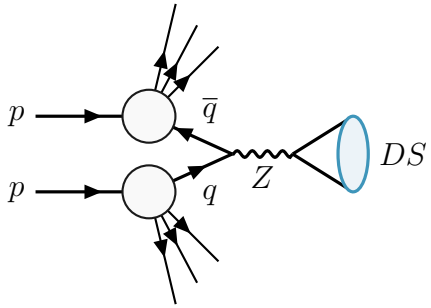

Figure 3.4: *Prototypical Drell-Yan process in Z portal for the DS production.*

Z-aligned JJ portal, the results of Z portal apply, once appropriately rescaled, if the couplings are assumed to be Z-aligned (both in axial-vector and isospin space). The Feynman diagram for such a process is shown in Fig. 3.4. Due to the similarity with Drell-Yan (DY) annihilation process we dub this production channel DY.

Consider first the Higgs portal. The leading interaction at the constituent level is due to *gluon-gluon fusion* (ggF) processes: indeed light quarks, while abundant in the proton, have a suppressed coupling to the Higgs, while heavy quarks are rare in the proton. Following [266], the effective ggF operator is, after integrating out the Higgs,

$$\mathscr{L} \supseteq F(\hat{s}) \frac{\kappa_{\mathcal{O}}}{\Lambda_{\rm UV}^{\Delta-2}} \frac{\alpha_s}{16\pi m_h^2} G^{\mu\nu\,a} G^a_{\mu\nu} \mathcal{O} \,, \tag{3.20}$$

where $F(\hat{s})$ is a function of the center of mass energy $\hat{s}$ of the process that accounts for the loops of internal quarks. Given that our computation is valid only for $p_{\rm DS}$ above the QCD scale, we retain in F only the contributions coming from the top, bottom, charm and strange quarks. This expression holds for center of mass energies much smaller than the Higgs mass (true for typical neutrino and beam dump experiments).

The cross section to produce a DS shell of total momentum $p_{\rm DS}^2$ can be computed by integrating over the DS phase space using optical theorem:

$$\begin{aligned} \sigma^{\rm DY(Higgs)} = A\,\sigma_{\rm pp}^{\rm DY(Higgs)} = \frac{A\,\alpha_s^2}{1024} \frac{\kappa_{\mathcal{O}}^2 c_{\mathcal{O}}}{m_h^4 \pi^{7/2}} \frac{\Gamma(\Delta_{\mathcal{O}}+1/2)}{\Gamma(2\Delta_{\mathcal{O}})\Gamma(\Delta_{\mathcal{O}}-1)} \times \\ \times \int_{Q_0^2}^{s} {\rm d}p_{\rm DS}^2 \left|F(p_{\rm DS}^2)\right|^2 \frac{p_{\rm DS}^{2(\Delta_{\mathcal{O}}-1)}}{\Lambda_{\rm UV}^{2\Delta_{\mathcal{O}}-4}} \times \\ \times \int_{p_{\rm DS}^2/s}^{1} \frac{{\rm d}x}{sx} f_g\left(p_{\rm DS}, x\right) f_g\left(p_{\rm DS}, p_{\rm DS}^2/(sx)\right) \,, \end{aligned} \tag{3.21}$$

where A is the atomic number of the target nucleus, f_g are the gluon PDFs[8], x is the longitudinal momentum fraction of one of the initial gluons in the CM frame and $\sqrt{s}$ is the center of mass energy of the protons. The lower limit of the integral over

[8]To compute the PDF integral, we used the nCTEQ15 PDF values [271], included in the MANEPARSE Mathematica package [272].

$p_{\rm DS}^2$ is cutoff at $Q_0^2 = (1.3\ {\rm GeV})^2$, the lowest for which the PDFs have been fitted, and below which the process does not probe a single parton and the DY picture breaks down. For consistency, Q_0^2 must be more than the minimum invariant mass of the DS system, $(n_{\rm LDSP}\Lambda_{\rm IR})^2$, which we impose internally.

Next consider the Z portal. Since the quark-Z coupling depends only on the up or down type of the quark, the process is dominated by light quark-antiquark annihilations. We will consider only contributions coming from up and down quarks, for which the couplings are given as

$$\begin{aligned} g_u^2 &= \frac{g_2^2}{\cos^2\theta_W}\left(\frac{1}{8} + \frac{4}{9}\sin^4\theta_W - \frac{1}{3}\sin^2\theta_W\right) , \\ g_d^2 &= \frac{g_2^2}{\cos^2\theta_W}\left(\frac{1}{8} + \frac{1}{9}\sin^4\theta_W - \frac{1}{6}\sin^2\theta_W\right) . \end{aligned} \tag{3.22}$$

Unlike the ggF case, the relevant PDFs depend on whether the target nucleon is a proton or a neutron. We approximate the neutron PDFs f_i^n to be the isospin-rotated PDFs of the proton f_i^p:

$$f_u^p = f_d^n\ ,\ \ f_d^p = f_u^n\ ,\ \ f_{\bar{u}}^p = f_{\bar{d}}^n\ ,\ \ f_{\bar{d}}^p = f_{\bar{u}}^n\ . \tag{3.23}$$

The partonic cross section for the pp/pn interaction in the limit of massless quarks reads:

$$\sigma_{pp/pn}^{\rm DY(Z)} = \frac{1}{1152\pi}\frac{g_2^2 v^4 \kappa_J^2 c_J}{m_Z^4\cos^2\theta_W\Lambda_{\rm UV}^4}\int_{Q_0^2}^{s} {\rm d}p_{\rm DS}^2 p_{\rm DS}^2 \int_{p_{\rm DS}^2/s}^1 \frac{{\rm d}x}{sx}\ X_{pp/pn}(s,x,p_{\rm DS}^2)\ , \tag{3.24}$$

where

$$\begin{aligned} X_{pp}(s,x,p_{\rm DS}^2) &= 2\sum_{i=u,d}\left(g_i^2 f_i^p(x) f_{\bar{i}}^p(p_{\rm DS}^2/(sx))\right)\ , \\ X_{pn}(s,x,p_{\rm DS}^2) &= g_u^2\, f_u^p(x) f_{\bar{d}}^p(p_{\rm DS}^2/(sx)) + g_u^2\, f_{\bar{u}}^p(x) f_d^p(p_{\rm DS}^2/(sx)) + \\ &\quad + g_d^2\, f_d^p(x) f_{\bar{u}}^p(p_{\rm DS}^2/(sx)) + g_d^2\, f_{\bar{d}}^p(x) f_u^p(p_{\rm DS}^2/(sx))\ . \end{aligned} \tag{3.25}$$

In the PDFs used, we have taken the factorization scale to be the exchanged momentum $p_{\rm DS}^2$ and not indicated it explicitly to keep the expressions simpler. Putting the contributions from the protons and neutrons together, the total DY cross section for the Z portal is:

$$\sigma^{\rm DY(Z)} = Z\sigma_{pp}^{\rm DY(Z)} + (A-Z)\sigma_{pn}^{\rm DY(Z)}\ , \tag{3.26}$$

where Z, A are respectively the atomic and weight number of the target nuclei. Notice that in both Higgs and Z portal scenarios the cross section increase with $p_{\rm DS}$, as expected on dimensional grounds. The drop at high $p_{\rm DS}$ seen in Fig. 3.1 is due to the PDF convolutions.

In order to estimate the decay probability, we estimate the average boost of the LDSP in the lab frame (not to be confused with the boost of the total DS system) as given in Eq. (3.18). The value for these averaged quantities is given in Table 3.1.

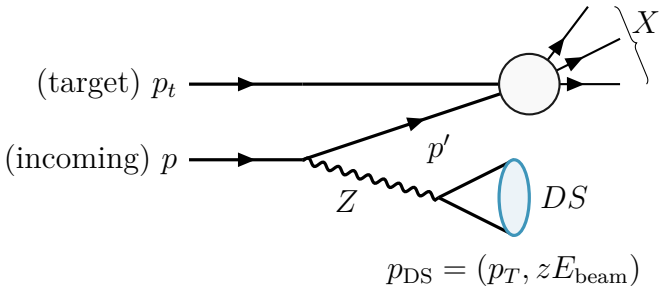

Figure 3.5: *DS produced via Z portal in the Bremsstrahlung production mode.*

In principle, the boost should take into account the angle in the DS frame: while particles in the DS frame have roughly the same energy, in the lab frame particles emitted along the beam are more boosted with respect to particles emitted in the opposite direction. We have checked that this effect is negligible, when restricting to particles hitting the detector. For the geometric acceptance, we notice that in the DY production mode, the DS system has no transverse momentum and is collinear to the beam axis. After boosting the LDSP momentum in the DS frame we compute the angles that corresponds to the detector. To estimate $\epsilon_{\rm geo}^{\rm DY}$, we follow the prescription given in App. H.2.

In general, in the DY production mode, events are produced with larger $p_{\rm DS}^2$ compared to other modes (see Fig. 3.1). We also find that the average energy of the DS system in the lab frame is not as high as in bremsstrahlung. These lead to lower γ of the DS system, a larger LDSP angular spread and therefore a slightly smaller $\epsilon_{\rm geo}$ for on-axis detectors.

3.2.3 Dark Bremsstrahlung ($pp \to \mathbf{DS} + X$)

Another possibility is for the DS states to be produced directly from proton as an initial state radiation. In this case, the exchanged momentum $p_{\rm DS}^2$ is not hard enough to probe the partonic structure. Following [273], we model the process using the initial state radiation (ISR) splitting function formalism. The idea is to treat the DS as incoming from the leg of the initial beam proton, which then becomes slightly virtual—an almost on-shell particle participating in the rest of the process. In the following, we will use the standard jargon: p_T for the transverse momentum of the DS system (in the plane orthogonal to the beam direction) and $z\,E_{\rm beam}$ for its longitudinal momentum, where $E_{\rm beam}$ is the beam longitudinal momentum (in the lab frame).

The splitting function formalism works well when the virtual particle is almost on shell. This means that in order to get reasonable cross sections, we must integrate the variables p_T and z in a sub-region of their kinematically allowed values, in which the virtual proton is not too off-shell. Denoting the proton after DS emission as p', concretely, we will consider the region in which the virtuality is small:

$$\frac{p'^2 - m_p^2}{E_{p'}^2} = \frac{z^2 m_p^2 + (1-z)p_{\rm DS}^2 + p_T^2}{z(1-z)^2 E_{\rm beam}^2} < 0.1\,. \tag{3.27}$$

The choice of 0.1 is arbitrary and our results are not sensitive to small changes in this. In order to compute the splitting functions, we need to compute the vertex between the proton and the Z or Higgs. For the Higgs, by using low energy theorems [274] we can compute the coupling between the Higgs and nucleon at zero momentum to be $g_{hNN} h\bar{N}N$, where $g_{hNN} = 1.2 \times 10^{-3}$. To model the momentum dependence of the form factor, we employ a generalization of the *extended Vector Meson Dominance* (eVMD) model, in which the DS state interacts with the hadron by mixing with the scalar, CP even hadronic resonances. The resonances' propagators are taken to be Breit-Wigners (BW), and the mixing coefficients are fixed by using sum rules and by fitting the zero momentum values. The form factor is taken from [273] and the specific values used are reported in App. G.1.1.

We also need to take into account the fact that for too high virtuality the quasi-real proton stops interacting with the target proton as a coherent object, and the bremsstrahlung computation breaks down. To do this we multiply the previous form factor by a smooth cutoff [275]:

$$F_D(Q^2) = \frac{\Lambda_p^4}{\Lambda_p^4 + Q^4} \,, \tag{3.28}$$

where $\Lambda_p = 1.5$ GeV is the cutoff, taken to be near the proton mass, and Q^2 is the virtuality of the intermediate proton:

$$Q^2 = \frac{z^2 m_p^2 + (1-z) p_{\rm DS}^2 + p_T^2}{z^2} \,. \tag{3.29}$$

Finally, the cross section for the process is calculated by factorizing the total cross section into the Bremsstrahlung part and a proton-nucleus (after Bremsstrahlung) part. The proton-nucleus cross section $\sigma_{pN}^{\rm nTSD}$ is calculated using the difference between the total inelastic proton-nucleus cross section and the *target single diffractive* (TSD) contribution, in which the target nucleus is diffracted but not disintegrated. This choice allows neglecting possible interference between the initial state and the final state radiation [260, 273]. According to [260, 276], $\sigma_{pN}^{\rm nTSD}$ is a slowly varying function of energy, and for the energies involved, we can approximate it as a constant

$$\sigma_{pN}^{\rm nTSD} = 762 \, (A/56)^{0.71} \left(1 - 0.021 \, (56/A)^{0.36}\right) \,, \tag{3.30}$$

where A is the target atomic weight. We will now generalize the results of [266, 273] to higher dimensional portals.

So far the discussion applies to any of the portals. However, once a portal is specified, the involved form factors change. Consider first the Higgs portal. Putting everything together, the inclusive production cross section is given as

$$\begin{aligned} \sigma_{pN}^{\rm Brem(Higgs)} = \sigma_{pN}^{\rm nTSD} g_{hNN}^2 \frac{v^2}{16\pi^{9/2} m_h^4} \frac{\Gamma(\Delta_{\mathcal{O}} + 1/2)}{\Gamma(\Delta_{\mathcal{O}} - 1)\Gamma(2\Delta_{\mathcal{O}})} \frac{\kappa_{\mathcal{O}}^2 c_{\mathcal{O}}}{\Lambda_{\rm UV}^{2\Delta_{\mathcal{O}}-4}} \times \\ \times \int {\rm d}p_{\rm DS}^2 {\rm d}p_T^2 {\rm d}z \, |F_H|^2 \times \; z \left((2-z)^2 m_p^2 + p_T^2\right) \times \\ \times \left(\frac{1}{m_p^2 z^2 + (1-z) p_{\rm DS}^2 + p_T^2}\right)^2 p_{\rm DS}^{2\Delta_{\mathcal{O}}-4} \,, \end{aligned} \tag{3.31}$$

where F_H is the Higgs bremsstrahlung form factor built as outlined before, and can be found in App. G.1.1. The limits of integration are chosen to respect the kinematic condition $p_{\rm DS}^2 \geq n_{\rm LDSP}^2 \Lambda_{\rm IR}^2$.

Next consider the Z portal case. The only difference is in the form factors of the axial and vector current of the proton. For the vector case, the production cross section is given as

$$\sigma_{pN}^{\text{Brem(Z, Vector)}} = \sigma_{pN}^{\text{nTSD}} \frac{\kappa_J^2 c_J}{2^{11}\pi^4} \frac{v^4}{m_Z^4 \Lambda_{\rm UV}^4} \frac{g_2^4}{\cos\theta_W^4} \int \mathrm{d}p_{\rm DS}^2 \mathrm{d}p_T^2 \mathrm{d}z \left|F_Z^{\rm V}\right|^2 \times \\ \times \left(\frac{2}{z} + \frac{4p_{\rm DS}^2 z \left(p_T^2 + m_p^2(z^2+2z-2)\right)}{\left(m_p^2 z^2 + (1-z)p_{\rm DS}^2 + p_T^2\right)^2} \right) . \tag{3.32}$$

The vector form factor $F_Z^V(p_{\rm DS}^2)$ is modeled by ρ (iso-triplet) and ω (iso-singlet) exchange. We take three states for each tower. Details are given in App. G.1. For the axial case, the cross section is given as

$$\sigma_{pN}^{\text{Brem(Z, Axial)}} = \sigma_{pN}^{\text{nTSD}} \frac{\kappa_J^2 c_J}{2^{11}\pi^4} \frac{v^4}{m_Z^4 \Lambda_{\rm UV}^4} \frac{g_2^4}{\cos\theta_W^4} \times \\ \times \int \mathrm{d}p_{\rm DS}^2 \mathrm{d}p_T^2 \mathrm{d}z \left|F_Z^{\rm A}\right|^2 \frac{2}{z} \left(\frac{1}{m_p^2 z^2 + (1-z)p_{\rm DS}^2 + p_T^2} \right)^2 \times \\ \times \left(p_{\rm DS}^2 (1-z)^2 + \left(p_T^2 + z^2 m_p^2\right)^2 + 2p_{\rm DS}^2 \left(m_p^2 z^2 \left(5 + (z-5)z + p_T^2(1+z^2-z)\right)\right)\right) . \tag{3.33}$$

Similar to the vector case, for the axial form factor we take the respective iso-triplet axial vector exchange (there is no contribution from the axial iso-singlet resonances). Details about the axial form factor $F_Z^A(p_{\rm DS}^2)$ are in App. G.1. Combining the vector and the axial pieces we get

$$\sigma_{pN}^{\text{Brem, (Z)}} = \sigma_{pN}^{\text{Brem, (Z, Vector)}} + \sigma_{pN}^{\text{Brem, (Z, Axial)}} . \tag{3.34}$$

Notice that in Eq. (3.34) the interference term between the vector and axial piece vanishes, due to the different quantum numbers under parity of the two possible states.

The vector contribution to the cross section is subdominant with respect to the axial one, due to an accidental cancellation in the vectorial quark coupling. The vector contribution has a more narrow distribution in $p_{\rm DS}^2$ than the axial one, and it's peaked at m_ω^2: this is because ω is much more narrow than the iso-triplet vectors and axial vectors resonances mixing with the Z. Notice that the same exact computation holds for a JJ portal aligned (in both Lorentz and flavor space) to the Z quantum numbers. For different coupling structure of $J_{\rm SM}$ for a generic JJ portal, we can decompose the proton vector and axial form factors in their iso-singlet and iso-triplet components to get the correct form factor, shown in App. G.1.

An estimate for the cross section can be given by exploiting the fact that the cross section is dominated by the Breit-Wigner (BW) peaks in the form factors. The $p_{\rm DS}^2$

integral of the BW associated with an intermediate meson $\mathfrak{m}$ can be estimated as $\pi f_{\mathfrak{m}}^2 m_{\mathfrak{m}}^3/(2\Gamma_{\mathfrak{m}})$, where we have used the notation of App. G.1. Therefore, using the splitting function to give the correct momentum scaling, upto an $\mathcal{O}(1)$ factor, the cross section for radiating DS particles through a dimension D portal made of a SM operator and a dimension $\Delta_{\mathcal{O}}$ DS operator can be estimated as:

$$\sigma \sim \sigma_{pN} g_{\rm SM}^2 \Phi(\Delta) f_{\mathfrak{m}}^2 \begin{cases} \frac{v^2}{m_h^4} \frac{m_{\mathfrak{m}}^{2\Delta_{\mathcal{O}}-1}}{\Lambda_{\rm UV}^{2\Delta_{\mathcal{O}}-4}\Gamma_{\mathfrak{m}}} & : \mathcal{O}H^\dagger H \text{ portal}\,, \\ \\ \frac{m_{\mathfrak{m}}^5}{\Lambda_{\rm UV}^4 \Gamma_{\mathfrak{m}}} & : JJ \text{ portal}\,, \end{cases} \tag{3.35}$$

where, as in the meson case, $g_{\rm SM}$ is a dimensionless SM factor built out of dimensionless couplings (like the gauge couplings), $\Phi(\Delta)$ is the phase space factor coming from the integration over the DS degrees of freedoms, $f_{\mathfrak{m}}$ is the coupling of proton to the meson $\mathfrak{m}$ and $\Gamma_{\mathfrak{m}}, m_{\mathfrak{m}}$, is its decay width and mass respectively (see App. G.1). In presence of multiple resonances, the estimate can be done by restricting to the leading contribution of the BW. For both the Higgs and Z portals the DS is produced as a collimated state forming an angle with the beam $\theta_{\rm DS} \sim p_T/E_{\rm DS}^{\rm lab} = p_T/(zE_{\rm beam})$. The average acceptance $\epsilon_{\rm geo}^{\rm brem}$ is computed by averaging over all the kinematic variables, and it doesn't differ much from the one obtained by replacing $\theta_{\rm DS}$ with its average. Details of the computation of the geometric acceptance are given in App. H.2. To estimate the average decay probability, we use the average LDSP boost, as defined in Eq. (3.18) (see also Table 3.1 for typical values), with the only difference being that the probability distribution is given by the splitting function. The typical energy of the DS system in the lab frame is roughly $(3/4)E_{\rm beam}$ for all the portals considered, larger than in DY case.

3.3 Experimental Setups, Signal and Background Estimation

In this section we briefly discuss the experiments we consider for obtaining the bounds on the $\Lambda_{\rm UV}$ and $\Lambda_{\rm IR}$ scales, and the assumptions we make when obtaining these bounds.

As explained in Sec. 3.1, the relevant characteristics of high intensity experiments are their beam energy $E_{\rm beam}$, their integrated luminosity (reported as the total protons on target $N_{\rm POT}$) and geometric details of the experimental setup. Further, the detectors in these experiments can be placed on-axis (i.e. along the line of the incoming beam) or off-axis (see Fig. 3.6 for a cartoon of the experimental setup), which can change the geometric acceptance if certain production modes are forward peaked. Specific to the MD production mode, the number of meson $N_{\rm M}$ produced at a given experiment is an additional input, as seen from Eq. (3.12). This depends on the target details as well as the energy in the centre of mass frame, $\sqrt{s} \approx \sqrt{2E_{\rm beam}m_p}$.

In this work we consider a representative set of past, present and future experiments. Table 3.2 gives the list of considered experiments with the relevant parameters.

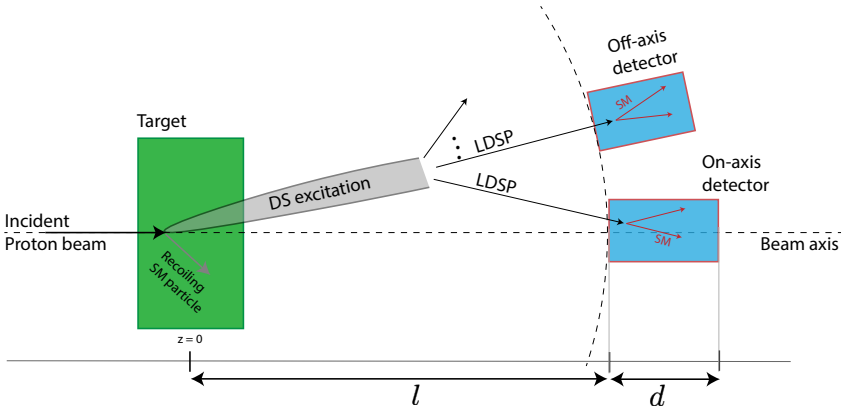

Figure 3.6: *A cartoon of DS events produced at a typical neutrino detector (drawn not to scale): both on-axis and off-axis cases are shown. In general the DS state may not be produced along the beam-axis, as shown, though this is dependent on the production mode: annihilation decays of Mesons and DY production modes produce DS along the beam-axis, while radiative decays of Mesons and DB production mode produce DS at a small angle from the beam-direction.*

We show bounds from recasts of BSM search results from past and current experiments, and projections from current and upcoming experiments, considering a few representatives from each category. We will also consider a future dedicated LLP search experiment, SHiP, for comparison, since it has a broad reach in typical DS models (e.g. see ref. [277]). We will take the SHiP parameters to be very optimistic, to have a conservative comparison with the neutrino experiments. A more comprehensive analysis that also considers other dedicated LLP experiments can be useful, and will be done in future. The best bounds from the high intensity experiments that we consider are from the currently under construction DUNE experiment and the proposed SHiP experiment. We also show bounds coming from other experiments running at the same beam energies of these two (120 GeV and 400 GeV respectively).

Out of past experiments, we show CHARM, a beam dump experiment that ran on the CERN SPS (400 GeV) beamline in the 1980s. CHARM searched for the decay of axion-like particles (ALPs) into a pair of photons, electrons and muons and found no events [278], and we will recast this search for our bounds. Our choice of the past experiments are representative, and not based on the strongest bounds, but rather on considering similar beam energies as DUNE and SHiP (e.g. PS191 and νCAL, with beam energy of 19.2 GeV and 70 GeV respectively, can give a slightly better bound than CHARM, but are much weaker than the advocated future experiment DUNE. We will comment in Sec. 3.4 about these two experiments).

We do not recast Heavy Neutral Lepton decay searches of CHARM or other past experiments like BEBC, or dark particle scatterings as done for example in [279, 280], given the different final state topology.

From existing experiments, we choose the MicroBooNE and ICARUS experiments,

based on the 120 GeV NuMI beamline. These are two of the three detectors of Fermilab's Short-Baseline Neutrino program (SBNP) [214].[9] For MicroBooNE, we will use the analysis in ref. [281] for dark scalars decaying into electron-positron pairs. For ICARUS, we will use the results in [219], which studied DS coupled through the renormalizable Higgs portal.[10] DM searches at another current experiment, MiniBooNE, based on 8 GeV BNB beamline, use scattering [247, 282], and as explained in Sec. 3.1, they require additional model dependent assumptions, so we will not consider them here. Another currently running NuMI-based experiment is NOνA. We are not aware of any search for DM decays done at this experiment (for a scattering analysis, see [247, 283], based on [284]). Since NOνA is currently running, we show a possible prospect of such a search. We assume that it will be possible to reduce the backgrounds to negligible amounts, given the good angular resolution of the detector.

For future experiments we look at the Deep Underground Neutrino Experiment (DUNE). Ref. [217] has proposed the use of the multipurpose, high pressure gaseous chamber- the Multi-Purpose Detector (MPD) present in DUNE near detector complex for DS searches. We show projections for our DS scenario for the future DUNE-MPD as well.

Another class of future and existing experiments that are worth considering are the ones that are built in a region directly forward of the beam interaction point at LHC, like the already running FASER [285] and FASERν [286] (see [287] for the recent analysis) and SND [288], and the proposed experiments at the Forward Physics Facility (FPF) [289]. These experiments are in spirit similar to proton beam dumps, given that unlike traditional collider experiments they are put directly in the forward region, but have a much higher beam energy. This can potentially be relevant for non-renormalizable portals. The reach of these detectors have been thoroughly studied in the recent past in the context of Dark Sectors: a non-exhaustive list of works includes [264, 290, 291, 292] for renormalizable portals at FASER, [293] for ALPS at FASER, [294] for SND prospects, [295] for a strongly coupled dark sector at the FPF, [296, 297] for renormalizable portals at the FPF and [266] for FASER2 prospects. We will briefly comment on their reach on these models in Sec. 3.4.

In order to estimate the sensitivity of the selected current and future experiments, an assessment of the background is needed. We assume that beam dump experiments can be made background free by imposing cuts with $\mathcal{O}(1)$ signal efficiencies, as seen in past searches, e.g. at CHARM [278]. On the other hand, at neutrino experiments, the neutrino beam itself can be a source of background events. At these experiments the typical mass of the LDSPs probed is $\mathcal{O}$(10-100) MeV, therefore the

[9]The third detector, SBND, is too far off-axis with respect to the NuMI beamline and therefore its geometric acceptance is too low to give meaningful constraints. These three detectors also run on the 8 GeV Booster Neutrino Beam (BNB), which is at a lower energy than the NuMI energy, 120 GeV. We find the bounds to be subleading compared to DUNE (but better than other detectors), and do not consider it.

[10]Since the target specifications for NuMI beamline experiments are the same as that of proposed DUNE-LBNF beamline, we recycle the meson production numbers for DUNE-LBNF [217] also for the NuMI beamline experiment ICARUS.

Experiment	$N_{\rm POT}$ (total)	$E_{\rm beam}$ (GeV)	l (m)	d (m)	Off-axis angle, $\theta_{\rm det}$ (rad)	$\theta_{\rm acc}$ (rad)
CHARM [278, 298, 299]	2.4×10^{18}	400	480	35	0.01	0.003
NOνA-ND [247, 284]	3×10^{20}	120	990	14.3	0.015	0.002
MicroBooNE (KDAR) [281]	1.93×10^{20}	120	100	10.4	-	0.013
ICARUS-NuMI [214, 219]	3×10^{21}	120	803	19.6	0.097	0.005
DUNE-MPD[217, 300]	1.47×10^{22}	120	579	5	0	0.004
SHiP [265, 277]	2×10^{20}	400	64	50	0	0.078

Table 3.2: *The relevant parameters for the experiments considered in this work. The quantities l and d are defined in Fig. 3.6. $\theta_{\rm det}$ stands for the position of the detector centre with respect to the beam line, with the origin taken at the interaction point. Entries with zero $\theta_{\rm det}$ indicate that the detector is placed along the beam axis. $\theta_{\rm acc}$ stands for the detector half angular opening. Note that for MicroBoone KDAR analysis, the K mesons are produced at rest (in the lab frame) so that θ_{det} is irrelevant. The angle θ_{acc} for this case is measured with the origin at the NuMI hadron absorber, placed $\mathcal{O}(600)$ m from the interaction point [281].*

available channels for the LDSP decay to the SM are mostly photons and electron-positron pairs, which produce electromagnetic showers in the detector. Heavier decay products, such as muons, will be reconstructed as tracks (but for all practical purposes, we will treat them similar to the showers in this section). The following discussions hold for any of the decay products.

In principle, the two shower signature has no irreducible background. Reducible background events come from hard radiation of a single photon, or from neutral-current ν scattering against a nucleus producing a π^0, which then decays into $\gamma\gamma$. The produced photons then can convert into e^+e^- pairs, that mimic the signal. However, it's not guaranteed that the two daughter particles will be reconstructed as separate showers.

The typical condition in order to reconstruct the two particles involves an isolation cuts between the decay products, or in other words an angular separation cut. The specific implementation depends on the specific detector and analysis strategy. We will briefly review what has been suggested in previous works. However many of the relevant aspects can be understood more generally, which we will elaborate with a relevant prototypical experiment in mind.

For the ICARUS experiment, as suggested in [219], an angular separation of 10° is enough to be able to separate the two showers. Background events instead have a narrow separation between the charged particles, or potentially two showers that do not originate from the same vertex. The angular cut reduces the background events to a negligible amount. In [246] the authors elaborate on an analysis with less stringent cuts but with $\mathcal{O}(100)$ background events. Indeed a strong isolation cut has low efficiency for lighter, and therefore more boosted, LDSPs. This is especially true for the models under consideration here, in which DB and DY production modes are non-negligible and generate LDSPs more boosted than the ones coming from meson decays. For example, in DB, for the weakly coupled case $n_{\rm LDSP} =$

$2, \Lambda_{\rm IR} = 100$ MeV, we expect the daughter particles to be separated by an angle of $1/\gamma_{\rm LDSP} \approx 0.15°$, which is smaller or comparable to the angular resolutions of some of the detectors. This highlights a potential problem in our framework, when reconstructing the signal. For this reason, we suggest that at ICARUS, it might be better to avoid a stringent cut in angular separation and work with $\mathcal{O}(100)$ background events [246], possibly reduced with an energy cut and a cut on the direction of the DS system with respect to the beam. Interestingly, for strongly coupled DS we expect the angular separation condition to be less stringent on the signal. Because of a larger $n_{\rm LDSP}$, the energy is split among more LDSPs, leading to a suppression of the single LDSP boost factor. For such sectors, assuming an average $n_{\rm LDSP}$ of $\mathcal{O}(10)$, the average separation angle is typically $\mathcal{O}(1°)$ for DB and 100 MeV masses, and less for other production modes. Since this is of the order of the angular resolution of ICARUS, it should be feasible to reconstruct the signal events as separated tracks for masses not too light.

Specific to the DUNE-MPD detector, in [217, 301, 302] it has been shown that boosted signal events have a narrower angular separation compared to the more isotropic background distributions. Due to this difference the search can effectively be rendered background free. Even in this case the two decaying particles must be reconstructed as separate particles, which these references claim to achieve. In these studies, the typical opening angle between the decay products is comparable to the weakly coupled scenarios we consider in this work. Therefore we take this search to be background free.

If instead the two decay products are not separated, the event will be reconstructed as a single electron event. The background to this kind of event comes from ν_e charged-current scattering, from ν-e elastic scattering events or ν neutral-current quasi-elastic events. The idea of decaying particle hiding behind the single electron signature has been explored in [303, 304]. In these works it is shown how to recast the analysis of the LSND experiment (with a beam energy of 0.8 GeV) that looked for ν_e charged-current scattering [305, 306] to put bounds on BSM particles decaying into e^-e^+, hiding as single electron events. In particular, the decaying particle would present as an excess of high energy electron events near the maximum value of the energy analyzed (200 MeV)[11]

Considering now a higher beam energy experiment, searches for charged-current at NuMI based experiment (with beam energy 120 GeV) typically look for neutrino with GeV energies, a bit lower than the typical LDSP energy (see for example [307]). Other scattering analysis typically look for ν-e elastic scattering. The cuts imposed require a low energy recoil, and a very forward electron. It's unclear whether or not they can be used to put stringent bounds on misidentified e^-e^+ pairs. It will be very interesting to explore this signature of single electron hiding in the high energy tail of scattering events at high beam energy experiments, but we will not study this

[11] We do not recast LSND bounds in the DB and DY modes, even if the intensity is one of the highest. For DY, due to a very low beam energy of 0.8 GeV, the integration range of the partonic center of mass energy is very small. For DB, the condition on the integration domain of Eq. (3.27) is very constraining. Relaxing the condition, by setting the RHS of Eq. (3.27) to 1, the bounds are still worse than DUNE.

signature here.

We would like to point out that it should be possible to run the neutrino experiments in a beam dump mode, essentially removing all the background, while keeping almost all the signal (except the one coming from charged meson decays). A beam dump proposal for DUNE has been studied in [308], showing that indeed running in the beam dump mode allows neglecting all the SM backgrounds in the DUNE detector, albeit at a reduced luminosity of roughly two orders of magnitude (one order of magnitude, for the optimistic scenario). The idea to suppress neutrino background by steering the beam off the target (as in the beam dump mode) has been already implemented at MiniBooNE [282] (although looking for DM scattering events) and MicroBooNE experiments. We will recast the MicroBooNe search, which however is quite different in spirit from the typical beam dump search, as it is optimized to look for Kaon Decay At Rest (KDAR). The idea is to look for the decay products of Kaons decaying at rest in the NuMI hadron absorber, which have a very peculiar directionality: in usual cases, the decay products of produced kaons are collected by a detector placed further down the beamline, whereas here the MicroBooNE detector is placed on the back side of the NuMI hadron absorber (e.g. see fig. 1 in ref. [281]). This peculiarity allows the signal events to be easily distinguished from background events, with an estimated efficiency of 0.14 on signal selection.

In addition to the backgrounds discussed so far, there is an extra component coming from *neutrino trident events*, in which a neutrino scatters against a nucleus in a purely electroweak process, to produce a lepton-antilepton pair. As argued in [217, 309], the expected number of events is $\mathcal{O}(10)$ events at DUNE-MPD, while it is lower in other liquid Argon detectors like ICARUS. In more conventional detectors like NOνA, $\mathcal{O}(10)$ e^-e^+ trident events are expected [220]. Given the rather peculiar kinematics, it's possible to bring down these background events and neglect them in the analysis [217].

For all these reasons, we will compute the signal yield contours for 10 and 100 event lines when discussing prospects for DUNE-MPD. Indeed 10 events represent a reasonable proxy for an almost background free search in the presence of $\mathcal{O}(1)$ experimental efficiency, although this number could be brought down in specific experiments by a more careful analysis of the reducible backgrounds. The 100 event lines instead can be representative of some signal loss due to selection cuts (which could be present for example in the weakly coupled case due to a small angular separation) or for a reduction in $N_{\rm POT}$, for example due to running in dump mode for a limited amount of time.

From the experimental analysis we recast, we use 95% confidence level, including the signal efficiencies reported. For CHARM [278] which observed 0 event, we set a bound at 95% confidence level of $N_{\rm signal} < 3$, using efficiency of 0.51 and 0.85 for the e^+e^- and $\mu^+\mu^-$ modes respectively. For MicroBooNE KDAR [281] which observed 1 event compared to a background expectation of 1.9 events, we require $N_{\rm signal} < 3.8$ at 95% confidence level, with a signal reconstruction efficiency of 0.14.

3.4 Results

In this section we present our bounds on the parameters $\Lambda_{\rm UV}, \Lambda_{\rm IR}$. As we have argued before, the dominant production mode is through the Z-portal, but the decay can proceed through either Z-portal or Higgs portal. As discussed in Sec. 3.2, there are three production modes for DS states, each of which has a different distribution in $p_{\rm DS}$ and therefore contributes differently depending on the energy and the detector geometries. In Fig. 3.7 we show the exclusion regions individually for the three production modes, keeping to the Z portal decay for simplicity, for both weakly and strongly coupled benchmark scenarios. We will assume that the LDSP has spin 1 in order to fix the decay parametrics. In Fig. 3.8, we show the combined bounds from this work, for both Z and Higgs portal decays, and compare against bounds from LHC and LEP from ref. [76]. The bounds for the Z-aligned $J^{\rm SM}_\mu J^\mu_{\rm DS}$ portal can be obtained from the Z portal bounds simply by re-scaling the signal cross section as $\sigma^Z_{\rm S}/\sigma^{JJ}_{\rm S} \sim (\kappa^2_Z/\kappa^2_{JJ})\,(v^2/m^2_Z)$. The case of generic JJ portal is obtained from the Z-portal by an appropriate combination vector/axial parts of the current and a rescaling of the couplings.

One can understand the general features of the excluded regions. The right edge of excluded region (on the high $\Lambda_{\rm IR}$ side) is due to the LDSPs being too short lived. Therefore the bound is roughly set by $\beta\gamma c\tau \sim \ell_{\rm detector}$. Given that typically for high $\Lambda_{\rm IR}$, $n_{\rm LDSP}$ for the weakly and strongly coupled cases are very similar, the right edge of the excluded region is almost identical for the weakly and strongly coupled cases. The left edge of the excluded region is instead due to the LDSPs being too long lived, $\beta\gamma c\tau \gg \ell_{\rm detector}$. In this case the exponentials appearing in the decay probability (Eq. (H.2)) can be expanded to linear order and it's possible to get the slope of the right edge. For example, in the weakly coupled case with both production and decay through Z portal (or any generic 6D operator) the right edge is set by a constant $(\Lambda^6_{\rm IR}/\Lambda^8_{\rm UV})$ line, where the factors come from the exponential expansion to linear order and the $1/\Lambda^4_{\rm UV}$ in the production cross-section. For the strongly coupled case the $n^2_{\rm LDSP}$ factors have a non trivial dependence on $\Lambda_{\rm IR}$, and in general it is not possible to get the slope. Its effect is to increase the total signal events since the number of LDSPs is larger than in the weakly coupled scenario considered. This enhancement asymptotes to the weakly coupled case when $\Lambda_{\rm IR}$ is close to threshold due to the behaviour of the chosen function.

In all these exclusion plots, regions bounded by solid lines show the excluded parameter space from recasts of past and recent DS searches (CHARM [278] and MicroBooNE [281]). The region bounded by dashed contours in our plots show the potential of current and future upcoming neutrino experiments: NOνA-ND and ICARUS (current), and DUNE-MPD (near future). To compare their potential with future DS experiments, we also show the projections coming from the future beam dump experiment SHiP. For these projected exclusions, we have shown the 10 signal events line assuming 100% reconstruction and detection efficiency. Following our discussion in Sec. 3.3, for DUNE-MPD, we also show the 100 events line in Fig. 3.8.

There are several features of the bounds which make the neutrino experiments a very powerful probe for dark sectors, in the parametrization considered in this work. First

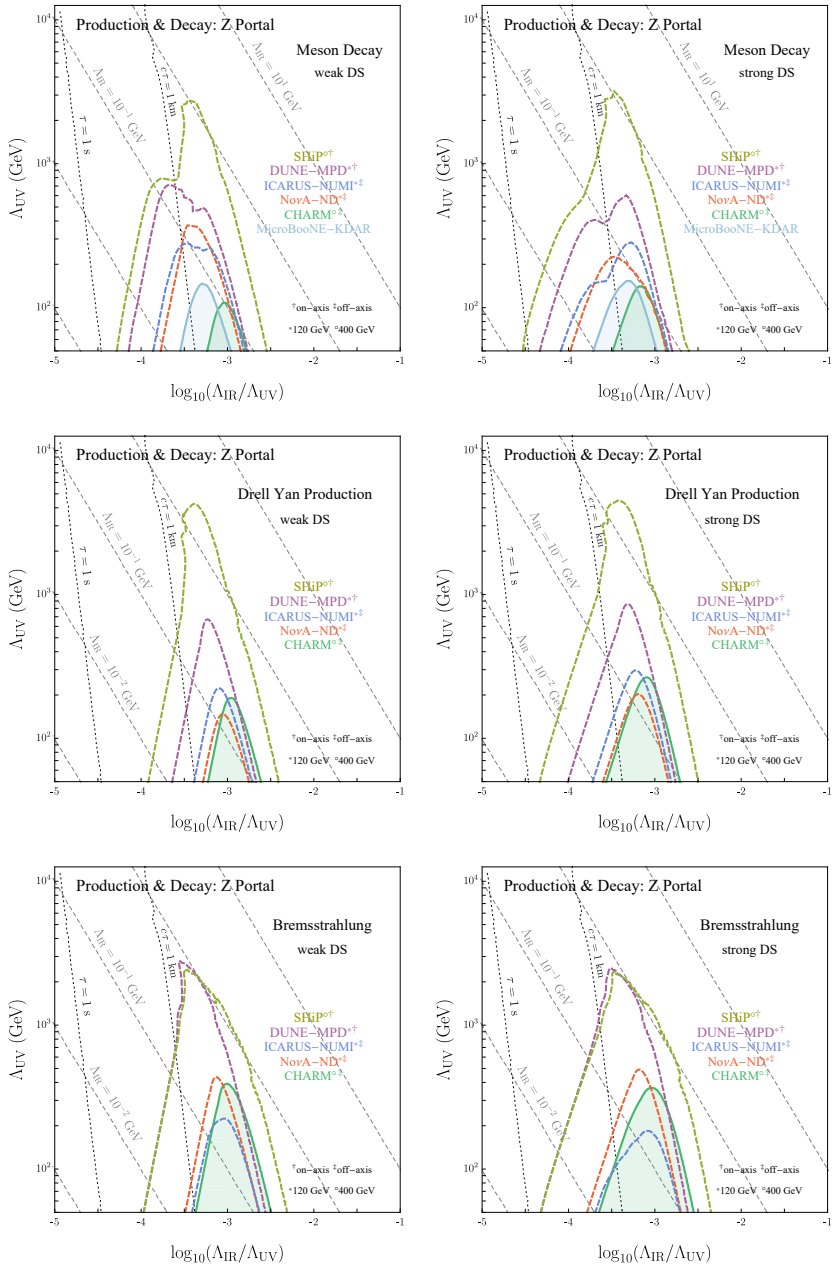

Figure 3.7: *Constraints on DS production and decay from $D = 6$ Z portal for various production modes: Meson Decay (top row), Drell-Yan (mid row) and Dark Bremsstrahlung (bottom row), for weakly coupled (left) and strongly coupled (right) benchmark cases. Exclusions are shown in solid lines, while future projections are shown in dotted lines. The superscripts indicate the beam energy and the on/off axis nature of detectors for each of the experiments considered. The black dotted lines show the LDSP lifetime τ isocurves, while the gray dashed lines show Λ_{IR} isocurves. The bounds assume $p_{\rm DS}^2/\Lambda_{UV}^2 < 0.1$ for EFT validity which is satisfied by restricting to $\Lambda_{UV} > 50$ GeV. All plots assume $\kappa_i^2 c_i = 1$, where i labels the portal, κ is the portal coupling and c is a measure of degrees of freedom of the DS.*

of all, we find that the bounds from current and upcoming neutrino experiments are comparable to dedicated DS experiments, with a reach of $\Lambda_{\rm UV}$ in multiple TeV range,

for $\Lambda_{\rm IR}$ in the MeV-GeV range. This is similar to the ranges probed in high energy experiments like LHC and LEP (as done in ref. [76]). The typical scale l at which the detectors are placed is much larger than the corresponding scale in the LHC DV searches, and the typical boosts involved are also different, which together select a somewhat larger τ and hence a smaller $\Lambda_{\rm IR}$ region compared to LHC. Importantly, neutrino experiments fill the gaps in the parameter space coming from trigger[12] and event selection requirements at LHC and LEP, since they are sensitive to much lower energy activity in the detector. Even more importantly, in portals which are not enhanced by a resonant production, the EFT condition $(p^2_{\rm DS})_{\rm max} < \Lambda^2_{\rm UV}$ makes LHC and LEP bounds inconsistent, an issue which is again alleviated at neutrino experiments due to a smaller $\sqrt{s}$ involved. All these features are seen in the bounds in Fig. 3.7, 3.8.

In the following subsections, we will discuss in detail how prospective DS searches at neutrino experiments can complement current bounds for different portals considered in this work. We will also emphasize the difference between the production modes, especially on how a particular detector geometry can favor one mode over the other.

3.4.1 Z Portal Production

Consider first the MD production mode through the Z portal (Fig. 3.7 first row), where we show bounds from various experiments. We also show bounds coming from the MicroBooNE KDAR analysis [281] which is only relevant for the MD mode. We find that for neutrino experiments based at 120 GeV proton beam, in general the strongest bounds come from radiative decays of K meson ($K \to \pi + \text{DS}$) due to the large number of K mesons produced with respect to other mesons. However, for the strongly coupled DS case where the kinematic condition on $p^2_{\rm DS}$ is stronger due to a larger $n_{\rm LDSP}$, we find that at DUNE and ICARUS, $\phi \to$ DS decays can give a stronger bound on $\Lambda_{\rm UV}$ as compared to K meson bounds. For experiments based on 400 GeV proton beam, heavier mesons like B, J/ψ can be produced in large numbers and can contribute to bounds at CHARM and SHiP. These heavier mesons can in principle probe larger $\Lambda_{\rm IR}$ due to the relaxed kinematic condition $n_{\rm LDSP}\Lambda_{\rm IR} \lesssim M$, where M is the mass of the decaying meson. The $\Lambda_{\rm IR}$ reach is correlated with the $\Lambda_{\rm UV}$ reach, for fixed lifetime. At SHiP, we indeed find that J/ψ decays probe the highest $\Lambda_{\rm UV}$ scales as opposed to K meson decays which suffer from the kinematic condition. However, we find that K mesons can still improve reach on lower $\Lambda_{\rm IR}$ values relative to J/ψ, B mesons due to larger geometric acceptance for $K \to \pi + \text{DS}$ and larger number of K mesons. At CHARM, we find that $J/\psi \to$ DS decays give the leading bounds which dominate those coming from $K \to \pi + \text{DS}$ decays.

For the Drell-Yan (direct partonic) production mode (Fig. 3.7 middle row), the best bounds come from SHiP, and the other experiments only give subleading bounds. Within them, due to the collinear nature of the produced DS beam, detectors of the

[12] This could be improved with dedicated trigger designs, as done in [310] for CMS in a different lifetime region than the typical one of the gap

on-axis type are more sensitive to this mode. Note that compared to the DB mode, the average DS boost is smaller for the DY mode, so that the LDSP spread is more and the off-axis detectors are penalized less.

For the case of dark bremsstrahlung (Fig. 3.7 bottom row), the DS is produced very collimated along the beam line, favoring detector geometries closer to it. We find that the best bounds from neutrino experiments for this mode come from DUNE-MPD. These are comparable in $\Lambda_{\rm UV}$ and only probe slightly smaller $\Lambda_{\rm IR}$ values, as compared to the future beam dump experiment SHiP. This is because in bremsstrahlung the typical $p^2_{\rm DS}$ is cut roughly around QCD scales, and an increase in $\sqrt{s}$ at SHiP as compared to DUNE does not lead to a large increase in the production cross section. The other experiments shown, ICARUS-NUMI, NOνA and CHARM give subleading reach in both $\Lambda_{\rm UV}$ and $\Lambda_{\rm IR}$. Despite an increase in the number of POTs with respect to NOνA, ICARUS still has lower sensitivity due to a reduced angular coverage. Both ICARUS and CHARM, due to their off-axis nature, miss out signal events from the forward DS beam, characteristic of the dark bremsstrahlung mode.

Combining all the production modes, in Fig. 3.8 we show the final excluded parameter space, for both weakly and strongly coupled benchmarks. We also show the results from [76] which studied resonant DS production through Z portals at high energy colliders and presented exclusion regions from ATLAS monojet search [311], displaced vertex search [312, 313], and from total Z width bounds from LEP [314]. The bounds presented here probe different parts of the parameter space, in particular in $\Lambda_{\rm IR}$, even if the $\Lambda_{\rm UV}$ reach is comparable to before, and also probe gaps in parameter space in earlier work which came from trigger requirements. The complementarity of the bounds at neutrino experiments, as compared to missing energy and displaced searches at LHC is due to the peculiar position of the near detectors of neutrino experiments, placed at $\mathcal{O}(10^2)$ meters. We also find that the bounds are stronger than past beam dump searches like E137 and NA64 (whose results can be found in [76, 235]) due to a larger $N_{\rm POT}$, and in some cases, a larger beam energy.

From Fig. 3.8 we see that one of the *current* strongest bounds for Z portal DS still comes from the indirect Z width measurement at LEP, $\Lambda_{\rm UV} > 525(k_J^2 c_J)^{1/4}$ GeV [76] which is independent of $\Lambda_{\rm IR}$ till the kinematic threshold. This bound is stronger than CHARM and MicroBooNE. Additionally, CHARM and MicroBooNE are also weaker than the LHC monojet and displaced vertex bounds except for the strongly coupled case (Fig. 3.8 top right) where they probe slightly higher $\Lambda_{\rm IR}$ values. Prospective DS searches at current Fermilab neutrino facilities, ICARUS and NOνA-ND, improve on CHARM and MicroBooNE, but they are still weaker than the LEP bound.

Most importantly however, we find that future neutrino detector DUNE-MPD will be sensitive to $\Lambda_{\rm IR}$ in the range $\mathcal{O}(0.1-1)$ GeV for $\Lambda_{\rm UV}$ of few TeVs, a region not covered by LHC exclusions. Future LLP experiment SHiP based on 400 GeV proton beam would further improve sensitivity with respect to DUNE-MPD and LHC searches. These improvements are either due to a higher geometric acceptance from being on-axis or from having a wider detector, or due to a higher beam energy.

Another past proton beam dump experiment νCAL, with a beam energy of 70

GeV, has searched for the decay of a scalar particle [315, 316]. Recasting this search [317, 318] gives bounds slightly better than CHARM, excluding in roughly the same $\Lambda_{\rm IR}$ region, and with $\Lambda_{\rm UV}$ up to 1 TeV. This is due to the fact that the bremsstrahlung cross section for this energy is the same as of CHARM, given the proton virtuality cutoff, the experiment has a similar luminosity, but it is closer to the beam and target. The bounds are still weaker than DUNE and SHiP. Recasting the Heavy Neutral Lepton search of PS191 [319, 320], as suggested in [321, 322], gives bounds better than CHARM but worse than νCAL and DUNE. We do not show these bounds to keep the plots uncluttered.

Emphasizing the complementarity of neutrino experiments with respect to the LHC searches, we note that for the strongly coupled case (Fig. 3.8 top right), the LHC (ATLAS) searches are not sensitive in a gap of parameter space values close to $\Lambda_{\rm UV} \sim 500$ GeV-2 TeV and $\Lambda_{\rm IR} \sim 0.1-0.5$ GeV. We find that both future neutrino experiment DUNE-MPD and dedicated LLP experiment SHiP would remarkably fill this gap in the Z portal DS parameter space. These gaps were due to trigger and event selection requirements.

So far we have only considered decay through the Z-portal, but the decay can also proceed through the Higgs portal. Before proceeding with that, a couple of comments about the interplay of the quantum numbers of LDSPs and the relevant decay portals is in order. According to the Landau-Yang theorem [323, 324], a massive spin-1 particle cannot decay into two massless spin-1 particles. This implies that if the LDSP is a spin-1 particle then for values of $\Lambda_{\rm IR} < 2m_e$, it will not decay into any visible SM particles, so that the only signal is a missing energy. If instead the LDSP is a spin-0 particle, there is no such condition. However for such small values of $\Lambda_{\rm IR}$, the LDSPs are too long lived and cannot be efficiently constrained at the experiments considered here. For this reason it's crucial to realize that while production from the Higgs portal is very suppressed, it might be relevant for decays if its the only available decay mode. We should clarify that if multiple portals are available for decay, one has to consider the dominant one. When considering the LDSP decay through the Higgs portal, we are assuming it to be dominant compared to other portals. Note that a spin-1 LDSP cannot decay through the Higgs portal due to quantum numbers.

In the bottom row of Fig. 3.8 we show the bounds where the LDSP decay occurs through the $\Delta = 4$ Higgs portal. The longer lifetime of the LDSPs, due to a very small coupling to leptons and the extra $\Lambda_{\rm IR}^2/m_h^2$ suppression factor, effectively shifts the exclusion regions to higher $\Lambda_{\rm IR}$ regions. However, bounds from such values of $\Lambda_{\rm IR}$ can be suppressed due to being too close to the edge of allowed phase space, effectively chopping off the bounded region. This makes these bounds typically weaker than colliders, in their $\Lambda_{\rm UV}$ reach, although they still cover regions unconstrained by Z portal decays at higher $(\Lambda_{\rm IR}/\Lambda_{\rm UV})$ ratio.

Finally, for completeness, we will now tabulate constraints coming from invisible meson decays where the LDSP is long-lived enough to escape detectors. Overall, we find that these bounds are weaker in their $\Lambda_{\rm UV}$ reach than the ones coming from both LHC and neutrino detectors.

For the Z portal (both production and decay), the strongest constraints from invisible meson decay come from flavour changing decays of B and K mesons (updated w.r.t ref. [76]). We take the BaBAR upper limit for $B^+ \to K^+$ decays [325]: $\mathcal{B}(B^+ \to K^+ \bar{\nu}\nu) < 1.6 \times 10^{-5}$, which gives

$$\begin{aligned} \frac{\Lambda_{\rm UV}}{\rm GeV} &> 60\,(\kappa_J^2\, c_J)^{1/4}, \\ \frac{\Lambda_{\rm IR}}{\rm MeV} &\ll 108\,(\kappa_J^2 c_J)^{-0.2}\,\text{(weak)}\,, \quad 65\,(\kappa_J^2 c_J)^{-0.2}\,\text{(strong)}\,. \end{aligned} \tag{3.36}$$

The Belle-II experiment put constraints on the same invisible decay. Current bounds are comparable to the BaBAR one [326], while prospects with the full run datasets (50ab^{-1}) will improve by roughly a factor of 5 the $\Lambda_{\rm UV}$ bound, making it still weaker than the ones from beam dumps.

For the case of $K \to \pi + \text{DS}$, we take the upper limit from the NA62 Collaboration [327]: $\mathcal{B}(K^+ \to \pi^+ + \bar{\nu}\nu) < 1.06 \times 10^{-10}$ which gives

$$\begin{aligned} \frac{\Lambda_{\rm UV}}{\rm GeV} &> 68.8\,(\kappa_J^2\, c_J)^{1/4}\,, \\ \frac{\Lambda_{\rm IR}}{\rm MeV} &\ll 83\,(\kappa_J^2 c_J)^{-0.2}\,\text{(strong)}\,. \end{aligned} \tag{3.37}$$

The bounds for a weakly coupled DS are similar. For the case in which the LDSP decay is via $\Delta_{\mathcal{O}} = 4$ Higgs portal instead, the bounds for the B and K meson decays respectively are:

$$\frac{\Lambda_{\rm UV}}{\rm GeV} > 60\,(\kappa_J^2\, c_J)^{1/4},\ \text{for}\ \frac{\Lambda_{\rm IR}}{\rm GeV} \ll 1.6\,(\kappa_J^2 c_J)^{-0.14}\,, \tag{3.38}$$

$$\frac{\Lambda_{\rm UV}}{\rm GeV} > 68.8\,(\kappa_J^2\, c_J)^{1/4},\ \text{for}\ \frac{\Lambda_{\rm IR}}{\rm MeV} \ll 77\,(\kappa_J^2 c_J)^{-0.14}\,. \tag{3.39}$$

In the above, the condition on $\Lambda_{\rm IR}$ has been calculated assuming a strongly coupled DS, and they do not change significantly for the weakly coupled case.

The invisible decays from J/ψ which have been searched for by the BES Collaboration [328] set an upper limit on $\mathcal{B}(J/\psi \to \bar{\nu}\nu) < 7.2 \times 10^{-4}$. However, we found the resulting bound on $\Lambda_{\rm UV}$ to be weaker than those coming from the BaBar and NA62 limits on B, K decays, and we do not report it here.

A preliminary study of FASER and SND, using an integrated luminosity of $\mathcal{L} = 150\ \text{fb}^{-1}$ and 3 signal event exclusion, shows that the exclusion power of these experiment comes mostly from the decays of SM forward object like mesons or on-shell Z, whose spectra can be taken from the FORESEE package [329]. For the decay through Z portal, the bounds are comparable to DUNE but are in a slightly different $\Lambda_{\rm IR}$ region due to a different boost, and a different distance at which the detectors are located, while for decays through Higgs portal ($\Delta = 4$) they can improve the bounds up to $\Lambda_{\rm UV}$ 1 TeV: this is because for resonant production through Z portal, $p_{\rm DS}^2 \simeq m_Z^2$, allowing for larger LDSP masses to be produced and tested. Future

experiments like FASER2 can exclude up to 10 TeV given the larger luminosity and the dimensions of the detector, compared to its predecessor. These will be studied in detail in a future work, together with other experiments at the lifetime frontier such as MATHUSLA and CODEX-b.

3.4.2 JJ Portal (Z-aligned) Production

Even though the Z-aligned JJ portal and Z-portal are equivalent at neutrino experiments after an appropriate rescaling of the κ, there is a distinction between them at high energy experiments that can produce a Z on-shell. Contrary to Z-portal case, for the Z-aligned JJ portal, the LHC bounds are generally weaker due to the lack of resonant production and EFT consistency condition on $\Lambda_{\rm UV}$. For the same reason, there is no bound coming from Z-width. In this scenario, the bounds on $\Lambda_{\rm UV}$ come only from LEP missing energy searches (see fig. 8 in ref. [76]). Therefore regions in the parameter space with too short lifetimes are not tested due to the requirement for the LDSP to decay outside the detector. On the other hand, the bounds coming from high-intensity experiments such as neutrino experiments are essentially unchanged with respect to the Z-portal case, so that all the discussion from before applies: they are able to exclude a larger portion of $\Lambda_{\rm UV}$ by roughly one order of magnitude in the large lifetime region (low $\Lambda_{\rm IR}$), compared to the LEP/LHC detector size, while it excludes a completely unexplored region at small lifetime (or large $\Lambda_{\rm IR}$).

3.4.3 JJ Portal (generic) Production

The previous sections can give us an insight on how high-intensity experiments can put a bound on a generic $J^{\rm SM}_\mu J^\mu_{\rm DS}$ portal, where $J^{\rm SM}_\mu$ is a generic flavor-conserving SM current. Missing-energy bounds coming from LHC will still hold provided $\mathcal{O}(1)$ couplings to light quarks, although as explained in the previous section they are limited by the EFT condition. If these are absent, (e.g. for $\bar{e}\gamma^\mu e\, J^{\rm DS}_\mu$ portal) the leading bounds come from LEP mono-photon searches ($\Lambda_{\rm UV} \gtrsim 10^2$ GeV for $\Lambda_{\rm IR} \lesssim$ 100 MeV), while electron beam dump experiments like E137 and missing energy searches at NA64 put weaker bounds, see ref. [76].

Proton-beam based neutrino experiments cannot probe hadrophobic current interactions given that couplings to quarks are essential for all production modes. Since neutrino experiments typically exclude LDSP masses for $\Lambda_{\rm IR} \lesssim 2m_\pi$, if the decay proceeds through generic JJ portal, we need non-zero couplings to electrons. If that is small, the Higgs portal may be relevant depending on couplings. This feature is not present in missing energy searches at high energy colliders and high intensity experiments, which only probe the production mode. This problem can be circumvented if instead of looking at displaced vertex signatures (where LDSP decays inside the detector), in which both DS production and DS decay into SM are required, scattering events are also considered. As mentioned in previous sections, we do not look at such signatures due to the extra assumptions needed with respect to LDSP decays.

We remark that no big difference is expected from changing the axial or vector nature of the SM current as long as their coupling is of the same order. While for Z portal the axial contribution to bremsstrahlung is larger than the vector counterpart, due to the accidentally small coupling of the vector component, this is not necessary for a generic case. A similar argument also hold for DY mode, while for MD mode the quantum numbers of the SM current select the relevant meson processes (see App. G.2 for details). To conclude, as long as DS has a coupling to proton and electrons in $J^{\mu}_{\rm SM}$, we expect the results to not change dramatically at fixed magnitude of the couplings: the bounds presented in Sec. 3.4.1 apply.

3.4.4 Higgs Portal Production

The bounds at neutrino experiment for production through $\Delta_{\mathcal{O}} = 4$ Higgs portal $\mathcal{O}H^{\dagger}H$ are very weak: assuming decay through Z portal $\Lambda_{\rm UV} \ll 10^2$ GeV for DB and DY modes since these modes are suppressed by a small Higgs coupling. Only radiative meson decays happening through a top loop do not suffer from such a problem. The strongest bounds for this case then come from meson decay K $\to$ DS where for DUNE-MPD, we get $\Lambda_{\rm UV} \lesssim 12$ GeV. This exclusion is much weaker than the bounds coming from missing energy searches at LHC and Higgs coupling fits [76], $\Lambda_{\rm UV} \gtrsim 450$ GeV. For $\Delta \geq 4$ the rate is suppressed with respect to the Z portal as explained in Sec. 3.2.1. The situation is slightly improved for high-energy beam experiments like SHiP (where $\Lambda_{\rm UV} \lesssim 74$ GeV is excluded for the B $\to$ K + DS meson decay), but is still not competitive with the ones coming from Higgs resonant production at LHC. For this reason, we do not show any plots for production through the Higgs portal.

For a $\Delta_{\mathcal{O}} = 3$ Higgs portal, at DUNE-MPD, K $\to$ DS decay gives the leading bound, $\Lambda_{\rm UV} \lesssim 540$ GeV. At SHiP, we find that the leading bounds come from B $\to$ K + DS decays which give $\Lambda_{\rm UV} \lesssim 10$ TeV for $\Lambda_{\rm IR} \sim 1.8 - 2.8$ GeV. The DUNE-MPD bounds are weaker than the LHC missing energy searches (which exclude $\Lambda_{\rm UV} \lesssim 8$ TeV) whereas the SHiP bounds are stronger.

The forward experiment FASER does not put strong constraint on DS production and decay through resonant Higgs portal. Only FASER2, due to a higher luminosity and geometric acceptance, can put bounds that are comparable with the conventional LHC searches in a narrow lifetime regions: up to $\Lambda_{\rm UV} = 10$ TeV for $\Delta = 3$, while up to $\Lambda_{\rm UV} = 1$ TeV for $\Delta = 4$.

3.5 Summary and Discussion

Secluded sectors that interact very feebly with the SM have the potential to be probed at the high-intensity frontier, particularly at neutrino experiments (as has been previously explored in refs. [217, 219, 251, 330], see also refs. [317, 318]). Most of the past work has focused on the case of relevant portals, while the case of irrelevant portal DS scenario has only recently been explored [75, 76, 235, 302]. In this work, we have considered the sensitivity of DS that interacts with SM through a dimension 6 irrelevant portal, at past and current neutrino experiments, and its

prospective discovery in both existing and future neutrino experiments based on proton beams.

We have performed a detailed study of the possible production mechanisms of DS through non-renormalizable portals: meson decays ($M \to m + \text{DS}$, $V \to \text{DS}$), direct partonic production ($\bar{q}q \to \text{DS}$, $gg \to \text{DS}$), and dark bremsstrahlung ($pp \to \text{DS}+X$). The interplay between the various production mechanisms as a function of the DS invariant mass squared p^2_{DS} can be summarized in the plot shown in Fig. 3.1. Compared to previous works on irrelevant portals, we have added production details, and also considered strongly coupled dark sectors, and done so in a model agnostic framework. Further, we have constrained such dark sectors using past and current analyses at beam dump/neutrino experiments, also showing projections for prospective searches at existing and future neutrino experiments. In order to emphasize the importance of these bounds, we have also compared our results with previous bounds on such portals.

In an earlier work of this scenario [76], the most stringent bounds on DS excitations produced from the decay of Z bosons was set by LHC monojet searches [311] and LHC displaced vertex search [312, 313], in a range of $(\Lambda_{\text{UV}}, \Lambda_{\text{IR}})$ values dictated by various factors such as the energy of the experiment and the lifetime of the DS etc. In the present work, we have tried to address the question if neutrino experiments, being placed farther from the interaction point (as compared to say the ATLAS detector at LHC) could probe a lower Λ_{IR} range, thereby testing a complementary parameter space with respect to high energy colliders for such elusive dark sectors. Our main summary plots can be found in fig. 3.8.

While the present work focuses on the utility of neutrino experiments for probing dark sectors, we would like to mention the status of other probes of the dark sectors considered here, for completeness. Colliders and beam-dump probes produce the DS states directly. Other setups that also produce DS states directly result in astrophysical bounds from Supernova cooling, from lifetime of horizontal branch stars and from positronium lifetime. Due to kinematics, bounds coming from astrophysical objects such as Supernovae can't probe the $\Lambda_{\text{IR}} \gtrsim 100$ MeV given the lower typical temperature. Therefore they are subleading in the region in which neutrino experiments are competitive with respect to LHC bounds, and we will not show them. However in the much lower Λ_{IR} regime, they can become the most competitive bounds, as can be seen for example by recasting the results of [331]. Complementary to those are indirect probes where the initial and final states are SM states, and DS degrees of freedom propagate internally. Examples of such probes are electroweak precision tests (EWPT), fifth-force constraints, torsion balance experiments, molecular spectroscopy, etc. Depending on the process, these indirect probes are UV sensitive (and in that case they do not probe the dark dynamics directly) or give weaker constraints. A careful analysis of all these direct and indirect effects was already carried out in ref. [76] and we refer the reader to there.

In this work, for the case of Z portal DS production, we find that past analyses and prospective DS searches at current neutrino experiments give weaker bounds when compared with the current bounds from LHC and LEP in resonant production sce-

narios. However, future neutrino experiments such as DUNE-MPD would improve on this, and will be sensitive to $\Lambda_{\rm IR}$ in the range $0.1 - 1$ GeV for $\Lambda_{\rm UV} \sim 1$ TeV. The current displaced vertex searches at LHC are already probing $\Lambda_{\rm UV}$ as high as few TeVs, but only in the $\Lambda_{\rm IR}$ range $\sim 0.6 - 2.5$ GeV for the strongly coupled DS case. The ATLAS DV searches lose sensitivity in the range of $\Lambda_{\rm IR} \sim 0.1 - 0.6$ due to trigger requirements (as can be seen from the gap on the right plot in Fig. 3.8).[13] Future neutrino experiment DUNE-MPD will have a unique sensitivity to access this gap in the parameter space for a range of $\Lambda_{\rm IR} \sim 0.1 - 1$ GeV for $\Lambda_{\rm UV}$ of a few TeVs.

We have also compared these results with projections from the proposed experiment SHiP which serves as a benchmark for LLP experiments. As can be seen from Fig. 3.8, SHiP will improve on the reach of DUNE-MPD by probing $\Lambda_{\rm UV}$ of few TeVs for a range of $\Lambda_{\rm IR} \sim 0.1 - 2$ GeV. This is mainly due to its higher proton beam energy of 400 GeV and larger geometric acceptance ($\epsilon_{\rm geo} \sim 1$ for the production modes bremsstrahlung and DY and $\epsilon_{\rm geo} \sim 0.1 - 0.9$ for K and J/ψ decays).

As we have described in the previous section, we can recycle our bounds at neutrino experiments on Z portal also for the case of $J^{\rm SM}_\mu J^\mu_{\rm DS}$ portal where $J^{\rm SM}_\mu = \bar{f}\gamma_\mu f, \bar{f}\gamma_\mu\gamma^5 f, f = l, q$. The earlier work in [76] found no bounds from LHC for this portal, once EFT considerations were taken into account. The only constraint presented is the one for $J^{\rm SM}_\mu = \bar{e}\gamma_\mu e$ from monophoton searches at LEP (see fig. 8 in ref. [76]) where the excluded space is restricted to $\Lambda_{\rm UV} \lesssim 200$ GeV for $\Lambda_{\rm IR} \lesssim 0.1$ GeV. These bounds are much weaker than the bounds we get at neutrino experiments. Therefore neutrino experiments are a useful tool to study DS that do not directly mix with the Z and that are not enhanced by resonant production at colliders. We have already explained how our Z portal bounds can be recycled for a JJ portal, since a JJ portal can be obtained from Z portal after integrating out Z mediator.

For the case of the Higgs portal $\mathcal{O}H^\dagger H$ production (for $\Delta_\mathcal{O} = 4$) the bounds from neutrino experiments are very weak, and are limited to values of $\Lambda_{\rm UV}$ much below the electroweak scale. Whereas, in comparison, bounds from Higgs resonant production derived in ref. [76] coming from missing energy and displaced vertex searches at high energy colliders are much stronger.

The bounds presented here are derived under a model agnostic approach, and are applicable to a large class of DS models (see [76] for explicit examples). Knowledge of the underlying dark dynamics can be used to study other possible signatures like DS scatterings with SM particles, but will need to be done on a case-by-case basis, and hence is out of the scope of this work. We have discussed in detail our assumptions and limitations of our approach in Sec. 3.1. Our results are conservative and can be improved if the full theory is defined explicitly. Despite this, we claim that our approach can be very useful in giving a qualitative picture.

[13] The trigger requirements imposed in [76] depend on the $n_{\rm LDSP}$ distribution. Events where the number of LDSPs produced has a downward fluctuation can loosen the cut, but will also affect the total cross-section, the decay probability and the geometric efficiency. Including this effect systematically will reduce the un-probed region but not entirely.

The point of this work is to convey the usefulness of a model agnostic approach to exploring dark sectors, and the potential of neutrino experiments (both current and future) as unique probes of irrelevant DS-SM portals. Future proposed LLP experiments at LHC interaction points like MATHUSLA, CODEX-b, ANUBIS are designed to improve reach on $\Lambda_{\rm IR}$ scales for such elusive DS. However, future neutrino experiment DUNE Multi-Purpose Detector (MPD) [300] running at the LBNF (Long Baseline Neutrino Facility) would probe low $\Lambda_{\rm IR}$ scales in a shorter timescale. The forward LHC detectors like FASER and SND (see [332] for a recent status report), built for searching feebly interacting particles would be taking data during the LHC Run 3, and could also give useful bounds for our DS. We hope our study would motivate analyses of neutrino-detector data for the search of such elusive dark sectors.

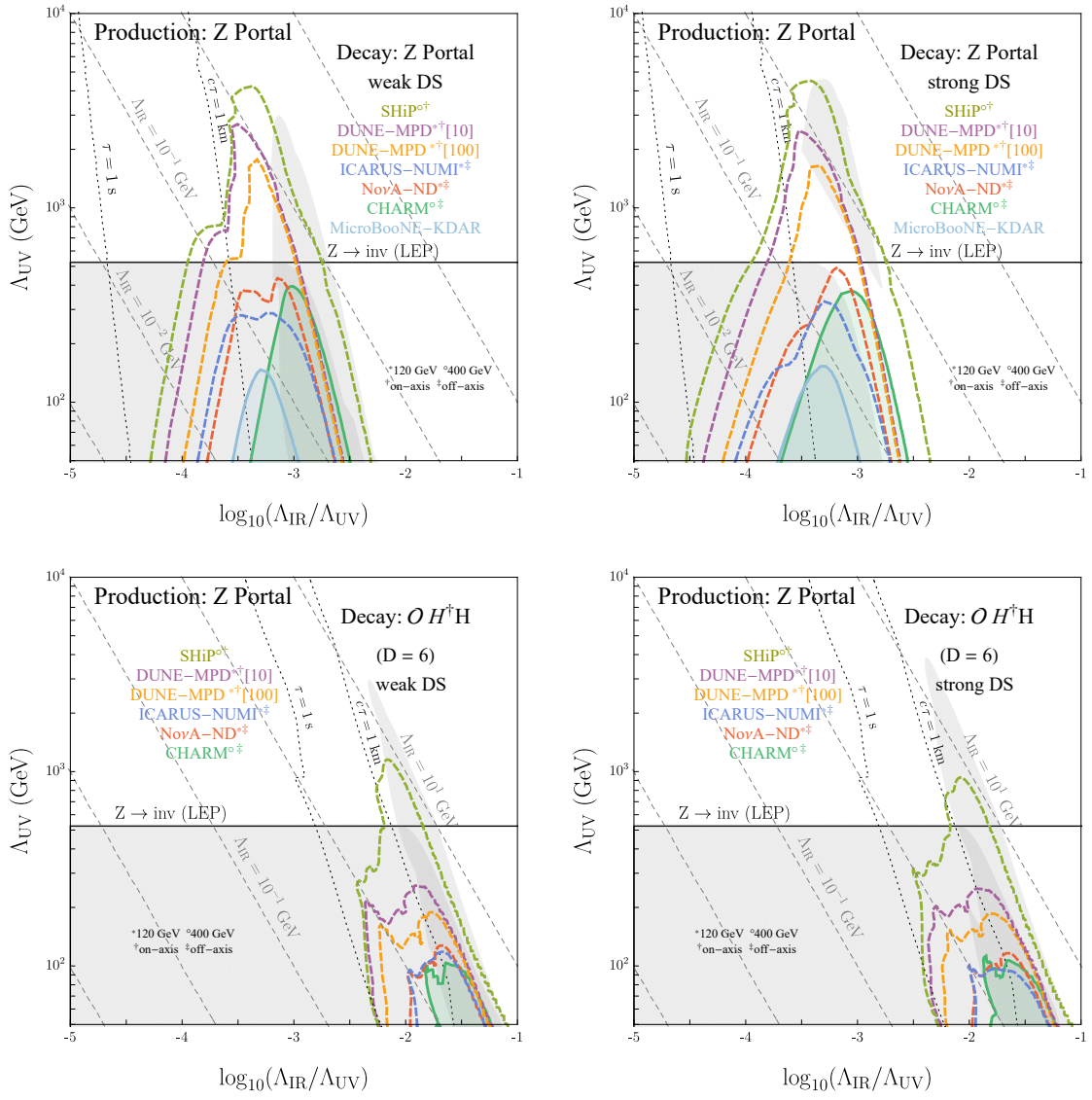

Figure 3.8: *Constraints on DS production through the $D = 6$ Z portal, and decay through the same Z portal (top), or through $D = 6$ $\mathcal{O}H^\dagger H$ portal (bottom), at various neutrino experiments. We have shown both the 10 event and the 100 event lines for DUNE. For comparison, bounds from high-energy colliders (obtained in ref. [76]) are also shown in gray. The left (right) plots assume weakly coupled (strongly coupled) dark dynamics. The exclusion from the Z invisible width measurement at LEP is shown by the horizontal solid black line. We restrict to $\Lambda_{UV} > 50$ GeV for EFT validity. All plots assume $\kappa_i^2 c_i = 1$, where i labels the portal, κ is the portal coupling and c is a measure of degrees of freedom of the DS.*

Chapter 4

Probing self-interactions with cosmology

In this Chapter we discuss the worst scenario: the one in wich there is no sizable interaction between the SM and the Dark Sector. As already anticipated, the idea is that the visible matter distribution tracks the DM one. The presence of Dark Matter self-interactions can modify how DM clumps with respect to the case in which the clustering is due to only gravitational interactions. In turn, these modifications of how DM clumps will be imprinted on how visible matter clumps evolve. With this idea in mind, we would like to understand, both qualitatively and quantitavely, what can be said about the nature of DM self-interactions with cosmological data. In order to do so, we must pick a model. We start from the simplest model possible to get a grasp of the physics: scalar DM particles χ interacting via a new scalar field ϕ. This allows both for an analytic and numerical understanding of the evolution of the DM perturbations. In [83] this program was started by studying how self-interacting DM affects observables on *linear* scales ($k \lesssim 0.1\,h/\mathrm{Mpc}$), such as CMB anisotropies [23]. The result is that a new attractive long range force is excluded if its strenght is more than roughly a few percent the strength of gravitational interactions. Here linearity refers to the regime in which the fluctuations δ around the homogenous background are small, and in which different modes evolve separately.

Potentially, the bound can be made stronger if additional data is considered. Cosmic Large Scale Structures (LSS) are a complementary source of informations on the cosmological history with respect to CMB. However, the scales involved are also non-linear. In this regime different fluctuation modes start to interact non-negligibly gravitationally, and it is not straightforward to get correct theoretical predictions. In order to model mildly non-linear scales ($0.1\,h/\mathrm{Mpc} \lesssim k \lesssim 0.3\,h/\mathrm{Mpc}$) we employ the so-called *Effective Field Theory of Large Scale Structure* (EFTofLSS) [88, 89, 334, 335, 336, 337, 338, 339, 340, 341]. The idea behind the EFTofLSS is to smooth the fluctuations over a short length Λ^{-1}. In this way only long modes are kept in the theory. The effect of the short modes over the evolution of the long ones is encapsulated in counterterms that modify the standard perturbation equations. The cutoff dependence disappears in physical observables when all the

possible counterterms allowed by symmetries are kept, while the finite contribution is fitted from the data. The outlined procedure has the advantage of being more systematic compared to other approaches to perturbation theory, in which for example long modes get contributions from short modes that are not under control in said approaches. Within this EFT framework it is possible to obtain a reliable prediction for the distribution of DM and ordinary matter at smaller scales. However these are not quantities that are directly measured by LSS experiments like galaxy surveys. Indeed these experiments measure the distribution of galaxies. In order to describe these collapsed objects we employ a *bias expansion* [85, 336]. Biases are a way to express the "composite" field of galaxy densities as a function of the fundamental fluctuations of baryons and DM. They are essentially the response function of short, collapsed modes to long wavelength ones, and like the counterterms their values are fitted from data (although it is possible to get a reasonable etimates from numerical simulations or phenomenological models of the collapse).

This Chapter is organized as follows: in Sec. 4.1 we introduce the framework and the models for self-interactions. In Sec. 4.2 we recap the results of the previous work done by collaborators [83], in which they set bounds on the self-interaction via linear cosmology (*e.g.* CMB data from Planck). In Sec. 4.3 we report part of our on-going work [342], in which we set bounds using non-linear cosmology. In particular we focus on data collected from past and future *galaxy surveys*, such as BOSS [3] and Euclid [84]. The observables that we discuss are the galaxy power spectrum, extended at 1-loop to better model small scales $k \gtrsim 0.1\,h/\text{Mpc}$, and the galaxy bispectrum. In Sec. 4.4 we summarize the results and comment on future directions.

4.1 Modeling a Dark Fifth Force

In order to describe the presence of a self-interaction, we specify a microscopic model, as done in [83]. We will start from a model with a local interactions between the scalar DM field mediated by a scalar field ϕ:

$$\mathscr{L} = -\frac{1}{2}\partial_\mu\chi\partial^\mu\chi - \frac{1}{2}m_\chi^2\chi^2 - \frac{1}{2}\partial_\mu\phi\partial^\mu\phi - V_\phi(\phi) - V_{\text{int}}(\phi)\chi^2 \tag{4.1}$$

This lagrangian can be written in terms of a dimensionless field s:

$$\mathscr{L} = -\frac{1}{2}\partial_\mu\chi\partial^\mu\chi - \frac{1}{2}m_\chi^2\chi^2 - \frac{1}{2G_s}\partial_\mu s\partial^\mu s - V_s(s) - V_{\text{int}}(s/G_s^{1/2})\chi^2 \tag{4.2}$$

where

$$s = G_s^{1/2}\phi\,, \quad V_\phi(\phi) = V_s(s)\,. \tag{4.3}$$

Here G_s is the analogue of the Newton constant G_N, that sets the strength of the self-interaction. Its definition follows from requiring the interaction to be equal to

$$V_{\text{int}}(\phi)\chi^2 = m_\chi^2 V_{\text{int}}(s)\chi^2 \equiv m_\chi^2 f(s)\chi^2\,. \tag{4.4}$$

It is useful to define a dimensionless quantity β that describes the relative strength of the self-interaction with respect to gravity:

$$\beta \equiv \frac{G_s}{4\pi G_N} \,, \tag{4.5}$$

where G_N is Newton constant. We always assume that the metric $g_{\mu\nu}$ of the universe is a small perturbation around the homogeneous universe described by the FLRW metric:

$$\mathrm{d}s^2 = -\left(1+2\Psi(\vec{x},t)\right)\mathrm{d}t^2 + a(t)^2\left(1+2\Phi(\vec{x},t)\right)\delta_{ij}\mathrm{d}x^i\mathrm{d}x^j \,, \tag{4.6}$$

where we employed the Newtonian gauge.

It can be shown [83] that the lagrangian of Eq. (4.1) can be matched to a particle lagrangian for χ, leading to the following action:

$$S_\chi = -\int \mathrm{d}\lambda \; m_\chi(s)\sqrt{-g_{\mu\nu}\frac{\mathrm{d}x^\mu}{\mathrm{d}\lambda}\frac{\mathrm{d}x^\nu}{\lambda}} \,. \tag{4.7}$$

As can be seen, the model is equivalent to one in which the mass of the particle varies as a function of the value of the (space-time dependent) field s. The specific relation between $m_\chi(s)$ and $V_{\rm int}$ will be discussed later. This observation allows to work with thermodynamics quantities like the DM number density n_χ, its pressure p_χ and energy density ρ_χ. This change in variables can be done by taking moments of the Vlasov equation for the phase space density f_χ of DM particles χ:

$$\frac{\partial f_\chi}{\partial t} + \frac{\mathrm{d}x^i}{\mathrm{d}t}\frac{\partial f_\chi}{\partial x^i} + \frac{\mathrm{d}p^i}{\mathrm{d}t}\frac{\partial f_\chi}{\partial p^i} = 0 \,. \tag{4.8}$$

The first two moments, obtained by multiplying by E and p^i Eq. (4.8) and integrating over the momenta gives the following set of equations for χ [83]:

$$\begin{aligned} &\dot{\rho}_\chi + 3(H+\dot{\Phi})\rho_\chi + \frac{1}{a}\partial_i(\rho_\chi v^i_\chi) - \dot{s}\frac{\partial \log m_\chi(s)}{\partial s}\rho_\chi \,, \\ &\dot{(\rho_\chi v^i_\chi)} + \frac{1}{a}\partial_j\Sigma^{ij} + 4H\rho_\chi v^i_\chi + \frac{\rho_\chi}{a}\partial^i\Psi + \frac{\rho_\chi}{a}\frac{\partial \log m_\chi(s)}{\partial s}\partial^i s \,, \end{aligned} \tag{4.9}$$

where we have defined the energy density, velocity and second moment respectively as:

$$\begin{aligned} \rho_\chi &\equiv \int \frac{\mathrm{d}^3p}{(2\pi)^3} E f_\chi \,, \\ v^i_\chi &\equiv \frac{1}{\rho_\chi}\int \frac{\mathrm{d}^3p}{(2\pi)^3} p^i f_\chi \,, \\ \Sigma^{ij} &\equiv \int \frac{\mathrm{d}^3p}{(2\pi)^3}\frac{p^ip^j}{E} f_\chi \,. \end{aligned} \tag{4.10}$$

We will see that in linear theory Σ^{ij} can be neglected for a CDM-like candidate, thus closing the Boltzmann hierarchy, while it will be important in non-linear computations.

Unlike χ, we will treat s as a field, and solve its second-order field equations to find how it evolves. Notice that the evolution of s is crucial to describe the evolution of DM perturbations since it changes the mass and therefore the geodesics of χ particles.

There are several scenarios that can be studied in this setup. For example, the field s can make up for a sizable fraction of the univere energy budget today, both in the form of CDM if it oscillates quickly ($m_\phi > H_0$), or of Dark Energy ($m_\phi \simeq H_0$). We focus on the simpler case in which the role of s is only to mediate the self-interaction, and in which its energy budget today is negligible. This allows to more clearly understand the role of the self-interaction in the growth of DM perturbations, and hence how cosmological structures are affected by it. In particular, this allows to simplify the equations and to neglect completely V_s. We dub this scenario "Fifth force" (5F). For the sake of definiteness, we will always fix $m_\phi = 0.1H_0$, but what we say is independent on the precise value of m_ϕ as long as it is much smaller than H_0.

To proceed with the study we have to specify a model. We will start with the simplest functional form, the Yukawa interaction, which written in terms of the original lagrangian reads:

$$V_{\rm int} = g_D m_\chi \phi \chi^2 \,, \tag{4.11}$$

where g_D is a dimensionless coupling (we have normalized it with respect to the relevant scale). Written in term of the dimensionless field, Eq. (4.11) becomes:

$$V_{\rm int} = m_\chi^2 s \chi^2 \,, \tag{4.12}$$

from which we see the relation between G_s and the microscopic couplings in this specific case (for generic interactions it follows a similar relation):

$$G_s = \frac{g_D^2}{m_\chi^2} \,. \tag{4.13}$$

We will see that many things that can be said about this interaction translate directly to other possible interactions in the 5F regime.

The Yukawa interaction has the property to always be attractive. Unlike forces mediated by vector fields, it does not suffer from screening effects. Also, since we are neglecting V_s, the mediator is massless. Hence DM particles will experience an extra coulombian force inside the horizon. Therefore this setup highlights the maximum possible effects of self-interactions.

We anticipate that the bounds are strong, leading to constraints on $\beta < 10^{-2}$. This justifies a perturbative treatment around $\beta = 0$ of the evolution equations, of both the homogeneous backgrounds and of the perturbations. Once that we specified the model, we can proceed to solve the evolution for the homogeneous background and the perturbations around it.

4.2 Linear cosmology

The first thing to do is to analyze the evolution of the spatially homogeneous backgrounds in the 5F regime. The Equations of Motions (EoMs) are obtained from Eq. (4.9) and Eq. (4.1) assuming a homogeneous FLRW background. This gives the following equation for the background DM energy density $\bar{\rho}_\chi$:

$$r\bar{h}o'_\chi + 3\mathcal{H}\bar{\rho}_\chi = \bar{\rho}_\chi \frac{\partial \log m_\chi(s)}{\partial s}\bar{s}' \ , \tag{4.14}$$

where $'$ indicates derivatives with respect to the conformal time $\tau = at$ and $\mathcal{H} = a'/a$ is the conformal Hubble parameter. From this point, we will omit the argument of m_χ, and we will always imply to be evaluated to the background value $\bar{s}$.

Similarly, we can find the evolution equation for the fifth force background $\bar{s}$:

$$\bar{s}'' + 2\mathcal{H}\bar{s}' + G_s a^2 \bar{\rho}_\chi \frac{\partial \log m_\chi(s)}{\partial s} \ , \tag{4.15}$$

where we neglected a piece depending on V_s. Given the ubiquity of the derivative of the m_χ, it's useful to define the following abbreviation:

$$\tilde{m} \equiv \frac{\partial \log m_\chi(s)}{\partial s} \ . \tag{4.16}$$

We recall that for a Yukawa interaction, the following holds:

$$m_\chi(s) = m_\chi\sqrt{1+2s} \to \tilde{m} = \frac{1}{1+2s} \ . \tag{4.17}$$

With Eq. (4.15), Eq. (4.15) we can solve for the background, provided we give enough initial conditions. In the 5F regime, s will not contribute to today's energy budget. We will set its initial value $\bar{s}_{\rm ini} = 10^{-4}$: we will see that for Yukawa interactions having a small starting value for $\bar{s}_{\rm ini}$ gives the desired results regardless of its precise value. Notice that in the small s limit, the effect of the field on the dynamics of χ does not vanish:

$$s \to 0 \Rightarrow \tilde{m} \to 1 \ . \tag{4.18}$$

This suggests that the evolution equations of χ will be affected even in the small s limit in a non-negligible way. The Hubble constant H_0 and the normalized energy density Ω_i^0 of the other fields (i=baryon, photons, neutrinos) are set to their value today. Initializing Ω_χ^0 actually presents a subtlety: indeed for other species (photons, neutrinos, baryons) knowing $\Omega_{0,i}$ is equivalent to the knowledge of their values at the initial time when the scale factor of the universe was $a_{\rm ini}$, at which we start solving the equation. This because the redshifting behaviours of the species are known as a function of a. For the self-interacting DM χ this is not true because how it redshifts depends on the value of s. Its reduced normalized energy density redshifts according to:

$$\frac{\omega_\chi(a)}{\tilde{\omega}_\chi} = \frac{m_\chi(\bar{s})}{m_\chi(\bar{s}_{\rm ini})} a^{-3} \ , \tag{4.19}$$

which is found by solving Eq. (4.14) and remembering the relation between ρ_χ and n_χ. In order to bypass this problem we initialize the energy density of χ using a dummy variable $\tilde{\omega}_d$:

$$\omega_\chi(a_{\rm ini}) \equiv \omega_\chi^{\rm ini} = \tilde{\omega}_d a_{\rm ini}^{-3} \ . \tag{4.20}$$

Similar expressions hold for $\tilde{\Omega}_d$, defined as $\tilde{\omega}_d/h^2$.

Once this is known, the value of the Cosmological Constant (CC) Λ is found via the closure condition $\sum_i \Omega_i^0 = 1$.

Now we can solve the background equations. We will put emphasis on the evolution of $\bar{s}$. This because it will allow us to make contact for the various possible interactions $f(s)$. Notice that in the absence of interactions with χ, or equivalently $\beta = 0$, $\bar{s}$ is constant (the decreasing solutions is discarded, as customary in cosmology). We start in the early universe, in an epoch of Radiation Domination (RD), followed by an epoch of matter domination (MD). This is beacuse throughout the cosmological history, given the setup, the energy of s is always negligible.

$$\begin{aligned} &\text{RD}: \qquad \mathcal{H} = 1/\tau \ , \quad a = \sqrt{\Omega_r^0} H_0 \tau \ . \\ &\text{MD}: \qquad \mathcal{H} = 2/\tau \ , \quad a = \frac{\Omega_m^0 H_0^2 \tau^2}{4} \ . \end{aligned} \tag{4.21}$$

where we are already setting the behaviour of the background quantities at their 0-th order value in β: at this order perturbatively β enters only in the last addendum of the modified Klein-Gordon equation, as seen in Eq. (4.15), and the 0-th order solution of $s = \bar{s}_{\rm ini}$ does not modify in this regime the evolution of other background quantities. We can solve Eq. (4.15) perturbatively by setting $\tilde{m}$ to a constant value. Under this assumption we can solve in the two regimes (RD and MD) and match them at equality time:

$$\tau_{\rm eq} = (\sqrt{2} - 1) \frac{2\sqrt{\Omega_r^0}}{H_0 \Omega_m^0} \ . \tag{4.22}$$

We get the following solutions:

$$\begin{aligned} &\text{RD}: \qquad \bar{s} \equiv \bar{s}_{\rm ini} - \frac{3}{4} \tilde{m} \frac{\tilde{\Omega}_d}{\sqrt{\Omega_r^0}} H_0 (\tau - \tau_{\rm ini}) \ , \\ &\text{MD}: \qquad \bar{s} = \bar{s}_{\rm eq} - 2\beta \tilde{m} f_\chi \log \frac{\tau}{\tau_{\rm eq}} \ , \end{aligned} \tag{4.23}$$

where $\Omega_r^0 = \Omega_\gamma^0 + \Omega_\nu^0$ if neutrino masses are neglected, $_{\rm eq}$ indicates quantity at equality and

$$f_\chi \equiv \frac{\bar{\rho}_\chi}{\bar{\rho}_m} \simeq \frac{\tilde{\Omega}_d}{\tilde{\Omega}_d + \Omega_b^0} \ , \tag{4.24}$$

where m, b indicates total non-relativistic matter and baryon respectively. Incidentally this tells the natural value of $\bar{s}'_{\rm ini}$ that we use as initial condition of the background equation:

$$\bar{s}'_{\rm ini} = -\frac{3}{4} \beta \tilde{m} \frac{\tilde{\Omega}_d}{\sqrt{\Omega_r^0}} H_0 \ . \tag{4.25}$$

Typically the evolution in RD can be neglected due to the short time the system stays in RD. The peculiarity of this solution is that it is an attractor for small $\bar{s}_{\rm ini}$. Indeed the specific value of $\bar{s}_{\rm ini}$ (and $\tau_{\rm ini}$) can be neglected for large τ. This is a peculiarity of the Yukawa interaction, and does not hold in general.

We are now ready to see what happens for a generic $V_{\rm int}(s)$. Since we expect that $\bar{s}$ will stay small for most of the evolution if $\bar{s}_{\rm ini} \ll 1$, we can expand the interaction operator in powers of s. This implies that what is important for the interaction in the 5F regime is the leading power of f. Hence the most general interaction is[1]:

$$\mathscr{L} \supseteq \frac{m_\chi^2}{2} s^n \chi^2 \,, \qquad\qquad (n \geq 1) \tag{4.26}$$

from which we have

$$m_\chi(s) = m_\chi \sqrt{1+s^n} \to \tilde{m} = \frac{n s^{n-1}}{2(1+s^n)} \,. \tag{4.27}$$

By taking the limit $s \to 0$ in Eq. (4.27), we can see that for $n \geq 2$

$$\tilde{m} \approx \frac{n s^{n-1}}{2} \to 0 \,. \tag{4.28}$$

Therefore in the small $\bar{s}_{\rm ini}$, small β limit the background evolution of χ is the same of the usual non-interacting ΛCDM model. In a sense all the other interaction have the constant zero solution as an attractor for s. This implies that in the 5F regime, only Yukawa interactions (or interactions that at leading order in s are Yukawa-like) can be detected, while the others are effectively undistinguishable from the non-interacting scenario.

The situation is different in the 5F scenario considering the large $\bar{s}_{\rm ini}$ solution. We will not treat this case.

With the solution of s, we can solve for ρ_χ. In MD it gives

$$\omega_\chi(a) = a^3 \tilde{\omega}_d \left(1 - \beta \tilde{m} \log \frac{a}{a_{\rm eq}}\right) \,. \tag{4.29}$$

This tells that DM redshifts faster than CDM: not only the expansion of the universe dilutes the number, it also dilutes s which in turn diminish the value of $m_\chi(s)$.

Analytic solutions are helpful to understand the physics of the system, but in order to get the final bound we will use numerical computations carried out via a suitably modified version of the CLASS code [343, 344]. The two methods are in good agreement.

After having solved the evolution equation for the background we can solve for the perturbations. We will focus only on *adiabatic* perturbations, following the procedure for setting their initial conditions outlined in the original work. These

[1]Notice that asking for the interaction expressed in terms of s to be in this form fixes G_s in terms of the coupling of the Lagrangian expressed in terms of ϕ.

equations are expressed in terms of the energy density contrasts $\delta_i \equiv \delta\rho_i/\bar{\rho}_i$ for all the different species i. It is useful to do the following change of variable:

$$\delta_m \equiv f_\chi \delta_\chi + (1 - f_\chi)\delta_b \ , \qquad \delta_r = \delta_\chi - \delta_b \ , \tag{4.30}$$

and similarly for the velocity perturbations $\vec{v}_m, \vec{v}_r$.

The evolution equation for the overdensities are obtained by expanding the densities around the homogenous backgrounds (see Eq. (4.23), Eq. (4.29) in the continuity and Euler equations. These equations are the first two momenta of the Vlasov equations written in Eq. (4.9). We do not report the details of the computations, referring to [83]. Notice that in order to be able to solve the system, we had to close the Boltzmann hierarchy by neglecting Σ^{ij}. This is a good approximation for the linear regime, however it will play an important role in Sec. 4.3. We focus on MD given that we will be interested in computing observables relevant in such era of cosmological history in later sections. In the subhorizon regime, in which $k/\mathcal{H} \gg 1$, the equations for baryons and χ in MD become a system of coupled equations:

$$\begin{aligned}
&\delta_m' + \theta_m = -\partial_i \left(\delta_m v_m^i\right) \ , \\
&\theta_m' + \mathcal{H}\left(1 - f_\chi \epsilon\right)\theta_m + \frac{3}{2}\Omega_m \mathcal{H}^2 \delta_m \left(1 + f_\chi \epsilon\right) = -\partial_i \left(v_m^j \partial_j v_m^i\right) \ , \\
&\delta_r' + \theta_r = -\partial_i \left(\delta_m v_r^i + \delta_r v_m^i\right) \ , \\
&\theta_r' + \mathcal{H}\theta_r - \epsilon\mathcal{H}\left(\theta_m - \frac{3}{2}\Omega_m \mathcal{H}\delta_m\right) = -\partial_i \left(v_m^j \partial_j v_r^i\right) - \partial_i \left(v_r^j \partial_j v_m^j\right) \ ,
\end{aligned} \tag{4.31}$$

where $\theta_{m,r} \equiv \partial_i v_{m,r}^i$, and we defined $\epsilon \equiv f_\chi \beta \tilde{m}$. The system of equations is complicated, but can be simplified by assuming the overdensities to be small and thus neglecting products of perturbations. In this linear regime, different Fourier modes are decoupled from one another. To further simplify the problem, we expand the evolution equation at first order in β. With these assumptions, the system can be analytically solved:

$$\delta_{m,r}(\vec{k}, \tau) = D_{1m,1r}(\tau)\delta_0(\vec{k}) \ , \tag{4.32}$$

where $\delta_0(\vec{k})$ represents the initial condition for the overdensity field for a given Fourier mode $\vec{k}$. The primordial power spectrum, defined as:

$$\langle \delta_0(\vec{k})\delta_0(\vec{q})\rangle = (2\pi^3)\delta_D^{(3)}(\vec{k} + \vec{q})P_0(k) = (2\pi)^3 \delta_D^{(3)}(\vec{k} + \vec{q})k^{-3} A_s \left(\frac{k}{k_P}\right)^{1-n_s} \ , \tag{4.33}$$

is characterized, as in ΛCDM, by the two quantities n_s (scalar spectrum tilt) and A_s (the amplitude of the fluctuations), that are fitted from the data. k_P is a pivot scale, taken to be 0.05 Mpc^{-1}. We assume the primordial perturbation fields to be gaussian fields, neglecting any possible contributions to the primordial connected higher point functions.

Coming back to Eq. (4.32), we have the following solutions for the linear growth factors D_1 in MD:

$$\begin{aligned}
D_{1m} &= \left[1 + \frac{2f_\chi}{5}\epsilon\left(\log\frac{\tau}{\tau_{\text{eq}}} - \frac{1}{5} + \frac{1}{5}\frac{\tau_{\text{eq}}^5}{\tau^5}\right)\right] D_{1m}^{\text{CDM}} \ , \\
D_{1r} &= \frac{5}{3}\epsilon\left(1 - \frac{3\tau_{\text{eq}}^2}{\tau^2} + \frac{2\tau_{\text{eq}}^3}{\tau^3}\right) D_{1m}^{\text{CDM}} \ ,
\end{aligned} \tag{4.34}$$

where $D_{1m}^{\rm CDM} = C\tau^2$ is the growth factor for non-interacting CDM in an Einstein-de Sitter background. We can recast Eq. (4.34) in terms of the scale factor a, since

$$a(\tau) \simeq C\tau^2 \left(1 - 2\epsilon f_\chi \log \frac{\tau}{\tau_{\rm eq}} + \frac{7}{3}\epsilon f_\chi\right) , \tag{4.35}$$

In terms of the scale factor Eq. (4.34) becomes:

$$D_{1,m} \simeq \left[1 + \frac{6f_\chi}{5}\epsilon \left(\log \frac{a}{a_{\rm eq}} - \frac{181}{90}\right)\right] D_{1m}^{\rm CDM}(a) , \tag{4.36}$$

in the limit $\tau \gg \tau_{\rm eq}$. Further, we retain in the β corrections only the log-enhanced piece, and neglect the others. This is a valid approximation since $\log a/a_{\rm eq} \simeq 8$ for the scale factors we are interested in. With this in mind we can write an analytic expression for the linear total matter power spectrum:

$$P_{m,L} = \left(1 + \frac{12}{5} f_\chi \log \frac{a}{a_{\rm eq}}\right) P_{m,L}^{\rm CDM}(k) , \tag{4.37}$$

with $P_{m,L}^{\rm CDM}$ the power spectrum in ΛCDM. We do not attempt to get a similar analytical estimate for the CMB anisotropies spectrum since it is not the focus of the future sections, but in principle its shape is governed by the same set of equations (together with the evolution of photons).

A result of [83] is that CMB [23, 345] and linear BAO [3, 4, 346, 347] data can set strong constraint on the self-interaction parameter. The strategy adopted was to employ Markov Chain MonteCarlo (MCMC) methods to scan the likelihood function, using the MontePython code [348, 349] and the suitably modified CLASS version. A total of 7 cosmological parameters were varied (5 in common with ΛCDM and two specific of the model):

$$\{\omega_b\ , n_s\ , A_s\ , \tau_{\rm reio}\ , H_0\ , \tilde{\Omega}_d\ , \beta\} , \tag{4.38}$$

where $\tau_{\rm reio}$ is the optical depths at reionization. Notice that there is one extra parameter with respect to the usual ΛCDM, which is the self-interaction strength β.

The result found is essentially that the 5 ΛCDM cosmological parameters are constrained to have their ΛCDM value, with the exception of H_0. This is due to the fact that the long range force changes background evolution and therefore it will correct the Hubble parameter. This makes the 5F scenario possibly relevant for the Hubble tension, but we do not attempt to give any explanation to such anomaly. The final bounds on β at 95% credible levels are:

$$\begin{aligned} &\beta < 0.0011 \qquad \text{Planck18} \\ &\beta < 0.0054 \qquad \text{Planck18} + \text{BAO} \end{aligned} \tag{4.39}$$

As anticipated, the bounds are strong and justify a perturbative treatment in the analytic estimates, although we remark that when extracting bounds via MCMC the full numerical solutions are employed.

4.3 Bounds from galaxy surveys

We want to expand the previous bounds by considering galaxy surveys. The key observable is the so called *galaxy power spectrum*, which is defined as follows:

$$\langle \delta_g(\vec{k})\delta_g(\vec{q})\rangle = (2\pi)^3\delta_D^{(3)}(\vec{k}+\vec{q})P_g(\vec{k}) \ . \tag{4.40}$$

Here δ_g is the galaxy overdensity:

$$\delta_g = \frac{n_g - \bar{n}_g}{\bar{n}_g} \tag{4.41}$$

where n_g is the galaxy number density, either as a function of the coordinate or of the wave number if in Fourier space. Galaxies are highly non-linear objects: the evolution of the baryon and DM perturbations at such small scales is beyond the reach of the perturbative Euler equation for small δ. If we want to extract some information from this data, we must be able to describe δ_g as a function of the fundamental fields $\delta_{m,r}$. In order to do so we employ the so called bias expansion [85]. The idea is that the galaxy overdensity field (in position space) can be expressed as a power series of fundamental fields. At linear level (meaning no power higher than the linear one in fundamental fields), this expansion is [350, 351]:

$$\delta_g = b_1\delta_m + b_r\delta_r + b_\theta\theta_r \ . \tag{4.42}$$

The magnitude of the biases can be estimated for example from simulations. Practically speaking, they are left as redshift-dependent parameters to be fitted in each given data set.

With the expansion in Eq. (4.42) we can write the analytic prediction for the linear galaxy power spectrum:

$$P_{g,L}(k) = b_1^2 P_{m,L} = b_1^2\left(1+\frac{12}{5}f_\chi\epsilon\log\frac{a}{a_{\rm eq}}\right)P_{m,L}^{\rm CDM}(k) \ . \tag{4.43}$$

We have neglected corrections proportional to b_r since they are not log-enhanced in Eq. (4.43), and the contributions proportional to b_θ that are suppressed sub-horizon by $\mathcal{H}^2/k^2$. While analytic estimates are useful for developing an intuition of the leading physical effects, when computing bounds we will always use the numerical expressions for the power spectra involved (in this example $P_{m,L}$) rather than their analytic estimates.

Galaxy surveys are counting experiments, and in order to model the associated shot noise the expansion Eq. (4.42) can be supplemented with operators built with a stochastic field ε (and its powers), whose expectation value follows a Poissonian statistics. In this way, the expression for the galaxy power spectrum at tree level becomes:

$$P_{g,L}(k) = b_1^2 P_{m,L} + \frac{1}{\bar{n}} \ , \tag{4.44}$$

with $\bar{n}$ the average galaxy number density. We will always implement the SN in our computations.

There are two additional effects that need to be taken into account when modeling the galaxy power spectrum. Indeed the position of galaxies can only be inferred through measurements of the redshift and assuming a fiducial cosmology. This is important when comparing the true theoretical prediction (P_g) with what is actually observed by experiments ($P_{g,\mathrm{obs}}$). Let the inferred observed position of a given galaxy be parametrized as:

$$\vec{x}_{\mathrm{obs}}(z,\theta,\phi) = \chi_{\mathrm{fid}}(z)\hat{n}(\theta,\phi) \ , \tag{4.45}$$

where χ is the comoving distance defined as:

$$\chi(z) = \int_0^z \frac{\mathrm{d}z'}{H(z')} \ , \tag{4.46}$$

and $\hat{n}$ the unit-vector inicating the direction of the galaxy location with respect to the observer. In Eq. (4.45) we used a fiducial cosmology to set $H(z)$ in the integral of Eq. (4.46). However the true cosmology might be different. We parametrize this difference in χ as:

$$\chi_{\mathrm{fid}} = \chi + \delta\chi \ . \tag{4.47}$$

It is useful to introduce the so called *distant observer* approximation: since galaxies of a survey are typically in a narrow cone around the line of sight of the observer, we can treat them as if they were on the 2D (x_1, x_2) plane orthogonal to the line of sight, fixed to be along the direction $\hat{x}_3$. We also pick the origin in the center of the redshift bin $\bar{z}$:

$$\vec{x}_{\mathrm{obs}} = 0 \Leftrightarrow \theta = 0, z = \bar{z} \ . \tag{4.48}$$

The observed coordinates can be parametrized using the comoving distance and the two angles on the 2D plane:

$$(x_{1,\mathrm{obs}}, x_{2,\mathrm{obs}}) = \chi(z)(\theta_1,\theta_2) \ , \quad x_{3,\mathrm{obs}} = \chi_{\mathrm{fid}}(z) - \chi_{\mathrm{fid}}(\bar{z}) \ . \tag{4.49}$$

In this approximation, the following relation holds between observed and true coordinates:

$$\begin{aligned} x_3(z) &= x_{3,\mathrm{obs}}\left(1 - \frac{\delta H(\bar{z})}{H_{\mathrm{fid}}(\bar{z})}\right) \equiv x_{3,\mathrm{obs}}\left(1-\alpha_{||}\right) \ , \\ (x_1,x_2) &= (x_{1,\mathrm{obs}}, x_{2,\mathrm{obs}})\left(1 - \frac{\delta\chi(z)}{\chi_{\mathrm{fid}}(z)}\right) \equiv (x_{1,\mathrm{obs}}, x_{2,\mathrm{obs}})\left(1-\alpha_{\perp}\right) \ , \end{aligned} \tag{4.50}$$

where δH is defined as the difference from the true and fiducial value of H. From Eq. (4.50) we can define the relation between observed Fourier modes and real Fourier modes:

$$\begin{aligned} k_3 &= k_{3,\mathrm{obs}}\left(1+\alpha_{||}\right) \ , \\ (k_1,k_2) &= (k_{1,\mathrm{obs}}, k_{2,\mathrm{obs}})\left(1+\alpha_{\perp}\right) \ . \end{aligned} \tag{4.51}$$

This distortion due to an error in the fiducial cosmology is called *Alcock-Paczynski effect* (AP) [91], and it will be important for example when expanding around a fiducial cosmology in the Fisher formalism.

The second error is due to the fact that the observed redshift z of a photon is affected by the projection $u_{||}$ along $\hat{n}$ of the peculiar velocity of the galaxy $\vec{u}_g$:

$$1 + z = \frac{1}{a_{\rm em}}(1 + u_{||}) \,, \qquad u_{||} = \vec{v}_g \cdot \hat{n} \,, \tag{4.52}$$

where $a_{\rm em}$ is the scale factor of the universe when the photon was emitted. This gives rise to the Redshift Space Distortions (RSD) [90].

Putting together the two effects, we obtain the following shift of the observed position $\vec{x}_{\rm obs}$ with respect to the true position $\vec{x}$:

$$\vec{x}_{\rm obs} = \vec{x} + \delta\chi(z)\hat{n} + \left.\frac{\partial \vec{x}_{\rm obs}}{\partial u_{||}}\right|_{u_{||}=0} u_{||} = \vec{x} + \left(\delta\chi(z) + \frac{1}{aH}u_{||}\right)\hat{n} \,, \tag{4.53}$$

where we assumed the error in z and $\delta\chi$ to be both small corrections. The key observation is that the number of galaxy in a given volume element is the same independently which coordinates are used:

$$n_{g,\rm obs}(\vec{x}_{\rm obs})\mathrm{d}^3 x_{\rm obs} = n_g(\vec{x})\mathrm{d}^3 x \,. \tag{4.54}$$

By computing the Jacobian induced by Eq. (4.53), we get the following formula for the observed galaxy density contrast (assuming $u_{||} \ll aHx$):

$$\begin{aligned}
&\delta_{g,\rm obs}(\vec{x}_{\rm obs}) = \\
&= \left(1 - 2\frac{\delta\chi(\bar{z})}{\chi(\bar{z})} + H^{-1}(\bar{z})\delta H(\bar{z})\right)\left(1 + \delta_g(\vec{x}[\vec{x}_{\rm obs}]) - \frac{1}{aH}\frac{\partial u_{||}}{\partial x}(\vec{x}[\vec{x}_{\rm obs}])\right) - 1 \,.
\end{aligned} \tag{4.55}$$

In order to proceed, we have to relate the galaxy-related quantities δ_g and $\vec{v}_g$ to the respective matter quantities. The density has already been treated via the bias expansion in Eq. (4.42). Instead we will assume the velocity to be the same to the matter velocity $\vec{v}_m$ due to equivalence principle considerations (also in our case this is true at order $\beta \log a/a_{\rm eq}$). At linear order we can substitute in Eq. (4.55) the solutions for $\vec{v}_m$:

$$\vec{v}_m = aHf\frac{i\vec{k}}{k^2}\delta_m \,, \qquad f \equiv \frac{\mathrm{d}\log D_{1m}}{\mathrm{d}\log a} \,. \tag{4.56}$$

We are neglecting non-longitudinal velocity modes since they are decaying modes.

After the substitution and expressing everything in Fourier space, we get the final formula for the observed galaxy density at linear order:

$$\delta_{g,\rm obs}(\vec{k}_{\rm obs}) = \left(b_1 + f\mu^2\right)\delta_m(\vec{k}[\vec{k}_{\rm obs}]) \tag{4.57}$$

with $\mu = k_{3,\rm obs}/|\vec{k}_{\rm obs}|$ if the AP effect is included.

Combining RSD, AP, and SN, the analytic expression for the linear observed galaxy power spectrum is:

$$P_{g,\rm obs}(\vec{k}_{\rm obs}) = \left(b_1 + f\mu^2\right)^2 P_{m,L}(\vec{k}[\vec{k}_{\rm obs}]) + \frac{1}{\bar{n}} \,. \tag{4.58}$$

Notice that now the observed power spectrum is not isotropic, and it depends on the direction of $\vec{k}$ with respect to the line of sight. In likelihoods and forecast the angular information is condensed in multipoles $P_l(\vec{k})$. Given the symmetry of the problem, only even l, $m = 0$ multipoles are considered. More specifically, current data includes typically only $l = 0, 2$, while in forecasts also $l = 4$ is kept.

4.3.1 1-loop Power Spectrum

The linear prediction for P_g of Eq. (4.43) can be trusted up to $k \lesssim 0.1\,h/\text{Mpc}$. If we want to extract informations from higher modes, we have to include the first corrections to the linearized equations describing the evolution of perturbations. This is not an useless endeavour: even managing to push the perturbative control of the theory up to Fouriers modes a factor of ~ 5 larger implies a gain in the number of modes of $\sim 5^3 \sim 100$, due to the 3D nature of galaxy survey data.

The goal is to understand how to include the first non-linear corrections to the galaxy power spectrum, called 1-loop contributions in analogy with particle physics. The procedure is similar in spirit to what we have done in the linear regime. First, we expand δ_g as a function of the fundamental fields, this time going up to operators quadratic in the fundamental fields[2]. Second, we solve for each fundamental field the Euler equations of Eq. (4.31), retaining up to third order solutions in the perturbations. In this way we have the expression for the fundamental δ as a function of up to three primordial overdensities δ_0. Then we multiply $\delta_g\delta_g$ and take the ensemble average. For illustrative purpose, we show the procedure for the total matter power spectrum:

$$\begin{aligned}
&\langle \delta_m(\vec{k}_1)\delta_m(\vec{k}_2)\rangle = \\
&= \langle \delta_m^{(1)}(\vec{k}_1)\delta_m^{(1)}(\vec{k}_2)\rangle + \langle \delta_m^{(2)}(\vec{k}_1)\delta_m^{(2)}(\vec{k}_2)\rangle + 2\langle \delta_m^{(3)}(\vec{k}_1)\delta_m^{(1)}(\vec{k}_2)\rangle = \\
&= (2\pi)^3\delta_D^{(3)}(\vec{k}_1+\vec{k}_2)\left(P_{m,L}(\vec{k}_1) + P_{m,22}(\vec{k}_1) + 2P_{m,13}(\vec{k}_1)\right) ,
\end{aligned} \tag{4.59}$$

where $P_{m,22}$ is obtained by expanding both δ_m in the product up to second order, while $P_{m,13}$ is obtained by expanding one δ_m at third order, and keeping the other at linear order. Repeating the procedure for all the possible terms in the expansion of $\delta_g\delta_g$ gives the 1-loop power spectrum. This procedure however is not completely sound: for example in the loop integrals the fluctuations receive contributions from short modes that are outside the control of perturbation theory. To improve the reliability of the computation, we have to resort to the EFTofLSS. The idea behind it is to smooth over small distances the fluctuations, and encode in effective operators, *the counterterms*, the physical effects of the short modes over the long ones. After the smoothing, a new term modifying the Euler equation is kept. This corresponds to not setting to 0 the second momentum tensor Σ^{ij} in Eq. (4.9), and expanding it in terms of operators built with the long wavelength modes. Assuming for the moment a ΛCDM cosmology, in real space (no RSD) there is at leading order a

[2]In principle cubic biases should enter the computation. However almost all are renormalization of lower order biases, and the only independent cubic term is set to 0 given the lack of constraining power on it[352].

single counterterm:

$$\frac{1}{\rho_\chi}\partial_i\Sigma^{ij} = c_s^2\partial^j\delta_m \ . \tag{4.60}$$

The value of the coefficient c_s is fitted from numerical simulations, and its contribution to the power spectrum is comparable to a 1-loop contribution:

$$P_{1-\text{loop}} = P_{m,L} + P_{m,22} + 2P_{m,13} + 2P_{\text{ctr}} = P_{m,L} + P_{m,22} + 2P_{m,13} - \alpha\frac{k^2}{k_*^2}P_{m,L} \ , \tag{4.61}$$

where $k_* = 1\,h/\text{Mpc}$ and α is related to c_s via a convolution integral between the Green function of the linear Euler equation and the new source term due to Σ^{ij}.

Now we sketch the passages for P_g. As mentioned above, for consistency we need to to extend the bias expansion up to second order (in position space):

$$\begin{aligned}\delta_g &= b_1\delta_m + b_r\delta_r + b_\theta\theta_r + \\ &+\frac{b_2}{2}\delta_m^2 + b_{K^2}K_{ij}K^{ij} + b_{mr}\delta_m\delta_r + b_{\delta\theta}\delta_m\theta_r + b_{\nabla\delta}\partial_i\delta_m v_r^i + b_K K_{ij}\partial^i v_r^j \ ,\end{aligned} \tag{4.62}$$

with $K_{ij} = (\partial_i\partial_j/\partial^2 - \delta_{ij}/3)\delta_m$ the tidal tensor.

The equations Eq. (4.31) at second order are solved in Fourier space by the following convolution integrals:

$$\begin{aligned}\delta_m^{(2)}(\vec{k},\tau) &= D_{1,m}^2\int\frac{\mathrm{d}^3k_1}{(2\pi)^3}\frac{\mathrm{d}^3k_2}{(2\pi)^3}(2\pi)^3\delta_D^{(3)}(\vec{k}-\vec{k}_1-\vec{k}_2)\tilde{F}_2(\vec{k}_1,\vec{k}_2)\delta_0(\vec{k}_1)\delta_0(\vec{k}_2) \ , \\ \delta_r^{(2)}(\vec{k},\tau) &= \epsilon\left(D_{1,m}^{\text{CDM}}\right)^2\int\frac{\mathrm{d}^3k_1}{(2\pi)^3}\frac{\mathrm{d}^3k_2}{(2\pi)^3}(2\pi)^3\delta_D^{(3)}(\vec{k}-\vec{k}_1-\vec{k}_2)F_{2r}(\vec{k}_1,\vec{k}_2)\delta_0(\vec{k}_1)\delta_0(\vec{k}_2) \ ,\end{aligned} \tag{4.63}$$

where the kernels $\tilde{F}_2, \tilde{F}_{2r}$ are given by:

$$\begin{aligned}\tilde{F}_2(\vec{k}_1,\vec{k}_2) &= \frac{5}{7} - \frac{6}{35}f_\chi\epsilon + \frac{\vec{k}_1\cdot\vec{k}_2}{2}\left(\frac{1}{k_1^2}+\frac{1}{k_2^2}\right) + \left(\frac{2}{7}+\frac{6}{35}f_\chi\epsilon\right)\frac{(\vec{k}_1\cdot\vec{k}_2)^2}{k_1^2k_2^2} \ , \\ F_{2r}(\vec{k}_1,\vec{k}_2) &= \frac{59}{30} + \frac{17}{6}\frac{\vec{k}_1\cdot\vec{k}_2}{2}\left(\frac{1}{k_1^2}+\frac{1}{k_2^2}\right) + \frac{13}{15}\frac{(\vec{k}_1\cdot\vec{k}_2)^2}{k_1^2k_2^2} \ .\end{aligned} \tag{4.64}$$

Similar expressions can be found for the velocties $\theta_{m,r}$, and for the third-order kernels [342].

The key observation for the 5F scenario is that the modifications of the loop kernels due to the long range interactions (the ones proportional to ϵ in Eq. (4.64)) are negligible, given that they lack the log-enhancement [342]. The same holds for the counterterms. This is because at order $\beta\log a/a_{\text{eq}}$ the symmetries of the theory are identical to ΛCDM, as seen from Eq. (4.31). Therefore leading modifications to the 1-loop power spectrum come from the modifications of the total matter growth factors. This allows us to run the available pipelines to analyze current data, like PyBird [353], and pipelines to do forecasts of future experiments, like FishLSS [354]. The only modification needed is to redirect the various codes to the modificed CLASS

version, but otherwise there is no change in how the loop integrals are handled. The codes used automatically implement the corrections to P_g due to SN, RSD and AP.

We have ran MCMC sampling the parameters reported in Eq. (4.38), with the Planck (lite) + BOSS data (with Full Shape)[353], and also adding lensing and linear BAO data at other redshifts[3]. The two results are essentially identical, and the bounds on β at 95% credible level are not too different from the ones obtained with linear cosmology alone:

$$\begin{aligned} &\text{Planck} + \text{BOSS} : && \beta < 0.005 \\ &\text{Planck} + \text{BOSS} + \text{lensing} + \text{BAO} : && \beta < 0.0046 \end{aligned} \tag{4.65}$$

A reason for the lack of improvement with respect to linear data is the fact that the extra information is compensated by the introduced bias parameters for each bin.

We report in Fig. 4.1 the degeneracies for the cosmological parameters whose fit value is affected the most by the dark fifth force.

In Fig. 4.1 we also give Fisher forecasts for future surveys, like Euclid [355] (which has launched in July 2023) and the more futuristic PUMA32k (a 21-cm survey [356]) and MegaMapper [357]. We took the following fiducial cosmology for the forecasts, which corresponds to the best fits obtained from PyBird runs:

$$\begin{aligned} &\omega_b = 0.0225 \, , A_s = 2.10 \times 10^{-9} \, , n_s = 0.97 \, , \tau_{\rm reio} = 0.057 \, , \\ &H_0 = 68.2 \text{km/(s Mpc)} \, , \tilde{\Omega}_d = 0.256 \, , \beta = 0 \, . \end{aligned} \tag{4.66}$$

For the values of the fiducial biases, volumes and other we refer to the default values found in [354]. We use 4 redshift bins for Euclid, while 5 for PUMA and MegaMapper. The biases used are, in each redshift bin, b_1, b_2, b_K, the 3 counterterms (one for each multipole) $\alpha_0, \alpha_2, \alpha_4$, and the galaxy number density needed to model the shot noise. For details on the Fisher computation, we refer to App. I.

The bound obtained by adding the Euclid data is projected to be $\beta < 0.002$ at 95% credible level, while adding the futuristic experiments bring the bound to $\beta \lesssim 0.001$. This can be considered as the ultimate reach for galaxy surveys experiments employing only the 1-loop P_g.

When showing the forecasts of future galaxy surveys, we have combined their Fisher with the inverse covariance matrix obtained from PyBird (a proxy for its Fisher information). This is not a completely sound procedure, since some parameters like the biases and especially β are not gaussianly distributed (by theoretical assumption $\beta > 0$). We will still combine it to get an estimate of the strenght of the bound given some prior information on β. Completely removing the prior on β reduces the bound strength by a factor of 2.5 roughly on the present data + Euclid forecast. It is important to notice that galaxy surveys by themselves do not completely constrain all the cosmological parameters (like ω_b alone for example), and therefore they need to be supplemented with prior informations coming from other types of experiments like Planck.

[3]Unlike BOSS, in which the dataset covers the full shape of the galaxy power spectrum at different k, what we call BAO is a fit of the sound horizon (at baryon drag epoch) parameter obtained by studying the BAO feature.

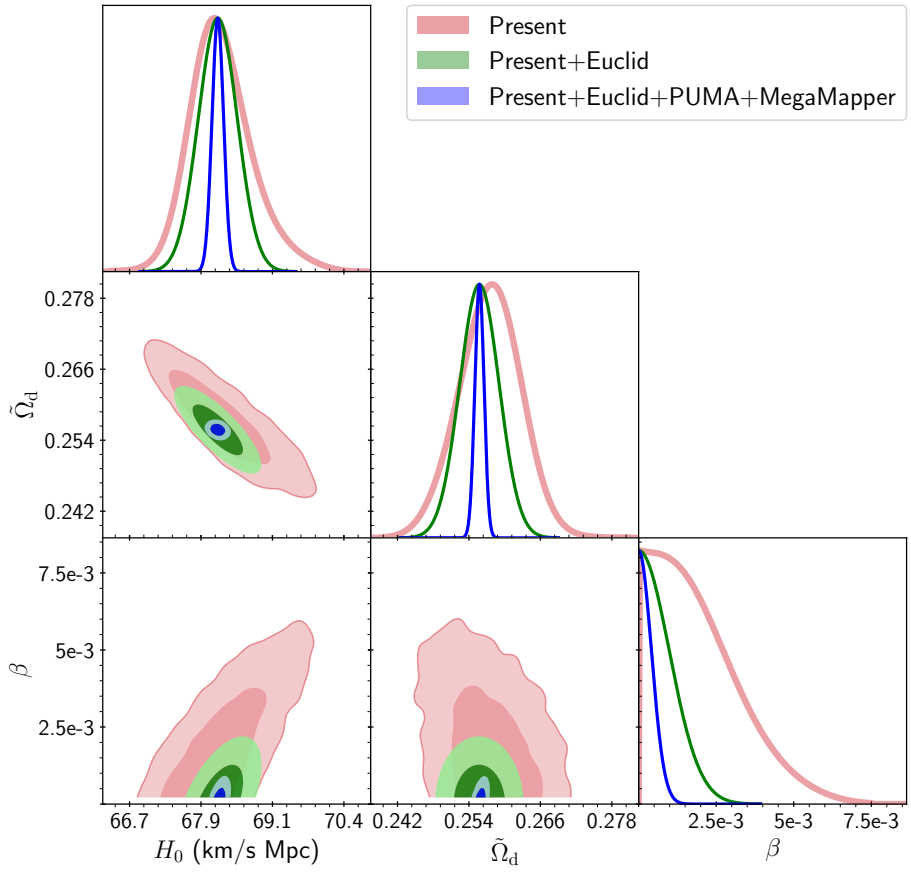

Figure 4.1: *Regions at 68% (dark) and 95% (light) credible level for the parameters whose fit values are most affected by the self-interaction: $H_0, \tilde{\Omega}_d, \beta$. **Red:** exclusion from present data (Planck+BOSS+lensing+BAO). The galaxy power spectrum has been modelled following [354] using RSD, AP, SN and counterterms. **Green:** forecast of Euclid survey combined with the prior coming from present data. **Blue:** as green, but also considering the combination of PUMA and MegaMapper.*

4.3.2 Bispectrum (Real Space)

Another probe of non-linearity is the galaxy bispectrum, that is related to the galaxy three-point function:

$$\langle \delta_g(\vec{k}_1)\delta_g(\vec{k}_2)\delta_g(\vec{k}_3)\rangle \equiv (2\pi)^3\delta_D^{(3)}(\vec{k}_1+\vec{k}_2+\vec{k}_3)B_g(\vec{k}_1,\vec{k}_2,\vec{k}_3)\ . \tag{4.67}$$

At linear order, the bispectrum vanishes since there is no way to contract three gaussian fields. Therefore second order contributions are needed. We will restrict ourselves to computing only the leading tree-level contribution, where one of the three densities is taken at second order, either through quadratic biases with first order matter densities or linear biases with second-order matter densities. As a first step we will write the bispectrum in real space, neglecting RSD and AP. After plugging the expansion of Eq. (4.62), we get the following analytic expression for the galaxy bispectrum:

$$B_g(\vec{k}_1,\vec{k}_2,\vec{k}_3) = \left(1+\epsilon f_\chi \frac{24}{5}\log\frac{a}{a_{\rm eq}}\right) B^{\rm CDM}(\vec{k}_1,\vec{k}_2,\vec{k}_3)\ , \tag{4.68}$$

where we neglected non-log enhanced contributions of $\mathcal{O}(\beta)$, like the ones proportional to b_r. In Eq. (4.68) $B^{\rm CDM}$ stands for the bispectrum in ΛCDM:

$$B_g^{\rm CDM}(\vec{k_1},\vec{k}_2,\vec{k}_3) = 2b_1^2\Bigg(P_{m,L}^{\rm CDM}(k_1)P_{m,L}^{\rm CDM}(k_2)F_{2,g}(\vec{k}_1,\vec{k}_2)+ \\ + P_{m,L}^{\rm CDM}(k_1)P_{m,L}^{\rm CDM}(k_3)F_{2,g}(\vec{k}_1,\vec{k}_3) + P_{m,L}^{\rm CDM}(k_2)P_{m,L}^{\rm CDM}(k_3)F_{2,g}(\vec{k}_2,\vec{k}_3)\Bigg) \,. \tag{4.69}$$

where $F_{2,g}$ is the following kernel:

$$F_{2,g}(\vec{k}_1,\vec{k}_2) = b_1 F_2(\vec{k}_1,\vec{k}_2) + \frac{b_2}{2} + b_{K^2}\left(\frac{(\vec{k}_1\cdot\vec{k}_2)^2}{k_1^2k_2^2} - \frac{1}{3}\right) \,, \tag{4.70}$$

with $F_2 = \tilde{F}_2|_{\epsilon=0}$ is the kernel of Eq. (4.64) evaluated in the $\epsilon = 0$ limit. Notice that despite the appearances of scalar products between the various momenta, the real space bispectrum only depends on their magnitude, or equivalently on the shape of the triangle.

When doing the forecasts for the bispectrum we keep only the term in Eq. (4.69), but using the 5F power spectrum rather than the ΛCDM one. We have checked that the neglected terms in Eq. (4.68) contribute negligibly for $b_r \simeq 0.1$.

We also include the SN terms that come from stochastic operators ε, ε^2, $\delta\varepsilon$ suitably contracted, so that the tree level expression becomes [358, 359]:

$$B_g(\vec{k}_1,\vec{k}_2,\vec{k}_3) = B_{\rm noSN} + \frac{b_1^2}{\bar{n}}(P_{m,L}(k_1)+P_{m,L}(k_2)+P_{m,L}(k_3)) + \frac{1}{\bar{n}^2} \,, \tag{4.71}$$

where $B_{\rm noSN}$ is the one reported in Eq. (4.69) with the 5F $P_{m,L}$ in place of the ΛCDM ones.

This simplified computation should give a preliminary idea on how the bispectrum can tighten the bounds on β and on the bias parameters, since it involves a different bias combination with respect to the power spectrum. We report our results in Fig. 4.2. In order to understand the improvement, we also show the 1-loop P_g computed in real space, to make the comparison more direct.

As can be seen, the addition of B_g improves the bounds on β by a factor of 2: $\beta < 10^{-3}$ at 95%. Notice also that the bounds obtained from the real space P_g are not much weaker than the one obtained with the RSD. This is true regardless of the prior on β coming from present data. The addition of the bispectrum improves only sligthly the bounds on β in presence of a CMB prior, but it helps to measure the biases, especially the ones like b_2 that give subleading contributions in P_g.

4.4 Discussion

In this Chapter we explored the possibility that DM interactions are totally hidden from the SM. In this case, information on its self-interactions can be gathered by studying how DM clumps on itself, which in turn can be studied by observing how

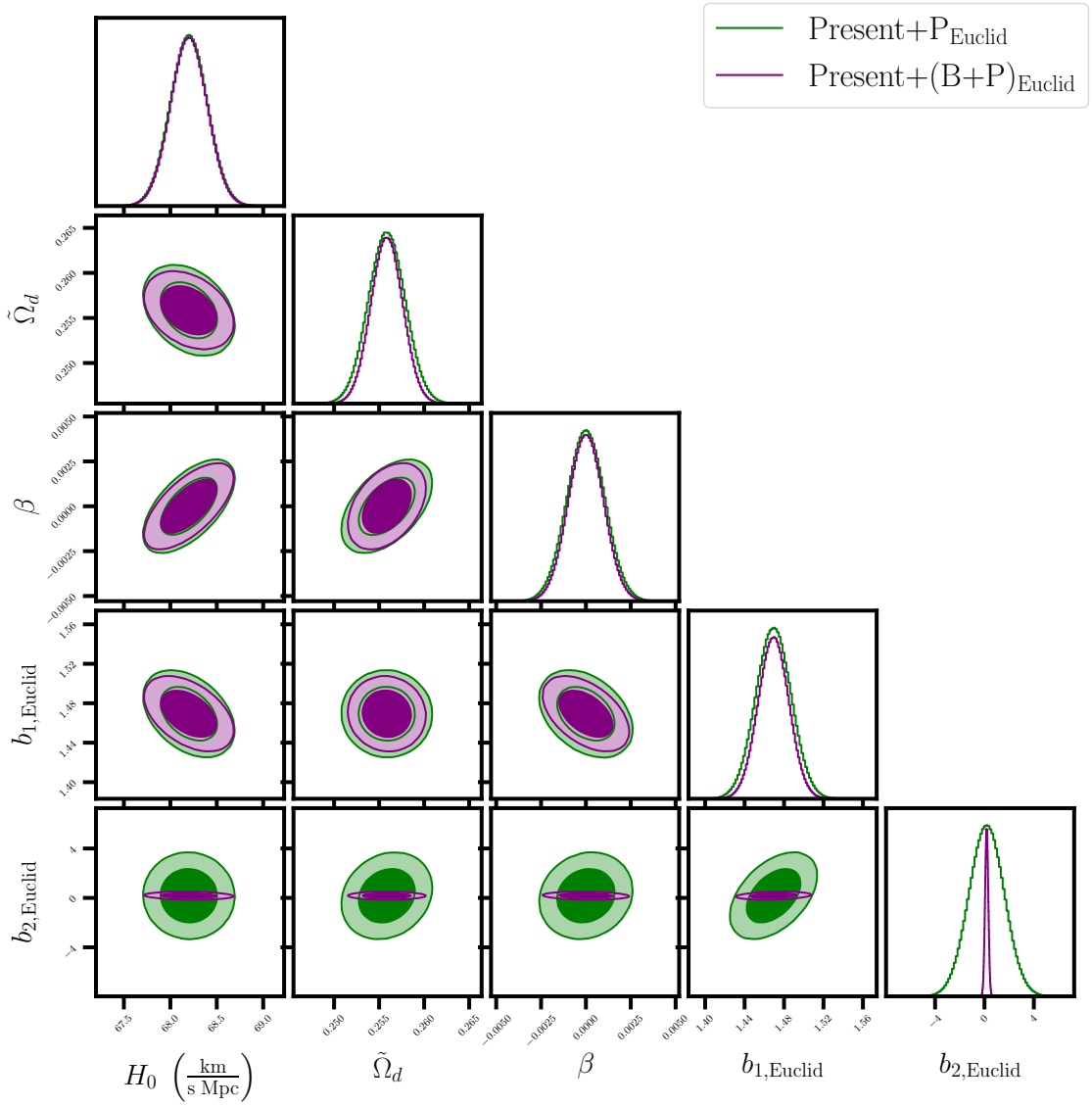

Figure 4.2: *Credibility intervals at 68% (dark) and 95% (light) for the parameters whose fit values are most affected by the self-interaction, $H_0, \tilde{\Omega}_d, \beta$, and the linear and quadratic bias of the first redshift bin of Euclid.* ***Green:*** *forecast of 1-loop P_g in real space for Euclid combined with the prior coming from present data.* ***Purple:*** *as green, but also considering the tree level B_g in real space.*

cosmological structures are formed. The starting point is the work done in [83], in which the authors set bounds on the self-interaction strength of a scalar DM particle χ interacting via a Yukawa interaction mediated by a very light scalar. The bounds were obtained via comparing linear cosmology predictions with CMB and BAO data. We expanded the study focusing on the 5F regime, in which the new mediator does not contribute to the energy budget of the universe during the cosmological history. The Yukawa interaction (or interactions that start at linear order in the mediator field) is the only one that can be studied, while the others are essentially indistinguishable from ΛCDM. Then we proceeded to study the consequences of the Yukawa interaction by adding two extra obervables: the 1-loop galaxy power

spectrum and the tree level bispectrum. At first we found analytical estimates for these quantities, which allowed to adapt current pipelines. We set bounds with the 1-loop galaxy power spectrum via MCMC methods with current BOSS data, and then we added the forecast from future surveys like Euclid. The 95% credible level upper bound on β with these future experiments can improve up to 10^{-3}, a factor of 5 stronger than the one from linear cosmology. We repeated the study with the bispectrum, with the goal in mind to understand how it can help with the bias degeneracies appearing in the power spectrum alone. We performed a simplified study in real space, with no AP effect. We found that the bispectrum can help improving the bound on β coming from P_g (and a cosmology prior) only slightly. In addition, it can improve measuring higher order biases like b_2. We mention that the bispectrum in presence of multiple tracers has a non-trivial pole structure [94], manifesting in the squeezed triangular configurations in Fourier space. It will be interesting to include it and understand how it can tighten the bounds. Another aspect left to do is to improve the bispectrum calculations including RSD and AP, and to quantify how much they can affect our results.

Chapter 5

Accidental Stability and Asymmetric Dark Matter

In the previous Chapters of the Thesis, we asked questions about the properties of Dark Matter from a purely phenomenological perspective. The fact that Dark Matter is stable on cosmological time scales hints that in a theory of Dark Matter, a symmetry is protecting it from fast decays. This phenomenological information can be complemented by theoretical insights. Indeed global symmetries are believed to be spoiled by quantum gravity (see [41] for example). Therefore, in a generic DM model we expect that all possible operators consistent with gauge symmetries will be generated at Planck scale $M_{\rm P}$, and some of these will cause DM to decay too fast. Gauge invariance can lead to an IR residual symmetry that protects the DM candidate from decaying, without the need to impose by hand further global or discrete symmetries if the dimensionality of these operators is large enough. This idea is called *Accidental Stability* (AS). Models realizing this concept are not generic. A possible way to get large dimensions for decay-inducing operators is to charge DM under some gauge symmetry. In the original Minimal Dark Matter models [43] the gauge symmetry protecting the accidentally stable $\mathrm{SU}(2)_{\rm L}$ 5-plet DM was the SM $\mathrm{SU}(2)_{\rm L}$ gauge group itself. A different possibility is to consider a new confining group in the dark sector. In this case DM is a stable dark bound state, which is stabilized against decays in the same way the SM proton is thanks to QCD.

The idea of Accidental Stability applied to composite Dark Sectors was studied in [42], in the so called *Accidental Composite Dark Matter* (ACDM) models. The prototypical composite DM scenario describes some constituent particles, that we will improperly label *dark quarks*, that are bound together via a new confining gauge interaction, called *dark color*, in baryon-like or pion-like bound states (respectively *dark baryons* and *dark pions*) [360]. The dark quarks can also carry non-trivial charges under the SM gauge group. The confinement of the dark quarks inside a dark color singlet bound state can be exploited to conceal their SM charges inside a globally SM-neutral (or weakly interacting) bound state [42, 361], if the charges of the constituents are properly chosen. In this way bounds from direct and indirect detection can be evaded, but the presence of potentially SM-charged resonances leads

to peculiar collider signatures, that can be tested at current or future experiments.

We want to understand if the AS principle can be applied with success to different frameworks, constraining the possible models. In the original ACDM paper, the DM was *symmetric*, meaning that it is made up by the same amount of particles and antiparticles. Anoter possibility is that it is *asymmetric* (ADM), being made only by particles and not their charge-conjugates. This is very similar to what happens in the visible universe, that possesses a matter-antimatter asymmetry (BAU) $\eta_b \equiv n_b/s \sim 10^{-10}$. If the DM is asymmetric, there are interesting differences with the symmetric scenario (in particular if it is also composite), regarding for example indirect detection (ID) bounds [189, 362], evolution of astrophysical objects [363, 364], and annihilation cross section predictions [365]. Therefore this property is not a mere academic curiosity, rather it bears a phenomenologically distinct scenario.

Historically ADM was motivated by the experimental fact that Dark Matter abundance is roughly of the same order of the baryonic (visible) abundance [23]:

$$\Omega_{\rm DM} \simeq 5\Omega_{\rm b} \, . \tag{5.1}$$

This numerical coincidence, in conjunction with the existence of BAU in the visible sector, has led to many speculations about a possible common origin for the DM and visible sector abundances (see [45, 46] for reviews). In particular, if the DM is asymmetric, the ratio between the two energy densities can be explained by building models that predict a $\mathcal{O}(1)$ relation between the asymmetry in the DS and in the visible sector. The relation of Eq. (5.1) is then obtained by taking the mass of the DM to be in the $1 \div 10$ GeV. Typically in this class of models only the numerical density coincidence is explained, while the explanation for having a DM mass near the proton mass (needed to enforce Eq. (5.1)) is not given[1]. The task is usually accomplished by transferring some primordial asymmetry between the visible and dark sector, for example through higher dimensional operators [367], or through anomalous electroweak (EW) interactions like *sphalerons* [368]. The primordial asymmetry can be generated in several ways. For example it can be generated in the visible sector via the decay of some heavy states (like in *leptogenesis* [369] or *GUT baryogenesis* [370]), in the dark sector first via decays[371] or dark first order phase transitions [372, 373, 374], or simultaneously in both sectors from the decay of a heavy particle [375].

The idea of combining DM compositeness and ADM is not new. Endowing DM with a new interaction, and making it not annihilate easily at late stages of the cosmological evolution open the possibility to form DM bound states, and of new distinct signatures. We now review past models that tried to do so, highlighting what is different from our attempt of making ACDM model asymmetric. Composite Asymmetric Dark Matter models were previously explored in the literature since the early days of *technicolor* (TC) theories [376, 377]. Unlike ACDM models, the field content of original TC theories is chiral and the mass of the composite technibaryon is naturally tied to the weak scale, given that the goal of such theories is to dynamically generate it. The chiral field content and the scale coincidence

[1] See [366] for an exception based on *mirror world* framework.

allows the possibility of having the transfer mechanism, the electroweak sphaleron [378], to decouple at temperatures at which the DM candidate starts to become non-relativistic. As a consequence, a Boltzmann suppression factor generates a hierarchy between the DM and visible number density asymmetries, and therefore a hierarchy in the masses needed to explain the DM abundance. Interestingly enough, the mass obtained from reproducing the observed DM relic density naturally falls into the TeV range, as predicted by TC theories [379, 380, 381, 382] (see [383] for a non-TC model in which the same happens)[2]. Other composite Asymmetric DM models instead do not link the scale of the DM with the EW scale. Typically they follow the route of predicting a $\mathcal{O}(1)$ relation between the DS and SM number densities, which implies $m_{\rm DM} \sim \mathcal{O}(1)$ GeV [384, 385, 386]. As previously stated, typical ADM models leave this connection unexplained[3]. As a consequence of the lightness of the DM candidate, the DS cannot be charged under the SM given current collider bounds. In such composite ADM models, the role of the new dynamics is not only to stabilize the DM candidate via residual symmetries, but to also open new avenues in the generation of the asymmetry, for example using dark sphalerons [388].

The rich spectrum of Asymmetric Composite Dark Matter models can be engineered to have peculiar signatures and cosmological histories [389, 390, 391]. In particular, the scarcity of anti-particles in the thermal bath can allow the formation of larger composite bound states like *dark nuclei* and *dark atoms*, leading to a very rich phenomenology [392, 393, 394, 395]. Hower, in the context of asymmetric ACDM models, not much attention has been given in actually discussing possible UV completions and asymmetry generation mechanisms.

The goal of this Chapter is to fill this gap. We start from ACDM models and try to extend them, sticking to the AS philosophy, in the most minimal way to build an UV completion that can dynamically generate the asymmetry for the DM candidate, and deplete its symmetric component. The completion should also be technically natural and not spoil the accidental IR symmetries responsible for the DM stability. Notice already that ACDM models differ from the previous composite asymmetric models presented above: the dynamical scale is unrelated to the EW scale, since it is set by requiring the correct DM relic abundance, and its values are typically in the range $10 \div 100$ TeV. Moreover, their field content is not chiral under the EW group, making the use of EW sphaleron impossible. Given the non-chiral nature of the dark quarks field content under dark color, also dark sphalerons are precluded. Since one of the main features of ACDM models are collider signatures, the mass of a ACDM candidate cannot be at the GeV scale. This implies that the asymmetries of the visible and dark sector cannot be related using standard model building tools as done in light composite DM models [396]. While there are mechanisms that allow a hierarchical asymmetry transfer [397], they typically rely on some coincidence of the DM scale with the scales of other processes, making such mechanisms fine-tuned

[2] In a certain sense, this class of TC-based models do not have a $\mathcal{O}(1)$ relation between the number densities, but naturally explain the relation in Eq. (5.1) by compensating an exponentially suppressed number density with a hierarchically larger mass of the technibaryon with respect to the proton mass.

[3] See [387] for an exception based on a common running of scales of the QCD and dark color group.

if applied to the ACDM scenario [398]. The additional constraint of having confined dark quarks in the model does not allow the possibility to have a Higgsed phase for the dark color, that could induce a first order phase transition [372, 373].

Given the model-building limitations stemming from the defining features of ACDM models, we will not pursue the route of relating the visible and DM asymmetries. We focus only on the generation of the DM asymmetry, leaving the SM asymmetry to be generated in an independent, unspecified way. Despite this, we find that there is indeed the possibility of generating simultaneously the SM and DS asymmetries in one particular realization of our models. We will briefly present it without working out the details.

The structure of the Chapter is the following: in Sec. 5.1 we review the ideas behind ACDM models, and their specific field content. In Sec. 5.2 the necessary conditions needed to asymmetrize ACDM models are given, with a step-by-step description of the features of the resulting models. In Sec. 5.3 the basic building block of the asymmetrization procedure of ACDM models is given. In Sec. 5.4 we present an asymmetric extension for each of the original *golden class* ACDM models, that feature a stable, asymmetric DM candidate; the asymmetrization of such models is based on the benchmark implementation, or slight modifications of it, described in Sec. 5.3. We then briefly sketch one of the phenomenological implications of this model building line in Sec. 5.5. Given that the goal we set for this Chapter is to delinate the model building constraints of AS applied to ADM, we leave details in the original work [44]. In Sec. 5.6 we also discuss a model in which DM is unstable but long-lived, and that can account for a simultaneous baryonic and DM asymmetry. In Sec. 5.7 we summarize the results and discuss alternative possibilities to generate the asymmetry in ACDM models to be explored in future works.

5.1 Review of Accidental Composite Dark Matter models

The idea behind Accidental Composite DM models [42] is to provide a DM candidate which is stable thanks to accidental symmetries in the Lagrangian, in a similar fashion to proton stability and baryon number conservation in QCD. The visible sector is thus enlarged with a DS made of new fermions Ψ, called *dark quarks* (DCquark, DCq), charged under a new *dark color* (DC) interaction, based on $\mathrm{SU}(N)_{\mathrm{DC}}$ or $\mathrm{SO}(N)_{\mathrm{DC}}$ gauge groups [4] that confines at a scale Λ_{DC}. The dark quarks are assumed to be in the fundamental representation of dark color, as well as vector-like representation under the SM. In particular, SM representations are taken to be "fragments" of the SU(5) GUT extension of the SM gauge group: the GUT framework motivates the choice of possible gauge representations for the DCquarks.

[4] Other confining gauge group like $\mathrm{Sp}(2N)$ or special group like G_2 were not considered in the original paper. Here we do not aim at making an analogous classification of DM models for the missing groups, so that we stick to the groups mentioned in the main text.

The DS renormalizable Lagrangian is simply given by:

$$\mathscr{L}_{\rm DS} = -\frac{1}{4}\,{\rm Tr}[\mathcal{G}_{\rm D}^{\mu\nu}\mathcal{G}_{{\rm D},\mu\nu}] + \overline{\Psi}_i(i\not{D} - m_\Psi)\Psi_i + y_{ij}\overline{\Psi}_i\Psi_j H + {\rm h.c.}\,, \tag{5.2}$$

where we have included a Dirac mass term m_Ψ for the DCquarks, given their vector-like nature. Below DC confinement, the dark quarks bind into *dark hadrons*:

- *dark pions* (DCπ), $m^2_{{\rm DC}\pi} \approx m_\Psi \Lambda_{\rm DC}$.
- *dark baryons* (DCb), $m_{\rm DCb} \approx N_{\rm DC}\Lambda_{\rm DC}$.

In SU(N)$_{\rm DC}$ models, the lightest DCb is stabilized by an accidental U(1)$_{\rm DB}$, the *dark baryon number*, under which all dark quarks rotate with the same phase, and by an accidental $\mathbb{Z}_2$ in SO(N)$_{\rm DC}$ models. The SM quantum numbers of the dark quarks must thus be chosen properly in order for this lightest DCb to be neutral and hence a good DM candidate. Charged DCπ are in general dangerous if protected by additional species symmetries, which must be broken either by Yukawas or by suitable higher dimensional operators. We focus on the so called *golden class models* (GC), in which all the extra species symmetries responsible for DCπ stability are broken by Yukawa with the SM Higgs. Neutral DCπ instead are always unstable at the level of 5d operators with the Higgs generated at the Planck scale $M_{\rm P} = 1.22 \times 10^{19}$ GeV, and are never good DM candidates. In App. J.1 we list the original GC models for reference . The cosmological evolution of ACDM models is rather simple and depends only on $\Lambda_{\rm DC}$ and m_Ψ. If $\Lambda_{\rm DC} \gg m_\Psi$, after DC confinement the DCb's go through a phase of non-perturbative annihilation, whose freeze-out determines the final DM abundance. Since in this regime both the DM mass and its annihilation cross-section are set solely by $\Lambda_{\rm DC}$, the DM abundance turns out to be a function of this parameter alone. In the absence of any pre-existing dark baryon asymmetry, the observed $\Omega_{\rm DM}h^2 \approx 0.119$ is reproduced for $m_{\rm DCb} \approx 100$ TeV.

If $\Lambda_{\rm DC} \ll m_\Psi$, instead, the cosmological evolution consists of two stages [399]: a first phase of perturbative annihilations among DCq's, which freezes-out around $T \approx m_\Psi/25$, followed, after DC confinement, by a phase of re-annihilation among DCbs. Indeed, in this regime the binding energy of DCbs is dominated by the Coulomb potential among the constituents rather than by confinement effects, so that the annihilation cross-section now is set by the Bohr radius $r_B \approx (\alpha_{\rm DC} m_\Psi)^{-1}$ of the bound state. Since $r_B \ll m_\Psi^{-1}$, the DCb-$\overline{\rm DCb}$ annihilation cross-section is much larger than that among the constituent DCq (see [400] for a detailed discussion of this regime in composite DM models). For simplicity, we will only analyze in the rest of the work the case $m_\Psi \ll \Lambda_{\rm DC}$. The presence of a pre-existing net dark baryon asymmetry alters in no way the different cosmological histories that we have outlined above: the requirement of annihilating the symmetric component only yields a different relation between the observed relic density $\Omega_{\rm DM}$ and $\Lambda_{\rm DC}$ or m_Ψ.

5.2 Making ACDM Models Asymmetric

In this Section we explore the different possibilities in order to make ACDM models asymmetric. Our goal is to write the minimal UV completions of the models of [42] that, at some UV scale $\Lambda_{\rm UV}$, can accommodate an asymmetry generation mechanism in the dark sector. Below $\Lambda_{\rm UV}$, we want to recover, at the EFT level, the original ACDM models. In other words, we want to build a UV completion for ACDM models with an initial non-zero asymmetry at the cutoff $\Lambda_{\rm UV}$. Of course, an asymmetric DM model makes sense only if it is possible to distinguish the DM candidate from its antiparticle. This very basic requirement already makes all the $\mathrm{SO}(N)_{\rm DC}$ models classified in [42] not suitable for asymmetrization: all the DM candidates in this case are of the form $(\overline{\Psi}_C\Psi_C)^n\Psi_R^m$, where Ψ_C (Ψ_R) is a DCq in a complex (real) representation of the SM[5]. Therefore, we shall assume in the following that the DS is charged under a $\mathrm{SU}(N)_{\rm DC}$ gauge group.

We stress again that the focus is to understand the consequences of Accidental Stabilty in ACDM models, not to give a common explanation to the asymmetry of the DS and of the visible one. One of the consequences of making DM asymmetric is to force a lower mass of the DCb $m_{\rm DCb}$ (or equivalently the confinement scale $\Lambda_{\rm DC}$) in order to satisfy cosmological constraints. Also, asymmetric DM models have different constraint coming from Indirect Detection, and in general have different phenomenology. In the following Sections we briefly sketch the necessary ingredients needed to build a succesful asymmetric ACDM model, from the generation of the correct amount of asymmetry to the annihilation of the symmetric component.

5.2.1 Sakharov conditions and DCb number

In order to generate an asymmetry in the DS, the model must satisfy the three Sakharov conditions [401]:

i) The presence of an out-of-equilibrium process.

ii) C and CP violation.

iii) Violation of the number species of the candidate to be asymmetrized.

The last condition is particularly delicate: in $\mathrm{SU}(N)_{\rm DC}$ models, the very same symmetry that we need to break in order to generate the asymmetry is the $\mathrm{U}(1)_{\rm DB}$ responsible for accidental DM stability. Therefore in order to satisfy the Sakharov conditions, this symmetry must be broken at some scale, possibly associated to new extra fields, but at the same time it must be recovered at the EFT level: indeed, our goal is to keep intact the IR physics of original ACDM models. This is a further constraint on the UV completion we are looking for: it must not mediate a fast decay of the DCb in order to describe the observed relic density. This in the spirit of [402], in which the authors engineered models of Asymmetric Dark Matter with a gauged $\mathrm{U}(1)_{\rm B-L}$ that was spontaneously broken in the UV, while kept as a global (approximate) symmetry in the IR, stabilizing the non-composite DM candidate. Instead here we explicitly break a global, ungauged symmetry, and do not

[5] In particular, such candidates do not carry any net species number.

rely on spontaneous symmetry breaking, since it would break $\mathrm{SU}(N)_{\mathrm{DC}}$ and forbid confinement.

In looking for minimal UV completions of asymmetric ACDM models, we restrict ourselves for simplicity to renormalizable UV Lagrangians.

5.2.2 How to break DCb number

Since ACDM models are vector-like, there is no analogue of the EW sphaleron [378] in the DS, unless we add a new gauge group under which DCquarks are chiral[6]. For the same reason, the DCquarks do not couple to the EW sphalerons. This implies that there is no way to break $\mathrm{U}(1)_{\mathrm{DB}}$ via non-perturbative effects, and we must resort to perturbative terms in the Lagrangian. If, by hypothesis, we restrict to renormalizable Lagrangians, adding only extra fermions will not allow to break in any way $\mathrm{U}(1)_{\mathrm{DB}}$. Indeed the only other terms compatible with $\mathrm{SU}(N)_{\mathrm{DC}}$ invariance are bilinear in the dark fermions: the extra gauge terms and Yukawas between the Higgs and another DCquark, in which the fermions form a $\mathrm{SU}(N)_{\mathrm{DC}}$ singlet. No $\mathrm{SU}(N)_{\mathrm{DC}}$ invariant bilinear can break $\mathrm{U}(1)_{\mathrm{DB}}$, since the complex nature of the $\mathrm{SU}(N)_{\mathrm{DC}}$ representations of DCquarks prevents real bilinears. Consistently with our hypothesis of minimality, we enlarge the DS with the addition of a scalar field ϕ. This scalar must fill a complex representation of $\mathrm{SU}(N)_{\mathrm{DC}}$ in order to carry a non-trivial $\mathrm{U}(1)_{\mathrm{DB}}$ charge. Since we want to leave untouched the light spectrum of the original models, we take this scalar to be heavier than Λ_{DC} and/or m_Ψ, so that it can later decay and disappear from present-day DM content. The only possible terms that we can add to the renormalizable interaction Lagrangian of the DS are:

$$\phi\Psi\Psi, \quad \phi\Psi\psi_{\mathrm{SM}}, \quad V(\phi, H) \ , \tag{5.3}$$

where $V(\phi, H)$ is the scalar potential. Notice that we have not included terms of the form $\phi\overline{\Psi}\Psi$: they do not violate the U(1) associated to the Ψ number. Moreover, if the scalar potential is to break $\mathrm{U}(1)_{\mathrm{DB}}$, it must contain terms of the form:

$$V(\phi, H) \supset \phi^3, \ \phi^4, \ \phi^3 H^* \ . \tag{5.4}$$

The use of such terms to break the dark baryon number has been explored previously in symmetric [403] and asymmetric [393] (although non ACDM) contexts. Similar ideas can also be found in the study of baryon number-violating processes in the SM alone [404, 405]. Terms containing the real combination ϕ^2, possible only for real ϕ, are not viable due to too fast decays. Notice that we need at least two terms involving the dark scalar to break the global $\mathrm{U}(1)_{\mathrm{DB}}$, since each operator in Eq. (5.3) is invariant under $\mathrm{U}(1)_{\mathrm{DB}}$ upon a different assignment of a dark baryon charge to ϕ. If there is such a surviving $\mathrm{U}(1)_{\mathrm{DB}}$, after the scalars decay the conservation of this enlarged $\mathrm{U}(1)_{\mathrm{DB}}$ implies that no asymmetry can be generated in the DS sector, assuming it is stored in the single lightest DCb species.
This last condition leads to three different realizations of Asymmetric ACDM models, according to the pair of $\mathrm{U}(1)_{\mathrm{DB}}$ violating operators present in the interaction Lagrangian:

[6]This might be problematic because even in simple models, the additional copies of DCquarks due to the new gauge group might bring SM Landau poles below the GUT scale.

- $\phi\Psi\Psi + V(\phi, H)$ (*class 1* models): These models will be explored in Sec. 5.4. Despite the breaking of $\mathrm{U}(1)_{\mathrm{DB}}$ at the renormalizable Lagrangian level, DM stability is guaranteed up to 5d operators included.
- $\phi\Psi\psi_{\mathrm{SM}} + V(\phi, H)$ (*class 2* models): these models predict unstable, but sufficiently long-lived DCb's. Some of these models will be illustrated in 5.6.
- No $\mathrm{U}(1)_{\mathrm{DB}}$-violating scalar potential (*class 3 models*). There are several possibilities to realize such models, depending on the nature of the two Yukawa portals: a "dark" Yukawa $\phi\Psi\Psi$ and a "mixed" Yukawa $\phi\Psi\psi_{\mathrm{SM}}$, two mixed Yukawa, two dark Yukawa. These models are not viable for $\mathcal{O}(1)$ couplings due to fast decay. We do not show these, leaving them to [44].

Therefore, we can consistently generate an asymmetry in the DS without spoiling the stability of the DM candidate only if the Lagrangian contains both a Yukawa and a $\mathrm{U}(1)_{\mathrm{DB}}$-violating term in the scalar potential. In this case, since the interactions of ϕ with the dark quarks constrain the possible representations under $\mathrm{SU}(N)_{\mathrm{DC}}$ to:

$$\phi \in \square\,, \begin{array}{|c|}\hline\square\\\hline\square\\\hline\end{array}\,, \square\square\,. \tag{5.5}$$

the only $\mathrm{SU}(N)_{\mathrm{DC}}$ gauge groups compatible with the terms in Eq. (5.4) are those with $N_{\mathrm{DC}} = 3, 4, 6, 8$. We remark that the role of the scalar is not to spontaneously break the dark color: the Higgsed phase inevitably makes the DM unconfined in the IR regime, and therefore with dangerous SM charges, excluding some highly non-trivial scenarios in the spirit of [406] in which the dark color symmetry is restored at low temperatures.

5.2.3 Generating the asymmetry

In order to build a successful asymmetric dark matter model, we must specify a proper out-of-equilibrium process to satisfy the Sakharov conditions. The easiest way to accomplish this is to consider heavy scalars (for example $M_\phi \gtrsim 10^{15}$ GeV $\sim M_{\mathrm{GUT}}$ as shown in Sec. 5.3.2) that decay as soon as the temperature of the plasma drops below its mass, like in the original GUT baryogenesis scenarios [370]. A necessary condition for the mechanism to work is that the scalar must have access to multiple decay channels with different dark baryon number in the final states. In viable models, a single heavy ϕ can decay to channels with different $\mathrm{U}(1)_{\mathrm{DB}}$ by inserting the pair of $\mathrm{U}(1)_{\mathrm{DB}}$-breaking operators chosen (for example the Dark Yukawa and the ϕ^3 term in the models of Sec. 5.4). However in this case the asymmetery turns out to be chirality suppressed as we explain in Sec. 5.3.

A simple solution to avoid the large suppression of the interference term, is to consider a second flavor of ϕ. For example, in models of Sec. 5.4, if the scalars are not degenerate, the decay

$$\phi_H \to \phi_L^\dagger \Psi\Psi \tag{5.6}$$

is allowed. As we will see, this decay violates the dark baryon number (if assigned to be conserved in the two-body decay), and therefore there are two channels with different dark baryon number for the heavy ϕ decay. Subsequent decays of the

lighter ϕ do not generate further asymmetries: they simply transfer to the other DCquarks their dark baryon number (up to the negligible asymmetry due to ϕ decays in more than 2 DCquarks). It's important to notice that in order for this scenario to work, the inverse decay processes must be suppressed, otherwise they will wash out any generated asymmetry. As we will show in Sec. 5.3.2, this translates into a bound on the mass of the heavy scalar, at fixed coupling, called the *weak wash-out condition*. For dimensionless Yukawa couplings $y \sim \mathcal{O}(0.1)$, this amounts to $M_\phi \gtrsim 10^{15}$ GeV. Besides, it is possible to show that these couplings get (non-multiplicatively) renormalized only at two-loop order. Hence, technical naturalness sets a lower bound on the Yukawas that can be estimated as $y \geq (16\pi^2)^{-2} \sim 10^{-4}$. This implies that the smallest scalar mass compatible with the weak wash-out condition and naturalness is $M_\phi \sim 10^{10}$ GeV.

5.2.4 Annihilating the symmetric part

Independently on the mechanism responsible for the generation of the asymmetry, in all these models it's possible on general grounds to relate the dynamical scale to the amount of asymmetry necessary to reproduce the correct DM abundance, requiring at the same time that the non-perturbative annihilations are sufficient to deplete the abundance of the symmetric DM component. In fact, if X is the DM and $\overline{X}$ its antiparticle and if we define

$$r \equiv \frac{n(\overline{X})}{n(X)} \,, \tag{5.7}$$

then solving the Boltzmann equation in the presence of an asymmetry gives the following relation between r evaluated at late times, r_∞, and the thermally averaged annihilation cross-section $\langle \sigma v \rangle \equiv \sigma_0$ [46],[365]:

$$r_\infty \approx \exp\left[-2\left(\frac{\sigma_0}{\sigma_{\rm WIMP}}\right)\left(\frac{1-r_\infty}{1+r_\infty}\right)\right] \,, \tag{5.8}$$

where σ_0 can be estimated as $\sigma_0 \approx \frac{25}{m_{\rm DCb}^2}$ and $\sigma_{\rm WIMP} \equiv \left(\frac{1}{23\ \text{TeV}}\right)^2$. In Fig. 5.1 we show how r_∞ depends on $m_{\rm DCb}$. As we can see, we need $m_{\rm DCb} \lesssim 50 \div 75$ TeV in order to have $r_\infty \lesssim 0.01$. Equivalently, discovering that the DM is composite and with mass in such range explicitly points to an asymmetric DM content.

At this point we can relate the dynamical scale to the asymmetry $\eta_{\rm DM}$ [46]:

$$\eta_{\rm DM} \approx 5\frac{m_p}{m_{\rm DCb}}\eta_b\,\frac{1-r_\infty}{1+r_\infty} \approx 2.2\times 10^{-14}\left(\frac{23\ \text{TeV}}{m_{\rm DCb}}\right) \,, \tag{5.9}$$

where $m_p \approx 1$ GeV is the proton mass. Notice that, unlike previous models such as in [393], we do not introduce any new gauged U(1) to deplete the symmetric component, and we only have a single DM candidate, not two oppositely charged species sharing the asymmetry.

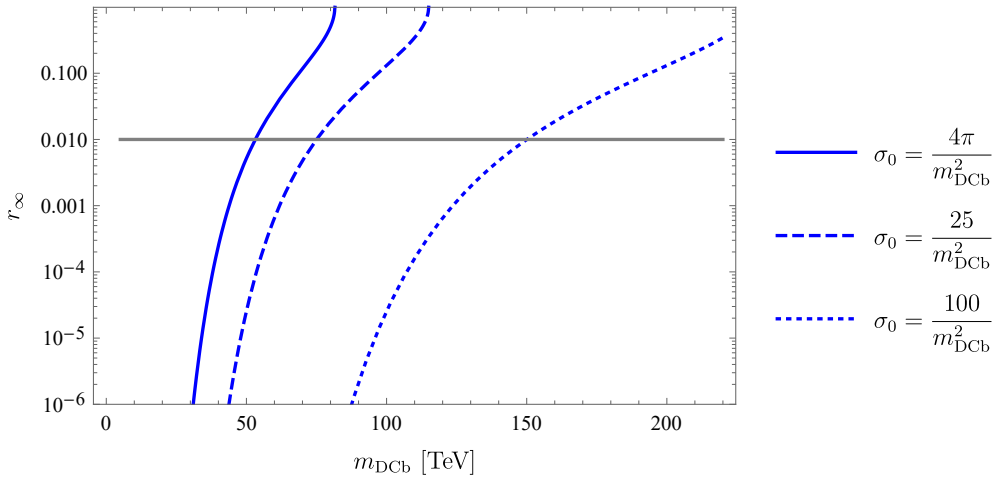

Figure 5.1: *r_∞ as a function of $m_{\rm DCb}$ assuming only non-perturbative annihilations. The solid line assumes a cross-section that saturates the perturbative unitarity limit. The dotted line corresponds to the annihilation cross-section obtained in QCD, which is 10 times larger. Given the large uncertainty, we shall use an intermediate value that reproduces the typical DM mass in ACDM models, $m_{\rm DCb} \approx 100$ TeV, as shown by the dashed line. Finally, the gray line represents the reference value $r_\infty = 0.01$.*

5.2.5 Brief cosmological history

Once the asymmetry has been generated from the decay of the heavy ϕ, the IR theory is essentially a standard ACDM model, with a non-zero asymmetry as initial condition for the (approximately) conserved $\mathrm{U}(1)_{\rm DB}$ charges. Above $\Lambda_{\rm DC}$, annihilation between DCquarks and their antiparticle are fast, and the two species are kept in chemical equilibrium. Below $\Lambda_{\rm DC}$, DCquarks will form DCbs and DCπ . In the GC model under scrutiny, the latter will decay into SM particles via Yukawa with the SM Higgs, or through a 5d operator generated at $M_{\rm P}$. Since in GC models all species symmetries are broken by the Yukawas[7], the various DCbs will undergo fast decays into the lightest one via the species number-breaking Yukawas with the Higgs once the masses are split due to SM gauge interactions[8]. Since all these interactions conserve $\mathrm{U}(1)_{\rm DB}$, the asymmetry will be stored and conserved in the lightest DCb containing the constituents that possess an initial asymmetry. The condition on $m_{\rm DCb}$ of Eq. (5.8) guarantees that there is no symmetric part left. In some asymmetric ACDM models, the possibility to radiate light SM states allows the DCbs to form *dark nuclei* [189, 394, 407], for temperatures below the typical dark nuclear binding energy E_B, with distinct phenomenological signatures. In some models the presence of the scalar in the UV Lagrangian (or equivalently of the specific asymmetry generation mechanism) is reflected in the IR with a Majorana mass term for the DCb, that can cause oscillations between the DCb and its antiparticle. Such effect will be discussed in Sec. 5.5.

[7] An exception to this is the $V \oplus N$ model, on which we will comment in Sec. 5.4.1.

[8] The mass difference can also be induced by different DCquarks bare masses.

5.3 Benchmark model

In this Section we will describe a simple model to show the mechanism of asymmetry generation and ensure that we can naturally obtain the correct amount of asymmetry. This benchmark model can be easily adjusted to fit in every ΛCDM model, as will be shown in Sec. 5.4. In particular, we consider as a benchmark case $\Psi = N$, $N_{\rm DC} = 3$, as shown in Table 5.1.

Field	$\mathrm{SU}(3)_{\rm DC}$	$(\mathrm{SU}(3)_c, \mathrm{SU}(2)_{\rm L})_Y$	$\mathrm{U}(1)_{\rm DB}$ (D)
N	3	$(1,1)_0$	1
ϕ	$\bar{6}$ (sym)	$(1,1)_0$	-2

Table 5.1: *Benchmark model field content.*

We will consider the following Lagrangian:

$$\mathscr{L} = \mathscr{L}_{\rm kin} + y\phi_{ij}N^iN^j + \lambda M_\phi \epsilon^{ijk}\epsilon^{i'j'k'}\phi_{ii'}\phi_{jj'}\phi_{kk'} + \lambda_4(\phi^\dagger\phi)^2 \,, \tag{5.10}$$

where ϵ stands for the totally antisymmetric Levi-Civita tensor of $\mathrm{SU}(3)_{\rm DC}$. In Eq. (5.10) $\mathscr{L}_{\rm kin}$ contains the kinetic and mass terms for ϕ and N, M_ϕ is the mass of ϕ, which is taken to be near the cutoff scale, and λ is a dimensionless parameter. Notice that in presence of SM fields, the only additional term allowed by gauge invariance and renormalizability to the ones in Eq. (5.10) is $\phi^\dagger\phi H^\dagger H$, which plays no role in $\mathrm{U}(1)_{\rm DB}$ asymmetry generation. A similar model can be found in [393], although employed in a different context. We remark that another possible benchmark model, in which the computations are essentially the same, is obtained by replacing N with the $\mathrm{SU}(2)_{\rm L}$ triplet V DCquark: indeed the Yukawa ϕVV can still exist if ϕ is a SM singlet by contracting the $\mathrm{SU}(2)_{\rm L}$ indices of the Vs together.

We will show a model with two flavors of ϕ, in which the asymmetry is generated via the out-of-equilibrium decay of the heaviest of the flavor of ϕ. This implementation leads to the correct amount of asymmetry, and will be employed in Sec. 5.4. The Yukawa coupling y and the trilinear coupling λ now carry also scalar flavor indices. Notice that the addition of the second flavor upgrades the U(1) related to ϕ rephasing to an SU(2). However, this symmetry is broken to the diagonal rephasing U(1) by different mass terms, and by the couplings y_i, λ_{ijk}. The easiest way to generate the asymmetry is to mimick GUT baryogenesis [370]. In this framework, the asymmetry is generated via the out-of-equilibrium decay of a heavy scalar. In order to do so we take a scalar ϕ_H heavier than the second ϕ_L: $M_H \gtrsim M_L$. Avoiding the hierarchy between the two flavors of ϕ keeps the model natural. For the sake of showing that the mechanism indeed works, we pick a specific region of the parameter space. In particular, we take the masses of the scalars close: $M_L < M_H \lesssim 2M_L$. In this way we avoid the possibility of ϕ_H decaying into a pair of light scalars $\phi_L^\dagger\phi_L^\dagger$ (however this is not mandatory and does not affect the discussion significantly). We stress that in this mechanism we do not need quasi-degenerate state, and the previous request is not a fine-tuning of the parameters. Both masses are taken to be much heavier than $\max(\Lambda_{\rm DC}, m_N)$, so that the IR spectrum of DCquark bound states is

untouched. The complete interaction Lagrangian therefore reads:

$$\begin{aligned}\mathscr{L}_I = \; & \frac{y_H}{2}\phi_H \overline{N}^c N + \frac{y_L}{2}\phi_L \overline{N}^c N + \frac{\lambda_{HHH}}{6} M_H \phi_H^3 + \frac{\lambda_{HHL}}{2} M_H \phi_H^2 \phi_L + \\ & + \frac{\lambda_{HLL}}{2} M_H \phi_H \phi_L^2 + \frac{\lambda_{LLL}}{6} M_H \phi_L^3 + \text{h.c.}\,,\end{aligned} \tag{5.11}$$

where we have taken the Yukawa couplings $y_{H,L}$ to be the same for the right-handed and left-handed components of the Dirac DCquark N. The couplings have been divided by numerical factors accounting for the symmetry factor in Feynman diagrams. In the model the heavy scalar has access to two decay channels with different dark baryon number D:

- $\phi_H \to \bar{N}\bar{N}$; $\Delta D = 0$
- $\phi_H \to \phi_L^\dagger N N$; $\Delta D = 6$

where ΔD stands for the difference of D charge between final and initial states. In principle ϕ_H can undergo a 4-body decay into $NNNN$, by simply attaching NN to the ϕ_L leg in the 3-body decay graph. This decay has the same ΔD of the 3-body decay, and can give a contribution to the asymmetry generation. However this decay is suppressed with respect to the 3-body decay by an additional coupling insertion and propagator suppression: it reduces to the 3-body decay only if the internal leg can go on-shell, which is true when it's ϕ_L. Therefore we will neglect this extra contribution.

The presence of the multiple decay channels with different ΔD is what allows the asymmetry generation. Indeed, let Γ, Γ_2 be the total decay width, and the decay width for the 2-body decay $\phi_H \to \bar{N}\bar{N}$ channel (with final $D = -2$) respectively. Neglecting further decay channels with respect to the two mentioned above, we can approximate the decay width in the $\phi_L^\dagger NN$ channel to be $\Gamma - \Gamma_2$. The decays of ϕ_H will produce the following contribution to the total D of the universe, accordingly to how the ϕ decays gets distributed in the two channels:

$$\frac{\Gamma_2(-2D_N - D_\phi) + (\Gamma - \Gamma_2)(-2D_\phi + 2D_N)}{\Gamma}\,. \tag{5.12}$$

By calling $\bar{\Gamma}_2$ the decay width in NN of $\phi_H^\dagger$, we get that the decays of $\phi_H^\dagger$ contribute as follows to the total D:

$$\frac{\bar{\Gamma}_2(2D_N + D_\phi) + (\Gamma - \bar{\Gamma}_2)(2D_\phi - 2D_N)}{\Gamma}\,, \tag{5.13}$$

where by CPT invariance the total decay width of the particle and antiparticle are the same. By putting together Eq. (5.12), Eq. (5.13), and assuming an equal initial abundance for ϕ_H, $\phi_H^\dagger$, we get that the asymmetry in dark baryon number generated after the decay of ϕ_H is:

$$\eta_{\text{DM}} = \frac{n_{\phi_H}}{s}\frac{1}{\Gamma}\left(\Gamma_2 - \bar{\Gamma}_2\right)(-4D_N + D_\phi) \equiv \frac{n_{\phi_H}}{s}\epsilon\,(-4D_N + D_\phi)\,. \tag{5.14}$$

So after all the $\phi_H, \phi_H^\dagger$ are decayed, even if their initial abundances were equal, a net dark baryonic asymmetry is created[9]. The asymmetry that is generated by the decay of the heaviest scalar is now split between the lighter scalar ϕ_L and the dark fermion N. If we can find a region in the parameter space in which we can neglect the $2 \to 2$ processes involving these two lighter species, the ϕ_L again undergoes an out-of-equilibrium decay. The scalar ϕ_L decays dominantly in $\bar{N}\bar{N}$, but it can also decay in $NNNN$. Thus in principle an asymmetry can be generated also at this step of the decay chain. However, the asymmetry parameter ϵ_L associated to the decay of ϕ_L is negligible with respect to the asymmetry ϵ of the heavy scalar decay: it's suppressed by an additional y^2 and by an additional propagator suppression. Therefore the asymmetry generated by ϕ_L decays can be neglected when computing the total dark baryon asymmetry, and such processes will simply transfer the net asymmetry generated by the decay of the heavy scalar to the DCquarks. After the decay of all the $\phi_L, \phi_L^\dagger$ no additional asymmetry will be generated, since there are no further active $\mathrm{U}(1)_{\mathrm{DB}}$-violating processes.
In order for this mechanism to be successful, we have to ensure two conditons:

- the presence of a complex phase in the decay amplitudes. It must come from both the phase in the couplings, and from the imaginary part of the graph associated to some particles going on shell in the propagators. The former is realized in our model by the presence of three phase-invariant, complex coupling combinations, as shown in Sec. 5.3.1: there are six couplings and 3 fields that can be rephased. The latter condition is accomplished considering fermionic bubbles inserted in the external scalar legs, or box diagrams with internal fermionic lines. Given that the mass of the scalars are both heavier than $2m_N$, the momentum circulating in such loops can make the virtual Ns go on-shell, giving an imaginary contribution to the integral. Bubbles can also be inserted in the internal propagators, but via a direct computation it can be shown that such amplitudes do not contribute to the asymmetry.

- We have to make sure that there is a region in the parameter space in which we can neglect washout processes coming from inverse decay and $2 \to 2$ scatterings. As shown in Sec. 5.3.1, by taking the two scalars heavy enough the inverse decays can be neglected: when the temperature of the bath drops below the mass of the heaviest available scalar the inverse decay process are kinematically blocked. The same argument can be applied to the scattering processes in the very weak washout regime, in which the decays are always the last processes to fall out thermal equilibrium. This requires $\Gamma_{\mathrm{D}}/H(M_\phi) \ll 1$, which sets a condition on the mass of the scalar and the coupling entering the decay process (mostly the two Yukawas y_i).

Taking the scalars heavy has the side effect of guaranteeing that the running of SM and dark color couplings is not modified below M_ϕ, avoiding the risk of Landau Poles at low energies. We stress that the freedom to take the scalars heavy comes with a price: the scalar sector will be hard to test. However, as will be shown in

[9]The presence of additional DCquarks does not spoil this argument since each decay channel has the same dark baryon number. This is because all the DCquarks are in the same representation of dark color and the dark baryon number can be assigned to be the N-ality of this representation

Sec. 5.5, its presence gives rise to IR phenomena like DM-$\overline{\text{DM}}$ oscillations that can be in principle testable.

As a final comment, we point out that the values of the couplings appearing in the potential should be such that the vacuum does not break $\text{SU}(N)_{\text{DC}}$, without tuning excessively the parameters (if tuning is allowed, the potential can always be made positive by taking for example λ close to 0). For $\text{SU}(3)_{\text{DC}}$ as gauge group and a single scalar flavor it has been shown in [408] that this is indeed possible by taking the couplings in a natural region in parameter space. With additional flavors, it should still be possible to realize this scenario without fine tuning by observing that a trilinear term in the potential can always be bounded between the sum of quadratic and quartic terms in the potential, up to $\mathcal{O}(1)$ factors. In later sections, we will always assume that it's possible to not break $\text{SU}(N)_{\text{DC}}$ by appropriately choosing the parameters, and that this procedure does not introduce unwanted fine tuning.

5.3.1 Estimating the conditions

In this section we will study in detail the two conditions mentioned previously. First we check if we can generate an interference in one of the decay channel to get a net CPV between the decays of $\phi_H, \phi_H^\dagger$. In the two-body decays, the asymmetry is generated by the interference between the tree level diagram and a two-loop one as shown in Fig. 5.2. In the three-body decays in Fig. 5.3, the asymmetry is generated by the interference among the tree level diagrams represented in Fig. 5.3a, that are identical up to the different virtual scalars circulating in the internal line, and the 1-loop diagrams in Figures 5.3b-5.3c. Indeed, a closer look at the diagram in Fig. 5.3d shows that it does not contribute to the asymmetry.

It's interesting to check that the two asymmetries are related, as implied by CPT invariance and unitarity [409]: indeed the three-body decay can be obtained by properly cutting the two-loops two-body decay. A quick parametric estimate tells that the asymmetry factor is expected to be proportional to $\epsilon \sim \lambda^2 y^2/(16\pi^2)^2$.

The remaining question is whether we can work in a regime in which we can neglect the washout processes.

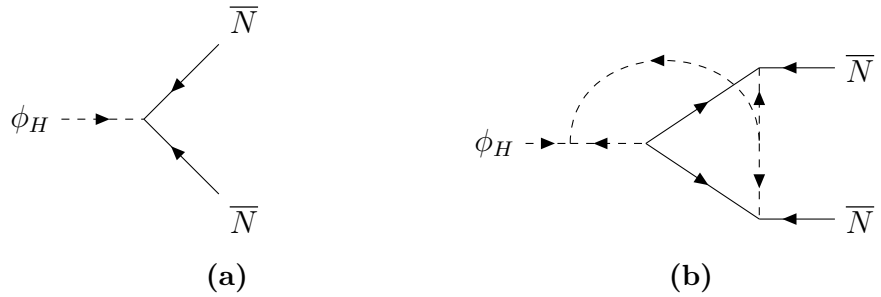

Figure 5.2: *Two-body decay of ϕ_H contributing to the generation of the asymmetry in N. The first loop diagrams appear only at two loops and an example is shown on the right. The arrows indicate the particle number flow.*

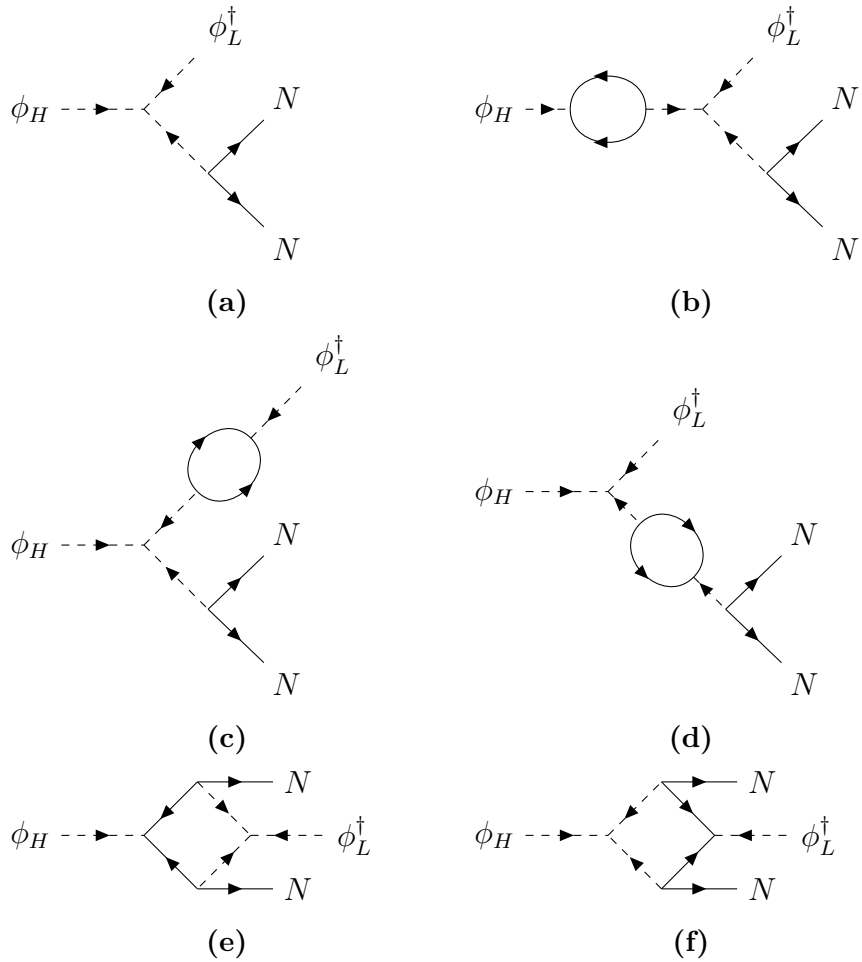

Figure 5.3: *Diagrams representing the three-body decays of ϕ_H. The different flavors of scalars flowing in the internal lines allows for a non-zero imaginary part in their interference term. It is possible to show that no contribution comes from diagram in Fig. 5.3d. The arrows indicate the particle number flow.*

Following the discussion in [410], the strength of the wash-out processes is determined by the parameter:

$$K \equiv \left(\frac{\Gamma_{\rm D}}{2H}\right)\Bigg|_{T=M_H} , \tag{5.15}$$

where $\Gamma_{\rm D}$ stands for a generic average decay rate of the scalars and H for the Hubble parameter. We are interested in $K \ll 1$, the so-called weak wash-out regime. In this regime, once that T drops below M_H, decays are not efficient and the number of ϕ_H gets no exponential suppression, so that $n_{\phi_H} \propto n_\gamma$. This guarantees the required departure from equilibrium necessary to produce a net asymmetry. We are also implicitly assuming that ϕ_H was in equilibrium at some large temperature and that interactions with the thermal bath (*e.g.* annihilations into dark gluons) are not efficient below $T = M_H$; this holds for masses larger than $\sim 10^{15}$ GeV. Moreover, under our assumptions, it is possible to relate the two- and three-body decay rates

Γ to the rates of their inverse processes $\Gamma_{\rm ID}$ and show that they negligible. Indeed, these inverse rates are given by:

$$\begin{cases} \Gamma_{\rm ID2} = \dfrac{n^{eq}_{\phi_H}}{n^{eq}_{N}} \Gamma_{\rm D2} \approx \left(\dfrac{M_H}{T}\right)^{\frac{3}{2}} e^{-\frac{M_H}{T}} \Gamma_{\rm D2} \\ \Gamma_{\rm ID3} = \dfrac{n^{eq}_{\phi_H}}{n^{eq}_{\phi_L}} \Gamma_{\rm D3} \ , \end{cases} \tag{5.16}$$

where we have defined

$$\Gamma_{\rm ID2} = n^{eq}_{N} \langle \sigma_{NN\to\phi_H} v_{\rm rel} \rangle, \quad \Gamma_{\rm ID3} = n^{eq,2}_{N} \langle \sigma_{NN\phi^\dagger_L \to \phi_H} v^2_{\rm rel} \rangle \ , \tag{5.17}$$

and the subscript number stands for the number of final bodies involved in a given process. Therefore, for $T < M_H$ and being $M_L < M_H$, Eq. (5.16) implies that the inverse decays are less efficient than direct decays, so that wash-out processes can be neglected. In this regime we can give a very simple estimate of the asymmetry that can be produced:

$$\eta_{\rm DM} \approx 2 \frac{\epsilon}{g_*} \ , \tag{5.18}$$

where $g_* \approx 10^2$ is the number of relativistic degrees of freedom, and the factor 2 comes from the fact that the three-body decay of ϕ_H has $\Delta D = 6$ while the DM DCb carries $D = 3$. From $\Omega_{\rm DM} \approx 5 \Omega_b$ we then have:

$$\Omega_{\rm DM} \propto m_{\rm DCb} \eta_{\rm DM} \approx \frac{2 \epsilon m_{\rm DCb}}{g_*} \approx 5 \eta_b m_p \ , \tag{5.19}$$

so that enforcing $m_{\rm DCb} \lesssim 75$ TeV translates in the following lower bound on ϵ:

$$\epsilon \gtrsim 3 \times 10^{-13} \ , \tag{5.20}$$

which can be easily accomplished with perturbative couplings.
For scalars lighter than $\sim 10^{15}$ GeV, the asymmetry in Eq. (5.18) is generated after the freeze-out of the scalars and receives a Boltzmann suppression approximately given by $x_{\rm f.o.}^{3/2} \exp(-x_{\rm f.o.})$, where $x_{\rm f.o.} = M_\phi / T_{\rm f.o.}$ and $T_{\rm f.o.}$ is the freeze-out temperature. Besides, the weak wash-out condition Eq. (5.15) now reads:

$$\left(\frac{\Gamma_D}{2H} \right) \Big|_{T = T_{\rm f.o.}} < 1 \tag{5.21}$$

This condition is equivalent to asking for the decay of the scalars to happen after their thermal freeze-out. As we shall see in the next Section, the largest asymmetry that we can get with heavy scalars is $\epsilon \approx 10^{-6}$. This implies that in order to satisfy the previous lower bound on ϵ we need $x_{\rm f.o.} \lesssim 18$. For the scalars annihilating into dark gluons or DCquarks, together with the condition on the naturalness of the couplings and the weak washout condition, this requires $M_\phi \gtrsim 10^{10}$ GeV.

5.3.2 Computation of the asymmetry

We are now ready to compute the asymmetry coefficient ϵ, defined as:

$$\epsilon = \frac{\Gamma(\phi_H \to \phi_L^\dagger NN) - \Gamma(\phi_H^\dagger \to \phi_L \overline{NN})}{\Gamma_H} \,, \tag{5.22}$$

where Γ_H is the total decay rate of ϕ_H. For simplicity, we shall take a very heavy scalar, such that Eq. (5.18) holds. As discussed in Sec. 5.3, the Lagrangian in Eq. (5.11) allows for three different physical phases, all of which are expected to appear in the expression of the asymmetry. Indeed, in App. J.2 we write the complete result for ϵ to show how the different phases contribute to the asymmetry. All the 1-loop computations have been carried out using `Package-X`[411, 412], taking the massless fermion limit $m_N = 0$. For simplicity, here we show the result obtained by fixing $\lambda_{LLL} = \lambda_{HLL} = 0$, thus isolating a single CP-violating phase (see App. J.2). In particular, such choice of coupling selects only the contributions coming from the diagrams in Fig. 5.3c and Fig. 5.3f. The asymmetry in Eq. (5.22) can be written as:

$$\epsilon = -\frac{4}{\Gamma_H}\frac{1}{6}\frac{1}{2M_H}\frac{1}{2}\int \mathrm{d}\Pi_N \mathrm{d}\Pi_N \mathrm{d}\Pi_{\phi_L} \sum_{i,j} \mathrm{Im}[\mathcal{C}_{T_i}^* \mathcal{C}_{L_j}] \,\mathrm{Im}[\mathcal{A}_{T_i}^* \mathcal{A}_{L_j}] \,, \tag{5.23}$$

where $\mathcal{A}_T$ and $\mathcal{A}_L$ are respectively the tree- and one-loop-level decay amplitudes, $\mathcal{C}_T$ and $\mathcal{C}_L$ the corresponding set of couplings, while Im denotes the imaginary part. Finally, the factor $\frac{1}{6}$ is the average over the initial dark color states. The sum runs over all possible diagrams. Here

$$\mathrm{d}\Pi \equiv g \frac{1}{(2\pi)^3}\frac{\mathrm{d}^3 p}{2E}$$

is the phase space measure. Under our simplifying assumptions we have:

$$\begin{aligned}\sum_{i,j} \mathrm{Im}[\mathcal{C}_{T_i}^* \mathcal{C}_{L_j}] \,\mathrm{Im}[\mathcal{A}_{T_i}^* \mathcal{A}_{L_j}] = &- \mathrm{Im}[\lambda_{LHH}^* \lambda_{HHH} y_L^* y_H] |y_H^2| \times \\ &\times \left(\frac{1}{(x-1)^2} \frac{M_L^2}{M_H^2 - M_L^2} \frac{C_{\mathrm{DC}}}{16\pi} - \frac{C'_{\mathrm{DC}}}{x-1} \mathcal{D}_2^{HH}\left(\frac{p_{N1}}{M_H}, \frac{p_{N2}}{M_H}, \frac{M_L}{M_H}\right)\right) \,,\end{aligned} \tag{5.24}$$

where $x \equiv \frac{(p_{N1}^\mu + p_{N2}^\mu)^2}{M_H^2}$, C_{DC} and C'_{DC} are dark color factors. The loop integral $\mathcal{D}_2^{HH}$ arises from the interference between the tree-level diagrams and the loop diagrams of Fig. 5.3f and is defined in App. J.2. The interference with diagrams of Fig. 5.3c is trivial and can be carried out analytically. Once that the integral in Eq. (5.23) is performed, we can compute the asymmetry generated in our model as a function of the different parameters.

In Fig. 5.4 we show the values of ϵ for some benchmark values of the relevant parameters.

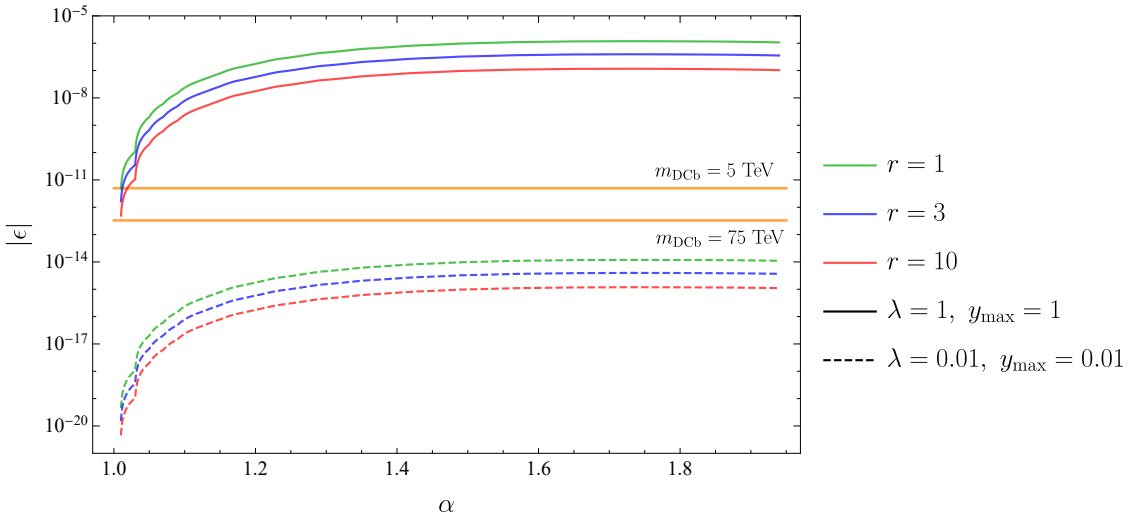

Figure 5.4: *Asymmetry corresponding to several benchmark values of the parameters as a function of* $\alpha = M_H/M_L$. *Here we have taken* $\lambda_{HHL} = \lambda_{HHH} = \lambda$ *and* $arg[\lambda^*_{LHH}\lambda_{HHH}y^*_L y_H] = \frac{\pi}{2}$ *for simplicity. We have defined* $r \equiv \left|\frac{y_L}{y_H}\right|$ *while always keeping* $y_{\rm max} \equiv \max(y_H, y_L) \leq 1$. *Finally, the orange solid lines show the limiting values for* ϵ *coming from the equivalent limiting values on* $m_{\rm DCb}$.

As we can see, in most of the cases we produce too much asymmetry and we need $\mathcal{O}(10^{-1})$ couplings to avoid the overclosure of the Universe. However, the plot is obtained by taking the largest possible CP-violating phase, so that we can gain some more parameter space by reducing its value. Moreover, this computation has been made for heavy scalars ($M_\phi \simeq 10^{15}$ GeV), with negligible wash-out processes and no Boltzmann suppression factor. If we take the scalar as light as $M_\phi \simeq 10^{10}$ GeV, instead, we get a suppression factor of order 10^{-6}, as anticipated, and still produce the correct abundance for TeV scale masses of the DCb. Even lighter scalars would lead to an underproduction of the needed asymmetry for $m_{\rm DCb} < 75$ TeV. Finally, a more general analysis is shown in the scatter plot of Fig. 5.5, where all the phases have been included, as discussed in App. J.2, sampling them randomly. Similarly to Fig. 5.4, we have assumed all the couplings in the scalar potential to have a common absolute value λ. As we can see, the qualitative results do not change with respect to the simplified choice of couplings.

The previous discussion shows that the presence of 2 scalars leads to a working asymmetry generation mechanism. If we tried instead to build a model with a single flavor of ϕ, the only way to get enough CPV phases is to take different Yukawas between left-handed and right-handed DCquarks. In order for both couplings to appear in any asymmetry generation process, a chirality flip of an internal DCquark line is needed. This brings an extra suppression of order $(m_\Psi/M_\phi)^2$ in an estimate for ϵ. Since M_ϕ must be large enough to avoid washouts as suggested in Sec. 5.3.1, and since we are working in the light $m_\Psi < \Lambda_{\rm DC}$ regime, ϵ will be too small to

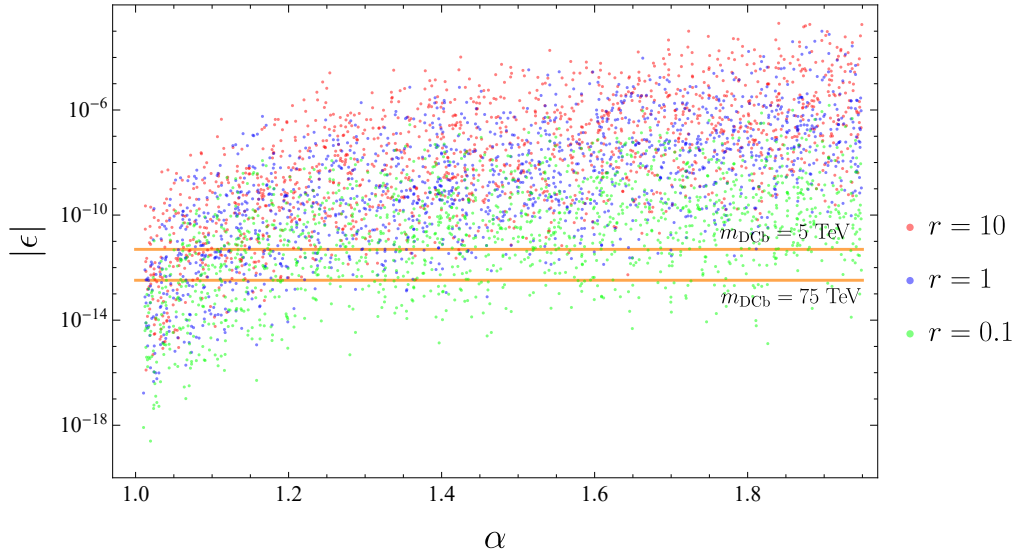

Figure 5.5: *Asymmetry obtained by randomly sampling the values of* $10^{-2} \leq \lambda, y_{\rm max} \leq 1$ *and the three physical phases in* $[-\pi, +\pi]$ *(see App. J.2). The colors of the dots correspond to three different values of* $r = \left|\frac{y_L}{y_H}\right|$.

generate the correct DM asymmetry as shown in Fig. 5.5.

5.4 Building the models: stable dark matter

In this Section we will comment on a specific implementation of the mechanism described in Sec. 5.3 in GC models, in which DM is stabilized by a remnant discrete symmetry. We mention that our analysis is done by studying renormalizable operators. A d-dimensional operator that breaks $\mathrm{U}(1)_{\rm DB}$ however could induce too fast DM decays. If it is generated at a cutoff scale $\Lambda_{\rm cut}$, the bound on the DCb lifetime reads:

$$\Gamma \simeq \frac{1}{8\pi}\left(\frac{m_{\rm DCb}}{\Lambda_{\rm cut}}\right)^{2(d-4)} m_{\rm DCb} \leq 10^{-53}\ \text{GeV}\ , \tag{5.25}$$

By substituting $\Lambda_{\rm cut}$ with $M_{\rm P}$ and $m_{\rm DCb} \sim 30$ TeV, we see that the only operator we need to worry about are up to $d = 5$. It can be shown that the same arguments that we will present prevent the existence of such operators[10]. We will not come back on this issue.

5.4.1 Non-colored GC models

We will analyze the original ACDM models whose DCquarks are not charged under $\mathrm{SU}(3)_c$. We will build models based on the ϕ^3 term used in Sec. 5.3, and on a slight modification based on ϕ^4 term.

[10]When substituting $M_{\rm P}$ in Eq. (5.25) we are tacitly assuming that at the cutoff $\Lambda_{\rm cut} = M_{\rm GUT} \simeq 10^{15}$ GeV only GUT partners of particles already present in the model are introduced. Actually the argument depends only on the fact that the only non-trivial $\mathrm{SU}(N)_{\rm DC}$ representations of extra fields below $M_{\rm P}$ are the (anti)fundamental for fermions and the 2-symmetric for the scalars.

Cubic ϕ^3

Since the goal is to implement the benchmark model, we fix $N_{\rm DC} = 3$. Notice that all the GC models whose DCquarks are not charged under $\mathrm{SU}(3)_c$ contain either the SM singlet N or the $\mathrm{SU}(2)_{\rm L}$ triplet V. Indeed if ϕ is a SM singlet, V can be seen as three copies of N, leading to a factor of three in the total asymmetry. If the scalar ϕ couples to either one of them, the computation of the asymmetry presented in Sec. 5.3.2 follows immediately. If there are additional similar couplings to other DCquarks, we get an additional DCb number asymmetry. This happens whenever in the model are present a DCquark and its "tilded" SM-conjugate partner (like L and $\tilde{L}$). This extra contribution to the asymmetry is numerically the same to the one computed in Sec. 5.3.2 (with the $\bar{N}\bar{N}$ finale states), differing only by some representation-dependent multiplicity coefficients. Each of these additional contributions are therefore expected to be equal to the asymmetry computed in the benchmark model, up to a $\mathcal{O}(1)$ coefficient. Since the quantum numbers of ϕ are such that the only additional Yukawa is of the form $\phi\Psi\Psi$, the models enjoy a $\mathbb{Z}_2$ symmetry, under which only the DCquarks are non-trivially charged. We summarize in Table 5.2 a possibile field content and the admitted extra Yukawa couplings for each of the original uncolored GC models. The ϕ^3 term is always present to ensure the implementation of the mechanism.

Model	ϕ	Couplings
V	$(\bar{6},1,1)_0$	ϕVV
$N \oplus L$		ϕNN
$N \oplus L \oplus \tilde{E}$		ϕNN
$V \oplus L$		ϕVV
$N \oplus L \oplus \tilde{L}$		$\phi NN, \phi L\tilde{L}$
$V \oplus L \oplus N$		$\phi VV, \phi NN$
$V \oplus L \oplus \tilde{E}$		ϕVV
$N \oplus L \oplus \tilde{L} \oplus \tilde{E}$		$\phi NN, \phi L\tilde{L}$
$L \oplus \tilde{L} \oplus E \oplus \tilde{E} \oplus N$		$\phi NN, \phi E\tilde{E}, \phi L\tilde{L}$
$N \oplus L \oplus \tilde{E} \oplus V$		$\phi NN, \phi VV$
$V \oplus N$	$(\bar{6},1,5)_0$	ϕVV

Table 5.2: *List of non-colored GC models, ϕ representation under $(\mathrm{SU}(3)_{\rm DC}, \mathrm{SU}(3)_c, \mathrm{SU}(2)_{\rm L})_Y$ and allowed Yukawa couplings (in addition to the ones of the original models with H). The models are based on a $\mathrm{SU}(3)_{\rm DC}$ gauge group and ϕ^3 $\mathrm{U}(1)_{\rm DB}$-breaking term.*

The only model in which a different SM representation for ϕ is needed to forbid the existence of multiple couplings is $V \oplus N$. This is the only GC model in which there are 2 extra unbroken U(1), the V and N species numbers. Each coupling with ϕ breaks one of them, or a combination of the two. Since these symmetries are only broken by the heavy ϕ, below M_ϕ the effective theory will enjoy the extra U(1) symmetries: afterall, the effective theory coincides with the original GC model in this regime. This implies that in general the model can possess a shared asymmetry between the two species in the IR. By properly choosing the SM representation of

ϕ, the scalars can be taken to couple to a single species, which for concreteness we will take to be V:

$$\mathscr{L} \supseteq \phi VV$$

In this case, even in the UV theory the N species number is unbroken, and therefore the dark sector will contain an asymmetric, non-thermally generated component stored in V DCquarks, and a symmetric, thermally produced component stored in the N DCquarks. Below confinement, the DCπ decay via the non-renormalizable 5d operators, leaving only the DCbs. By taking $m_{\rm DCb} \lesssim 75$ TeV, as shown in Sec. 5.2.4, only the asymmetric part survives. It is stored in the form of DCbs containing V as valence DCquark. Notice however that given the symmetries of the IR theory, the asymmetry will in general be shared among the different type of DCbs containing V. If instead the ϕ couples to both species, like:

$$\mathscr{L} \supseteq y_N \phi NN + y_V \phi VV \ , \tag{5.26}$$

both species number will be broken. Virtual ϕ exchange will mediate the conversion of DCbs with different species number, together with a DCπ emission (if kinematically allowed) or SM gauge boson radiation. For the sake of showing what can go wrong if the coupling in Eq. (5.26) is not forbidden, we assume a splitting $m_V - m_N \simeq \Lambda_{\rm DC}$. The rate of species conversion followed by a DCπ emission can be estimated roughly as

$$\begin{aligned} \Gamma &\approx \frac{y^2}{8\pi}\left(\frac{m_{\rm DCb}}{M_\phi}\right)^4 \Lambda_{\rm DC} \approx \\ &\approx \frac{1}{N_{\rm DC}}\left(\frac{y}{0.1}\right)^2\left(\frac{m_{\rm DCb}}{30\ \text{TeV}}\right)^5\left(\frac{10^{15}\ \text{GeV}}{M_\phi}\right)^4 10^{-46}\ \text{GeV} \ . \end{aligned} \tag{5.27}$$

Since DCπ quickly decay after production via the $M_{\rm P}$-suppressed 5D operator, they decay shortly after the species conversion of the DCbs. The same is true for direct gauge boson emission. For generic values of the coupling we expect N and V asymmetries to be of the same order, and therefore the DM abundance is roughly equally stored in the heavier and lighter DCbs. For this reason the fraction of DM energy injected in the SM is expected to be roughly proportional to the splitting-DCb mass ratio, which in this example is $\mathcal{O}(1)$. Such late energy injection is in tension with bounds coming from ID experiments [113],[413]:

$$\Gamma < 10^{-53}\ \text{GeV} \ . \tag{5.28}$$

Such constrain can be evaded by ad hoc model building, *e.g.* by tuning the splittings or by avoiding the simultaneous coupling of ϕ to both DCquarks, as accomplished with the representation presented in Table 5.2. In the other models, even if the DCb species conversion is kinematically allowed, it happens shortly after $\Lambda_{\rm DC}$ via renormalizable Yukawas with H, rather than with the different ϕ couplings. Therefore there are no dangerous late time DCπ decays and no further restrictions.

Quartic ϕ^4

In principle, it's possible to pick SU(4) as dark color gauge group, and to have a quartic potential term

$$V = \lambda \epsilon^{ijkl} \epsilon^{i'j'k'l'} \phi_{ii'} \phi_{jj'} \phi_{kk'} \phi_{ll'} \ , \tag{5.29}$$

with ϕ in the 10-dimensional symmetric representation of SU(4). This term substitutes the cubic term of the benchmark model, while the Yukawas with the DCquarks are the same. Notice that here the coefficient of the quartic term is automatically dimensionless, and it's $\mathcal{O}(1)$ in a natural theory. The difference with the mechanism of the benchmark model is that now the secondary decay channel for the heaviest scalar is a 4-body decay: $\phi_H \to \phi_L^\dagger \phi_L^\dagger N N$. In Fig. 5.6 we show the tree level expression and an example of loop level contribution.

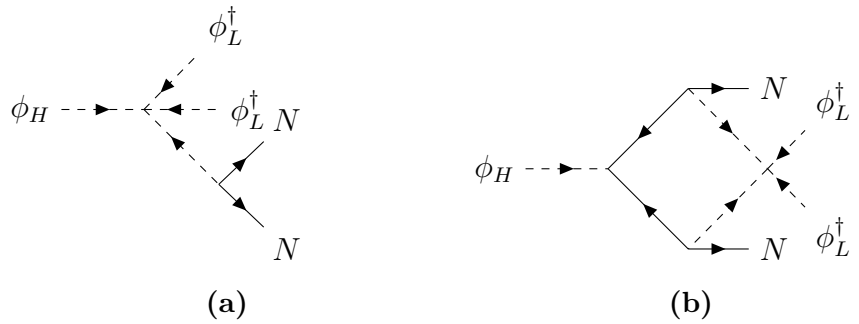

Figure 5.6: *Tree level process (left) and an example of a 1-loop correction (right) in the ϕ^4 models.*

For simplicity, we will not do the explicit computation, but we expect the generated asymmetry to be suppressed by an additional phase-space factor, leading even in this case to the correct amount.

It's interesting to see that even in this SU(4) scenario, there is still an accidental remnant $\mathbb{Z}_8$ symmetry, whose charges are listed in Table 5.3. DCbs, being made by

Field	$\mathbb{Z}_8$
ϕ	ω^2
Ψ	ω
SM	1

Table 5.3: $\mathbb{Z}_8$ *charges of the* SU(4) *model, where* $\omega = e^{i\frac{\pi}{4}}$.

four generic DCquarks Ψ, carry -1 charge under this $\mathbb{Z}_8$, making the lightest DCb stable.

5.4.2 Colored GC models

In this scenario it is not possible to directly use the benchmark model. Indeed the consequence of the cubic term in the potential is to force the hypercharge of ϕ to

be 0. This hypercharge assignment excludes the possibility of a Yukawa between ϕ and the two colored DCfermions, as seen from the field content of colored ACDM models in App. J.1. The need to have the Yukawa $\phi\Psi\Psi$ then forces ϕ to have non-zero hypercharge, and therefore to resort to a different potential term.

Quartic $\phi^3 H^*$

The only other way to write a potential term that violates the $\mathrm{U}(1)_{\mathrm{DB}}$ charge for ϕ (fixed by the Yukawa), and that can be used to mediate the decay of ϕ, is to involve an additional light scalar. If we stick to a single representation for ϕ, the only other light scalar is the Higgs field[11]. This forces the gauge group to be $\mathrm{SU}(3)_{\mathrm{DC}}$. If $\phi \in (\bar{6}, \bar{6}, 2)_{1/6}$ of $\mathrm{SU}(3)_{\mathrm{DC}} \times G_{\mathrm{SM}}$[12], we can build the following Yukawa:

$$\phi_{ij,ab} Q^{ia} \tilde{D}^{jb}, \tag{5.30}$$

and the following $\mathrm{U}(1)_{\mathrm{DB}}$-violating potential term:

$$\lambda \epsilon^{abc} \epsilon^{a'b'c'} \epsilon^{ijk} \epsilon^{i'j'k'} \phi_{ii'aa'} \phi_{jj'bb'} \phi_{kk'cc'} H^* \ , \tag{5.31}$$

where i, j, k and a, b, c are dark color and color indices respectively (the $\mathrm{SU}(2)_{\mathrm{L}}$ contraction is left implicit). No other terms are allowed by gauge invariance at the renormalizable level. Notice that the coefficient in the potential is dimensionless, like in ϕ^4 models of Sec. 5.4.1. The DCbs are stabilized by the same $\mathbb{Z}_2$ of ϕ^3 models, under which only the DCquarks are charged. Like for the models described in Sec. 5.4.1 in this scenario the secondary decay of the heaviest scalar is a 4-body process: $\phi_H \to \phi_L^\dagger Q \tilde{D} H$. A difference is that here three out of four of the final-state particles are ultrarelativistic (the DCquarks and H), making it more similar to the process described in Sec. 5.3. In Fig. 5.7 we show the tree level secondary decay channel and one of its 1-loop corrections.

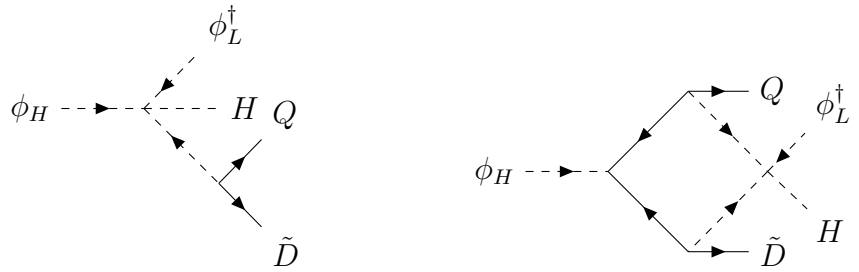

Figure 5.7: *Tree level process (left) and an example of a 1-loop correction (right) in the $\phi^3 H^*$ models.*

We expect that the asymmetry computed in this scenario is simply suppressed by an additional $\sim 1/(16\pi^2)$ phase space factor with respect to the one computed for

[11] and possibly its SU(5) partner, that we will not consider.

[12] This SM representation cannot fit in any SU(5) multiplet. A possible choice compatible with the SU(5) embedding is $(\bar{6}, 3, 2)_{1/6}$. In this case, we need at least 3 scalar flavors to write the $\mathrm{U}(1)_{\mathrm{DB}}$-violating potential.

the benchmark model in Sec. 5.3.2. By comparing with the results of Fig. 5.4 we expect that even in the presence of the additional phase space the correct amount of asymmetry can still be produced.

If $\phi \in (3,3,2)_{1/6}$, we could have built the same lagrangian terms, however the presence of the mixed Yukawa $\phi^\dagger \bar{l}\tilde{D}$ would have made the DM unstable, although sufficiently long-lived to satisfy current bounds.

5.5 DCb-$\overline{\text{DCb}}$ oscillations

A feature of the models presented in Sec. 5.4 is that the symmetry that stabilizes the DCb below the confinement scale is a $\mathbb{Z}_2$ under which the DCb is non-trivially charged. However, this implies that also its conjugate, $\overline{\text{DCb}}$, carries the same charge. Therefore, oscillations between the two are not forbidden by any quantum number that was protecting the DCb from decaying. A symmetry that would prevent this to happen is a symmetry that admits complex charges for the DCb (like $\mathbb{Z}_3$ or $\mathbb{Z}_4$). However, this is not what happens in the models under scrutiny. In a certain sense, our models have a "minimally" asymmetric DM candidate, given that the only property that distinguishes between the DM and its conjugate is the complex representation of the dark color gauge group, which is confined below Λ_{DC}. The presence of oscillations can significantly alter the cosmological history of the DM, regenerating the symmetric component, washing-out the asymmetry and possibly recoupling the annihilation process between the DCb and its conjugate [414],[415]. It's paramount to understand if they happen in the models we are considering. In the IR EFT the oscillations are due to a "Majorana" mass term that depends on whether the DCb is a fermion or a scalar, which in turn depends on the number of its constituent DCquarks:

$$\mathscr{L} \supseteq c m_{\text{DCb}} \mathcal{B}\mathcal{B} \quad (N_{\text{DC}} \text{ odd}) \,, \qquad \mathscr{L} \supseteq c m^2_{\text{DCb}} \mathcal{B}\mathcal{B} \quad (N_{\text{DC}} \text{ even}) \,, \tag{5.32}$$

where $\mathcal{B}$ is a generic DCb, c a dimensionless constant, and we assume that the scale at which the term is generated is around the confinement scale Λ_{DC}. For simplicity, we will work only the benchmark model of Sec. 5.3. In this case $N_{\text{DC}} = 3$, and the DCb is a fermionic candidate. For the $N_{\text{DC}} = 4$ case we expect a higher suppression of the oscillation-mediating operator due to its higher dimensionality. In order to show the role of the number of color, we will write the formualae without setting N_{DC} to its value of 3, and only setting it at the end to make the estimate of the mass splitting in our specific models. In a generic ACDM model the term in Eq. (5.32) can mix different DCb species, but this remark will not affect future conclusions about oscillations.

We have to estimate c in Eq. (5.32). The term in the UV theory that interpolates the Majorana mass term is:

$$\mathscr{L} \supseteq \frac{\lambda}{M_\phi^{3N_{\text{DC}}-4}} (N)^{N_{\text{DC}}} (N)^{N_{\text{DC}}} \,, \tag{5.33}$$

where as we have seen, $N_{\text{DC}} = 3$ for ϕ^3 models[13]. Since the operator is generated

[13]The $\phi^3 H^*$ model leads to a "Majorana term plus Higgs".

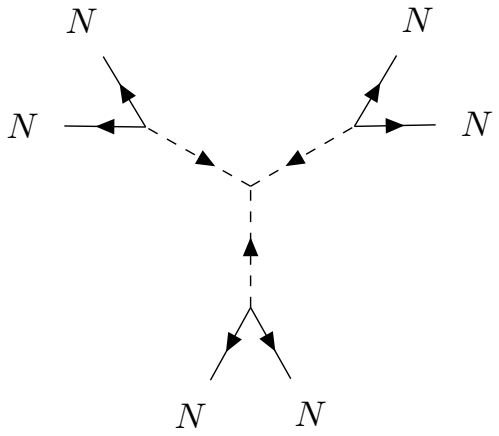

Figure 5.8: *UV diagram leading to the DCb-$\overline{\text{DCb}}$ oscillations in the IR phase.*

by integrating out the heavy scalars of mass of order M_ϕ, this scale appears in the effective operator in Eq. (5.33). In particular, the diagrams that generate this term are in Fig. 5.8.

This leads to an estimate for c:

$$c \sim k\lambda y^{N_{\rm DC}} \left(\frac{m_{\rm DCb}}{M_\phi}\right)^{3N_{\rm DC}-4} , \tag{5.34}$$

where the M_ϕ power have been set by the previous argument, while the $m_{\rm DCb}$ power comes from dimensional analysis and the fact that it is the relevant scale to use when interpolating the DCb with the DCquarks. Here λ is the dimensionless coupling appearing in the cubic term of the potential $\lambda M_\phi \phi^3$ for the ϕ^3 models. The coefficient k is non-perturbative in nature and we will assume that is $\mathcal{O}(1)$. For the $\phi^3 H^*$ model, the Majorana term is only obtained when the Higgs gets a vev, leading to a further suppression factor v/M_ϕ with respect to the pure ϕ^3 case. This small mixing term leads to a splitting in mass between the two mass eigenstates of the DCb-$\overline{\text{DCb}}$ system. The mass splitting comes from diagonalizing the matrix:

$$\begin{bmatrix} m_{\rm DCb} & m_{\rm DCb}\frac{\lambda y^{N_{\rm DC}}}{2}\left(\frac{m_{\rm DCb}}{M_\phi}\right)^{3N_{\rm DC}-4} \\ m_{\rm DCb}\frac{\lambda y^{N_{\rm DC}}}{2}\left(\frac{m_{\rm DCb}}{M_\phi}\right)^{3N_{\rm DC}-4} & m_{\rm DCb} \end{bmatrix} \tag{5.35}$$

The splitting is approximately proportional to the ratio of the off diagonal term and the diagonal one times the common mass $m_{\rm DCb}$, in the limit of small mixing (satisfied since $M_\phi \gg m_{\rm DCb}$). Therefore we have that the splitting is:

$$\Delta m \approx \lambda y^{N_{\rm DC}} m_{\rm DCb} \left(\frac{m_{\rm DCb}}{M_\phi}\right)^{3N_{\rm DC}-4} . \tag{5.36}$$

For the $\mathrm{SU}(3)_{\rm DC}$ ϕ^3 models, we have[14]:

$$\Delta m \approx 7\lambda y^3 \left(\frac{m_{\rm DCb}}{30\text{TeV}}\right)^6 \left(\frac{10^{16}\text{GeV}}{M_\phi}\right)^5 10^{-49}\ \text{GeV} . \tag{5.37}$$

[14]For the $\phi^3 H^*$ models there is the additional v/M_ϕ suppression.

Sizable oscillations (of the order of the initial asymmetric abundance) can begin only if they are faster than the Hubble rate H [414, 416]: $\Delta m \gtrsim H$. Since the present value of H is 10^{-42} GeV, it's possible to avoid this constrain by taking $m_{\rm DCb}$ in the multi-TeV range (as required by the constrain from elimination of the symmetric component and collider bounds), and M_ϕ around the GUT scale. In this case the DM candidate will not oscillate for all the practical purposes, and the asymmetry will be preserved. In the $\phi^3 H^*$ and ϕ^4 models the oscillations are further suppressed, therefore this effect cannot be seen at the current stage of cosmological history even in the other models presented.

However, in some of our models, even in the presence of fast oscillations, washout can be avoided due to the peculiarity of the IR dynamics. For concreteness, we will consider the $N_{\rm DC} = 3$, $\Psi = V$ model, in which the DCquark is a $\mathrm{SU}(2)_{\rm L}$ triplet. The DCb is itself a $\mathrm{SU}(2)_{\rm L}$ triplet, and it can form dark nuclei [394]. For TeV scale masses of the DCb, roughly up to $\mathcal{O}(1)$ fraction of the DCbs gets bound in a deuterium-like bound state, while much less for 100 TeV DCbs. DCbs inside a nucleus experience a different potential with respect to free DCbs, shifting the diagonal upper and lower entries of the mass matrix in Eq. (5.35) by $\mp E_n$ respectively. The same is true also in the SM for neutrons and antineutrons, where the energy difference between the two particles inside a nucleus is $E_{\bar{n}} - E_n \simeq 100$ MeV [417]. The energy splitting is due to the strong nuclear potential, and so to the SU(3) structure of QCD. Therefore, a similar result apply to our case, and we will assume, for practical purpose, the energy difference inside a dark nucleus between the two DCbs to be of order $\Lambda_{\rm DC}$. By following the arguments in [418], the oscillation rate inside a nucleus not only is slowed by the larger mass splitting induced by the nuclear potential, but it gets damped by scattering events between the constituents happening at a rate proportional to the inverse size of the nucleus $\Lambda_{\rm DC}$. This leads to a suppression of the oscillation rate by an extra factor

$$\frac{\Delta m}{\Lambda_{\rm DC}} = N_{\rm DC} \left(\frac{m_{\rm DCb}}{M_\phi}\right)^5 \simeq 0.7 \times 10^{-53} \left(\frac{m_{\rm DCb}}{30\mathrm{TeV}}\right) \left(\frac{10^{15}\mathrm{GeV}}{M}\right) , \tag{5.38}$$

forbidding oscillations even for lighter ϕ. So, for $M_\phi \lesssim 10^{14}$ GeV it's possible to regenerate via oscillations a symmetric component of the unbounded DCbs, while preserving the asymmetric component intact and stored in the dark nuclei, avoiding the washout of this component. Notice that this scenario is peculiar to our models: it needs the DCbs to be able to form dark nuclei and a small Majorana mass for the DCbs. The presence of a symmetric component of unbounded DCb's leads to residual annihilations that can in principle be tested using Indirect Detection experiments. Since the scalars are heavy, both for naturalness and to avoid washing out the asymmetry, they are hardly detectable at current or future collider experiments. Testing the presence of oscillations can therefore be a probe of the mass of the scalar. As a consequence of oscillations, unbounded DCb-$\overline{\rm DCb}$ residual annihilation is enhanced, and possibly it can even recouple. This suggests the possibility to probe the oscillation rate, and therefore M_ϕ, via ID experiments [414]. In general, we expect the DCb-$\overline{\rm DCb}$ annihilations to produce a number of DCπ, similarly to what happen in the SM with proton-antiproton annihilations [419]. Such channels

were analyzed in [420], although in different models of composite DM. For example, in the $N_{\rm DC} = 3$, $\Psi = V$ model we expect the DCb to be a $\mathrm{SU}(2)_{\rm L}$ triplet, and therefore the DCb-$\overline{\rm DCb}$ system can be decomposed in its different isospin components. Each of these components can annihilate in a different number of DCπ, consistently with $\mathrm{SU}(2)_{\rm L}$ invariance and G-parity (the conservation stems from the fact that the annihilation process proceeds through the $\mathrm{SU}(N)_{\rm DC}$ interaction, which conserves the other quantum numbers). Each of the final state DCπ will then decay in the SM, either via the chiral anomaly in photons, or via Higgs and other SM gauge bosons (if there are extra DCquarks and Higgs portals). A precise spectrum computation of such lines is outside the scope of the current work. To give a crude estimate of the feasibility to probe the residual annihilations, we assume that the number of DCπ in all relevant final states is $\mathcal{O}(1)$. Given that such states can then give rise to lines, we expect that the γ-ray spectrum will be peaked roughly at $m_{\rm DCb}/2$, although it will present a spread due to the multi-body nature of the DCb annihilation processes. Current experiments like HESS are sensitive to γ-rays in the multi-TeV range, and are able to exclude annihilation cross sections of order $\langle\sigma v\rangle \sim 10^{-22} \div 10^{-24}$ cm^3/s [421]. Although such exclusions are taken for monochromatic annihilation spectra, we will study two benchmark values of $\langle\sigma v\rangle$, to get a crude picture of whether or not it's possible at current experiments to probe the oscillations.

To recast the bound, we notice that in the oscillating case, for large oscillation periods $t_{\rm osc}$, the ratio between $\overline{\rm DCb}$ and DCbs is roughly $(t/t_{\rm osc})^2$, given that the probability of conversion is proportional to $\sin^2(t/t_{\rm osc})$ Therefore the quantity to be compared with the experimental limits is:

$$\left(\frac{t}{t_{\rm osc}}\right)^2 \langle\sigma v\rangle \approx \left(\frac{\Delta m}{H}\right)^2 \frac{25}{m_{\rm DCb}^2} \,, \tag{5.39}$$

where Δm is the DCb mass splitting of Eq. (5.37). This kind of estimate only works if the residual annihilation and elastic scattering processes do not make the oscillations lose their coherence, as suggested in [415, 416]. In our models this is possible because the elastic scattering with thermal bath particles can be suppressed via mass splitting of the DCb components (due for example to EW mass splittings in the V model) or be mediated by higher dimensional operators involving the Higgs (if N^3 is the DCb for example), while annihilations and scatterings with other DCbs are always Boltzmann suppressed in a fully asymmetric regime. So we will neglect such processes and use Eq. (5.39). We plotted the results in Fig. 5.9. The horizontal lines are due to the fact that Eq. (5.39) only works for $t \ll t_{\rm osc}$, since for t large enough the densities of particles and antiparticles will reach and oscillate around half the initial particle density. In this case the bound on the cross section (and therefore on $m_{\rm DCb}$) saturates since no larger value for $n_{\rm DCb} n_{\overline{\rm DCb}}$ can be reached. We checked that for $M_\phi \gtrsim 10^{10}$ GeV oscillations start only at temperatures too low for the residual annihilations to recouple and change the total DM abundance, therefore there is no thermal recoupling of the annihilations. For M_ϕ in the range of the plot in Fig. 5.9, the weak washout condition can be fulfilled by taking the Yukawa of the heavy scalar y_H to be around 10^{-3}. Notice that only a thin portion of the plane, around $M_\phi \lesssim 10^{13}$ GeV has a cross section in range of current γ-ray experiments.

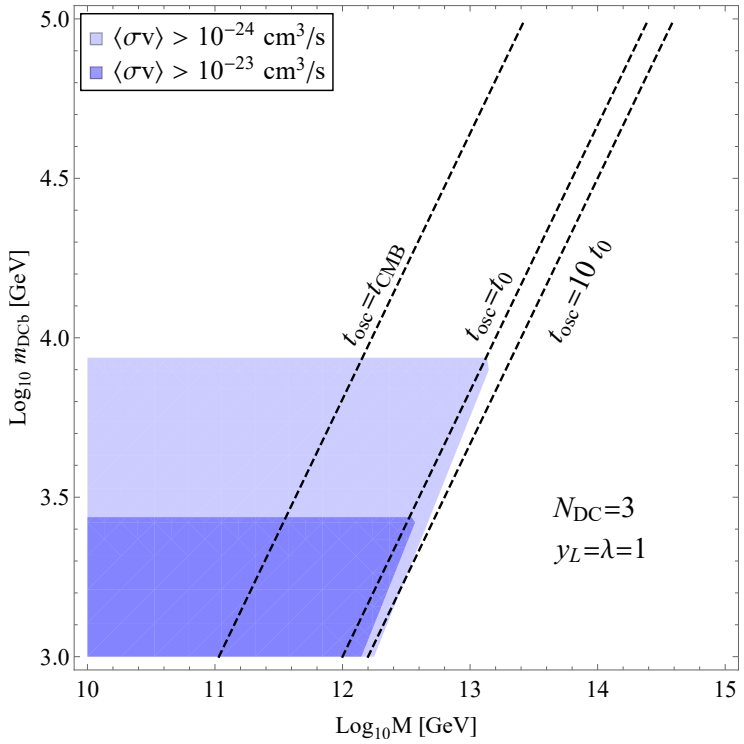

Figure 5.9: *γ-ray bounds from dwarf galaxies in the M_ϕ-$m_{\rm DCb}$ plane for two different values of the cross section. Bounds are computed by assuming $\lambda = y_L = 1$. Shadowed regions can be potentially tested and excluded.*

However, for lighter ϕ, oscillations can start even at CMB or before, as shown by the dashed lines. In this case, the asymmetry can be totally washed-out if it's not stored in dark nuclei. CMB bounds could then in principle be studied for such models, possibly leading to stronger bounds. To conclude, in our models the region 10^{12} GeV $\lesssim M_\phi \lesssim 10^{13}$ GeV can be probed by studying residual annihilations, while for $M_\phi \lesssim 10^{12}$ GeV bounds from CMB could be applied. For heavier M_ϕ no bound from oscillations arises. Another interesting fact to test the oscillations is that the asymmetry in the DCbs bound in dark nuclei is preserved, as argued in Sec. 5.5. This could lead to signatures of a dark nucleus "annihilating" with a $\overline{\rm DCb}$, and possibly to spectral shapes which are unique to our models.

What we have just shown is a genuine signature of the new physics responsible for the asymmetry generation (the scalars). Other hints to the asymmetric nature of the DM comes from other well studied phenomenological properties. As shown in Fig. 5.1, the value of the DM mass is lighter than in the symmetric ACDM scenario, in order to explain the observed DM abundance. Measuring a DM mass in the 50 TeV ballpark (at future colliders for example) would clearly exclude the symmetric scenario. The fact that DCb is lighter in ADM scenarios also gives differences in other typical signatures of compositeness (detection of Gravitational Waves (GW) from the confinement phase transtion, characteristic Direct Detection signatures, formations of dark nuclei,...). These makes asymmetric ACDM models a phenomenologically distinct possibility.

5.6 An example of unstable DM

In Sec. 5.4 we classified models with a stable DCb. Another possibility is for the DM to be unstable but still long-lived. In this class of models $\mathrm{U}(1)_{\mathrm{DB}}$ breaking happens through a potential term for the scalar ϕ and a mixed Yukawa between the DS and SM (unlike class 1 models in which the Yukawa was only involving DS fields). The presence of the mixed Yukawa forces ϕ to be in the (anti)fundamental of $\mathrm{SU}(N)_{\mathrm{DC}}$. The DCb decays into SM but is long lived for heavy enough scalars. The potential term forces additional M_ϕ suppression in $\mathrm{U}(1)_{\mathrm{DB}}$-breaking EFT operator due to more internal propagators, bringing its dimensionality to be 7. In this case bounds on the lifetime of the DCb can be satisfied for $M_\phi \gtrsim 10^{15}$ GeV, as low as allowed by the weak washout condition for $\mathcal{O}(0.1)$ couplings. We leave the full classification of field content to our original paper [44]. We sketch in a particular case the consequences of this class of model on BAU. For concreteness we fix $G_{\mathrm{DC}} = \mathrm{SU}(3)_{\mathrm{DC}}$ and the complex dark scalar ϕ in its antifundamental, while the dark quarks field content (and the respective SM quantum numbers) are the left handed $Q = (3,2)_{1/6}$ and $D = (3,1)_{-1/3}$ and their right-handed conjugates (in principle there are many different possibilities, here we only pick one). The possible portals are:

$$\mathscr{L} \supseteq y_q \phi \bar{q}_L Q_R + y_d \phi \bar{d}_R D_L + \text{h.c.} \,, \tag{5.40}$$

while the cubic term for the scalars is:

$$M \lambda \epsilon^{ABC} \epsilon^{ijk} \phi_{Ai} \phi_{Bj} \phi_{Ck} \,. \tag{5.41}$$

where ABC are flavor indices and ijk the $\mathrm{SU}(3)_{\mathrm{DC}}$ gauge indices, and M is the scale of the cubic interaction. This term would vanish in the presence of a single flavor: that's why we need 3 at least to make a non-zero cubic term. Notice that this type of asymmetric extension is rather general since it can be applied to any $\mathrm{SU}(N)_{\mathrm{DC}}$ model listed in [42] simply by pairing the DCquarks to the corresponding SM fermions.

As a side effect of the mixed Yukawa, the SM and DS asymmetries are related by an unbroken symmetry rotating the DCquark and SM fermion:

$$n_{\mathrm{SM}} = -n_{\mathrm{DS}} \,. \tag{5.42}$$

Notice that now the Yukawa couplings in Eq. (5.40) become 3×3 matrices: there is enough room to have a physical CP violating phase. Eq. (5.42) implies the following relation between the dark and visible sector abundances:

$$\Omega_{\mathrm{B}} = \frac{m_p}{m_{\mathrm{DCb}}} \Omega_{\mathrm{DM}} \tag{5.43}$$

so that for $\mathcal{O}(1)$ TeV DM mass, assuming the correct DM relic density Ω_{DM} is reproduced, the asymmetry generated from this process in the visible sector is only a subdominant fraction of the present-day observed SM asymmetry. Hence, despite being a viable model on his own, it cannot be a successful baryogenesis model unless the DM mass itself is in the GeV ballpark. In fact, this last possibility can

be achieved by taking the model with the SM singlet N as the only DCquark. Indeed, due to the absence of any charged state, it is possible in principle to take $\Lambda_{\rm DC}$ close to the GeV scale and achieve a scenario where the asymmetry is correctly generated for both the SM and DM. The fermionic field content of such model forces ϕ to carry hypercharge in order to have a non trivial Yukawa with the SM. So the potential term has to be $\phi^3 H^*$, which, together with the request of the existence of the Yukawa, determines the SM quantum number of ϕ, and forces the Yukawa to be

$$\phi^\dagger q_L N \ , \tag{5.44}$$

where ϕ has to carry also $\mathrm{SU}(3)_c$ and $\mathrm{SU}(2)_{\rm L}$ charges. Investigating this scenario is outside the scope of this work.

5.7 Summary

In this Chapter we showcased how a theory-inspired principle like Accidental Stability of DM can be applied to phenomenologically interesting models such as Asymmetric Dark Matter. We have built a class of possible minimal UV completions to the Accidental Composite Dark Matter models that can produce the correct amount of asymmetry in the DS. In order to do so, we simply added two flavors of a heavy scalar ϕ, with mass around the cutoff of the full theory $\Lambda_{\rm cut}$. The scale $\Lambda_{\rm cut}$ can be taken to be the Planck scale $M_{\rm P}$, the GUT scale (which is a natural cutoff of ACDM models), or as low as $M_\phi \simeq 10^{10}$ GeV, provided the additional fields at the cutoff do not introduce new non-trivial $\mathrm{SU}(N)_{\rm DC}$ representations. Below the mass of the heavy scalars, the model behaves like the original ACDM models with a non-zero initial asymmetry. The DM candidate is a dark baryon, and with our choice of gauge representations it is accidentally stable in the IR theory. The mechanism we provided can be easily adapted to all the golden class ACDM models, even allowing the possibility for generic SU(5) GUT completions and asymmetry generation in the visible sector via, for example, thermal leptogenesis. The symmetric component of DM is eliminated thanks to non-perturbative annihilations below $\Lambda_{\rm DC}$ due to residual dark color interactions, provided $m_{\rm DCb} \lesssim 75\,\mathrm{TeV}$, without the need of having new dark forces. This lower even further the scale of the DM mass (and of the typical resonances of the dark sector) with respect to the original symmetric ACDM models. The asymmetry generation mechanism can produce enough asymmetry for $m_{\rm DCb}$ in this range. The choice of the coupling of the UV sector responsible for the asymmetry generation can be made natural (or at most fine-tuned at the percent level). We have also built models in which the DM candidate is unstable but long-lived enough to satisfy current experimental bounds, and additionally that can generate the correct BAU. Future directions of this work include the exploration of other mechanisms that can give a common explanation to the asymmetry of the DS and the visible sector. The main obstruction to this kind of construction is that collider constraints force $\Lambda_{\rm DC}$ to be larger than at least the TeV scale. This implies a natural hierarchy between the asymmetries in the two sectors, that can hardly be achieved through usual cogenesis mechanism realized via renormalizable

portals[15]. Possible solutions to this problem could be found exploiting peculiarities of the strong dynamics [422], and the dynamical generation of the $\Lambda_{\rm DC}$ scale.

[15]Unless one consider hierarchical couplings in the two sectors. This simply moves the problem from the hierarchy of the asymmetries to the hierarchy of the couplings.

Chapter 6

Conclusions

In this Thesis we have analyzed possible DM interactions, both with other Dark Sector particles and with ordinary Standard Model particles.

In Chapter 1 we introduced the Dark Matter fluid, why it is phenomenologically necessary to describe the Universe and the need to characterize its properties. We introduced the possible interactions in terms of the DM quantum numbers, highlighting their implications for detection strategies.

In Chapter 2, we discussed the possibility for the DM to interact with SM gauge forces. Barring some exceptions [59], the only possibility is for the DM to be the neutral component of a n-dimensional EW multiplet with hypercharge Y (indicated as n_Y) [43, 50, 52]. We call this candidate WIMP. We consider both fermion and scalar candidates. We distinguish between real WIMPs, with odd n and $Y = 0$, and complex WIMPs, with even n and semi-integer Y or odd n and integer Y. Real WIMPs automatically satisfy phenomenological constraints from lightness of DM and Z boson direct detection. Complex WIMPs need an inelastic coupling with the Z, which is induced by a non renormalizable operator with a suitably large coefficient. This condition forces the multiplets to be $n_{1/2}$ for $n < 12$ (from calculability) and 3_1, 5_1, otherwise such operators have a too large dimensionality and hence suppression to generate the correct splitting. Additionally, for complex multiplets with non-maximal Y the condition for DM to be the lightest implies the existence of another operator generating the correct mass splitting hierarchy. In both cases we always assume operators mediating the WIMPs decay to be suppressed to guarantee the DM stability. We completely characterized the thermal history of the DM particle as a function of its EW charges, and predicted its mass via thermal freeze-out calculations. In order to obtain reliable results, especially for larger EW charges, we had to include both Sommerfeld enhancement [49] and Bound States Formation [51] in the computation of its annihilaton cross section. The obtained masses for the fermions range from 1.1 TeV for $2_{1/2}$ up to more than 50 TeV for $n \geq 7$. The lightest fermionic candidates, the $2_{1/2}$, 3_0, 3_1 and $4_{1/2}$, have masses of 1.1 TeV, 2.9 TeV, 2.9 TeV, 4.8 TeV respectively. These are suited to be tested at future proposed muon colliders [53]. Promising channels to probe these candidates are mono-X, with X $= \gamma, W$. Real WIMPs also have a model independent macroscopic decay

length of order few cm. This implies that for such DM particles disappearing tracks (DT) can be observed at future colliders. This signature is very strong, especially for the 3_0, while for larger n it becomes comparable to mono-X. Complex WIMPs have a lifetime that depends on the precise splitting hiearchy induced by the UV operators, and hence in this case tracks are not a robust prediction. We find that the for fermionic WIMPs, a 6 TeV machine can exclude at 95% confidence level the $2_{1/2}$ and 3_0 with a combination of mono-γ and mono-W and DT respectively. Instead the 3_1 and 5_1 need roughly a 8 and 12 TeV machine via mono-X. Scalar WIMPs are heavier than their fermionic candidates and have smaller production cross sections, making them more challenging to test at colliders. Larger n candidates are too heavy to be probed at such facilities. Instead, we found that future Direct Detection experiments like DARWIN [54] can in principle test the full landscape of the EW DM via spin-independent scattering, with the exclusion of the $2_{1/2}$ and 5_1. This paves the way to determine whether or not DM interacts via ordinary SM gauge bosons. We also analyzed other signatures such as residual annihilations in prospective Indirect Detection experiments [55]. This can in principle be a powerful signature for large n multiplets, but it suffers from large theoretical uncertainties that need further study to be tamed.

In Chapter 3 we considered the scenario in which the DM is a SM gauge singlet. In this case the interaction between the Dark Sector and the SM can happen through portal operators, that are made by the product of SM and DM singlet operators. In the past decade this scenario has received a lot of attention due to the fact that there are only 3 possible portals between the SM and DS at the renormalizable level [63, 64, 67]. In our work we focused on a less explored possibility, namely that the portal between the DS and the visible sector is a non-renormalizable portal. While this might seem a less minimal hypothesis, there are plenty of realistic and simple models in which the leading portal appears at higher dimensionality (see for example [72, 73, 74]). In order to be as general as possible, we characterized the DS via two scales: $\Lambda_{\rm UV}$, the scale of the cutoff at which the portal operator is generated, and $\Lambda_{\rm IR}$, the typical mass gap of the theory. We studied several non-renormalizable portal operators, as a function of their dimensionality D and their quantum numbers. Inclusive production cross-sections, leading to missing energy signatures, are a model-independent prediction and have already been studied to set bounds on the portals [76]. We extended the work studying in this framework displaced decays, detected at beam dumps and neutrino experiments. Indeed the lightest DS particle (LDSP) can decay back to SM particle through the same operators, provided it is not protected by any symmetry. First, we computed the production of DS states in meson decays, direct partonic production and bremsstrahlung from proton (the latter channel being often neglected). We then computed the fraction of events leading to LDSP decays inside displaced detectors at proton beam dumps and neutrino experiments, under mild theoretical assumptions assumptions. We found out that the future neutrino experiment DUNE will set bounds for $\Lambda_{\rm IR}$ in the MeV range up to $\Lambda_{\rm UV} \simeq$ few TeVs on the Z-portal $J^\mu_{\rm DS} H^\dagger D_\mu H$. Similar results hold also for a generic dimension 6 JJ portal. These bounds are stronger than the ones derived from LHC searches. Instead, for non-renormalizable Higgs portals the couplings to the proton of the beamline is too weak to put constraints stronger than the ones from resonant

production through Higgs decays at LHC. Notice that in the framework we used to characterize the DS we cannot say anything about the cosmology of the model. Indeed we set bounds thanks to unstable resonances that decay in the detectors, far from the production location. While these resonances are an expected feature of strongly coupled DS, they are not guaranteed to always exist. In particular, they cannot constitute the DM abundance due to their instability.

In Chapter 4 we entertained the possibility that the interaction between DM and visible particles is absent or negligible. We studied if it is possible to say something about self-interactions of DM thanks to how its clustering properties, which imprint on how visible matter clusters, are modified. We expanded previous work done for Yukawa-like interactions [83]: if the mediator is massless (or very light), the ratio β between the self-interaction strength and gravity cannot be larger than 5×10^{-3} [83]. In the previous work, bounds were set via linear cosmology prediction confronted against CMB [23] and BAO [4] data. We expanded this line of work by employing galaxy surveys data, like the ones from BOSS [3], namely the galaxy power spectrum P_g and the galaxy bispectrum B_g. In order to use the full shape of the galaxy power spectrum and tame the first non-linear corrections to the cosmological evolution of perturbations, we had to resort to the Effective Field Theory of Large Scale Structures [88, 89], and related pipelines [353, 354]. While current galaxy surveys are not powerful enough to significantly improve the past bound, future surveys like Euclid [84] will improve the upper bound on β at least by a factor of 2. The bispectrum can help to tighten constrain on the bias parameters [85] needed to model the galaxy density field.

The focus of the discussion has been purely phenomenologically driven. It is interesting to also understand how theoretical insights can complement this approach. One of the few well established DM properties is its stability on cosmological time scales. This suggests that a symmetry is protecting DM from decaying. Global symmetries seem to be at odds with general properties of a quantum theory of gravity [41]. Therefore DM must be protected by an accidental symmetry in the IR arising from gauge invariance in the UV. One possible class of models achieving this are Accidental Composite DM models [42]. The Dark Sector is endowed with a new vector-like confining gauge group responsible for binding dark quarks into stable dark baryons, which play the role of DM. In this case DM stability in the IR is essentially identical to proton stability in the SM. In Chapter 5 we tried to apply this idea to models of Asymmetric Dark Matter (ADM) [45, 46]. Composite ADM models have been studied in the past due to very peculiar features such as formation of Dark Nuclei, that can lead to potentially interesting experimental signatures [189, 394, 407]. However there was no thorough study of possible UV completions of such models accounting for the generation of the asymmetry. With the guidance of the Accidental Stability principle we have completely classified such models. The simplest mechanism to naturally make DM asymmetric is to introduce two heavy decaying scalars ϕ (with $M_\phi \gtrsim 10^{10}$ GeV) charged under the new confining group, and couple it to the DM. Having more than one scalar is a necessary condition to get enough CP violation. We found that the only dark gauge groups allowing for an asymmetry are $\mathrm{SU}(N)_{\mathrm{DC}}$. We implemented the mechanism for models with gauge group SU(3) and SU(4) (al-

though in some cases also SU(6) and SU(8) should be possible). The symmetric DM component is depleted by dark baryons annihilations through their contact interactions, provided DM is lighter than ~ 75 TeV. Once integrated out, the scalar can potentially induce oscillations between DM and its antiparticle, provided they are not bound in a dark nucleus. This can have interesting phenomenological consequences, such as residual DM annihilations. However we could not reconcile the asymmetry generation of DM with the generation of baryon asymmetry, except in a single model.

From here, several directions can be taken to further push our understanding of DM. To mention just a few, computing bounds from Indirect Detection can offer a complementary probe to DD for heavy WIMPs. In order to to this, NLO corrections to the non-relativistic potentials are needed.

The model-independent formalism employed for singlet DM could be extended to include other observables, like production inside neutrino detectors from LDSP particles disintegrating against nuclei. This would allow to probe longer LDSP lifetimes, that could now be the DM. Additionally, a further study on model-independent cosmological bounds of these secluded Dark Sectors could prove helpful in exploring the parameter space.

The bounds from cosmology on the self-interaction could be extended to more realistic models, such as interactions mediated by vector gauge bosons. The main difficulty is that, unlike Yukawa interactions which are always attractive, vector-mediated interactions are both repulsive and attractive, depending on the sign of the charges. This suggests that structures growing in the universe will be preferentially neutral. Therefore the effect of the self-interaction falls faster than $1/r^2$. In this case, we expect growth to be dominated by gravity, and potentially the large logarithms due to different background evolution could disappear and make the β bounds much weaker. Another possible avenue is to study cosmological observables that test directly violations of the equivalence principle, like the squeezed bispectrum for multiple tracers. This has a peculiar pole structure in Fourier space, that is not found in ΛCDM [94], and that could potentially distinguish the two models robustly. Another natural follow-up is to study the self-interaction outside the fifth force regime, and make the mediator either oscillate ($m_\phi > H_0$), or to make up dark energy ($m_\phi \simeq H_0$). In both cases the introduction of this new scale could potentially generate signatures such as shifts of BAO, and lead to powerful constraints.

In conclusion, the goal of the Thesis was to chart the landscape of possible DM interactions, and to give an experimental roadmap to characterize this mysterious fluid that makes up for the majority of pressureless matter in the Universe.

Appendix A

WIMP stability

In this appendix we discuss the stability of the various EW candidates.

A.1 Real WIMPS

In the case of the 3_0 candidate, the renormalizable operators $\chi H^\dagger H$ and χHL, for scalars and fermions, respectively, can induce fast DM decay. We assume these operators to be forbidden by a symmetry (e.g. a discrete $\mathbb{Z}_2$-symmetry) acting only on the DM sector. For all the other n_0-plets with $n \geq 5$, instead, $\mathbb{Z}_2$-odd operators are accidentally absent at renormalizable level.

Higher dimensional operators that break the $\mathbb{Z}_2$-symmetry are in general expected to be generated at the ultraviolet cut-off scale $\Lambda_{\rm UV}$. We sketch here the operators of lowest dimension that can induce the decay of scalar and fermionic WIMPs for generic n:

$$\mathscr{L}_{\rm s} \supset \frac{C_1^{(s)}}{\Lambda_{\rm UV}^{n-4}}\chi(H^\dagger H)^{\frac{n-1}{2}} + \frac{C_2^{(s)}}{\Lambda_{\rm UV}^{n-4}}\chi W_{\mu\nu}W^{\mu\nu}(H^\dagger H)^{\frac{n-5}{2}} + \cdots \tag{A.1}$$

$$+ \frac{C_w^{(s)}}{\Lambda_{\rm UV}^{n-4}}\chi(W_{\mu\nu}W^{\mu\nu})^{\frac{n-1}{4}} + \frac{C_{3\chi}^{(s)}}{\Lambda_{\rm UV}}\chi^3 H^\dagger H, \tag{A.2}$$

$$\mathscr{L}_{\rm f} \supset \frac{C_1^{(f)}}{\Lambda_{\rm UV}^{n-3}}(\chi HL)(H^\dagger H)^{\frac{n-3}{2}} + \frac{C_2^{(f)}}{\Lambda_{\rm UV}^{n-3}}(\chi\sigma^{\mu\nu}HL)W_{\mu\nu}(H^\dagger H)^{\frac{n-5}{2}} + \cdots \tag{A.3}$$

$$+ \frac{C_w^{(f)}}{\Lambda_{\rm UV}^{n-3}}(\chi HL)(W_{\mu\nu}W^{\mu\nu})^{\frac{n-3}{4}} + \frac{C_{3\chi}^{(f)}}{\Lambda_{\rm UV}^{3}}\chi^3 HL, \tag{A.4}$$

where $\mathrm{SU}(2)_{\rm L}$ contractions are implicit, and the dots indicate operators of the same dimension with different combinations of W and H fields.[1] Higher-dimension operators with additional SM fields or derivatives are of course also possible. The first operators in the two equations above are just the renormalizable operators of the

[1] If $(n-1)/4$ is not integer, the operator with the highest number of W fields in Eq. (A.2) is $\chi(H^\dagger H)(W_{\mu\nu}W^{\mu\nu})^{\frac{n-3}{4}}$. Similarly, for the fermions in Eq. (A.4) it is $(\chi\sigma_{\mu\nu}HL)W^{\mu\nu}(W_{\rho\sigma}W^{\rho\sigma})^{\frac{n-5}{4}}$.

3_0-plet case "dressed" with extra Higgs insertions. The dominant contribution to the decay width at tree-level always comes from the operator with the highest number of W insertions (namely $(n-3)/2$ for fermions and $2\lfloor(n-1)/4\rfloor$ for scalars). Notice that for fermionic DM, dipole-like operators with an odd number of W fields can always be constructed. In the last operator in both Eq. (A.2) and Eq. (A.4), χ^3 is the unique isospin triplet constructed out of three $\mathrm{SU}(2)_\mathrm{L}$ irreducible representations of odd isospin [96, 123]. These operators contribute to the WIMP decay at one-loop as

$$\Gamma_{\mathrm{s,f}} \sim \frac{M_\chi}{2048\pi^5}\left(\frac{\alpha_2(n^2-1)}{4\pi}\right)^{\frac{n-3}{2}}\left[C_{3\chi}^{(s,f)}\left(\frac{M_\chi}{\Lambda_{\mathrm{UV}}}\right)^q\right]^2, \tag{A.5}$$

where the exponent $q = 1$ (3) holds for scalars (fermions). For both scalar and fermionic WIMPs these are the dominant contributions for multiplets with $n > 5$.

More precise results for specific n_0-plets have been computed in Ref.s [96, 123] but do not modify our conclusions. For *all* the scalar n_0-plets, DM decay is induced by a dimension 5 operator, and the required scale for stability is well above M_{Pl}. As a consequence, the stability of scalar WIMPs can be determined only by understanding the subtle issues related to the fate of discrete symmetries in quantum gravity [423]. For fermionic representations, DM decay is instead induced by dimension 6 operators for $n \leq 5$, and dimension 7 operators for $n > 5$, and the DM stability can be determined within quantum field theory.

A lower bound on Λ_{UV} is obtained by requiring the DM lifetime to be long enough to circumvent cosmological bounds [424, 425] ($\tau_{\mathrm{DM}} \gtrsim 10^{19}$ sec) or astrophysical bounds on the decay products of decaying DM [113, 426, 427] ($\tau_{\mathrm{DM}} \gtrsim 10^{28}$ sec). We can then quantitatively measure the required *quality* of the $\mathbb{Z}_2$-symmetry by considering the ratio between the minimal Λ_{UV} allowed by the constraints and the WIMP freeze-out mass. A naive dimensional analysis (NDA) estimate of Λ_{UV}, assuming all the Wilson coefficients to be $\mathcal{O}(1)$, is given in Table 2.1 for all the relevant n_0-plets.

A.2 Complex WIMPs

The Lagrangian in Eq. (2.6) preserves the DM number parity and as a consequence the DM is automatically stable. Gauge invariant interactions beyond those of Eq. (2.6) can however induce fast DM decay. Here we discuss whether the effect of these operators can be small enough to allow the DM to be accidentally stable. Throughout this discussion we not only require the DM lifetime to be long enough to circumvent cosmological bounds [424, 425] ($\tau_{\mathrm{DM}} \gtrsim 10^{19}$ sec) but also to satisfy the stronger astrophysical bounds on decaying DM [113, 426, 427] ($\tau_{\mathrm{DM}} \gtrsim 10^{28}$ sec).

For $2_{1/2}$ and 3_1 we can write renormalizable interactions $\overline{\chi^c} H e_R$ and $\overline{\chi} L^c H$ that break the DM number and lead to a fast DM decay. These EW multiplets require a DM number symmetry, for example a discrete $\mathbb{Z}_2$-symmetry acting only on the DM field to provide a viable DM candidate.

For even multiplets with $Y = 1/2$ and $n > 2$, we can write the following series of higher dimensional operators inducing DM decay

$$\mathscr{L}_{\text{even}} = \frac{C_1}{\Lambda_{\text{UV}}^{n-3}}\overline{L^c}\chi(H^\dagger H)^{\frac{n-2}{2}} + \frac{C_2}{\Lambda_{\text{UV}}^{n-3}}\overline{L^c}\chi W_{\mu\nu}W^{\mu\nu}(H^\dagger H)^{\frac{n-6}{2}} + \\ + \frac{C_3}{\Lambda_{\text{UV}}^{n-3}}\overline{L^c}\chi(W_{\mu\nu}W^{\mu\nu})^{\frac{n-2}{4}} + \frac{C_4}{\Lambda_{\text{UV}}^{n-3}}\overline{L^c}\sigma^{\mu\nu}\chi W_{\mu\nu}(H^\dagger H)^{\frac{n-4}{2}} + \frac{C_5}{\Lambda_{\text{UV}}^{2}}\overline{\chi}\chi^c\overline{L^c}\chi \ , \tag{A.6}$$

where the Higgs bosons are appropriately contracted to make every term an $\text{SU}(2)_\text{L}$ singlet. For $4_{1/2}$, the leading contribution to DM decay comes from the operators with coefficients C_1 and C_4, while for $n \geq 6$ this is given by the operator with coefficient C_5 by closing the χ loop and attaching $(n-2)/2$ $W^{\mu\nu}$ operators, in a similar fashion to real candidates [47]. In all cases, we need at least $\Lambda_{\text{UV}} > 10^{10} M_{\text{DM}}$ for $\mathcal{O}(1)$ Wilson coefficients to preserve DM stability. This lower bound is incompatible with the upper bound on the UV physics scale required to generate the inelastic splitting δm_0. This result implies that the DM stability depends upon the properties of the UV physics generating the neutral splitting in Eq. (2.8).

For the 5_1 WIMP the lowest dimensional operators inducing DM decay are

$$\mathscr{L}_5 = \frac{C_1}{\Lambda_{\text{UV}}^2}(\overline{\chi}L^c H)(H^\dagger H) + \frac{C_2}{\Lambda_{\text{UV}}^2}(\overline{\chi}\sigma^{\mu\nu}L^c H)W_{\mu\nu}. \tag{A.7}$$

These require $\Lambda_{\text{UV}} > 10^{10} M_{\text{DM}}$ to ensure DM accidental stability which is again incompatible with the upper bound of $\Lambda_{\text{UV}} < 20 M_{\text{DM}}$ needed to generate the inelastic splitting.

Appendix B

Complex WIMP classification

In this appendix we give further details on our complex WIMP classification. In Sec. B.1 we explicitly classify the non-renormalizable operators introduced in Chapter 2. In Sec. B.2 we give the results for scalar WIMPs.

B.1 UV Operators

In Chapter 2 we showed that in order to make complex WIMPs with $Y \neq 0$ viable, new UV sources of splitting between the charged and neutral components and among the neutral components are necessary. In Eq. (2.6) we showed how the neutral splitting can be generated by $\mathcal{O}_0$ and the charged-neutral splitting by $\mathcal{O}_+$. Here we take a step back and investigate the generality of this choice.

The general form of an operator responsible for a Majorana mass term for a fermionic χ_N after EWSB is

$$\overline{\chi}(y_0 + y_{0,5}\gamma_5)\mathcal{I}\chi^c H^{4Y} \ , \tag{B.1}$$

where the H^{4Y} is necessary to match the hypercharge of the χ^2 piece, while $\mathcal{I}$ is a $\mathrm{SU}(2)_\mathrm{L}$ tensor. We are crucially assuming that the Higgs is the only scalar picking a VEV after EWSB. Under this assumption, since the Higgs is a boson, the only surviving $\mathrm{SU}(2)_\mathrm{L}$ structure is the totally symmetric combination. This can be seen as the symmetric combination of $2Y$ Higgs pairs in the isotriplet representation (the isosinglet is antisymmetric and vanishes identically), so that we are left with $\mathcal{O}_0$ defined in Eq. (2.6) and its axial counterpart with the γ_5 insertion. The latter can be shown to give only subleading contributions to the mass splitting between the neutral components of χ. Assuming y to be real, the shift on δm_0 induced by $y_{0,5} \neq 0$ with respect to its expression in Eq. (2.8) is

$$\delta m_0 \to \delta m_0 \sqrt{1 + 4\,\mathrm{Re}[y_{0,5}]^2 \frac{\Lambda_\mathrm{UV}^2}{M_\mathrm{DM}^2} \left(\frac{v}{\sqrt{2}\Lambda_\mathrm{UV}}\right)^{8Y}} \ , \tag{B.2}$$

which is highly suppressed for $\Lambda_\mathrm{UV} > M_\mathrm{DM} > v$. The operator $\mathcal{O}_0$ in Eq. (2.6) is then the dominant contribution to the inelastic splitting among the neutral components.

The isospin structure and field content of $\mathcal{O}_+$ is already the minimal required to generate additional splitting between the charged components, the only possibility is again to change its chiral structure writing the general operator inducing charged-neutral splitting as

$$\overline{\chi}T^a(y_+ + y_{+,5}\gamma_5)\chi H^\dagger\sigma^a H \ . \tag{B.3}$$

Similarly to the neutral case, the γ_5 insertion leads to a subleading shift in the mass splittings with respect to the value of Eq. (2.16)

$$M_Q^2 \to M_Q^2 + y_{+,5}^2\frac{v^4}{16M_{\rm DM}^2\Lambda^2}(Q-Y)^2 \ . \tag{B.4}$$

Finally, we comment on the implications on DD signals. Both operators with the γ_5 insertions give additional contributions to the SI cross-section and match to the effective operators:

$$\begin{aligned}\mathscr{L}_{\rm eff}^{\rm SI} =& \tilde{f}_q m_q \bar{\chi} i\gamma_5\chi\bar{q}q + \frac{\tilde{g}_q}{M_{\rm DM}}\bar{\chi}i\partial^\mu\gamma^\nu i\gamma_5\chi\mathcal{O}^q_{\mu\nu} + \\ &+ \tilde{f}_G\bar{\chi}i\gamma_5\chi G_{\mu\nu}G^{\mu\nu}.\end{aligned}$$

However, all these operators are strongly momentum-suppressed [428, 429], so that their corrections to $\sigma_{\rm SI}$ are expected to be $(q/m_N)^2 \sim 10^{-6}$ smaller than those from Eq. (2.5.1), and thus negligible.

B.2 Complex Scalar WIMPs

Following the discussion in Chapter 2 for the fermions, supported by the previous App. B.1, the minimal Lagrangian for a scalar complex WIMP is

$$\begin{aligned}\mathscr{L}_{\rm S} &= |D_\mu\chi|^2 - M_\chi|\chi|^2 + \frac{y_0}{\Lambda_{\rm UV}^{4Y-2}}\mathcal{O}_0^S + y_+\mathcal{O}_+^S + \text{h.c.}\,, \\ \mathcal{O}_0^S &= \frac{1}{2(4Y)!}\left(\chi^\dagger(T^a)^{2Y}\chi^c\right)\left[H^{c\dagger}\frac{\sigma^a}{2}H\right]^{2Y}\ , \\ \mathcal{O}_+^S &= -\chi^\dagger T^a\chi H^\dagger\frac{\sigma^a}{2}H\,.\end{aligned} \tag{B.5}$$

Conversely to the fermionic case, no additional operators can be written to generate the fundamental mass splitting. The neutral and charged *squared* mass splitting, $\mu_Q^2 = M_Q^2 - M_{\rm DM}^2$, can be written as

$$\begin{aligned}\mu_0^2 &= 4y_0 c_{nY0}\Lambda_{\rm UV}^2\left(\frac{v}{\Lambda_{\rm UV}\sqrt{2}}\right)^{4Y}\ , \\ \mu_Q^2 &= \frac{\mu_0^2}{2} + 2M_{\rm DM}\delta_g Q^2 + \text{sgn}(Q)\sqrt{\left(\frac{4Y\delta_g M_{\rm DM}}{\cos\theta_W} - \frac{y_+v^2}{4}\right)^2 Q^2 + \frac{\mu_0^2}{4}\frac{c_{nYQ}^2}{c_{nY0}^2}}.\end{aligned} \tag{B.6}$$

The linear mass splittings, $\delta m_Q = M_Q - M_{\rm DM}$, are then given by $\delta m_Q = \mu_Q^2/(2M_{\rm DM})$. Notice that for $Y = 1/2$ all the operators are renormalizable and any dependence on the cutoff disappears.
The lower bound on δm_0 from DD is identical to that for fermions, since $\sigma_{\rm SI}$ does not change. Instead, the BBN bound differs since the one-loop decay channel $\chi_0 \to \chi_{\rm DM}\gamma$ now is now heavily suppressed with respect to the three-body decays. As a consequence, the BBN condition becomes

$$\Gamma_{\chi_0} \equiv \Gamma_{\bar{\nu}\nu} + \Gamma_{\bar{e}e} > 6.58 \times 10^{-25}\ {\rm GeV}\,, \tag{B.7}$$

which explains why the bound on $\delta m_0^{\rm min} \simeq 4-5$ MeV for scalars is so much stronger than the one for fermions, as shown in Fig. 2.2. For $Y \neq 1/2$, the lower bound on δm_0 sets the upper bound of the allowed window for $\Lambda_{\rm UV}$

$$10\, M_{\rm DM} < \Lambda_{\rm UV} \leq \left(\frac{2y_0 c_{nY} v^{4Y}}{2^{2Y}\delta m_0^{\rm min} M_{\rm DM}}\right)^{\frac{1}{4Y-2}}\,, \tag{B.8}$$

which is the analogous of Eq. (2.18) for scalar WIMP. Once set $y_0 = (4\pi)^{4Y}$ to its NDA maximal value and given the scaling $M_{\rm DM} \sim n^{5/2}$ Eq. (B.8) can be used to determine the viable EW multiplets. It turns out that the allowed multiplet are the same as for fermions, *i.e.* all even $n_{1/2}$ plus 3_1 and 5_1.

Finally, we discuss DM stability for scalars. All the $Y = 1/2$ scalars are never accidentally stable, since DM decay can be induced by the renormalizable operator $\chi^2\chi^\dagger H^c$. Similarly, for 3_1 we can write $\chi^\dagger H^2$, while for 5_1 the lowest dimensional operators are:

$$\mathscr{L} = \frac{C_1}{\Lambda_{\rm UV}}\chi^\dagger H^2 (H^\dagger H) + \frac{C_2}{\Lambda_{\rm UV}}(\chi^\dagger\chi)(\chi^\dagger H^2)\,, \tag{B.9}$$

which ensures stability for $\Lambda_{\rm UV} > 10^{21} M_{\rm DM}$, way larger than $\Lambda_{\rm UV} < 20 M_{\rm DM}$ from δm_0 perturbativity.

Results for the collider reach on the scalars are given in Fig. F.6 in App. F.

Appendix C

Complex WIMP cosmology

In this Appendix, we briefly describe the cosmological evolution of the Complex WIMP candidates. In particular, we highlight the main differences with respect to real WIMPs discussed in Chapter 2.

C.1 Sommerfeld Enhancement and Bound State Formation

At small velocities and in the symmetric limit, the Sommerfeld enhancement for Complex EW WIMPs can be approximated as

$$S_E^I \approx \frac{2\pi\alpha_{\rm eff}}{v_{\rm rel}} \ , \tag{C.1}$$

where now $\alpha_{\rm eff} = \alpha_2(I^2+1-2n^2)/8 + Y^2\alpha_Y \equiv \alpha_{2,\rm eff} + Y^2\alpha_Y$ includes also the contribution coming from the non-zero hypercharge. With this replacement, the annihilation cross-section takes the form as in the real case in Eq. (2.27):

$$\langle \sigma_{\rm ann}^{\rm SE} v_{\rm rel}\rangle = \sum_I \langle S_E^I \sigma_{\rm ann}^I v_{\rm rel}\rangle \ , \tag{C.2}$$

where $\sigma_{\rm ann}^I$ is the perturbative, s-wave, hard annihilation cross-section in the isospin channel I. The $\mathrm{SU}(2)_{\rm L}$ symmetric limit approximate better the exact result the more we increase the dimensionality of the EW multiplet. This is because most of the freeze-out dynamics for large n-plets occurs before the EWSB. For smaller multiplets the symmetric approximation generically fails because EWSB becomes important. In our computation, we always assume the symmetric limit for $n \geq 6$, while we compute the SE in the broken phase for smaller multiplets.

Besides, the mass splittings generated by $\mathcal{O}_0$ and $\mathcal{O}_+$ can alter the pattern of resonances in the SE, so that the thermal mass becomes a function of δm_0 and δm_+ as well. In Table 2.2 we assume the minimal δm_0, where the effect of the splitting is safely negligible, and account for the dependence on δm_+ in the theoretical

uncertainty. More details about the effect of these UV operators are discussed in App. C.2.

Concerning BSF, the main difference with respect to real WIMPs is the different selection rules selecting the bound states allowed by symmetries. In the real case, the bound states are of the form $\chi\chi$ and the (anti-)symmetry of the wave function allows only for those BS satisfying $P_{\rm BS} \equiv (-1)^{L+S+\frac{I-1}{2}} = 1$, while for complex WIMPs the bound states are of the form $\overline{\chi}\chi$ and the above selection rule no longer applies.

The BSF cross-section can be computed in the $\mathrm{SU}(2)_{\rm L}$-symmetric limit with good approximation and scales as:

$$\sigma_{B_I} v_{\rm rel} \simeq \frac{E_{B_I} a_B}{M_{\rm DM} n^2} (\alpha_{2,\rm eff} S_E^{I\pm 2} + Y^2 \alpha_Y S_E^I) \ , \tag{C.3}$$

where the first and second term account for weak and hypercharge vector boson emmission, respectively, $E_{B_I} \approx \alpha_{\rm eff}^2 M_{\rm DM}/4n_B^2$ - n_B being the energy level - is the binding energy and $a_B = 1/\alpha_{\rm eff} M_{\rm DM}$ the Bohr radius.
Once the BS is formed, it can annihilate into SM, decay to lower lying BS, both with rate $\Gamma \approx \alpha_{2,\rm eff}^2 \alpha_{\rm eff}^3 M_{\rm DM}$ or $Y^2 \alpha_Y^2 \alpha_{\rm eff}^3 M_{\rm DM}$, depending on the mediator, or be broken by the interactions with the plasma (ionization). The ionization rate limits the efficiency of DM annihilation through BSF and it is Boltzmann suppressed as $\sim e^{E_{B_I}}/T$. The Boltzmann suppression gets bigger as we increase the dimensionality of the multiplet, due to the larger binding energies, so that neglecting BS ionizations is a good approximation for large EW multiplets. Under this approximation, we write the overall DM effective annihilation cross-section as follows:

$$\langle \sigma_{\rm eff} v_{\rm rel} \rangle \equiv \langle \sigma_{\rm ann}^{\rm SE} v_{\rm rel} \rangle + \sum_{B_J} \langle \sigma_{B_J} v_{\rm rel} \rangle, \tag{C.4}$$

that is, once a BS is formed it eventually annihilates to SM without being destroyed. In Chapter 2 we checked the validity of this approximation for $n \leq 7$ and found that it overestimates the thermal mass of about 5 TeV. We assume this holds also for complex WIMPs and include this uncertainty in the estimate of our theoretical uncertainty, see also Ref. [430]. In the symmetric limit the effect of the mass splittings generated after EWSB are not taken into account. We expect these to make the heavier components of the multiplet decouple earlier than the lighter ones, thus reducing the cross-section. In order to estimate the error due to this approximation, we compute the thermal mass first setting to zero σ_{B_I} for $T < \max \delta m_Q$ and then including BSF until the DM abundance saturates. These two effects are the dominant sources of error for $n \lesssim 8$. Instead, for $n \gtrsim 8$, the theoretical uncertainty is dominated by NLO corrections to the potential controlling the SE

$$\frac{\Delta V_{\rm NLO}}{V_{\rm LO}} \sim \beta_2^{\rm SM} \frac{\alpha_2}{4\pi} \log\left(\frac{m_W}{M_{\rm DM}}\right) . \tag{C.5}$$

C.2 Impact of mass splittings

Here we discuss under which conditions the effect of the UV splittings can be neglected in the prediction of the thermal mass. The UV splittings can affect the freeze-out computation in two ways: i) they directly contribute to the DM annihilation cross-section into Higgs bosons, ii) after the EWSB, the interaction Eq. (2.61) generates a Higgs-mediated Yukawa potential, thus affecting the Sommerfeld enhancement. For definiteness, we focus on fermionic WIMPs and on the $\mathcal{O}_0$ contributions. We checked that similar conclusions hold for scalar WIMPs and for the contrbutions from $\mathcal{O}_+$.

For $Y = 1/2$ WIMPs, the hard annihilation cross-section into higgses induced by $\mathcal{O}_0$ can be estimated as

$$\sigma_{2H} v_{\rm rel} \simeq \frac{3 y_{0,+}^2}{32 n^2 \pi \Lambda_{\rm UV}^2} T_R \,, \tag{C.6}$$

where $T_R = n(n^2-1)/16$ is the Dynkin index of the DM $\mathrm{SU}(2)_{\rm L}$ representation. This should be compared with the typical EW hard cross-section, which is

$$\sigma_{\rm EW} v_{\rm rel} \simeq \frac{\pi \alpha_2^2 (n^2-1)^2}{32 n M_{\rm DM}^2} \,. \tag{C.7}$$

The condition $\sigma_{2H}/\sigma_{\rm EW} < 1$ can be translated into an upper bound on the mass splittings. For instance for the inelastic mass splitting we get

$$\delta m_0 < 1.6 \text{ GeV} \left(\frac{1 \text{ TeV}}{M_{\rm DM}} \right) n^2 \,. \tag{C.8}$$

Since $M_{\rm DM} \sim n^{5/2}$ we get stronger upper bound on the splitting for large multiplets. All in all, we do not expect significant changes from what found in Chapter 2 even though for large splittings (above 1 GeV) one can get $\mathcal{O}(1)$ effects on the thermal freeze-out predictions for small multiplets.

For $Y = 1$ the contribution from $\mathcal{O}_0$, which now is a 7D operator which controls the 4-body process $\overline{\chi}\chi \to 4H$, can be estimated as

$$\sigma_{4H} v_{\rm rel} \approx \frac{\pi y_0^2 M_{\rm DM}^4}{(16\pi^2)^3 \Lambda_{\rm UV}^6} \frac{(n^2-1)^2}{64 n} \,. \tag{C.9}$$

The condition $\sigma_{4H}/\sigma_{\rm EW} < 1$ translates into

$$\delta m_0 < 0.45 \text{ GeV} \left(\frac{1 \text{ TeV}}{M_{\rm DM}} \right)^3 n^2, \tag{C.10}$$

which, for $n = 3, 5$ is much looser than the upper bound on δm_0. As a consequence, the UV splittings do not impact the freeze-out prediction for $Y = 1$ WIMPs.

Finally, concerning the contribution to the Sommerfeld enhancement, the potential arising from the Yukawa interaction in Eq. (2.61) is:

$$V_H(r) = -\left(\frac{\lambda_D v}{8\pi \Lambda_{\rm UV}} \right)^2 \frac{e^{-m_h r}}{r}. \tag{C.11}$$

Such potential is shorter range with respect to typical EW Yukawa potentials, due to the larger Higgs mass as compared to weak boson masses. We find that $V_H(r)$ is negligible compared to the size of the EW potential α_2/r for the mass splittings of our interest.

Appendix D

The WIMP Unitarity Bound

We now analyze the constraint of perturbative unitarity on the annihilation cross-section, including bound state formation. The perturbative unitarity of the S-matrix sets an upper bound on the size of each partial wave contribution to the total annihilation cross-section [1]

$$(\sigma_{\rm eff} v_{\rm rel})^J \leq \frac{4\pi(2J+1)}{M_\chi^2 v_{\rm rel}} \ , \tag{D.1}$$

where $\vec{J} = \vec{L} + \vec{S}$ is the total angular momentum. The stronger inequality comes from the s-wave channel (i.e. $J = 0$) which can be written as

$$(\sigma_{\rm ann} v_{\rm rel}) + \sum_{B_J} f^0_{B_J} (\sigma_{B_J} v_{\rm rel}) \leq \frac{4\pi}{M_\chi^2 v_{\rm rel}} \ , \tag{D.2}$$

where $f^0_{B_i}$ selects the BS contributions that can be formed by $J = 0$ initial wave, which are limited by the selection rules discussed in the previous Section.

For a real scalar WIMP selecting the s-wave implies $L = 0$, and only BS in p-orbitals can contribute to the s-wave cross-section with $f^0_{\rm BS} = 1$. The spin statistics of the wave function in Eq. (2.22) forces these BS to have odd $(I-1)/2$. In practice, the s-wave unitarity bound for scalars is determined solely by the SE. For Majorana fermionic WIMP selecting the s-wave implies the same selection rules of the scalar when $S = 0$. Additional contributions arise from $S = 1$ s-orbital states, whose isospin must be odd due to Fermi statistics. In this case, the projection onto the $J = 0$ wave gives $f^0_{\rm BS} = \frac{1}{9}$.

Solving the constraint in Eq. (D.2) we find that s-wave unitarity is violated for $n \geq 15$ for both fermion and scalar WIMPs. In both cases the s-wave cross-section is largely dominate by the SE. We checked that a similar constraint can be obtained by looking at the $p-$wave unitarity, where the cross-section is instead dominated by the formation of $1s$ BS.

[1] This constraint was derived for e^+e^- annihilations in [431, 432] and then used for the first time in the DM context in [97]. It can be checked that this constraints is not modified in the presence of long range interactions [433].

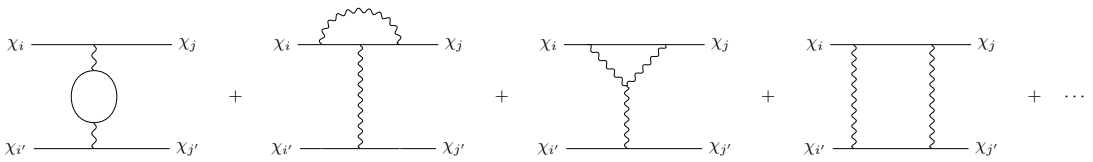

Figure D.1: *Examples of Feynman diagrams contributing at NLO to the non-relativistic potentials as estimated in Eq. (D.4).*

As we noticed in the main text, the BSF contribution is larger for complex WIMPs compared to the real case due to the larger multiplicity of bound states that can be formed.

The selection rules that regulates the BS dynamics derive from the dipole Hamiltonian which is written for completeness in Eq. (2.20). These selection rules are only broken by NLO contributions in gauge boson emission which can be estimated as

$$\frac{\Delta\sigma_{\rm BSF}^{\rm NLO}}{\sigma_{\rm BSF}^{\rm LO}} \sim \frac{\alpha_{\rm eff}^3}{64\pi} \,, \tag{D.3}$$

where the extra $\alpha_{\rm eff}^2$ correctly accounts for the phase space suppression in the limit of small velocities as detailed in [124] As a result, the LO selection rules hold all the way till the breaking of perturbative unitarity.

Interestingly, the upper bound on n from perturbative unitarity derived from Eq. (D.2) is significantly stronger than the one derived from the perturbative unitarity of the Born cross-section which is violated for $n \geq 38$ (i.e. $\alpha_{\rm eff} \geq 4\pi$). This suggests that because of SE, the ratio between the NLO and the LO cross-section should appreciably deviate from the NDA scaling of the Born cross-section: $\sigma_{\rm Born}^{\rm NLO}/\sigma_{\rm Born}^{\rm LO} \sim \alpha_{\rm eff}/4\pi$. Estimating the NLO correction to the potentials controlling the SE we indeed get

$$\frac{\Delta V_{\rm NLO}}{V_{\rm LO}} \sim \frac{\alpha_{\rm eff}}{4\pi} \log\left(\frac{m_W\sqrt{z}}{M_\chi}\right) \,, \tag{D.4}$$

where the NLO potential is resumming ladder diagrams like the ones in Fig. D.1, and where we substituted the de Broglie length $1/Mv_{\rm rel} \approx \sqrt{z}/M_\chi$ as the typical lenght scale for the annihilation process. Our estimate above matches the explicit NLO computation of the SE for the 3-plet in Ref. [434]. Requiring this correction to be $\lesssim 1$ across the freeze-out temperatures leads to a similar upper bound on n than the one inferred from perturbative unitarity.

We use the estimate above to assess the theory uncertainty on the WIMP thermal masses in Table 2.1. Indeed, Eq. (D.4) results in a correction to the Sommerfeld factor S_E, which affects both $S_{\rm ann}$ and S_{B_J} as introduced in Eq. (2.25). We find that neglecting the NLO contribution dominates the DM mass theory uncertainty for $n \geq 7$. The uncertainty grows as we increase the dimensionality of the multiplet becoming as large as $\mathcal{O}(30\%)$ for $n = 13$.

Finally, we compare our results to the ones obtained in Ref. [103]. Numerically, the upper bound on the WIMP mass corresponding to the saturation of the unitarity bound is roughly 500±200 TeV, which is the expected thermal mass for $n = 15$ as can be seen from Fig. 2.1. The unitarity boundary was set instead to 150 TeV for $n = 13$ in Ref. [103] without a quoted theory uncertainty. Beside the numerical differences, our computation differ from the one in Ref. [103] in two crucial instances: *i*) at large n we find that large isospin channels enhance significantly the BSF cross-section making the WIMP DM mass *heavier* than in Ref. [103] at fixed n; *ii*) we find that including BSF does not accelerate by much the saturation of the unitarity bound because of the selection rules of the dipole Hamiltonian at LO. As we discussed above, the LO selection rules are not lifted by NLO corrections until the boundary of perturbative unitarity is reached. These two effects together push the heaviest calculable WIMP mass very close to the PeV scale appreciably enlarging the EW WIMP scenarios beyond the reach of any realistic future collider.

Appendix E

Millicharged WIMPs

Complex WIMPs with $Y = 0$ have an unbroken U (1) flavor symmetry which can be gauged by a new dark photon. Generically the dark photon would mix with the visible one through a kinetic mixing operator $\epsilon FF'$ and the complex WIMP would acquire a EM charge ϵ. In this scenario the dark gauge symmetry makes the DM accidentally stable as noticed in Ref. [96] at the price of giving up charge quantization. Here we want to summarize the freeze-out predictions and the basic phenomenology of millicharged WIMPs in the limit of very small ϵ (i.e. $\epsilon < 10^{-10}$) when their phenomenology resemble the one of the real WIMPs discussed in Ref. [47].

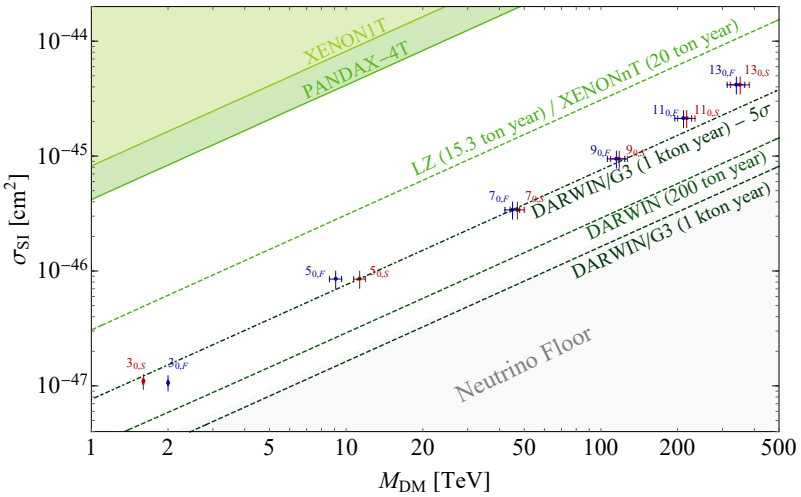

Figure E.1: *Expected SI cross-sections for different millicharged complex WIMPs with* $\epsilon \lesssim 10^{-10}$. *The* **blue dots** *correspond to Dirac WIMPs and the* **red dots** *to complex scalar WIMPs. The vertical error bands correspond to the propagation of LQCD uncertainties on the elastic cross-section (Eq. (2.53)), while the horizontal error band comes from the uncertainty in the theory determination of the WIMP freeze out mass in Table E.1. The* **light green** *shaded region is excluded by the present experimental contraints from XENON-1T [133] and PandaX-4T [114], the* **green dashed** *lines shows the expected 95% CL reach of LZ/Xenon-nT [127, 128] and DARWIN [54, 129].*

Concerning the freeze-out dynamics, the only difference between real and millicharged

WIMPs is in the existence of BS with $P_{\rm BS} = (-1)^{L+S+\frac{I-1}{2}} = -1$ formed by $\bar{\chi}\chi$ pairs of millicharged WIMPs. These are forbidden by the spin-statistic properties of the $\chi\chi$ wave function for real WIMPs. Since $P_{\rm BS}$ is preserved by dipole interactions for $Y = 0$, to leading order no transitions can occur between states with opposite $P_{\rm BS}$ and excited BS with $P_{\rm BS} = -1$ will dominantly decay to $1s$ and $2s$ states with the same $P_{\rm BS}$. The latter have small decay widths with respect to their $P_{\rm BS} = 1$ counterparts. $ns_1^{S=1}$ and $ns_5^{S=1}$ annihilate into four vectors with a rate

$$\Gamma(ns_{1,5}^{S=1} \to VVVV) \simeq \frac{\alpha_{\rm eff}^4}{16\pi^2 M_{\rm DM}^2} \frac{|R_{n0}(0)|^2}{M_{\rm DM}^2}\,, \tag{E.1}$$

while $ns_3^{S=0}$ annihilates into three vectors with rate:

$$\Gamma(ns_3^{S=0} \to VVV) \simeq \frac{\alpha_{\rm eff}^3}{4\pi M_{\rm DM}^2} \frac{|R_{n0}(0)|^2}{M_{\rm DM}^2}\,. \tag{E.2}$$

where $R_{n0} \sim (\alpha_{\rm eff} M_{\rm DM})^{3/2}$ is the radial wave function of the BS at the origin. As noticed in Ref. [96] for the millicharged 3-plet a large resonance in the Sommerfeld enhancement leads to two different freeze out predictions. We summarize our freeze out predictions in Table E.1.

DM spin	n_ϵ	$M_{\rm DM}$ (TeV)	$\Lambda_{\rm Landau}/M_{\rm DM}$	$(\sigma v)_{\rm tot}^{J=0}/(\sigma v)_{\rm max}^{J=0}$
Complex scalar	3	$1.60 \pm 0.01 - 2.4^*$	$> M_{\rm Pl}$	-
	5	11.3 ± 0.6	$> M_{\rm Pl}$	0.003
	7	47 ± 3	2×10^6	0.02
	9	118 ± 9	110	0.09
	11	217 ± 17	7	0.25
	13	352 ± 30	3	0.6
Dirac fermion	3	$2.0 \pm 0.1 - 2.4^*$	$> M_{\rm Pl}$	-
	5	9.1 ± 0.5	4×10^6	0.002
	7	45 ± 3	80	0.02
	9	115 ± 9	6	0.09
	11	211 ± 16	2.4	0.3
	13	340 ± 27	1.6	0.7

Table E.1: *Freeze-out mass predictions for millicharged WIMP DM. The annihilation cross-section includes both the contribution of SE and BSF. For the triplets, a second prediction, denoted with a *, for the thermal mass is present due to the emergence of a large resonance in the Sommerfeld enhancement for $M_{DM} \approx 2.4$ TeV. We provide a measure of how close the DM annihilation cross-section is to the unitarity bound for s-wave annihilation $(\sigma v)_{max}^{J=0} = 4\pi/M_{DM}^2 v$. We derive the scale where EW gauge coupling will develop a Landau pole by integrating-in the WIMP multiplet at its freeze-out mass.*

For completeness, in Fig. E.1 we show the SI scattering cross-section of DM on xenon nuclei for the different millicharged candidates. This cross-section is identical

to that computed for real candidates with $\epsilon \lesssim 10^{-10}$ [96, 102], while larger ϵ would open up new opportunities for direct detection (see e.g. Fig 1 of [96]). From Fig. E.1 we see that even in the worst case scenario of very small millicharge large exposure experiments will be able to fully probe millicharged WIMPs with 200 ton-year exposure. The heavier multiplets could be also firmly discovered at DARWIN with kiloton exposure.

Appendix F

More on WIMPs at future lepton colliders

F.1 The scalar WIMPs

Probing scalar WIMPs with typical missing mass searches is quite hard. This is due to multiple reasons: i) the scalar production cross-sections are roughly one order of magnitude smaller than for fermions with same n, as shown on the left of Fig. F.1. A factor of 4 suppression comes from the lower number of degrees of freedom for scalar final states, while the remaining suppression comes from a velocity suppressed production cross-section compared to the fermionic case. Since the reach is a very slow function of the mass of the WIMP M_χ, as shown in the right panel of Fig. F.1, a reduction of the signal cross-section implies a drastic change in the reach. ii) The scalar WIMPs have typically larger freeze-out masses compared to fermionic WIMPs with same EW charge n.

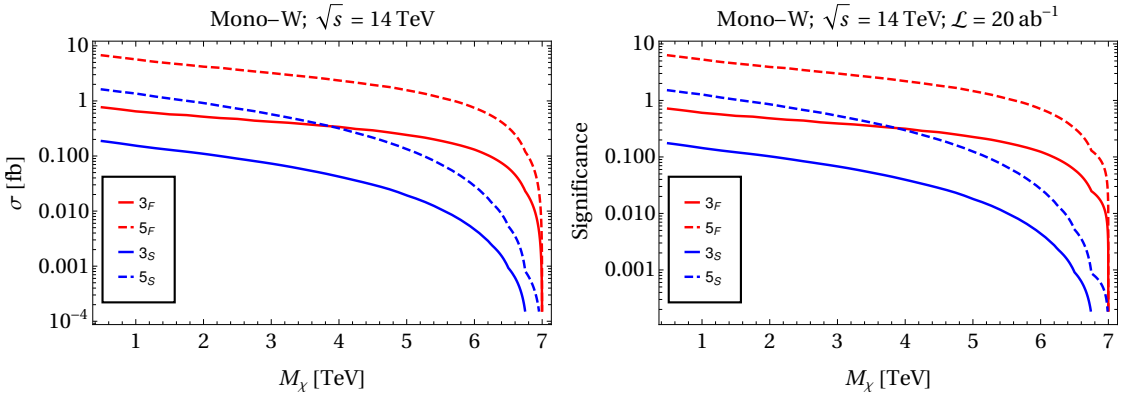

Figure F.1: Left: *Drell-Yan Mono-W cross-section for* $\sqrt{s} = 14\,\text{TeV}$. **Right:** *Significance of the mono-W search for* $\sqrt{s} = 14\,\text{TeV}$. *In both plots, the only cuts applied are* $|\eta_W| < 2.5$ *(geometric acceptance) and* $\text{MIM} > 2M_\chi$.

All in all, scalar WIMPs give dimmer signals at colliders and are generically heavier than fermionic WIMP. It is thus not surprising that the results expected from collider

searches of scalar WIMPs, shown in Fig. F.2, are far less exciting than those for fermions in Fig. 2.7.

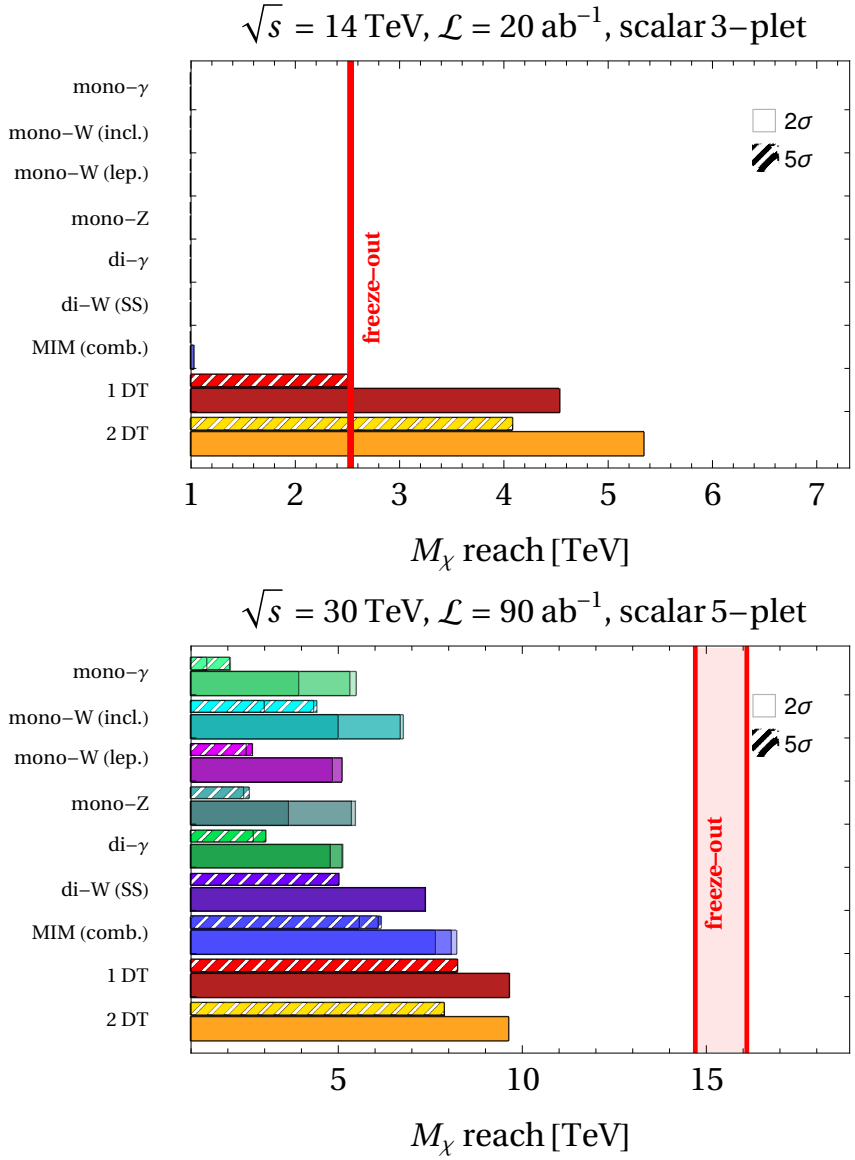

Figure F.2: *Different bars show the reach at* 2σ *(full wide) and at* 5σ *(hatched thin) on the WIMP mass at a muon collider with baseline luminosity given by Eq. (2.31) for the different search channels discussed in Sec. 2.4.1: mono-gamma, inclusive mono-W, charged mono-W, mono-Z, di-gamma, same-sign di-W , the combination of all these MIM channels (blue). We also show the reach of disappearing tracks as discussed in Sec. 2.4.2: at least 1 disappearing track (red), or exactly 2 tracks (orange). All the results are obtained assuming systematic uncertainties to be: 0 (light), 1 ‰ (medium), or 1% (dark). The vertical red lines show the freeze-out prediction band.* **Above:** *Real Scalar 3-plet for* $\sqrt{s} = 14\,\text{TeV}$ **Below:** *Real Scalar 5-plet for* $\sqrt{s} = 30\,\text{TeV}$.

The overall picture in the landscape of possible beam energy and luminosity options for a future very high energy lepton collider is displayed in Fig. F.3. At variance with the fermionic case presented in Fig. 2.6, the potential to probe scalar WIMPs

with mono-X signals is very limited.

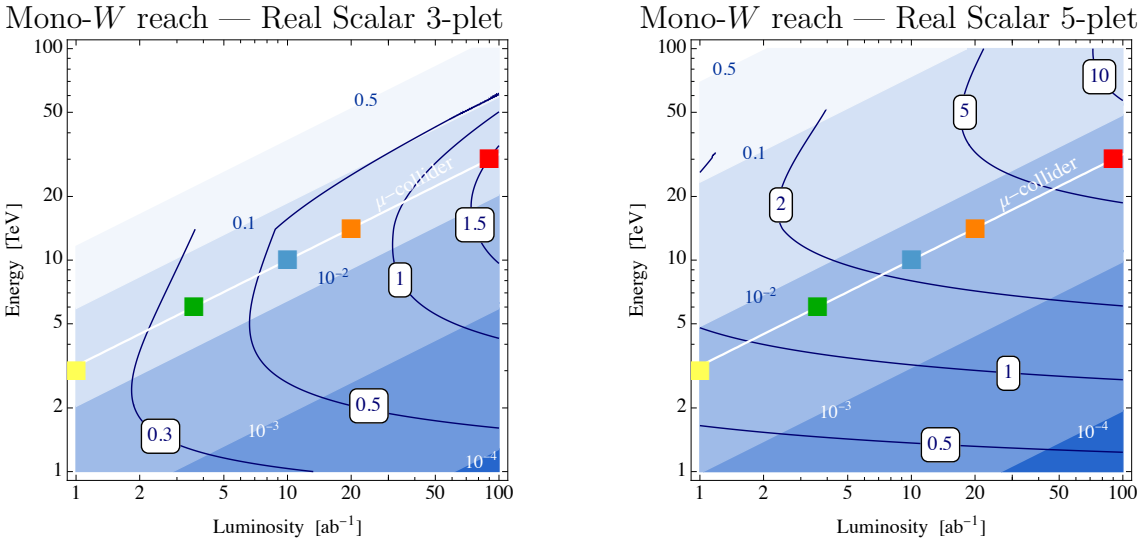

Figure F.3: *Same as Fig. 2.6, but for real scalar WIMPs.* **Left:** *Real Scalar 3-plet.* **Right:** *Real Scalar 5-plet.*

We stress that our results are based purely on Drell-Yan production of χ, which accounts perfectly for the total production rate of WIMPs of mass comparable with $\sqrt{s}$. For significantly lighter WIMPs it is possible to add further production modes and discovery channels, such as production by vector boson fusion and mono-muon channels studied for lighter fermionic WIMPs [112], which may result in a bound for light enough scalar WIMPs. In Fig. F.4 we plotted the cross-sections for scalar $\chi\chi$ production in W-fusion (as a representative for VBF modes) and Drell-Yan as a function of M_χ. It can be seen that the VBF cross-section decreases quickly, while DY remains almost constant except near the kinematic threshold. In particular, for the real scalar 5-plet at $\sqrt{s} = 30$ TeV our DY 2σ reaches can be trusted, as the VBF contribution is smaller than 10% of the DY one. For the scalar triplet at $\sqrt{s} = 14$ TeV, the inclusion of VBF modes is not expected to improve the reach for masses $\gtrsim 1$ TeV.

It is remarkable that for real scalars the mass splitting between charged and neutral states in the n-plet is dominated by EW interactions. Indeed, no splitting term with the Higgs can be written at the quartic level, due to the antisymmetry of the $\mathrm{SU}(2)_\mathrm{L}$ contraction. By hypercharge conservation, and assuming the scalar does not get any extra VEV, the leading terms contributing to the mass splitting are dimension 6 in the SM. Therefore the stub-track prediction is robust and does not depend on peculiar UV completions of the model. Results for searches of scalar WIMPs from stub-track analyses are reported in Fig. F.5.

We also report results for scalar complex WIMPs. A summary of the collider searches is found in Fig. 2.5. A zoomed picture of the results is given in Fig. F.6.

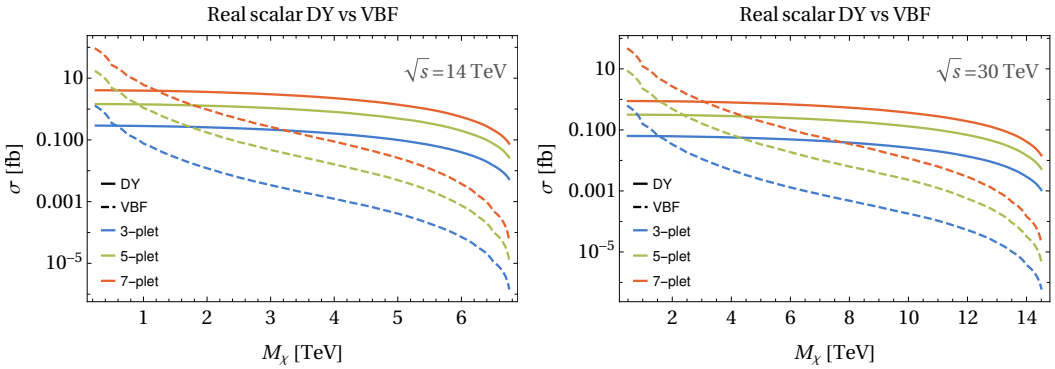

Figure F.4: *Drell-Yan and W-fusion $\chi\chi$ production as a function of M_χ.* **Left:** *Real Scalar 3-plet cross-section for $\sqrt{s} = 14\,\text{TeV}$.* **Right:** *Real Scalar 5-plet cross-section for $\sqrt{s} = 30\,\text{TeV}$.*

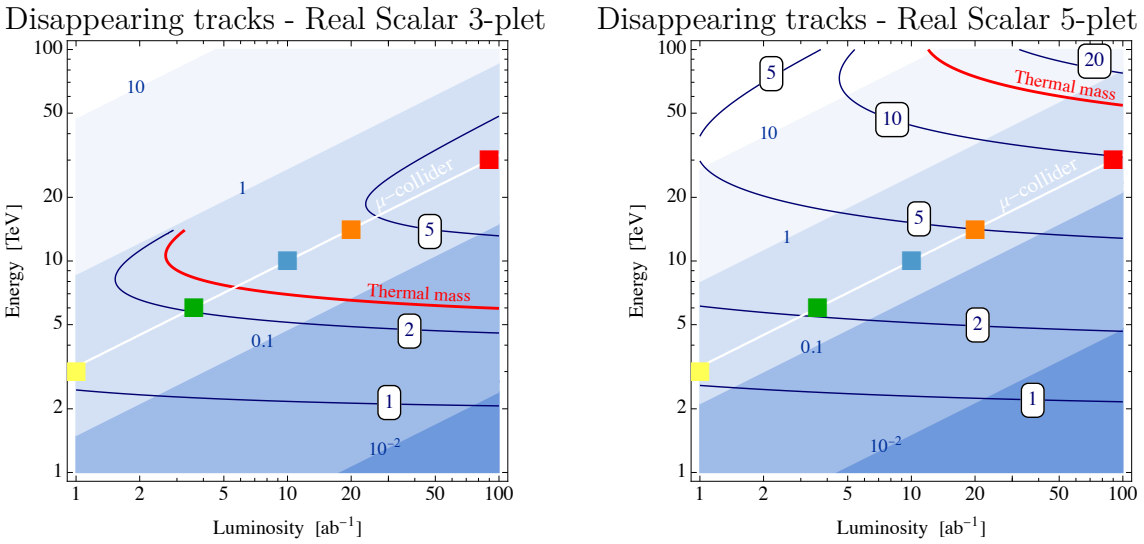

Figure F.5: *Same as Fig. 2.12, but for real scalar WIMPs.* **Left:** *Real Scalar 3-plet.* **Right:** *Real Scalar 5-plet.*

F.2 Details of the missing momentum analyses

In Table F.1 and Table F.2 we provide the results of the optimized cuts for all the considered mono-V and di-V channels, for the case of a Majorana n-plet, or a real scalar, respectively. The optimization was carried out in an equally spaced 25×12 grid in the rectangle $[0, \sqrt{s}/2] \times [0, 2.4]$ in the $p_{T,X}^{\text{cut}} - \eta_X^{\text{cut}}$ plane.

In Table F.3, F.4 we report the same for the fermionic complex WIMP for completeness

We also report the expected number of signal events, the signal-to-noise ratio, and the value of the mass that can be excluded at 95% C.L. We provide results for muon colliders with $\sqrt{s} = 3, 14, 30$ TeV with integrated luminosity as in Eq. (2.31), and for systematic uncertainties $\epsilon_{\text{sys}} = 0, 1‰, 1\%$.

Among all the channels considered, the only background that needs some careful

			Majorana 3-plet					Majorana 5-plet				
	$\sqrt{s}$	$\epsilon_{\rm sys}$	$\eta_X^{\rm cut}$	$p_{T,X}^{\rm cut}$ [TeV]	$S_{95\%}$	$S_{95\%}/B$	$M_{95\%}$ [TeV]	$\eta_X^{\rm cut}$	$p_{T,X}^{\rm cut}$ [TeV]	$S_{95\%}$	$S_{95\%}/B$	$M_{95\%}$ [TeV]
Mono-γ	3 TeV	0	2.4	0.18	1007	0.004	0.72	2.4	0.0	3038	0.001	1.4
		1‰	2.2	0.24	746	0.006	0.67	1.2	0.0	3683	0.003	1.3
		1%	1.2	0.78	107	0.05	0.58	0.6	0.3	639	0.02	1.1
	14 TeV	0	1.6	2.5	360	0.01	2.2	2.2	0.28	3693	0.001	5.5
		1‰	1.6	2.8	323	0.01	2.2	1.2	0.84	1300	0.004	5.2
		1%	1.0	4.5	108	0.05	1.9	0.8	2.8	331	0.03	4.4
	30 TeV	0	1.2	7.8	174	0.02	4.4	1.6	1.8	1795	0.002	11
		1‰	1.2	7.8	175	0.02	4.4	1.0	2.4	1312	0.004	11
		1%	1.2	8.4	190	0.03	4.0	0.8	6.0	455	0.03	8.8
Mono-W (inclusive)	3 TeV	0	1.6	0.36	842	0.005	0.79	2.2	0.06	5625	0.0007	1.2
		1‰	1.4	0.48	534	0.008	0.78	1.0	0.24	1649	0.004	1.2
		1%	1.0	0.84	172	0.04	0.64	0.6	0.54	515	0.02	1.0
	14 TeV	0	1.6	2.0	819	0.005	3.4	1.8	0.56	5325	0.0008	5.5
		1‰	1.6	2.2	665	0.007	3.3	1.0	1.4	1342	0.004	5.2
		1%	0.8	4.2	155	0.04	2.8	1.2	2.5	635	0.03	4.4
	30 TeV	0	1.4	5.4	696	0.006	6.7	1.8	1.8	3946	0.001	12
		1‰	1.4	5.4	606	0.007	6.7	1.4	2.4	2771	0.003	11
		1%	1.0	9.0	211	0.03	5.2	0.8	5.4	813	0.02	9.3
Mono-W (leptonic)	3 TeV	0	1.4	0.6	88	0.05	0.64	2.4	0.12	1175	0.003	1.1
		1‰	1.4	0.6	88	0.05	0.64	1.6	0.24	506	0.009	1.1
		1%	1.4	0.6	97	0.05	0.6	1.4	0.42	261	0.03	1.0
	14 TeV	0	1.4	3.1	92	0.05	2.6	1.6	1.1	610	0.007	5.0
		1‰	1.4	3.1	92	0.05	2.6	1.6	1.1	642	0.007	4.9
		1%	1.2	3.4	77	0.06	2.5	1.4	2.0	308	0.03	4.5
	30 TeV	0	1.2	7.8	72	0.06	5.1	1.6	2.4	642	0.006	10
		1‰	1.2	7.8	72	0.06	5.1	1.4	3.0	442	0.01	10
		1%	1.2	7.8	65	0.07	5.0	1.2	5.4	177	0.04	9.4
Mono-Z	3 TeV	0	1.4	0.72	330	0.02	0.37	1.4	0.0	1798	0.002	1.2
		1‰	1.4	0.72	277	0.02	0.36	1.0	0.0	1946	0.003	1.2
		1%	1.2	0.9	127	0.04	0.29	0.6	0.48	563	0.02	0.9
	14 TeV	0	1.2	3.6	263	0.02	1.1	1.2	0.28	4458	0.001	5.0
		1‰	1.4	3.4	273	0.02	1.1	0.6	1.4	827	0.006	4.8
		1%	0.8	5.3	82	0.06	0.9	0.4	3.1	260	0.03	3.7
	30 TeV	0	1.8	5.4	470	0.01	2.1	1.0	1.8	2515	0.002	10
		1‰	1.6	6.0	443	0.01	1.9	0.8	3.0	1159	0.005	9.8
		1%	0.8	11	80	0.06	1.5	0.2	6.0	267	0.03	7.5
Di-γ	3 TeV	0	2.4	0.42	106	0.04	0.31	2.4	0.0	509	0.008	1.2
		1‰	2.4	0.42	106	0.04	0.31	1.8	0.0	404	0.01	1.2
		1%	2.4	0.48	84	0.07	0.29	1.0	0.12	160	0.04	1.1
	14 TeV	0	2.2	2.8	71	0.07	1.3	1.4	0.56	331	0.01	4.8
		1‰	2.2	2.8	71	0.07	1.3	1.4	0.56	332	0.01	4.8
		1%	2.0	3.6	58	0.08	1.2	1.0	1.4	125	0.04	4.5
	30 TeV	0	2.4	6.6	103	0.04	2.6	1.6	1.2	580	0.007	9.9
		1‰	2.4	6.6	103	0.04	2.5	1.6	1.2	574	0.008	9.9
		1%	2.4	9.0	47	0.1	2.4	1.0	2.4	274	0.03	9.0
Di-W (same-sign)	3 TeV	0	2.5	0.3	6	2.6	0.32	2.5	0.3	5	3.9	1.0
		1‰	2.5	0.3	6	2.6	0.32	2.5	0.3	5	3.9	1.0
		1%	2.5	0.3	6	2.6	0.32	2.5	0.3	5	3.9	1.0
	14 TeV	0	2.5	1.5	10	0.66	1.7	2.5	1.5	9	0.89	4.8
		1‰	2.5	1.5	10	0.66	1.7	2.5	1.5	9	0.89	4.8
		1%	2.5	1.5	10	0.66	1.7	2.5	1.5	9	0.89	4.8
	30 TeV	0	2.5	3	14	0.4	3.7	2.5	3	12	0.52	10
		1‰	2.5	3	14	0.4	3.7	2.5	3	12	0.52	10
		1%	2.5	3	14	0.4	3.7	2.5	3	12	0.52	10

Table F.1: *95% C.L. reach on the mass of a Majorana 3-plet and 5-plet from the various mono-X channels. The excluded number of signal events $S_{95\%}$ and the relative precision $S_{95\%}/B$ are also given, together with the values of the optimal event selection cuts on η_X and $p_{T,X}$, where X is either the single vector boson or the compound diboson system for Di-W and Di-γ. The numbers are shown for different collider energies $E_{\rm cm}$ and systematic uncertainties $\epsilon_{\rm sys}$.*

			Scalar 3-plet					Scalar 5-plet				
	$\sqrt{s}$	$\epsilon_{\rm sys}$	$\eta_X^{\rm cut}$	$p_{T,X}^{\rm cut}$ [TeV]	$S_{95\%}$	$S_{95\%}/B$	$M_{95\%}$ [TeV]	$\eta_X^{\rm cut}$	$p_{T,X}^{\rm cut}$ [TeV]	$S_{95\%}$	$S_{95\%}/B$	$M_{95\%}$ [TeV]
Mono-γ	3 TeV	0	1.2	0.9	–	–	–	0.	1.6	2749	0.002	0.79
		1‰	1.2	0.9	–	–	–	1.4	0.18	916	0.005	0.72
		1%	1.2	0.9	–	–	–	0.8	0.54	252	0.03	0.53
	14 TeV	0	1.	5.0	–	–	–	1.2	1.4	809	0.005	2.6
		1‰	1.	5.0	–	–	–	1.2	1.7	619	0.007	2.5
		1%	1.	5.0	–	–	–	0.8	3.6	201	0.03	2.0
	30 TeV	0	1.	9.6	–	–	–	1.2	4.8	447	0.009	5.5
		1‰	1.	9.6	–	–	–	1.2	4.8	459	0.009	5.3
		1%	0.8	11	–	–	–	0.6	7.8	186	0.04	3.9
Mono-W (inclusive)	3 TeV	0	1.4	0.72	213	0.02	0.23	1.4	0.36	881	0.005	0.76
		1‰	1.4	0.78	213	0.02	0.22	1.2	0.48	523	0.008	0.74
		1%	1.	0.96	118	0.04	0.2	0.8	0.78	197	0.03	0.64
	14 TeV	0	1.2	4.2	181	0.02	0.82	1.6	1.7	1016	0.004	3.3
		1‰	1.2	4.2	160	0.02	0.82	1.2	2.2	642	0.007	3.2
		1%	0.8	5.0	80	0.06	0.72	0.6	3.6	256	0.03	2.6
	30 TeV	0	1.2	9.	160	0.03	1.5	1.4	3.6	988	0.004	6.8
		1‰	1.2	9.	160	0.03	1.5	1.2	5.4	605	0.007	6.7
		1%	1.	10	103	0.05	1.3	0.6	10	103	0.05	5.0
Mono-W (leptonic)	3 TeV	0	1.2	0.84	–	–	–	1.6	0.48	149	0.03	0.6
		1‰	1.2	0.84	–	–	–	1.6	0.48	150	0.03	0.6
		1%	1.2	0.84	–	–	–	1.2	0.6	96	0.05	0.58
	14 TeV	0	1.2	4.2	–	–	–	1.6	2.2	178	0.02	2.5
		1‰	1.2	4.2	–	–	–	1.6	2.2	178	0.02	2.5
		1%	1.2	4.2	–	–	–	1.2	3.4	82	0.06	2.3
	30 TeV	0	1.	10.2	30	0.2	0.94	1.4	6.0	139	0.03	5.1
		1‰	1.	10.2	30	0.2	0.94	1.4	6.0	131	0.03	5.1
		1%	1.	10.2	31	0.2	0.93	1.4	6.6	107	0.05	4.9
Mono-Z	3 TeV	0	1.4	0.72	–	–	–	1.2	0.0	1737	0.002	0.76
		1‰	1.4	0.72	–	–	–	0.8	0.18	1049	0.005	0.71
		1%	1.	1.0	–	–	–	0.8	0.72	245	0.03	0.57
	14 TeV	0	1.4	3.4	–	–	–	1.	1.4	996	0.004	2.9
		1‰	1.4	3.4	–	–	–	0.6	1.4	815	0.006	2.7
		1%	0.8	5.3	–	–	–	0.6	3.9	209	0.03	2.1
	30 TeV	0	1.4	7.2	–	–	–	1.2	3.0	1207	0.003	5.5
		1‰	1.4	7.8	–	–	–	1.	4.2	669	0.007	5.4
		1%	0.8	11	–	–	–	0.6	7.2	340	0.03	3.7
Di-γ	3 TeV	0	1.8	0.78	–	–	–	1.4	0.0	318	0.01	0.63
		1‰	1.8	0.78	–	–	–	1.2	0.0	285	0.02	0.63
		1%	1.8	0.78	–	–	–	1.	0.18	116	0.05	0.58
	14 TeV	0	2.2	3.6	–	–	–	1.0	1.4	117	0.04	2.6
		1‰	2.2	3.6	–	–	–	1.0	1.4	117	0.04	2.6
		1%	2.2	3.9	–	–	–	1.0	1.4	135	0.04	2.5
	30 TeV	0	2.4	9.0	–	–	–	1.4	3.0	224	0.02	5.1
		1‰	2.4	9.0	–	–	–	1.4	3.0	225	0.02	5.1
		1%	2.4	9.0	–	–	–	1.	4.2	116	0.05	4.8
Di-W (same-sign)	3 TeV	0	2.5	0.3	–	–	–	2.5	0.3	6	2.9	0.7
		1‰	2.5	0.3	–	–	–	2.5	0.3	6	2.9	0.7
		1%	2.5	0.3	–	–	–	2.5	0.3	6	2.9	0.7
	14 TeV	0	2.5	1.5	–	–	–	2.5	1.5	10	0.71	3.4
		1‰	2.5	1.5	–	–	–	2.5	1.5	10	0.71	3.4
		1%	2.5	1.5	–	–	–	2.5	1.5	10	0.71	3.4
	30 TeV	0	2.5	3	–	–	–	2.5	3	14	0.42	7.4
		1‰	2.5	3	–	–	–	2.5	3	14	0.42	7.4
		1%	2.5	3	–	–	–	2.5	3	14	0.42	7.4

Table F.2: *Same as Table F.1 but for real scalar 3-plet and 5-plet. A '–' indicates that no 95% C.L. exclusion is possible.*

			Dirac $2_{1/2}$					Dirac 3_1				
	$\sqrt{s}$	$\epsilon_{\rm sys}$	$\eta_X^{\rm cut}$	$p_{T,X}^{\rm cut}$ [TeV]	$S_{95\%}$	$S_{95\%}/B$	$M_{95\%}$ [TeV]	$\eta_X^{\rm cut}$	$p_{T,X}^{\rm cut}$ [TeV]	$S_{95\%}$	$S_{95\%}/B$	$M_{95\%}$ [TeV]
Mono-γ	3 TeV	0	2.4	0.24	492	0.01	0.5	2.4	0.01	3181	0.001	1.3
		1‰	1.6	0.54	213	0.02	0.49	1.4	0.12	1217	0.004	1.2
		1%	1.	0.9	94	0.05	0.43	0.6	0.42	353	0.03	0.94
	6 TeV	0	1.8	0.96	296	0.02	0.83	2.4	0.	6895	0.0006	2.5
		1‰	1.4	1.4	282	0.02	0.82	1.4	0.24	1453	0.004	2.2
		1%	1.	1.9	83	0.06	0.69	0.8	1.1	309	0.03	1.7
	10 TeV	0	1.2	3.	101	0.05	1.1	2.	0.2	3159	0.001	3.6
		1‰	1.2	3.	99	0.04	1.1	1.4	0.8	867	0.006	3.5
		1%	0.8	3.8	56	0.08	0.98	1.	2.	348	0.03	2.7
	14 TeV	0	1.2	4.2	107	0.04	1.5	1.8	0.56	2080	0.002	4.9
		1‰	0.8	4.5	110	0.04	1.5	1.6	1.1	991	0.005	4.7
		1%	0.6	5.9	46	0.1	1.3	0.6	2.8	290	0.03	3.7
	30 TeV	0	1.	9.6	107	0.04	3.	1.8	1.8	1423	0.003	10.
		1‰	1.	9.6	107	0.04	3.	1.6	3.	911	0.005	9.6
		1%	0.8	10.	98	0.05	2.7	1.	6.6	309	0.03	7.6
Mono-W (inclusive)	3 TeV	0	1.4	0.6	336	0.01	0.53	2.	0.18	1833	0.002	1.1
		1‰	1.2	0.72	228	0.02	0.52	1.6	0.3	1180	0.004	1.
		1%	0.8	1.	92	0.06	0.47	1.	0.66	345	0.03	0.85
	6 TeV	0	1.4	1.2	361	0.01	1.	2.	0.48	1572	0.003	2.
		1‰	1.4	1.2	351	0.01	1.	1.4	0.72	1051	0.005	2.
		1%	1.	1.8	140	0.04	0.86	0.8	1.2	480	0.03	1.6
	10 TeV	0	1.6	2.	336	0.01	1.5	1.6	1.	1424	0.003	3.3
		1‰	1.6	2.	331	0.01	1.5	1.4	1.2	1065	0.005	3.2
		1%	0.8	3.4	100	0.05	1.3	0.8	2.	429	0.03	2.7
	14 TeV	0	1.2	3.4	298	0.01	2.1	1.6	1.4	1566	0.003	4.6
		1‰	1.2	3.4	322	0.01	2.1	1.4	1.7	1066	0.005	4.4
		1%	0.8	4.8	107	0.05	1.7	0.8	3.6	225	0.03	3.6
	30 TeV	0	1.4	6.6	344	0.01	4.1	1.8	3.	1433	0.003	9.6
		1‰	1.4	7.2	283	0.01	4.1	1.6	4.2	976	0.005	9.3
		1%	0.8	11.	75	0.07	3.4	0.8	8.4	216	0.03	7.5

Table F.3: *95%C.L. reach on the mass of the Dirac* $2_{1/2}$ *and* 3_1 *from the various mono-X channels. The excluded number of signal events* $S_{95\%}$ *and the relative precision* $S_{95\%}/B$ *are also given,together with the values of the optimal event selection cuts on* η_X *and* $p_{T,X}$*,where* X *is the single vector boson.The numbers are shown for different collider energies* $\sqrt{s}$ *and systematic uncertainties* $\epsilon_{\rm sys}$*.*

			Dirac $4_{1/2}$					Dirac 5_1				
	$\sqrt{s}$	$\epsilon_{\rm sys}$	$\eta_X^{\rm cut}$	$p_{T,X}^{\rm cut}$ [TeV]	$S_{95\%}$	$S_{95\%}/B$	$M_{95\%}$ [TeV]	$\eta_X^{\rm cut}$	$p_{T,X}^{\rm cut}$ [TeV]	$S_{95\%}$	$S_{95\%}/B$	$M_{95\%}$ [TeV]
Mono-γ	3 TeV	0	2.4	0.01	3026	0.001	1.4	2.4	0.01	2823	0.001	1.5
		1‰	1.4	0.01	4092	0.003	1.3	1.6	0.01	3906	0.003	1.4
		1%	0.6	0.3	517	0.02	1.1	0.4	0.12	1245	0.02	1.2
	6 TeV	0	2.4	0.01	6776	0.0006	2.7	2.4	0.01	6400	0.0006	2.9
		1‰	1.2	0.24	1732	0.004	2.4	1.2	0.01	6084	0.003	2.7
		1%	0.8	0.96	478	0.02	2.	0.6	0.72	697	0.02	2.3
	10 TeV	0	2.4	0.01	7217	0.0008	4.1	2.4	0.01	10886	0.0004	4.7
		1‰	1.2	0.6	1264	0.004	3.8	1.2	0.2	3073	0.003	4.4
		1%	0.8	1.6	424	0.03	3.1	0.4	1.2	531	0.02	3.7
	14 TeV	0	2.2	0.28	3174	0.001	5.5	2.4	0.01	15838	0.0003	6.4
		1‰	1.2	1.1	936	0.005	5.2	1.	0.56	1967	0.003	6.
		1%	0.6	2.8	276	0.03	4.3	0.4	2.	483	0.02	5.1
	30 TeV	0	1.6	1.2	2374	0.002	11.	1.6	0.6	4145	0.001	13.
		1‰	1.2	2.4	1134	0.004	11.	0.8	1.2	2078	0.003	13.
		1%	0.8	6.	356	0.03	8.7	0.6	4.2	671	0.02	11.
Mono-W (inclusive)	3 TeV	0	2.4	0.06	5317	0.0008	1.2	2.4	0.	6314	0.0006	1.3
		1‰	1.2	0.24	1409	0.004	1.2	1.	0.18	1705	0.004	1.3
		1%	0.8	0.54	460	0.02	1.	0.6	0.36	1255	0.02	1.1
	6 TeV	0	2.2	0.12	8969	0.0004	2.4	2.4	0.	16721	0.0002	2.6
		1‰	1.2	0.48	1855	0.003	2.3	1.	0.36	2629	0.003	2.5
		1%	0.8	1.1	467	0.03	2.	0.6	0.72	1010	0.02	2.2
	10 TeV	0	2.	0.4	4213	0.001	4.	2.2	0.2	9661	0.0004	4.4
		1‰	1.4	1.	1202	0.004	3.8	1.2	0.6	2786	0.003	4.2
		1%	0.6	2.	441	0.03	3.2	0.4	1.6	622	0.02	3.7
	14 TeV	0	1.8	0.56	4093	0.001	5.5	2.2	0.28	10846	0.0004	6.1
		1‰	1.2	1.4	1215	0.004	5.3	1.2	0.84	2859	0.003	5.8
		1%	1.	2.8	486	0.02	4.4	0.2	2.5	315	0.03	5.
	30 TeV	0	1.6	2.4	2888	0.002	12.	2.2	0.6	8056	0.0006	13.
		1‰	1.2	2.4	1922	0.003	11.	1.2	2.4	1829	0.003	12.
		1%	1.	6.	627	0.02	9.3	0.4	5.4	395	0.03	11.

Table F.4: *95%C.L. reach on the mass of the Dirac $4_{1/2}$ and 5_1 from the various mono-X channels. The excluded number of signal events $S_{95\%}$ and the relative precision $S_{95\%}/B$ are also given,together with the values of the optimal event selection cuts on η_X and $p_{T,X}$,where X is the single vector boson.The numbers are shown for different collider energies $\sqrt{s}$ and systematic uncertainties $\epsilon_{\rm sys}$.*

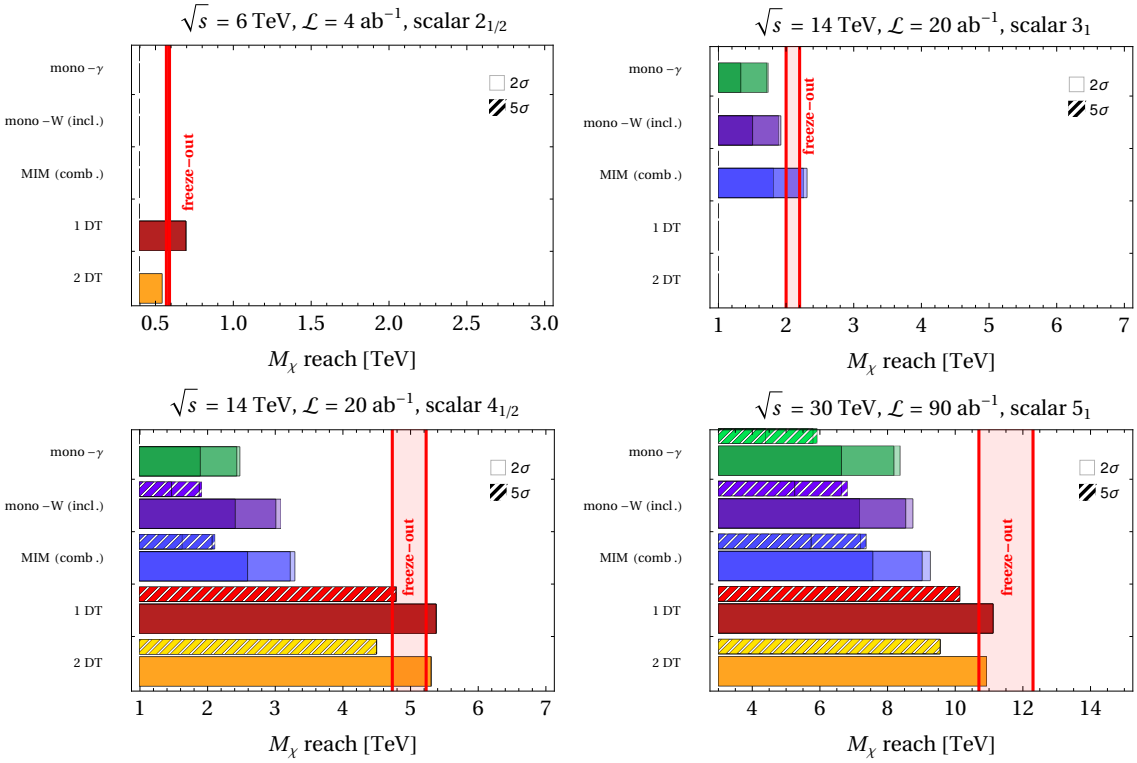

Figure F.6: *Collider results for scalar WIMPs. Same notation as in Fig. 2.11.*

treatment is the mono-W one. We split this background in two contributions. For pseudo-rapidities of the final state lost muon $\eta_\mu > \eta_{\rm match}$ (computed with respect to the direction of the initial state muon with the same charge), we compute the cross-section of the process $\gamma\mu^\mp \to W^\mp\nu$, using the improved Weizsäcker-Williams approximation [435]. For $2.5 < \eta_\mu < \eta_{\rm match}$, we compute the full hard process $\mu^-\mu^+ \to W^\mp\nu\ell^\pm$. The values used for $\eta_{\rm match}$ are $5.4, 6.2, 6.5, 7.0, 7.5$ for $\sqrt{s} = 3, 6, 10, 14, 30$ TeV, respectively. These values are such that the two background contributions are the same in the pseudorapidity region $(\eta_{\rm match}, \eta_{\rm match} + 0.2)$ for the lost muon.

F.3 Recasting the disappearing tracks

We recast the two search strategies discussed in Ref. [122] that exploit the presence of a single short reconstructed disappearing track or a two-track analysis that require at least one of them to be a short disappearing track, in addition to a trigger photon. The requirements are summarized in Table F.5 from Ref. [122].

Single-track search. For the single-track analysis we take the background cross-section quoted in [122]. This rate is mainly determined by the combinatorial of track reconstruction induced by beam-induced backgrounds.[1] To determine the rate of the

[1] As acknowledged in [122], this estimate of the background is quite conservative because it is based on detailed beam dynamics simulation for $\sqrt{s} = 1.5$ TeV. Due to the relativistic dilution of muon decays, we expect smaller background cross-section at higher $\sqrt{s}$.

single-track events, we compute the mono-photon cross-section doubly differential in the polar angles of the charged particles χ_1, χ_2. This $d\sigma/d\theta_1 d\theta_2$ is obtained at LO in perturbation theory with MadGraph5_aMC@NLO and is further reweighted to take into account angular and distance sensitivity to stub-tracks reported in Ref. [122]. Let $P(\theta_1)$ be the probability that the particle χ_1 is reconstructed as a track:

$$P(\theta, r_{\min}, r_{\max}) = \int_{r_{\min}}^{r_{\max}} \frac{\mathrm{d}r\, \epsilon_{\rm rec}(r,\theta)}{c\tau\beta\gamma \sin\theta} e^{-r/(c\tau\beta\gamma\sin\theta)}, \tag{F.1}$$

where r is the transverse radius and $\epsilon_{\rm rec}(r,\theta)$ is the probability to reconstruct as a track a particle travelling at an angle θ that decayed at a transverse radius r given in Fig. 11 of Ref. [122]. For single tracks $\epsilon_{\rm rec}(r,\theta)$ is 0 outside the interval $r \in [50\,\mathrm{mm}, 127\,\mathrm{mm}]$, and outside $\pi/6 < \theta < 5\pi/6$. The radial condition reflects the fact that tracks can only be reconstructed if the particles make at least 4 hits in the vertex detector, which for the considered geometry means that the particle must travel at least a minimum distance of 50 mm in the detector, while the upper limit stems from the disappearing condition of the track. The latter condition will be relaxed in the 2-tracks search. With the knowledge of $\epsilon_{\rm rec}$ the integral in Eq. (F.1) can be performed numerically. As per Table F.5, the hard cross-section $\sigma_{S,\gamma}$ is subject to trigger requirements: the leading observed track is required to have

$$p_{\rm T} > 300 \text{ GeV} \tag{F.2}$$

to help discriminate it against fake tracks, and it must lie within the cone

$$\frac{2\pi}{9} < \theta < \frac{7\pi}{9}. \tag{F.3}$$

In our recast, due to lack of a detailed tracking and detector simulation, these cuts are implemented at parton level on the DM particles momenta, which leads us to overestimates the number of events that pass the selection. To account for this effect we assume that only a fraction $\epsilon_{\rm tran}$ of the events with parton $p_{\rm T} > 300$ GeV gives a track whose $p_{\rm T}$ fulfils the same conditions. The transfer factor $\epsilon_{\rm tran} \approx 0.5$ is estimated from the $p_{\rm T}$ distribution of χ obtained at generator level, and track $p_{\rm T}$ distribution given in Ref. [122]. We assume that tracks with $p_{\rm T} > 300$ GeV can only come from χ with $p_{\rm T} > 300$ GeV. To properly avoid over-counting events with two reconstructed tracks, we divide the final state phase space into two non-overlapping regions that require different reconstruction constraints:

	Single track (1T)	Double track (2T)
E_γ	> 25 GeV	> 25 GeV
$p_{\rm T}$ leading track	> 300 GeV	> 20 GeV
$p_{\rm T}$ subleding track	/	> 10 GeV
θ leading track	$\frac{2\pi}{9} < \theta < \frac{7\pi}{9}$	$\frac{2\pi}{9} < \theta < \frac{7\pi}{9}$
Δz tracks	/	< 0.1 mm

Table F.5: *Event selections in the two signal regions considered in the original work [122].*

i) Both χ fulfil the conditions to be considered as leading track (Eq. (F.2) and Eq. (F.3)). In this case both tracks are subject to the detection and reconstruction efficiencies ϵ_{tran} and $\epsilon_{\text{rec}}(\theta, r)$. These events may give rise to zero, one, or two reconstructed stub-tracks. We count events with at least one stub-track.

ii) Exactly one χ fulfils the conditions to be considered as leading track. Only events in which this track is reconstructed according to detection and reconstruction efficiencies ϵ_{tran} and $\epsilon_{\text{rec}}(\theta, r)$ are counted. The fate of the sub-leading χ (if any) is irrelevant.

The largest contribution to the single-track cross-section comes from events in region i), where both DM particles satisfy the p_{T} and θ requirements to be considered as a leading track. The preference for this configuration reflects the approximate 2-body kinematics of the mono-γ events with small p_{T}. In order to understand the nature of signal we can split it into two further sub-categories with: a) exactly one reconstructed track which fulfils the conditions Eq. (F.2) and Eq. (F.3); b) exactly 2 reconstructed stub-tracks, of which at least one fulfils the same conditions. The respective rates are given by:

$$\frac{\mathrm{d}^2\sigma^{1\text{T}}_{S,\gamma}}{\mathrm{d}\cos\theta_1 \mathrm{d}\cos\theta_2} \cdot \begin{cases} \epsilon_{\text{tran}} 2P(\theta_1)(1-P(\theta_2)) & \text{1 track,} \\ \left(1-(1-\epsilon_{\text{tran}})^2\right) P(\theta_1)P(\theta_2) & \text{2 tracks,} \end{cases}$$

where the hard cross-section $\sigma^{1\text{T}}_{S,\gamma}$ is restricted to the phase-space region where both χ particles fulfil the requirements of Eq. (F.2) and Eq. (F.3). The boost factor $\beta\gamma$ and the angular distribution are both taken from a MC sample with cuts only on the photon at generator level.

The resulting number of events is used to compute the reach on the DM mass reported in Fig. 2.7, according to Eq. (2.39) with $\epsilon_{\text{sys}} = 0$.

Interestingly, the results obtained from the MC sample can also be understood semi-analytically thanks to the simple kinematics of the mono-photon process. Given that the photon tends to be soft, the kinematics of the three body process is not too different from direct production of a pair of oppositely charged DM particles without the photon. Therefore a very good analytic approximation of the above results can be obtained, with the χ boost factor and flight directions approximated by the ones for pair-produced DM particles with energy $\sqrt{s}/2$,

$$\beta\gamma \approx \sqrt{\frac{s}{4M_\chi^2} - 1}\,, \qquad \theta_1 = \pi + \theta_2. \tag{F.4}$$

The angular distribution can also be computed analytically in the 2-body limit,

$$\frac{1}{\sigma_{S,\gamma}} \frac{\mathrm{d}\sigma_{S,\gamma}}{\mathrm{d}\cos\theta} \propto \begin{cases} 1 + 4\frac{M_\chi^2}{s} + \left(1 - 4\frac{M_\chi^2}{s}\right)\cos^2\theta\,, & \text{fermion,} \\ \sin^2\theta\,, & \text{scalar.} \end{cases}$$

Results obtained using the MC 3-body angular distributions are in good agreement with the ones obtained with this analytic two-body approximation.

Double-track search. The signal of the double tracks is computed by requiring both DM particles to be reconstructed as tracks. The rate in this case is

$$\frac{\mathrm{d}^2\sigma^{2\mathrm{T}}_{\mathrm{S},\gamma}}{\mathrm{d}\cos\theta_1 \mathrm{d}\cos\theta_2} P(\theta_1)P(\theta_2) \ . \tag{F.5}$$

We additionally require the two tracks to originate from points that are close to each other along the direction of the beam axis, $\Delta z < 0.1$ mm (see Table F.5). This effectively reduces the background to negligible levels. In this limit, we use 4 signal events as a conservative estimate of the 95% C.L. exclusion for a Poissonian counting.

The angular cuts on the tracks are the same as in the single track case, while the p_{T} cuts are much milder: $p_{\mathrm{T}} > 10, 20$ GeV for the sub-leading and leading tracks, respectively. In this case the mismatch between the p_{T} of the reconstructed track and the p_{T} of the charged χ obtained at generator level is negligible. The additional cuts do not affect significantly the signal events. Note that, following Ref. [122], the disappearing condition is required on at least one track, i.e. this analysis includes in the signal all events in which the second track extends up to a transverse radius of $r = 1153$ mm. Following Ref. [122], we assumed for such long tracks a reconstruction efficiency equal to the tracks decaying between 101 mm $< r <$ 127 mm. Also for double tracks, the result obtained using the MC sample $\beta\gamma$ and θ distributions are in agreement with the ones computed analytically in the 2-body limit.

For complex WIMPs, the DT results shown in Fig. 2.11 are a particular sub-case of those shown in Fig. 2.14, as in Fig. 2.11 we fixed some choice of the mass splitting governing the spectrum specifically for each WIMP as described in the following. For the $2_{1/2}$ the splitting between the charged and neutral components has been set to its asymptotic gauge contribution $\delta m_+ = 354$ MeV. Its 1-loop value computed at the thermal mass is 343 and 335 MeV for the fermion and scalar respectively. Using the latter values increases the 2σ mass reach by 10% (20% for the two DT search for the scalar). This does not change appreciably the minimum collider energy required for exclusion. For the 3_1 the splitting has been set to its gauge value of $\delta m_+ \simeq 540$ MeV. For the $4_{1/2}$, the splitting δm_+ has been taken equal to its value at the maximal mixing point, for which it is equal to δm_-, up to corrections of order δm_0. This choice implies that the χ^+ and χ^- particles are maximal admixtures of the gauge eigenstates, hence they have same cross-sections and lifetimes. The latter are governed by the mass splitting δm_+ and δm_-, which, from Eq. (2.16) are constrained to satisfy $\delta m_+ + \delta m_- = \delta m_0 + 2\delta_g$. This equation implies that for $\delta m_0 \ll \delta_g$ in the $\delta m_+ = \delta m_-$ case we obtain lifetimes that have relatively challenging detector acceptances. Thus we can consider this choice as a representative but somewhat pessimistic estimate of the mass reach. The χ^{++} has been assumed to promptly decay equally into χ^+ and $\chi^{-,c}$. For the 5_1 WIMP we proceeded similarly to the $4_{1/2}$ case.

Appendix G

Form Factors

In this appendix we discus the form factors of nucleons and mesons relevant for the production cross sections.

G.1 Time-like form factors

In the extended Vector Meson Dominance (eVMD) formalism, form factors are modelled as sum over meson states $\mathfrak{m}$ sharing the same quantum numbers of the SM operator X involved in the matrix element. Typically the formalism is applied in the space-like region, and the form factors are essentially the sum of the propagators of the virtual mesons. However given that the exchanged momentum $p_{\rm DS}$ in our case is time-like, the form factors are modelled as Breit-Wigners, to allow the virtual exchanged meson to go on-shell and resonantly mix with the DS system:

$$F_{\mathfrak{m}}(p^2_{\rm DS}) = \sum_i f_{\mathfrak{m}_i} \frac{m^2_{\mathfrak{m}_i}}{p^2_{\rm DS} - m^2_{\mathfrak{m}_i} + i m_{\mathfrak{m}_i}\Gamma_{\mathfrak{m}_i}} \,, \tag{G.1}$$

where $m_{\mathfrak{m}}, \Gamma_{\mathfrak{m}}, f_{\mathfrak{m}}$ are the mass, the decay width and the "couplings" for the meson $\mathfrak{m}$ respectively. The number of resonances in the meson tower sharing the $\mathfrak{m}$ quantum numbers is such that it allows to enforce the correct asymptotic behaviour in q^2 of the form factor coming from sum rules. The couplings $f_{\mathfrak{m}_i}$ are fitted from data and by the overall coupling normalization. In order to get the total form factor F_X, we need to also take into account the cut-off for too high virtuality of Eq. (3.28):

$$F_X = F_D(Q^2) F_{\mathfrak{m}}(p^2_{\rm DS}) \,. \tag{G.2}$$

We next discuss the Higgs and the Z portal case separately.

G.1.1 Higgs portal

The Higgs coupling to the protons is of the form

$$g_{hNN} F_H(q^2)\, h\, \bar{u}_p\, u_p \,, \tag{G.3}$$

	f_0 (Scalar)			ω (Z, vector iso-singlet)			ρ (Z, vector iso-triplet)			a_1 (Z, axial iso-triplet)	
$m_{\mathfrak{m}}$ (GeV)	0.5	0.980	1.37	0.782	1.42	1.67	0.775	1.45	1.72	1.23	1.647
$\Gamma_{\mathfrak{m}}$ (GeV)	0.275	0.5	0.35	8×10^{-3}	0.2	0.3	0.149	0.4	0.25	0.4	0.254
$f_{\mathfrak{m}}$	0.28	1.8	-0.99	1.011	-0.881	0.369	0.616	0.223	-0.339	2.26	-1.26

Table G.1: *Masses $m_{\mathfrak{m}}$, width $\Gamma_{\mathfrak{m}}$ and coupling $f_{\mathfrak{m}}$ of the mesons $\mathfrak{m}$ for the scalar, vector iso-singlet, vector iso-triplet, and axial iso-triplet proton Form Factors used in the eVMD approach.*

where u_p is the proton spinor. The form factor F_H also includes the virtuality cut-off of Eq. (3.27):

$$F_H = F_D F_S \tag{G.4}$$

The form factor $F_S(p_{\rm DS}^2)$ is estimated using Eq. (G.1), and we include the first three CP-even, scalar resonances. The values used for masses, width and f used in the FF are given in Table G.1.

G.1.2 Z portal

The effective Z vertex for the proton is modelled as:

$$\begin{aligned}&\frac{g_2}{\cos\theta_W}\bar{u}_p\gamma^\mu\left(F^\rho(q^2)\left(\frac{1}{2}-\sin^2\theta_W\right)-\sin^2\theta_W F^\omega(q^2)\right)u_p+\\&+\frac{g_2}{4\cos\theta_W}g_A F_A(q^2)\bar{u}_p\gamma^\mu\gamma^5 u_p\,,\end{aligned} \tag{G.5}$$

where q is the exchanged momentum between the virtual and real proton ($p_{\rm DS}$ in our case) and u_p is the proton spinor. The prefactors in front of the iso-singlet and iso-triplet vector form factors (F^ω and F^ρ respectively) come from the decomposition of the vector piece of the quark Z-current in the singlet and triplet component in isospin space, using the approximate isospin symmetry of proton and neutron. The axial-vector form factor has a slightly different normalization than the vector one. In particular, there is an extra $g_A \simeq 1.2$ multiplying the overall form factor in Eq. (G.1), as shown in Eq. (G.5). We can see that the vector part is subleading with respect to the axial current due to the absence of $\sin^2\theta_W$ suppressing factor and a $\mathcal{O}(1)$ coupling g_A. Notice that in principle, along with the Dirac-like form factors appearing in Eq. (G.5), there should be the non-renormalizable Pauli-like terms [436]:

$$G_V(q^2)i\frac{[\gamma^\mu,\gamma^\nu]}{m_p}q_\nu + G_A(q^2)\gamma^5\frac{1}{m_p}q^\mu\,, \tag{G.6}$$

where the second piece (the axial one) is mediated by pion exchange. It turns out that this contribution vanishes when contracted with the JJ correlator, due to current conservation. The vector piece, corresponding to the anomalous magnetic proton contribution, does not vanish. Given that it's numerically subleading, and that there are large uncertainties to extrapolate such form factor in the time-like region [437, 438], we will neglect this contribution.

The form factors appearing in Eq. (G.5) are again computed in the eVMD formalism, as a sum of Breit-Wigners of ρ, ω, a_1 meson for F^ρ, F^ω, F_A respectively. The coefficients used in the form factors are found in Table G.1.

The final form factors appearing in Eq. (3.32),Eq. (3.33) are defined respectively as:

$$\begin{aligned} F_Z^{\mathrm{V}} &= F_D \left(-\sin^2\theta_W F^\omega + F^\rho \left(\frac{1}{2} - \sin^2\theta_W \right) \right) , \\ F_Z^{\mathrm{A}} &= F_D \frac{g_A}{4} F_A \, . \end{aligned} \tag{G.7}$$

We can generalize the formalism for any combination of iso-singlet and iso-triplet axial and axial-vector currents, meaning that we can get the form factor for all the possible flavor-conserving quark coupling structures of generic JJ portals.

Notice that in Table G.1 there are no axial-vector iso-singlets form factors, but they can be obtained from lattice computations.

G.2 Meson decay matrix elements

Here we summarise the QCD matrix elements and form factor parametrizations we use for computing decays of mesons. For the case of annihilation decays, the meson decays to DS states entirely, while for radiative decays, a heavier meson decays to lighter mesons, along with DS. The matrix element for the process can be factorized into a short distance contribution (and only involves DS matrix elements) and a long distance (QCD) contribution. For the process $\mathbf{M} \to \mathrm{DS}$, where $\mathbf{M}$ is the decaying meson, the full amplitude $\langle \mathrm{DS}|\mathcal{O}_{\mathrm{SM}}\,\mathcal{O}_{\mathrm{DS}}|\mathbf{M}\rangle$ factors into $\langle 0|\mathcal{O}_{\mathrm{SM}}|\mathrm{M}\rangle \times \langle \mathrm{DS}|\mathcal{O}_{\mathrm{DS}}|0\rangle$ while for the process $\mathbf{H} \to \mathbf{L} + \mathrm{DS}$, where $\mathbf{H}$ ($\mathbf{L}$) are the heavy (light) SM mesons, the amplitude $\langle \mathbf{L}, \mathrm{DS}|\mathcal{O}_{\mathrm{SM}}\,\mathcal{O}_{\mathrm{DS}}|\mathbf{H}\rangle$ factors as $\langle \mathbf{L}|\mathcal{O}_{\mathrm{SM}}|\mathbf{H}\rangle \times \langle \mathrm{DS}|\mathcal{O}_{\mathrm{DS}}|0\rangle$. For the annihilation case, we only consider vector mesons, denoted by V[1]. The SM matrix element for annihilation decay is simple, and is generically given as

$$\langle 0|\bar{u}\gamma_\mu u|V(p)\rangle = i f_V m_V \epsilon_\mu(p) \, , \tag{G.8}$$

where u are the quark spinors, $\epsilon_\mu(p)$ is the polarization vector of the vector meson V, f_V is the decay constant, and m_V is the mass of the meson.

For the radiative decay case, the SM contribution to the amplitude is the same as SM semileptonic meson decays, and is less straightforward than the annihilation case. We now give details of the matrix elements and form factors used to compute width of decays of $\mathrm{H} \to \mathrm{L} + \mathrm{DS}$ where H can be B, K and L can either be a light pseudoscalar P (e.g. K, π) or vector V (e.g., K^*, ρ, ϕ).

G.2.1 Decay to Pseudoscalars

For the decay of mesons to pseudoscalars P (e.g., K, π) we use the usual matrix element definitions (see [439] for example):

[1]For pseudoscalar mesons, the matrix element is proportional to p_μ and vanishes when contracted with the DS current, by current conservation.

$$\langle P(p_P)|\, V^\mu \,|H(p_H)\rangle = f_+(q^2)p^\mu + \big(f_0(q^2) - f_+(q^2)\big)\; D\, q^\mu \,, \tag{G.9}$$

where $V^\mu = \bar{u}_L \gamma^\mu u_H$, $p^\mu = p_H^\mu + p_P^\mu$, $D = (M_H^2 - M_P^2)/p_{\rm DS}^2$, and $q^\mu \equiv p_{\rm DS}^\mu = p_H^\mu - p_P^\mu$. Here, u_L (u_H) denotes a light (heavy) quark field, $p_H(p_P)$ is the 4-momentum of the decaying heavy (light) meson with mass $m_H(m_P)$, and $f_0(q^2), f_+(q^2)$ are dimensionless form factors which encode the strong interaction effects. For the case of $\mathcal{O}_{\rm DS} = J_\mu^{\rm DS}$, a conserved current, terms proportional to $q^\mu\, J_\mu^{\rm DS}(q)$ vanish, so that we only need to specify the $f_+(q^2)$ form factors.

For $K^+ \to \pi^+ + {\rm DS}$ decay we use the explicit form factor data points defined at each q^2 in Table IV of ref. [440]. For $B \to \pi, K$ decays, we use the form factor definitions and values from ref. [439]:

$$\begin{aligned} f_+^{B\to\pi}(q^2) &= \frac{A}{\big(1 - q^2/D^2\big)\big(1 - q^2/E^2\big)} \,, \\ f_+^{B\to K}(q^2) &= \frac{B}{1 - q^2/F^2} + \frac{C}{\big(1 - q^2/F^2\big)^2} \,, \end{aligned} \tag{G.10}$$

where $A = 0.258, B = 0.173, C = 0.162$ and $D = 5.32$ GeV, $E = 6.38$ GeV, and $F = 5.41$ GeV.

G.2.2 Decay to Vector Mesons

For the case of B meson decaying to light vector mesons V (e.g., K^*, ρ, ϕ), the QCD matrix element is defined as (see ref. [441]):

$$\begin{aligned} &\langle V(p_V)|\, J_\mu \,|B(p_B)\rangle = \\ &= -i\epsilon_{\mu *}(p_V)(m_B + m_V)\, A_1(q^2) + i p_\mu (\epsilon^*(p_V)\cdot q)\, \frac{A_2(q^2)}{m_B + m_V} + \\ &+ i\, q_\mu (\epsilon^*(p_V)\cdot q)\, \frac{2m_V}{q^2}(A_3(q^2) - A_0(q^2)) + \epsilon_{\mu\nu\rho\sigma}\epsilon^{\nu *}(p_V) p_B^\rho p_V^\sigma\, \frac{2V(q^2)}{m_B + m_V} \,, \end{aligned} \tag{G.11}$$

where $J^\mu = \bar{q}_L \gamma^\mu (1 - \gamma_5) q_H$, $p^\mu = (p_B + p_V)^\mu$, and $q^\mu \equiv p_{\rm DS}^\mu = p_B^\mu - p_V^\mu$. Here p_B (p_V) are the 4-momentum of the B (vector) meson, m_B (m_V) is the mass of the B (V) meson, ϵ^μ is the polarization vector of V, and $A_i(q^2), V(q^2)$ are the dimensionless form factors encoding strong interaction effects. Note that, unlike the pseudoscalar case, in the case of vector meson, the $\gamma_5\gamma^\mu$ part of the current does not vanish. Further, the third term in the above does not contribute since it is zero by current conservation, as in the pseudoscalar case.

For the form factors, we use the parametrizations as given in ref. [441]:

$$V(q^2) = \frac{r_1}{1 - q^2/m_R^2} + \frac{r_2}{1 - q^2/m_{fit}^2} \,, \tag{G.12}$$

$$A_1(q^2) = \frac{r_2}{1 - q^2/m_{fit}^2} \,, \tag{G.13}$$

$$A_2(q^2) = \frac{r_1}{1 - q^2/m_{fit}^2} + \frac{r_2}{(1 - q^2/m_{fit}^2)^2} \,. \tag{G.14}$$

	r_1	r_2	m_R^2 [GeV^2]	m_{fit}^2 [GeV^2]
$V^{B\to K^*}$	0.923	-0.511	28.30	49.4
$A_1^{B\to K^*}$	-	0.290	-	40.38
$A_2^{B\to K^*}$	-0.084	0.342	-	52.00
$V^{B\to \rho}$	1.045	-0.721	28.30	38.34
$A_1^{B\to \rho}$	-	0.240	-	37.51
$A_2^{B\to \rho}$	0.009	0.212	-	40.82
$V^{B_s\to \phi}$	1.484	-1.049	29.38	39.52
$A_1^{B_s\to \phi}$	-	0.308	-	36.54
$A_2^{B_s\to \phi}$	-0.054	0.288	-	48.94

Table G.2: *Fit parameters for the form factors defined in Eq. (G.12), Eq. (G.13), Eq. (G.14) for various $B \to V$ transitions where $V = K^*, \rho, \phi$ (taken from [441]).*

We give the values of the various fit parameters for the different decays in Table G.2. To evaluate further the squared matrix element, we make the calculations in the rest frame of B meson, where only the longitudinal polarization of $\epsilon_\mu^*(p_V)$ contributes. Thus, using $\epsilon_\mu^*(p_V) = \left(\frac{|\vec{p}_V|}{m_V}, \frac{\vec{p}_V}{|\vec{p}_V|}\frac{E_V}{m_V}\right)$ and $p_{\rm DS} = p_B - p_V$, we can find the production width of DS from radiative $B \to V$ decays.

G.2.3 Sensitivity to non-conformal contributions in K, B meson decays

For the case of DS production from irrelevant portals, we expect the production cross-section to grow with $p_{\rm DS}^2$ which is necessary to make the contribution away from the IR threshold more important, and is needed for usefulness of our model agnostic approach. For radiative meson decays however, the DS production cross-section does not grow as $p_{\rm DS}^2$, but is rather flat, upto the kinematic threshold. For annihilation decays, $p_{\rm DS}^2$ is fixed and equals the parent meson mass-squared. To justify our model agnostic approach we need to ensure we are away from the thresholds, which must be imposed as a self-consistent criteria.

The overall signal is obtained by an integral over the range of allowed $p_{\rm DS}$. The kinematic condition $p_{\rm DS}/(n_{\rm LDSP}\,\Lambda_{\rm IR}) \geq 1$ is always stronger than the condition to be in the conformal regime $p_{\rm DS}/\Lambda_{\rm IR} \gtrsim 1$. We also need to make sure that the relevant $\Lambda_{\rm IR}$ probed in the experiment under consideration (which depends on the portal and the lifetime) is away from the kinematic threshold $M - m$. For $\Lambda_{\rm IR}$ close to $M - m$, a small change in the lower limit of $p_{\rm DS}$ integration would have a bigger impact, but this does not happen in the cases we consider. For $B \to K + \text{DS}$, $(m_B - m_K) \sim 5$ GeV is larger than typical $\Lambda_{\rm IR}$ probed which is $0.001 - 1$ GeV, while for $K \to \pi + \text{DS}$, $(m_K - m_\pi) \sim 0.4$ GeV, while the typical $\Lambda_{\rm IR}$ probed is $0.001 - 0.1$ GeV.

Appendix H

Details of Beam Dumps computations

H.1 Probability of Decay

To compute the number of signal events, we need to calculate the number of LDSPs that decay inside the detector. To correctly compute this quantity, the differential cross section (in both energy and angle) of LDSP production must be convoluted with the probability P for at least an LDSP to decay inside the detector. The probability P_1 for a particle to decay inside the detector can be roughly estimated as the probability $P_{1,\mathrm{dec}}$ to decay within the radial distance at which the detector is, multiplied with ϵ_{geo}, the geometric acceptance accounting for the particles flying in the detector direction:

$$P_1 \approx \epsilon_{\mathrm{geo}} P_{1,\mathrm{dec}} \ , \tag{H.1}$$

In a simplified setup (see Fig. 3.6), $P_{1,\mathrm{dec}}$ can be estimated to be

$$P_{1,\mathrm{dec}} = \exp\left(-\frac{l}{c\tau(\gamma\,\beta)_{\mathrm{LDSP}}}\right) - \exp\left(-\frac{l+d}{c\tau(\gamma\,\beta)_{\mathrm{LDSP}}}\right) \ , \tag{H.2}$$

where l and d are the distance of the detector from the target location and the length of the detector respectively [1], γ_{LDSP} is the (energy dependent) Lorentz factor of the decaying particle, β_{LDSP} is its velocity and τ is its proper lifetime. In general, for more than 1 LDSP, a slightly more refined procedure accounting for the presence of multiple particles that can go inside the detector is needed. We now discuss our procedure for multiple particle events. We consider both the weakly coupled case, where $n_{\mathrm{LDSP}} = 2$, and a generic strongly coupled case in which $n_{\mathrm{LDSP}} \sim \mathcal{O}(10)$ are produced.

[1] Notice that the distance should be a function of the direction of the LDSP for generic geometry of the detector. We will work under the assumption of spherical detectors, where the distances appearing in P are independent of the line of flight. This is a good approximation for neutrino experiments, since they consist of small boxes (of size $\mathcal{O}(10)$ m) positioned far ($\mathcal{O}(10^3)$ m) from the target. The error due to the geometrical approximation is therefore of order 1% (the ratio of the typical distances).

For the weakly coupled case, the directions of the two LDSPs are fully correlated, at fixed $p_{\rm DS}$, by momentum conservation. If the direction of the DS sytem (*i.e.* $\vec{p}_{\rm DS}$) does not intersect the detector, at most one of the two LDSPs can have the correct direction to hit the detector. Indeed, the two particles have opposite azimuthal angle ϕ (computed with respect to the DS momentum in the lab frame), so that only one particle at most can travel to the correct side. Therefore the probability to have at least one particle decaying inside the detector is (in the notation of Eq. (3.9)):

$$\epsilon_{\rm geo}\, P_{\rm decay} = 2\epsilon_{\rm geo} P_{\rm 1,dec}\ ,$$

where the 2 reflects the fact that $\epsilon_{\rm geo}$ has been computed for a single particle only, and there are two possible particles that can decay in the detector (or in other words, we only considered one of the particles to be aimed toward the detector, but the opposite direction is also a valid choice given the presence of the other LDSP).

If instead the DS direction intersects the detector there is the possibility for both LDSPs to fall inside the detector. This can happen only if the LDSP velocity in the DS frame is slower than the velocity of the DS system in the lab frame, so that the LDSP traveling in the direction $\theta > \pi/2$ (the backward direction) in the DS frame is boosted in the forward direction. The events in which the backward LDSP gets boosted forward in the lab frame are only significant if the DS system velocity is much larger than the velocity of the LDSP in the DS frame. Given that typically $n_{\rm LDSP}\Lambda_{\rm IR} \ll \sqrt{p_{\rm DS}^2}$, and that the bulk of the cross section is dominated by high $p_{\rm DS}^2$ events, the events will have fast LDSPs in the DS frame. Therefore events with two particles boosted forward are negligible, and the formula to have a particle decaying inside the detector holds unchanged.

In the strongly coupled case, where $n_{\rm LDSP}$ is large, we can neglect the fact that the momenta are correlated by momentum conservation. Therefore we will assume that the $n_{\rm LDSP}$ particles share democratically the energy in the rest frame, and that the directions are independent samples from an isotropic distribution in such a frame. In this scenario, multiple particles can in principle have the correct direction to get inside the detector in the lab frame. Using the probability for a single particle to decay inside the detector from Eq. (H.2), and recalling that this probability is very small (both $P_{\rm 1,dec}$ and typical $\epsilon_{\rm geo}$ are small), it follows that events in which multiple particles simultaneously decay inside the detector are very rare. Therefore we can approximate the probability for a single event to contain at least one particle decaying inside the detector as

$$\epsilon_{\rm geo}\, P_{\rm decay} = n_{\rm LDSP}\, \epsilon_{\rm geo}\, P_{\rm 1,dec}\ .$$

Notice that in the end (although for slightly different reason) this formula matches the one in the weakly coupled case for $n_{\rm LDSP} = 2$.

H.2 $\epsilon_{\rm geo}$ estimates

In order to compute the signal events, we have to compute the fraction of events that contain at least one LDSP with the direction intersecting the detector. Given the

assumptions outlined in Sec. H.1, we define ϵ_{geo} as the probability for a single particle to have such a direction. We work under the assumption that LDSPs are produced isotropically in the DS rest frame, the frame in which only the time component of p_{DS} is non-zero. We will also assume that in this frame, all the LDSPs produced share the same energy $p^0_{\text{DS}}/n_{\text{LDSP}}$. We take the beam direction to be aligned to the z-axis ($\theta = 0$ in polar coordinates), and ϕ as the azimuthal angle (measured in the plane orthogonal to the beam line).

In order to get an estimate for the angular coverage of the neutrino detector, we work under the simplifying assumption that the detector surface lies on a 2D plane orthogonal to the beam (for the off-axis case, the angle is very small) and all points on the detector are at the same distance from the interaction point. This is a good approximation for neutrino detectors since corrections are of order $(d/l)^2 \ll 1$, where l is the distance at which the detector is placed, and d is the typical size of the detector. There are two relevant cases where this approximation fails.

For a closer experiment like SHiP, l and d are of same order, and the proposed shape is a rectangle of dimensions $(a, 2a)$, $a = 5$ m. We will compute the angular acceptance by taking the largest side of the rectangle and requiring the trajectory to intersect the first layer, which gives $\theta_{\text{acc}} = \text{ArcTan}\,(2a/2l)$. Being more specific about the shape of the detector does not change the estimate significantly since the DS is produced very boosted, with a small opening angle, and is fully covered by the extent of the detector. The geometric acceptances are close to unity, see Table 3.1.

For MicroBooNE, the produced Kaons are at rest in the lab frame, and not collimated, so that the DS is produced isotropic in the lab frame. In this case, the above approximation again does not hold. We calculate ϵ_{geo} without this approximation for MicroBooNE.

To calculate ϵ_{geo}, we need to find the overlap of the LDSPs with the detector, which is easier to do in the $*$ frame. By the assumption of isotropic decay, the LDSP directions are distributed uniformly in the $(\cos\theta^*, \phi^*)$ plane. In this plane ϵ_{geo} is the area (normalized by $1/4\pi$) that corresponds to lab frame configurations in which the LDSP falls inside the detector. This in general depends on p_{DS} and n_{LDSP} through the boost factor.

To be precise, we need to introduce some notation. There are two frames to consider, the lab frame, and the DS frame (the one where p_{DS} only has a time component). We refer to the DS frame as the * frame, in what follows. The angles and the boost factors with a * superscript are defined in the DS frame, and without a * superscript are in the lab frame.

The detector direction, the DS direction, and the LDSP direction are all defined by a θ, and the last two depend in general on kinematical quantities such as p_{DS} and other process-dependent quantities *e.g.* z in bremsstrahlung. We take the detector to be positioned at $\theta = \theta_{\text{det}}$. The accepted directions form a cone around it with an angle θ_{acc} around it. The DS system may be along the beam line or at an angle from it. We define the DS system to be at $\theta = \theta_{\text{DS}}$. Finally, the LDSP is at an angle θ_{LDSP} w.r.t. the DS system, so that the DS direction has a cone of angle θ_{LDSP}

around it. It is useful to also define the DS direction w.r.t. the detector, which is denoted by $\theta_{\rm det}^{\rm eff} \approx (\theta_{\rm DS}^2 + \theta_{\rm det}^2 - 2\theta_{\rm det}\theta_{\rm DS}\cos\phi_{\rm DS})^{1/2}$. All these quantities are shown in Fig. H.1 (drawn not to scale), and are defined in the lab frame.

We additionally denote the LDSP in the * frame to be at (θ^*, ϕ^*). For a given $p_{\rm DS}$ and θ^*, $\theta_{\rm LDSP}$ is given as

$$\tan\theta_{\rm LDSP} = \frac{\sin\theta^*}{\gamma_{\rm DS}\left(\beta_{\rm DS}/\beta^*_{\rm LDSP} + \cos\theta^*\right)}\,, \tag{H.3}$$

where $\beta_{\rm DS}, \gamma_{\rm DS}$ are the boost factors to go from $*$ to the lab frame and $\beta^*_{\rm LDSP}$ is the velocity of the LDSP with respect to the $*$ frame. Note that the boosts along the DS direction do not change ϕ. Given the width $\theta_{\rm LDSP}$ of the lab cone there is only a range of $\phi_* = \phi_{\rm lab}$ for which the LDSP direction intersects the detector. $\epsilon_{\rm geo}$ is then the area (computed in the $*$ frame) of the overlap between the circular detector and all the possible LDSP cones in the lab frame, in general a function of z and of $p_{\rm DS}$. To compute such area, we will make a *linearization approximation*: we will consider that in the $*$ frame the shape of allowed $\cos\theta^* - \phi^*$ is bound by straight lines and not curved ones. This approximation is expected to hold at the 10% level for the relevant boosts.

We now discuss the details specific to the three production modes considered in this work.

H.2.1 $\epsilon_{\rm geo}$ for meson decay production

In order to find $\epsilon_{\rm geo}$ for LDSPs in the meson case, we use the prescription explained in the section before. For this, we must boost the DS kinematic variables twice: once from the meson rest frame to the lab frame, then from the lab frame to the DS rest frame (or $*$ frame). We will denote all quantities in the meson rest frame with a subscript 0.

The energy and 3-momentum of the DS can be easily computed using momentum conservation in the parent meson rest frame as shown in Eq. (3.19). Using the parent meson boost γ_M and velocity v_M (obtained from simulation), we can find the DS lab frame variables and express them as a function of $\cos\theta_0$ (angle of DS with meson flight direction in the meson rest frame, DS is isotropic in this) and $p^2_{\rm DS}$ i.e. $E^{\rm lab}_{\rm DS}(\cos\theta_0, p^2_{\rm DS})$, $\left|\vec{p}^{\,\rm lab}_{\rm DS}\right|\left(\cos\theta_0, p^2_{\rm DS}\right)$.

In order to compute $\epsilon_{\rm geo}$ we must find the θ^* values corresponding to the angular coverage of the detector. For this, we must boost the lab frame DS variables to the DS rest frame (or $*$ frame) using the DS boost given by $\gamma_{\rm DS}(\cos\theta_0, p^2_{\rm DS}) = E^{\rm lab}_{\rm DS}/\sqrt{p^2_{\rm DS}}$ and DS velocity $\beta_{\rm DS}(\cos\theta_0, p^2_{\rm DS}) = \left|\vec{p}^{\,\rm lab}_{\rm DS}\right|/\,E^{\rm lab}_{\rm DS}$ (which will be close to 1). Note that for the annihilation decay mode $M \to$ DS, $E^{\rm lab}_{\rm DS}$ gets fixed by momentum conservation to $\sqrt{M^2 + |\vec{p}_{\rm M}|}$ where M is the parent meson mass, and $|\vec{p}_{\rm M}|$ is the parent meson momentum in the lab frame. Thus, $\gamma_{\rm DS}$ is fixed to $\sqrt{M^2 + |\vec{p}_{\rm M}|}/M$.

We can now solve for the θ^* angle using Eq. (H.3), plugging $\beta^*_{\rm LDSP} = |\vec{p}^{\,*}_{\rm LDSP}|/\,E^*_{\rm LDSP}$, $E^*_{\rm LDSP} = \sqrt{p^2_{\rm DS}}/n_{\rm LDSP}$ and using $\Lambda_{\rm IR} = \sqrt{(E^*_{\rm LDSP})^2 - |\vec{p}^{\,*}_{\rm LDSP}|^2}$ to get $|\vec{p}^{\,*}_{\rm LDSP}|$.

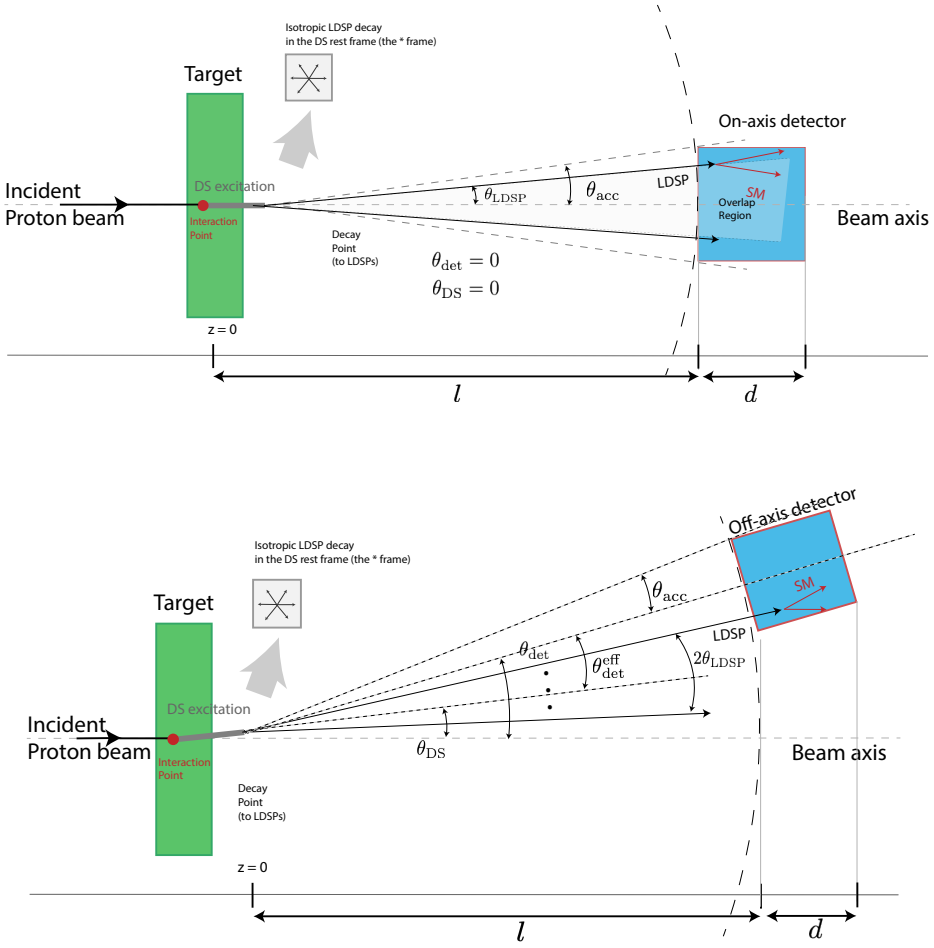

Figure H.1: *The geometry relevant for the estimation of $\epsilon_{\rm geo}$ in the on- and off-axis case (top and bottom respectively). Various quantities defined in the text, and involved in the estimation of $\epsilon_{\rm geo}$ are shown, not to scale. In particular, the DS line (gray thick) is drawn exaggerated for clarity.*

We also need $\theta_{\rm DS}$ for estimating $\epsilon_{\rm geo}$. Note that in the annihilation decay case, $\theta_{\rm DS}$ is 0 due to momentum conservation, Whereas for the radiative decay case, $\theta_{\rm DS}$ can be expressed in terms of meson rest frame variables as

$$\tan\theta_{\rm DS} = \sin\theta_0\,|\vec{p}|_{\rm DS,0} \,/\, \left(\gamma_M\left(|\vec{p}|_{\rm DS,0}\cos\theta_0 + v_M E_{\rm DS,0}\right)\right) \ . \tag{H.4}$$

Finally, we calculate $\langle\epsilon_{\rm geo}\rangle$ by a weighted average over the differential decay width $d\Gamma/dp^2_{\rm DS}\,d\lambda_i$, which is a function of $\Lambda_{\rm IR}$ only (the $\Lambda_{\rm UV}$ dependence factors out):

$$\langle\epsilon_{\rm geo}\rangle = \frac{\int {\rm d}p^2_{\rm DS}\,{\rm d}\lambda_i\;\epsilon_{\rm geo}(\lambda_i, p^2_{\rm DS})\;\frac{d\Gamma}{dp^2_{\rm DS}d\lambda_i}}{\int {\rm d}p^2_{\rm DS}\,{\rm d}\lambda_i\;\frac{d\Gamma}{dp^2_{\rm DS}d\lambda_i}} \ , \tag{H.5}$$

where λ_i are the angular variables θ_0, ϕ_0 integrated over the full range and $p^2_{\rm DS}$ is integrated in the allowed kinematic range. Note that for the annihilation decay case,

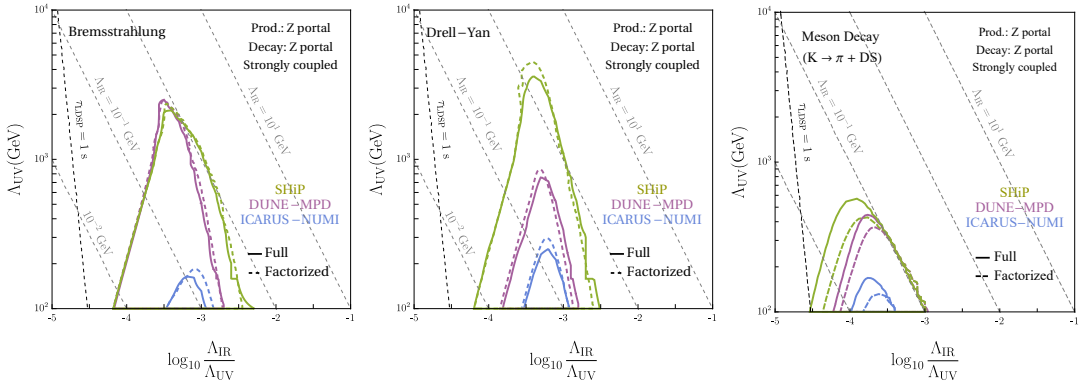

Figure H.2: *Comparison of the factorized (dashed) vs full (solid) approach for production and decay through Z portal of a strongly interacting DS, for various production modes: DB (left), DY (mid) and MD (right). The experiments considered are ICARUS-NuMI (blue), DUNE-MPD (purple) and SHiP (green).*

$p_{\rm DS}^2 = M^2$ and $\theta_{\rm DS} = 0$ by momentum conservation, which simplifies the equation above.

H.2.2 $\epsilon_{\rm geo}$ for DY

In DY mode the DS system is by construction directed along the original beam line (the z direction). The boost of the DS system is $\gamma_{\rm DS} = E_{\rm DS}/\sqrt{p_{\rm DS}^2}$, where $E_{\rm DS}$ is the energy of the DS system in the lab frame. While $p_{\rm DS}$ is already one of the variables used in DY production, $E_{\rm DS}$ is computed by first getting the DS energy in the DY CM frame, $E_{\rm DS,CM} = \sqrt{s}(x + p_{\rm DS}^2/(sx))/2$ using the DY variables introduced in Sec. 3.2.2, and then boosting it to the lab frame with Lorentz parameter $\gamma_{\rm CM} = E_{\rm beam}/\sqrt{s}$. This gives $E_{\rm DS} = xE_{\rm beam}$. Putting everything together, the boost factor to go from the lab frame to the DS system is $\gamma_{\rm DS} = xE_{\rm beam}/\sqrt{p_{\rm DS}^2}$. To get the average value of $\epsilon_{\rm geo}$, we compute the integral as in Eq. (H.5) with the appropriate distribution where now we average over the kinematic variables x and $p_{\rm DS}^2$.

H.2.3 $\epsilon_{\rm geo}$ for DB

DB mode is different from the DY mode because in general the DS system will be produced at an angle with the beam-line. We will call $\theta_{\rm DS}, \phi_{\rm DS}$ the pair of angles indicating the direction of the radiated DS system relative to the beam line. Using the kinematic variables introduced in Sec. 3.2.3, we have $\theta_{\rm DS} = \tan^{-1}(p_T/zE_{\rm beam})$. The boost factor to go from the lab to the DS frame is $\gamma_{\rm DS} \approx zE_{\rm beam}/\sqrt{p_{\rm DS}^2}$. As before, to get the average value of $\epsilon_{\rm geo}$, we average over the kinematic quantities z, p_T^2, and $p_{\rm DS}^2$. we have checked that these values are in good agreement with the $\epsilon_{\rm geo}$ for the average DS angle, as expected for very collimated DS excitations.

H.3 Factorization approximation

In this appendix we compare the approximate method we delineated in the main text with the correct procedure of doing the integral of the product of the differential quantities ($\epsilon_{\rm geo}$, cross-section, decay probability) without factorizing them.

In order to get the correct number of signal events, the differential cross section $\mathrm{d}\sigma/\mathrm{d}\lambda_i$ must be folded with $n_{\rm LDSP}\,\epsilon_{\rm geo}\,P_{1,\rm dec}$, all of which are a function of kinematic variables λ_i:

$$N_S(\Lambda_{\rm IR},\Lambda_{\rm UV}) = \frac{N_{\rm POT}}{\sigma_{pN}}\int \mathrm{d}\lambda_i\,\frac{\mathrm{d}\sigma}{\mathrm{d}\lambda_i}\,n_{\rm LDSP}\,\epsilon_{\rm geo}\,P_{1,\rm dec}\,. \tag{H.6}$$

We call this procedure the *full* approach. We compute the integrals numerically, using the CUBA integration tools [442]. The method used in the main text is done instead by replacing the full integral with the average $\epsilon_{\rm geo}$ and using average kinematic quantities to estimate the decay probability and the average $n_{\rm LDSP}$[2]:

$$N_S \approx N_{\rm POT}\,\frac{\sigma_S}{\sigma_{pN}}\,n_{\rm LDSP}(\langle\lambda_i\rangle)\,P_{1,\rm dec}(\langle\lambda_i\rangle)\,\langle\epsilon_{\rm geo}\rangle\,. \tag{H.7}$$

where the average is defined by a weighted integral over the differential cross-section/decay-width (e.g. see Eq. (H.5)). We call this approach the *factorized* approach. The advantage of this approach is that the production integral must be done only once, and not repeated for each $(\Lambda_{\rm IR},\Lambda_{\rm UV})$ pair: the dependence on them is essentially factorized. In particular, for a fixed production portal, this allows changing the decay portal, without having to redo the production integral from scratch. This is particularly useful when exploring all the various combinations of production and decay portals.

To compare the factorized and the full approach, and to show that the factorized approach is very efficient, in Fig. H.2 we show the comparison for DB, DY and radiative meson decay $K\to\pi+\mathrm{DS}$, for the strongly coupled DS, for DUNE, SHiP and ICARUS. The two approaches are in very good agreement. The factorized approach is conservative at most, and can miss rare events appearing in the tails of distributions (see e.g. ref. [443]). However for the purposes of the present work, the factorized approach suffices.

[2]We have checked that this procedure agrees very well (percent level) to a true average of $n_{\rm LDSP}$.

Appendix I

Details of Fisher matrices

Fisher matrices are a powerful tool to forecast how strongly can future experiments constrain the parameters of a given cosmological model [444], without having access to any kind of data (real or simulated). The idea is based on the properties of the Maximum Likelihood Estimator (MLE) of the parameters that we want to constrain. The discussion follows the second edition of [445]. We do not aim here for rigor, but to get the intuition behind the Fisher formalism.

Consider a cosmological model described by a set of unknown parameters, collectively denoted as θ, that we want to constrain. Assume that the real world is well described by the chosen model with a specific set of "true" parameters, denoted as θ_0. The experiment will be able to measure a set of observables $\mathcal{O}_k^{\rm exp}$, indicated by the index k, for which there is a known covariance matrix $\sigma_{kk'}$. For these experimental observables there is a known theoretical expression as a function of the parameters $\mathcal{O}_k^{\rm th}(\theta)$. Assume that the future experiment we want to forecast has a gaussian likelihood, so that its log-likelihood, given a realization of the data, is:

$$\chi^2(\theta) = \sum_{k,k'} \left(\mathcal{O}_k^{\rm exp} - \mathcal{O}_k^{\rm th}(\theta)\right) \left(\sigma^{-1}\right)_{kk'} \left(\mathcal{O}_{k'}^{\rm exp} - \mathcal{O}_{k'}^{\rm th}(\theta)\right) \ . \tag{I.1}$$

The quantity in Eq. (I.1) is maximized by the MLE $\hat{\theta}$, which asymptotically converge to the true parameter θ_0. Then we can expand the likelihood around this point, and get the following expression for the likelihood function:

$$\begin{aligned} \chi^2(\theta) \simeq\ & \chi^2(\theta_0) + \\ & + (\theta-\theta_0)^i(\theta-\theta_0)^j \sum_{k,k'} \frac{\partial^2 \mathcal{O}_k^{\rm th}(\theta_0)}{\partial\theta_i \partial\theta_j} \left(\sigma^{-1}\right)_{kk'} \left(\mathcal{O}_{k'}^{\rm exp} - \mathcal{O}_{k'}^{\rm th}(\theta_0)\right) + \\ & + (\theta-\theta_0)^i(\theta-\theta_0)^j \sum_{k,k'} \frac{\partial \mathcal{O}_k^{\rm th}(\theta_0)}{\partial\theta_i} \left(\sigma^{-1}\right)_{kk'} \frac{\partial \mathcal{O}_{k'}^{\rm th}}{\partial\theta_j}(\theta_0) \ , \end{aligned} \tag{I.2}$$

where we set to 0 the first order term since the likelihood derivative vanishes when evaluated at the MLE by definition, and we used the fact that the only quantities that depends on the parameters are the $\mathcal{O}^{\rm th}$. If the sample is large enough, we can

expect the likelihood to reach its expected value. The only quantities in Eq. (I.2) that are stochastic are the $\mathcal{O}^{\rm exp}$, and since we assume the theory to correctly model the data,

$$\mathbb{E}\left[\mathcal{O}^{\rm exp}\right] = \mathcal{O}^{\rm th}(\theta_0) \ . \tag{I.3}$$

This implies that

$$\mathbb{E}\left[\chi^2(\theta)\right] = \chi^2(\theta_0) + (\theta-\theta_0)^i(\theta-\theta_0)^j \sum_{k,k'} \frac{\partial \mathcal{O}^{\rm th}_k(\theta_0)}{\partial\theta_i} \left(\sigma^{-1}\right)_{kk'} \frac{\partial \mathcal{O}^{\rm th}_{k'}}{\partial\theta_j}(\theta_0) \ . \tag{I.4}$$

The quantity

$$\mathcal{F}_{ij} \equiv \sum_{k,k'} \frac{\partial \mathcal{O}^{\rm th}_k(\theta_0)}{\partial\theta_i} \left(\sigma^{-1}\right)_{kk'} \frac{\partial \mathcal{O}^{\rm th}_{k'}(\theta_0)}{\partial\theta_j} \tag{I.5}$$

is the Fisher matrix. Its importance lies in the fact that it is an estimator of the inverse covariance of the MLE $\hat{\theta}$, and hence it gives an estimate of the constraining power of a future survey. Since it does not depend on any data, it can be computed theoretically in a given model.

Notice that the estimator for β is expected to be highly non gaussian: $\beta > 0$ by assumption, but its MLE is 0 in a ΛCDM cosmology, with a variance of order 10^{-3}. In this case, the 95% credibility interval for the 1D posterior is found to be at 1.64σ rather than the usual 2σ [446]. The result cannot be generalized without further assumptions to get the 95% regions for the 2D posteriors. We will neglect this subtlety, noting that the standard procedure is more conservative.

I.1 Fisher matrix for the Power Spectrum (real space)

We want to compute the Fisher matrix for $\mathcal{O}^{\rm th} = P_g(k)$ in real space, for which we already reported the computation in Chapter 4. We must define what is $\mathcal{O}^{\rm exp}$, as its covariance matrix enters the computation. Practically speaking, given a dataset an estimator $\hat{P}_g$ of the power spectrum can be defined by averaging modes in a narrow shell in Fourier space:

$$(2\pi)^3\delta_D^{(3)}(\vec{k}_1+\vec{k}_2)\hat{P}_g \equiv \frac{1}{\hat{V}_2}\int_{q_i\in I_i} \frac{{\rm d}^3q_1}{(2\pi)^3}\frac{{\rm d}^3q_2}{(2\pi)^3}(2\pi)^3\delta_D^{(3)}(\vec{q}_1+\vec{q}_2)\delta_g(\vec{q}_1)\delta_g(\vec{q}_2) \ , \tag{I.6}$$

where the integrals over the module of q's are in a narrow window (denoted as I_i) centered around the respective k_i of width Δk , and $\hat{V}_2$ is the normalized volume (in Fourier space) over which the average is taken:

$$\hat{V}_2 = \int_{q_i\in I_i} \frac{{\rm d}^3q_1}{(2\pi)^3}\frac{{\rm d}^3q_2}{(2\pi)^3}(2\pi)^3\delta_D^{(3)}(\vec{q}_1+\vec{q}_2) \simeq \frac{1}{2\pi^2}k_1^2\Delta k \ , \tag{I.7}$$

where we used $\Delta k \ll k_1$. It can be shown that the expectation value of $\hat{P}(k)$ is $P(k)$.

We must now study the covariance of $\hat{P}$, which plays the role of $\mathcal{O}^{\rm exp}$ in Eq. (I.1). This is done by applying Wick theorem when computing the ensemble averages of products of the Gaussian fields $\delta(\vec{q}_i)$. It can be shown that the covariance for different modes $k \neq k'$ is 0, while

$$\text{Var}\left[\hat{P}_g(k)\right] = \frac{4\pi^2}{Vk^2\Delta k} P_g^2 \ . \tag{I.8}$$

The Fisher is then obtained by taking the derivatives of $\mathcal{O}_k^{\rm th} = P(k)$ with respect to the parameters, and summing over all modes. The parameters of the model for P_g at 1-loop in real space are:

$$\{\omega_b,\ A_s,\ n_s,\ \tau_{\rm reio},\ H_0,\ \tilde{\Omega}_d,\ \beta,\ (N, \alpha_0, b_1, b_2, b_K)_i\} \ , \tag{I.9}$$

where $N = 1/\bar{n}$, α the counterterm, and the parameters outside the parenthesis are common to all the $n_{\rm bin}$ redshift bin, while the ones inside the parenthesis exist in $n_{\rm bin}$ copies, one for each bin. The smallest mode of the sum $k_{\rm min}$ is taken to be equal to the smallest mode available for a given redshift bin:

$$k_{\rm min} = \frac{2\pi}{V^{1/3}} \ , \tag{I.10}$$

where V is the spatial volume of the redshift bin. The same value is used for the width of the bin Δk, and for the step-size between the different modes appearing in the sum. The largest mode $k_{\rm max}$ in the sum is taken to be the largest integer multiple of Δk such that:

$$k_{\rm max} < \frac{1}{\sqrt{\Sigma}} \ , \quad \Sigma = \frac{1}{6\pi^2} \int dk P_{m,L} \ . \tag{I.11}$$

With this procedure, the Fisher matrix can be obtained for each of the $n_{\rm bin}$ resdhift bins of a given survey. Fisher matrices of different redshift bins can be combined by considering the $n_{\rm bias}$ biases of different redshifts as distinct rows and columns of the combined Fisher matrix. In this way, the combined Fisher is a square matrix of side $N_{\rm tot}$, where

$$N_{\rm tot} = n_{\rm cosmo} + n_{\rm bin} \times n_{\rm bias} \ . \tag{I.12}$$

The entries corresponding to the common parameters (in this case the cosmological ones), are obtained by summing over all the Fisher matrices. The entries corresponding to a redshift-dependent bias are obtained by cosidering only the entries of the respective Fisher, without summing. Notice we are assuming power spectra in different bins to be completely uncorrelated.

I.2 Fisher matrix for the Power Spectrum (redshift space)

We are now ready for the Fisher of the P_g in redshift space. The RSD corrections make P_g depend non-trivially on the line of sight component of the chosen *veck*. It

is customary to project this dependence onto multipoles:

$$P_{g,\mathrm{RSD}}(k,\mu) \simeq \sum_{l=0,2,4} \mathcal{L}_l(\mu) P_l(k) \,, \tag{I.13}$$

where $\mathcal{L}$ are Legendre polynomials and P_l the multipoles. As mentioned in Chapter 4, we include the first 3 non-zero multipoles in the computations ($l = 0, 2, 4$). We can now apply what learnt in Sec. I.1. We refer to [354] for the full expression of the 1-loop power spectrum (see also [447] for a model independent approach). The difference with real case is that now there are two extra counterterms, one for each allowed μ structure [337]. Now the sum of the Fisher matrix runs also over the possible cosine of the angle with respect to the line-of-sight μ.

I.3 Fisher matrix for the Bispectrum (real space)

The arguments are very similar to the ones presented in Sec. I.1. The difference now is that the sum runs over all possible triangle configurations in Fourier space. In real space the bispectrum does not depend on the orientation of the triangle in the sky, but only on its shape, which is uniquely determined by the module of the three sides k_1, k_2, k_3 The estimator playing the role of $\mathcal{O}^{\mathrm{exp}}$ is defined as follows:

$$\begin{aligned} &(2\pi)^3 \delta_D^{(3)}(\vec{k}_1 + \vec{k}_2 + \vec{k}_3)\hat{B}_g \equiv \\ &\equiv \frac{1}{\hat{V}_3} \int_{q_i \in I_i} \frac{\mathrm{d}q_1^3}{(2\pi)^3} \frac{\mathrm{d}q_2^3}{(2\pi)^3} \frac{\mathrm{d}q_3^3}{(2\pi)^3} (2\pi)^3 \delta_D^{(3)}(\vec{q}_1 + \vec{q}_2 + \vec{q}_1) \delta_g(\vec{q}_1) \delta_g(\vec{q}_2) \delta_g(\vec{q}_3) \,, \end{aligned} \tag{I.14}$$

with the normalization factor defined as:

$$\hat{V}_3 = \int_{q_i \in I_i} \frac{\mathrm{d}^3 q_1}{(2\pi)^3} \frac{\mathrm{d}^3 q_2}{(2\pi)^3} \frac{\mathrm{d}^3 q_3}{(2\pi)^3} (2\pi)^3 \delta_D^{(3)}(\vec{q}_1 + \vec{q}_2 + \vec{q}_3) \simeq \frac{8\pi^2}{(2\pi)^6} k_1 k_2 k_3 \Delta k^3 \,. \tag{I.15}$$

Notice that also here in the thin shell limit two different triangle configurations are uncorrelated. The variance for a given configuration is:

$$\begin{aligned} &\mathrm{Var}\left[\hat{B}_g(k_1,k_2,k_3)\right] = f(k_1,k_2,k_3) \frac{\pi}{k_1 k_2 k_3} P_g(k_1) P_g(k_2) P_g(k_3) = \\ &= f(k_1,k_2,k_3) \frac{\pi}{k_1 k_2 k_3} \left(b_1^2 P_{m,L}(k_1) + \frac{1}{\bar{n}}\right) \left(b_1^2 P_{m,L}(k_2) + \frac{1}{\bar{n}}\right) \left(b_1^2 P_{m,L}(k_3) + \frac{1}{\bar{n}}\right) \end{aligned} \tag{I.16}$$

where f is a function that is equal to 2 for strictly isosceles triangles, 6 for equilateral triangles and 1 if the three sides are all different in module.

The sum runs over all possible triangle with sides that are integer multiples of Δk. Here k_{max} is taken conservatively to be $0.11\,h/\mathrm{Mpc}$, and $k_{\mathrm{min}} = \Delta k$.

We can combine the Fisher information of B_g in real space with the on for P_g 1-loop in real space. At the order in perturbation theory that we are interested, the B_g and P_g are uncorrelated: the connected 5 point function is 0 at this order.

Also, when combining B_g with P_g of the same survey, we consider all the biases in a given redshift bin to be in common between the two observables, so that their information gets summed. The only exception to this is the number density $\bar{n}_g$. Indeed in P_g the SN terms appear through the contraction of two stochastic operators ε. In B_g instead it appears through the contraction of quadratic stochasti biases, $\delta\varepsilon$ and ε^2, with the product of two linear biases, $\delta \cdot \varepsilon$ and $\varepsilon \cdot \varepsilon$ respectively. Since the various SN terms come from different operators[1], they are in principle different biases. However, for B_g we will only retain one since there is not enough constraining power to fix them both. So we take the two SN terms with same fiducial but treat them as distinct biases, without summing their information together (which is equivalent to set the fiducial of the various additional biases to 1 but let them vary independently).

[1]In [359] the constant SN in the bispectrum is the square of the SN of the power spectrum. THis difference does not change substantially our results: our approach is more conservative since we have one extra free paramete.

Appendix J

Asymmetric DM details

In this Appendix we report some details of the computations done in Chapter 5.

J.1 Golden Class models

In GC models the fermions are taken to be in the fundamental representation of $\mathrm{SU}(N)_{\mathrm{DC}}$, and to be vector-like representations under the SM. In particular, it's assumed that the SM representations must be in SU(5) fragments. In table J.1 we list the possible DCquarks out of which GC models are built.

SU(5)	$\mathrm{SU}(3)_c$	$\mathrm{SU}(2)_L$	$\mathrm{U}(1)_Y$	charge	name
1	1	1	0	0	N
$\bar{5}$	$\bar{3}$	1	1/3	1/3	D
	1	2	-1/2	0,1	L
10	$\bar{3}$	1	-2/3	-2/3	U
	1	1	1	1	E
	3	2	1/6	2/3,-1/3	Q
15	3	2	1/6	2/3, -1/3	Q
	1	3	1	0,1,2	T
	6	1	-2/3	-2/3	S
24	1	3	0	-1,0,1	V
	8	1	0	0	G
	$\bar{3}$	2	5/6	4/3,1/3	X
	1	1	0	0	N

Table J.1: *List of possible DCquarks. Tilded DCquarks have same* $\mathrm{SU}(N)_{\mathrm{DC}}$ *representation (*i.e. *the fundamental), but conjugate SM representations with respect to the untilded counterparts.*

In Table J.2 we list the various golden class models identified in the original work [42].

DCq content	Allowed $N_{\rm DC}$	DM candidates
$N_{\rm DF}=3$		
$\Psi = V$	3	VVV =3
$\Psi = N \oplus L$	3,...,14	$N^{N_{\rm DC}*}$
$N_{\rm DF}=4$		
$\Psi = V \oplus N$	3	VVV, VNN =3, VVN =1
$\Psi = N \oplus L \oplus \tilde{E}$	3,4,5	$N^{N_{\rm DC}*}$=1
$N_{\rm DF}=5$		
$\Psi = V \oplus L$	3	VVV =3
$\Psi = N \oplus L \oplus \tilde{L}$	3	$NL\tilde{L}$=1
=	4	$NNL\tilde{L}$, $L\tilde{L}L\tilde{L}$=1
$N_{\rm DF}=6$		
$\Psi = V \oplus L \oplus N$	3	VVV, VNN =3, VVN=1
$\Psi = V \oplus L \oplus \tilde{E}$	3	VVV =3
$N \oplus L \oplus \tilde{L} \oplus \tilde{E}$	3	$NL\tilde{L}$, $\tilde{L}\tilde{L}\tilde{E}$=1
=	4	$NNL\tilde{L}$, $L\tilde{L}L\tilde{L}$, $N\tilde{E}\tilde{L}\tilde{L}$=1
$N_{\rm DF}=7$		
$\Psi = L \oplus \tilde{L} \oplus E \oplus \tilde{E} \oplus N$	3	LLE, $\tilde{L}\tilde{L}\tilde{E}$, $L\tilde{L}N$, $E\tilde{E}N = 1$
$\Psi = N \oplus L \oplus \tilde{E} \oplus V$	3	VVV, $VNN = 3$, $VVN = 1$
$N_{\rm DF}=9$		
$\Psi = Q \oplus \tilde{D}$	3	$QQ\tilde{D} = 1$
$N_{\rm DF}=12$		
$\Psi = Q \oplus \tilde{D} \oplus \tilde{U}$	3	$QQ\tilde{D}$, $\tilde{D}\tilde{D}\tilde{U} = 1$

Table J.2: $\mathrm{SU}(N)_{DC}$ *golden-class models as classified in [42]. For each model we specify the allowed number of dark colors which guarantee the perturbativity of the SM gauge group up to* $M_{\rm P}$*, and the DM DCb candidate with the corresponding* $\mathrm{SU}(2)_L$ *representation. A* $*$ *denotes a higher spin representation.*

J.2 Complete asymmetry parameter

In order to compute the asymmetry Eq. (5.23), we first need to evaluate:

$$\delta \equiv |\mathcal{M}|^2 - |\overline{\mathcal{M}}|^2 = -4(\mathcal{I}_H + \mathcal{I}_L) \,, \tag{J.1}$$

where $\mathcal{I}_H$ ($\mathcal{I}_L$) collects the contributions coming from the interference of the loop diagrams in Fig. 5.3 with the tree-level one with ϕ_H (ϕ_L) in the internal line. They are given, respectively, by:

$$\begin{aligned}\mathcal{I}_H =& \frac{\mathrm{Im}[\lambda^*_{LHH}\lambda_{HLL}y^*_L y_H]}{x-1}\left(\frac{\alpha^2}{\alpha^2-1}\frac{|y_H|^2}{16\pi}\frac{1}{x-1} + 4|y_H|^2\mathcal{D}_1^{HL} + 2|y_L|^2\mathcal{D}_2^{LL}\right) + \\ &+ \frac{\mathrm{Im}[\lambda^*_{LHH}\lambda_{LLL}y^{*2}_L y^2_H]}{x-1}\left(\frac{\alpha^2}{\alpha^2-1}\frac{\alpha^2}{16\pi(\alpha^2 x-1)} + 2\mathcal{D}_1^{LL}\right) + \\ &+ \mathrm{Im}[\lambda^*_{HLL}\lambda_{LLL}y^*_L y_H]\frac{\alpha^2}{\alpha^2-1}\frac{|y_L|^2\alpha^4}{16\pi(\alpha^2 x-1)^2} - \mathrm{Im}[\lambda_{LHH}\lambda^*_{HHH}y^*_L y_H]\frac{2|y_H|^2\mathcal{D}_2^{HH}}{x-1}\end{aligned} \tag{J.2}$$

$$\begin{aligned}\mathcal{I}_L =& \frac{\mathrm{Im}[\lambda^*_{LHH}\lambda_{HLL}y^*_L y_H]}{\alpha^2 x-1}\left(\frac{1}{\alpha^2-1}\frac{|y_L|^2}{16\pi}\frac{\alpha^2}{\alpha^2 x-1} - 2|y_H|^2\mathcal{D}_1^{HH} - 4|y_L|^2\mathcal{D}_2^{HL}\right) + \\ &+ \frac{\mathrm{Im}[\lambda_{HLL}\lambda^*_{HHH}y^{*2}_L y^2_H]\alpha^2}{16\pi(\alpha^2 x-1)(x-1)}\frac{1}{\alpha^2-1} + \frac{2\,\mathrm{Im}[\lambda^*_{HLL}\lambda_{LLL}y^*_L y_H]|y_L|^2\alpha^2}{\alpha^2 x-1}\mathcal{D}_2^{LL} + \\ &+ \mathrm{Im}[\lambda_{LHH}\lambda^*_{HHH}y_H y^*_L]\frac{1}{\alpha^2-1}\frac{|y_H|^2}{16\pi(x-1)^2}\end{aligned} \tag{J.3}$$

where $x \equiv \frac{(p^\mu_{N1}+p^\mu_{N2})^2}{M_H^2}$, p_{N1} and p_{N2} being the momenta of the final fermions, and $\alpha = \frac{M_H}{M_L}$. The functions $\mathcal{D}^{ij}_{1,2} \equiv \mathcal{D}^{ij}_{1,2}\left(\frac{p_{N1}}{M_H}, \frac{p_{N1}}{M_H}, \frac{M_L}{M_H}\right)$ are the imaginary parts of the diagrams 5.3e and 5.3f, respectively, and are given by:

$$\mathcal{D}_1^{ij} = \mathrm{Im}\left[\int \frac{\mathrm{d}^4 l}{(2\pi)^4}\frac{\mathrm{Tr}\left[\not{p}_{N1}\not{p}_{N2}\not{l}(\not{p}_H - \not{l})\right]}{l^2(p_H-l)^2((p_H-l-p_{N2})^2 - M_i^2)((l-p_{N1})^2 - M_j^2)}\right] \tag{J.4}$$

$$\mathcal{D}_2^{ij} = \mathrm{Im}\left[\int \frac{\mathrm{d}^4 l}{(2\pi)^4}\frac{\mathrm{Tr}\left[\not{p}_{N1}\not{p}_{N2}(\not{l} - \not{p}_{N1})(\not{p}_H - \not{l} - \not{p}_{N2})\right]}{(l^2 - M_i^2)((p_H-l)^2 - M_j^2)(p_H-l-p_{N2})^2(l-p_{N1})^2}\right] \tag{J.5}$$

where p_H is the 4-momentum of the initial ϕ_H scalar, and i, j run over the scalar flavors. These integrals have been evaluated by means of `Package-X`, setting $m_N =$

0. Despite the different combination of couplings in the above interference terms, there are only three independent phases, as expected from Eq. (5.11). Indeed, if we define:

$$\arg[\lambda^*_{LHH}\lambda_{HLL}y^*_L y_H] \equiv \theta_1, \;\; \arg[\lambda^*_{LHH}\lambda_{LLL}y^{*2}_L y^2_H] \equiv \theta_2, \;\; \arg[\lambda_{LHH}\lambda^*_{HHH}y^*_L y_H] \equiv \theta_3 \tag{J.6}$$

then the phases in the remaining combinations of couplings are given by:

$$\arg[\lambda^*_{HLL}\lambda_{LLL}y^*_L y_H] = \theta_2 - \theta_1, \quad \arg[\lambda_{HLL}\lambda^*_{HHH}y^{*2}_L y^2_H] = \theta_1 + \theta_3 \tag{J.7}$$

In Eq. (J.2), Eq. (J.3) we have omitted the color factors to avoid cluttering. To properly account for them, each function $\mathcal{D}^{ij}_{1,2}$ (related to box diagrams) must be multiplied by $C'_{\rm DC} = -27$, while the other terms (related to bubble diagrams) by $C_{\rm DC} = 24$. Once we plug the previous expressions into Eq. (5.23) and perform the integral over phase space, we get the asymmetry generated in our benchmark model with the complete set of parameters. Instead, if we set $\lambda_{LLL} = \lambda_{HLL} = 0$ we recover Eq. (5.24).

Bibliography

[1] G. Bertone, D. Hooper, and J. Silk, *Particle dark matter: Evidence, candidates and constraints*, *Phys. Rept.* **405** (2005) 279–390, [hep-ph/0404175].

[2] G. Bertone and D. Hooper, *History of dark matter*, *Rev. Mod. Phys.* **90** (2018), no. 4 045002, [arXiv:1605.04909].

[3] **BOSS** Collaboration, S. Alam et al., *The clustering of galaxies in the completed SDSS-III Baryon Oscillation Spectroscopic Survey: cosmological analysis of the DR12 galaxy sample*, *Mon. Not. Roy. Astron. Soc.* **470** (2017), no. 3 2617–2652, [arXiv:1607.03155].

[4] A. J. Ross, L. Samushia, C. Howlett, W. J. Percival, A. Burden, and M. Manera, *The clustering of the SDSS DR7 main Galaxy sample – I. A 4 per cent distance measure at $z = 0.15$*, *Mon. Not. Roy. Astron. Soc.* **449** (2015), no. 1 835–847, [arXiv:1409.3242].

[5] M. Bartelmann, *Gravitational Lensing*, *Class. Quant. Grav.* **27** (2010) 233001, [arXiv:1010.3829].

[6] K. G. Begeman, A. H. Broeils, and R. H. Sanders, *Extended rotation curves of spiral galaxies: Dark haloes and modified dynamics*, *Mon. Not. Roy. Astron. Soc.* **249** (1991) 523.

[7] **Planck** Collaboration, Y. Akrami et al., *Planck 2018 results. IV. Diffuse component separation*, *Astron. Astrophys.* **641** (2020) A4, [arXiv:1807.06208].

[8] G. Arcadi, M. Dutra, P. Ghosh, M. Lindner, Y. Mambrini, M. Pierre, S. Profumo, and F. S. Queiroz, *The waning of the WIMP? A review of models, searches, and constraints*, *Eur. Phys. J. C* **78** (2018), no. 3 203, [arXiv:1703.07364].

[9] L. Roszkowski, E. M. Sessolo, and S. Trojanowski, *WIMP dark matter candidates and searches—current status and future prospects*, *Rept. Prog. Phys.* **81** (2018), no. 6 066201, [arXiv:1707.06277].

[10] L. J. Hall, K. Jedamzik, J. March-Russell, and S. M. West, *Freeze-In Production of FIMP Dark Matter*, *JHEP* **03** (2010) 080, [arXiv:0911.1120].

[11] N. Bernal, M. Heikinheimo, T. Tenkanen, K. Tuominen, and V. Vaskonen, *The Dawn of FIMP Dark Matter: A Review of Models and Constraints*, *Int. J. Mod. Phys. A* **32** (2017), no. 27 1730023, [arXiv:1706.07442].

[12] M. S. Turner, *Coherent Scalar Field Oscillations in an Expanding Universe*, *Phys. Rev. D* **28** (1983) 1243.

[13] D. J. E. Marsh, *Axion Cosmology*, *Phys. Rept.* **643** (2016) 1–79, [arXiv:1510.07633].

[14] J. Preskill, M. B. Wise, and F. Wilczek, *Cosmology of the Invisible Axion*, *Phys. Lett. B* **120** (1983) 127–132.

[15] M. Dine and W. Fischler, *The Not So Harmless Axion*, *Phys. Lett. B* **120** (1983) 137–141.

[16] L. Hui, J. P. Ostriker, S. Tremaine, and E. Witten, *Ultralight scalars as cosmological dark matter*, *Phys. Rev. D* **95** (2017), no. 4 043541, [arXiv:1610.08297].

[17] B. Carr and F. Kuhnel, *Primordial Black Holes as Dark Matter: Recent Developments*, *Ann. Rev. Nucl. Part. Sci.* **70** (2020) 355–394, [arXiv:2006.02838].

[18] **Supernova Search Team** Collaboration, A. G. Riess et al., *Observational evidence from supernovae for an accelerating universe and a cosmological constant*, *Astron. J.* **116** (1998) 1009–1038, [astro-ph/9805201].

[19] A. G. Riess, S. Casertano, W. Yuan, L. M. Macri, and D. Scolnic, *Large Magellanic Cloud Cepheid Standards Provide a 1% Foundation for the Determination of the Hubble Constant and Stronger Evidence for Physics beyond ΛCDM*, *Astrophys. J.* **876** (2019), no. 1 85, [arXiv:1903.07603].

[20] E. Di Valentino, O. Mena, S. Pan, L. Visinelli, W. Yang, A. Melchiorri, D. F. Mota, A. G. Riess, and J. Silk, *In the realm of the Hubble tension – a review of solutions*, *Class. Quant. Grav.* **38** (2021), no. 15 153001, [arXiv:2103.01183].

[21] N. Schöneberg, G. Franco Abellán, A. Pérez Sánchez, S. J. Witte, V. Poulin, and J. Lesgourgues, *The H_0 Olympics: A fair ranking of proposed models*, *Phys. Rept.* **984** (2022) 1–55, [arXiv:2107.10291].

[22] A. H. Guth, *The Inflationary Universe: A Possible Solution to the Horizon and Flatness Problems*, *Phys. Rev. D* **23** (1981) 347–356.

[23] **Planck** Collaboration, N. Aghanim et al., *Planck 2018 results. VI. Cosmological parameters*, *Astron. Astrophys.* **641** (2020) A6, [arXiv:1807.06209]. [Erratum: Astron.Astrophys. 652, C4 (2021)].

[24] J. S. Bullock and M. Boylan-Kolchin, *Small-Scale Challenges to the ΛCDM Paradigm*, *Ann. Rev. Astron. Astrophys.* **55** (2017) 343–387, [arXiv:1707.04256].

[25] D. H. Weinberg, J. S. Bullock, F. Governato, R. Kuzio de Naray, and A. H. G. Peter, *Cold dark matter: controversies on small scales*, *Proc. Nat. Acad. Sci.* **112** (2015) 12249–12255, [arXiv:1306.0913].

[26] L. Perivolaropoulos and F. Skara, *Challenges for ΛCDM: An update*, *New Astron. Rev.* **95** (2022) 101659, [arXiv:2105.05208].

[27] W. J. G. de Blok, *The core-cusp problem*, *Advances in Astronomy* **2010** (2010) 1–14.

[28] A. A. Klypin, A. V. Kravtsov, O. Valenzuela, and F. Prada, *Where are the missing Galactic satellites?*, *Astrophys. J.* **522** (1999) 82–92, [astro-ph/9901240].

[29] M. Boylan-Kolchin, J. S. Bullock, and M. Kaplinghat, *The Milky Way's bright satellites as an apparent failure of ΛCDM*, *Mon. Not. Roy. Astron. Soc.* **422** (2012) 1203–1218, [arXiv:1111.2048].

[30] M. Boylan-Kolchin, J. S. Bullock, and M. Kaplinghat, *Too big to fail? The puzzling darkness of massive Milky Way subhaloes*, *Mon. Not. Roy. Astron. Soc.* **415** (2011) L40, [arXiv:1103.0007].

[31] S. McGaugh, F. Lelli, P. Li, and J. Schombert, *Dynamical Regularities in Galaxies*, in *IAU Symposium 353: Galactic Dynamics in the Era of Large Surveys*, 9, 2019. arXiv:1909.02011.

[32] S. S. McGaugh, J. M. Schombert, G. D. Bothun, and W. J. G. de Blok, *The baryonic tully-fisher relation*, *The Astrophysical Journal* **533** (mar, 2000) L99.

[33] S. S. McGaugh, F. Lelli, and J. M. Schombert, *Radial acceleration relation in rotationally supported galaxies*, *Phys. Rev. Lett.* **117** (Nov, 2016) 201101.

[34] M. Milgrom, *A Modification of the Newtonian dynamics as a possible alternative to the hidden mass hypothesis*, *Astrophys. J.* **270** (1983) 365–370.

[35] M. Milgrom, *A Modification of the Newtonian dynamics: Implications for galaxies*, *Astrophys. J.* **270** (1983) 371–383.

[36] B. Famaey and S. McGaugh, *Modified Newtonian Dynamics (MOND): Observational Phenomenology and Relativistic Extensions*, *Living Rev. Rel.* **15** (2012) 10, [arXiv:1112.3960].

[37] A. Pontzen and F. Governato, *How supernova feedback turns dark matter cusps into cores*, *Mon. Not. Roy. Astron. Soc.* **421** (2012) 3464, [arXiv:1106.0499].

[38] S. Tulin, H.-B. Yu, and K. M. Zurek, *Beyond Collisionless Dark Matter: Particle Physics Dynamics for Dark Matter Halo Structure*, *Phys. Rev. D* **87** (2013), no. 11 115007, [arXiv:1302.3898].

[39] S. Tulin and H.-B. Yu, *Dark Matter Self-interactions and Small Scale Structure*, *Phys. Rept.* **730** (2018) 1–57, [arXiv:1705.02358].

[40] P. Schwaller, *Gravitational Waves from a Dark Phase Transition*, *Phys. Rev. Lett.* **115** (2015), no. 18 181101, [arXiv:1504.07263].

[41] M. Reece, *TASI Lectures: (No) Global Symmetries to Axion Physics*, arXiv:2304.08512.

[42] O. Antipin, M. Redi, A. Strumia, and E. Vigiani, *Accidental Composite Dark Matter*, *JHEP* **07** (2015) 039, [arXiv:1503.08749].

[43] M. Cirelli, N. Fornengo, and A. Strumia, *Minimal dark matter*, *Nucl. Phys. B* **753** (2006) 178–194, [hep-ph/0512090].

[44] S. Bottaro, M. Costa, and O. Popov, *Asymmetric accidental composite dark matter*, *JHEP* **11** (2021) 055, [arXiv:2104.14244].

[45] K. M. Zurek, *Asymmetric Dark Matter: Theories, Signatures, and Constraints*, *Phys. Rept.* **537** (2014) 91–121, [arXiv:1308.0338].

[46] K. Petraki and R. R. Volkas, *Review of asymmetric dark matter*, *Int. J. Mod. Phys. A* **28** (2013) 1330028, [arXiv:1305.4939].

[47] S. Bottaro, D. Buttazzo, M. Costa, R. Franceschini, P. Panci, D. Redigolo, and L. Vittorio, *Closing the window on WIMP Dark Matter*, *Eur. Phys. J. C* **82** (2022), no. 1 31, [arXiv:2107.09688].

[48] S. Bottaro, D. Buttazzo, M. Costa, R. Franceschini, P. Panci, D. Redigolo, and L. Vittorio, *The last complex WIMPs standing*, *Eur. Phys. J. C* **82** (2022), no. 11 992, [arXiv:2205.04486].

[49] J. Hisano, S. Matsumoto, M. Nagai, O. Saito, and M. Senami, *Non-perturbative effect on thermal relic abundance of dark matter*, *Phys. Lett. B* **646** (2007) 34–38, [hep-ph/0610249].

[50] M. Cirelli, A. Strumia, and M. Tamburini, *Cosmology and Astrophysics of Minimal Dark Matter*, *Nucl. Phys. B* **787** (2007) 152–175, [arXiv:0706.4071].

[51] A. Mitridate, M. Redi, J. Smirnov, and A. Strumia, *Cosmological Implications of Dark Matter Bound States*, *JCAP* **05** (2017) 006, [arXiv:1702.01141].

[52] M. Cirelli and A. Strumia, *Minimal Dark Matter: Model and results*, *New J. Phys.* **11** (2009) 105005, [arXiv:0903.3381].

[53] C. Accettura et al., *Towards a Muon Collider*, arXiv:2303.08533.

[54] **DARWIN** Collaboration, J. Aalbers et al., *DARWIN: towards the ultimate dark matter detector*, *JCAP* **11** (2016) 017, [arXiv:1606.07001].

[55] V. Lefranc, E. Moulin, P. Panci, F. Sala, and J. Silk, *Dark Matter in γ lines: Galactic Center vs dwarf galaxies*, *JCAP* **09** (2016) 043, [arXiv:1608.00786].

[56] M. E. Peskin and T. Takeuchi, *Estimation of oblique electroweak corrections*, *Phys. Rev. D* **46** (1992) 381–409.

[57] R. Barbieri, A. Pomarol, R. Rattazzi, and A. Strumia, *Electroweak symmetry breaking after LEP-1 and LEP-2*, *Nucl. Phys. B* **703** (2004) 127–146, [hep-ph/0405040].

[58] R. Alarcon et al., *Electric dipole moments and the search for new physics*, in *2022 Snowmass Summer Study*, 3, 2022. arXiv:2203.08103.

[59] V. De Luca, A. Mitridate, M. Redi, J. Smirnov, and A. Strumia, *Colored Dark Matter*, *Phys. Rev. D* **97** (2018), no. 11 115024, [arXiv:1801.01135].

[60] C. Gross, A. Mitridate, M. Redi, J. Smirnov, and A. Strumia, *Cosmological Abundance of Colored Relics*, *Phys. Rev. D* **99** (2019), no. 1 016024, [arXiv:1811.08418].

[61] M. Fabbrichesi, E. Gabrielli, and G. Lanfranchi, *The Dark Photon*, arXiv:2005.01515.

[62] A. Caputo, A. J. Millar, C. A. J. O'Hare, and E. Vitagliano, *Dark photon limits: A handbook*, *Phys. Rev. D* **104** (2021), no. 9 095029, [arXiv:2105.04565].

[63] B. Holdom, *Two U(1)'s and Epsilon Charge Shifts*, *Phys. Lett. B* **166** (1986) 196–198.

[64] B. Patt and F. Wilczek, *Higgs-field portal into hidden sectors*, hep-ph/0605188.

[65] G. Arcadi, A. Djouadi, and M. Raidal, *Dark Matter through the Higgs portal*, *Phys. Rept.* **842** (2020) 1–180, [arXiv:1903.03616].

[66] J. March-Russell, S. M. West, D. Cumberbatch, and D. Hooper, *Heavy Dark Matter Through the Higgs Portal*, *JHEP* **07** (2008) 058, [arXiv:0801.3440].

[67] S. Dodelson and L. M. Widrow, *Sterile-neutrinos as dark matter*, *Phys. Rev. Lett.* **72** (1994) 17–20, [hep-ph/9303287].

[68] T. Asaka and M. Shaposhnikov, *The νMSM, dark matter and baryon asymmetry of the universe*, *Phys. Lett. B* **620** (2005) 17–26, [hep-ph/0505013].

[69] A. Atre, T. Han, S. Pascoli, and B. Zhang, *The Search for Heavy Majorana Neutrinos*, *JHEP* **05** (2009) 030, [arXiv:0901.3589].

[70] B. Batell, R. Essig, and Z. Surujon, *Strong Constraints on Sub-GeV Dark Sectors from SLAC Beam Dump E137*, *Phys. Rev. Lett.* **113** (2014), no. 17 171802, [arXiv:1406.2698].

[71] G. Krnjaic, *Probing Light Thermal Dark-Matter With a Higgs Portal Mediator*, *Phys. Rev. D* **94** (2016), no. 7 073009, [arXiv:1512.04119].

[72] M. J. Strassler and K. M. Zurek, *Echoes of a hidden valley at hadron colliders*, *Phys. Lett. B* **651** (2007) 374–379, [hep-ph/0604261].

[73] J. E. Juknevich, D. Melnikov, and M. J. Strassler, *A Pure-Glue Hidden Valley I. States and Decays*, *JHEP* **07** (2009) 055, [arXiv:0903.0883].

[74] J. E. Juknevich, *Pure-glue hidden valleys through the Higgs portal*, *JHEP* **08** (2010) 121, [arXiv:0911.5616].

[75] H.-C. Cheng, L. Li, and E. Salvioni, *A Theory of Dark Pions*, arXiv:2110.10691.

[76] R. Contino, K. Max, and R. K. Mishra, *Searching for elusive dark sectors with terrestrial and celestial observations*, *JHEP* **06** (2021) 127, [arXiv:2012.08537].

[77] M. Costa, R. K. Mishra, and S. Verma, *Model Agnostic Probes of Dark Sectors at Neutrino Experiments*, arXiv:2211.13253.

[78] **DUNE** Collaboration, J. Strait et al., *Long-Baseline Neutrino Facility (LBNF) and Deep Underground Neutrino Experiment (DUNE): Conceptual Design Report, Volume 3: Long-Baseline Neutrino Facility for DUNE June 24, 2015*, arXiv:1601.05823.

[79] M. Redi and A. Tesi, *General freeze-in and freeze-out*, *JHEP* **12** (2021) 060, [arXiv:2107.14801].

[80] S. Hong, G. Kurup, and M. Perelstein, *Conformal Freeze-In of Dark Matter*, *Phys. Rev. D* **101** (2020), no. 9 095037, [arXiv:1910.10160].

[81] D. Clowe, M. Bradac, A. H. Gonzalez, M. Markevitch, S. W. Randall, C. Jones, and D. Zaritsky, *A direct empirical proof of the existence of dark matter*, *Astrophys. J. Lett.* **648** (2006) L109–L113, [astro-ph/0608407].

[82] S. W. Randall, M. Markevitch, D. Clowe, A. H. Gonzalez, and M. Bradac, *Constraints on the Self-Interaction Cross-Section of Dark Matter from Numerical Simulations of the Merging Galaxy Cluster 1E 0657-56*, *Astrophys. J.* **679** (2008) 1173–1180, [arXiv:0704.0261].

[83] M. Archidiacono, E. Castorina, D. Redigolo, and E. Salvioni, *Unveiling dark fifth forces with linear cosmology*, *JCAP* **10** (2022) 074, [arXiv:2204.08484].

[84] **Euclid** Collaboration, A. Blanchard et al., *Euclid preparation: VII. Forecast validation for Euclid cosmological probes*, *Astron. Astrophys.* **642** (2020) A191, [arXiv:1910.09273].

[85] V. Desjacques, D. Jeong, and F. Schmidt, *Large-Scale Galaxy Bias*, *Phys. Rept.* **733** (2018) 1–193, [arXiv:1611.09787].

[86] M. Mirbabayi, F. Schmidt, and M. Zaldarriaga, *Biased Tracers and Time Evolution*, *JCAP* **07** (2015) 030, [arXiv:1412.5169].

[87] L. Senatore, *Bias in the effective field theory of large scale structures*, *Journal of Cosmology and Astroparticle Physics* **2015** (nov, 2015) 007–007.

[88] D. Baumann, A. Nicolis, L. Senatore, and M. Zaldarriaga, *Cosmological Non-Linearities as an Effective Fluid*, *JCAP* **07** (2012) 051, [arXiv:1004.2488].

[89] J. J. M. Carrasco, M. P. Hertzberg, and L. Senatore, *The Effective Field Theory of Cosmological Large Scale Structures*, *JHEP* **09** (2012) 082, [arXiv:1206.2926].

[90] N. Kaiser, *Clustering in real space and in redshift space*, *Mon. Not. Roy. Astron. Soc.* **227** (1987) 1–27.

[91] C. Alcock and B. Paczynski, *An evolution free test for non-zero cosmological constant*, *Nature* **281** (1979) 358–359.

[92] S. Schlamminger, K. Y. Choi, T. A. Wagner, J. H. Gundlach, and E. G. Adelberger, *Test of the equivalence principle using a rotating torsion balance*, *Phys. Rev. Lett.* **100** (2008) 041101, [arXiv:0712.0607].

[93] P. Touboul et al., *MICROSCOPE Mission: First Results of a Space Test of the Equivalence Principle*, *Phys. Rev. Lett.* **119** (2017), no. 23 231101, [arXiv:1712.01176].

[94] P. Creminelli, J. Gleyzes, L. Hui, M. Simonović, and F. Vernizzi, *Single-Field Consistency Relations of Large Scale Structure. Part III: Test of the Equivalence Principle*, *JCAP* **06** (2014) 009, [arXiv:1312.6074].

[95] T. Hambye, F. S. Ling, L. Lopez Honorez, and J. Rocher, *Scalar Multiplet Dark Matter*, *JHEP* **07** (2009) 090, [arXiv:0903.4010]. [Erratum: JHEP 05, 066 (2010)].

[96] E. Del Nobile, M. Nardecchia, and P. Panci, *Millicharge or Decay: A Critical Take on Minimal Dark Matter*, *JCAP* **04** (2016) 048, [arXiv:1512.05353].

[97] K. Griest and M. Kamionkowski, *Unitarity Limits on the Mass and Radius of Dark Matter Particles*, *Phys. Rev. Lett.* **64** (1990) 615.

[98] J. Hisano, S. Matsumoto, and M. M. Nojiri, *Explosive dark matter annihilation*, *Phys. Rev. Lett.* **92** (2004) 031303, [hep-ph/0307216].

[99] N. Arkani-Hamed, D. P. Finkbeiner, T. R. Slatyer, and N. Weiner, *A Theory of Dark Matter*, *Phys. Rev. D* **79** (2009) 015014, [arXiv:0810.0713].

[100] S. Cassel, *Sommerfeld factor for arbitrary partial wave processes*, *J. Phys. G* **37** (2010) 105009, [arXiv:0903.5307].

[101] B. von Harling and K. Petraki, *Bound-state formation for thermal relic dark matter and unitarity*, *JCAP* **12** (2014) 033, [arXiv:1407.7874].

[102] M. Cirelli, P. Panci, K. Petraki, F. Sala, and M. Taoso, *Dark Matter's secret liaisons: phenomenology of a dark U(1) sector with bound states*, *JCAP* **05** (2017) 036, [arXiv:1612.07295].

[103] J. Smirnov and J. F. Beacom, *TeV-Scale Thermal WIMPs: Unitarity and its Consequences*, *Phys. Rev. D* **100** (2019), no. 4 043029, [arXiv:1904.11503].

[104] J. P. Delahaye, M. Diemoz, K. Long, B. Mansoulié, N. Pastrone, L. Rivkin, D. Schulte, A. Skrinsky, and A. Wulzer, *Muon Colliders*, arXiv:1901.06150.

[105] **ALEGRO** Collaboration, E. Adli et al., *Towards an Advanced Linear International Collider*, arXiv:1901.10370.

[106] C. Aime et al., *Muon Collider Physics Summary*, arXiv:2203.07256.

[107] **Muon Collider** Collaboration, J. de Blas et al., *The physics case of a 3 TeV muon collider stage*, arXiv:2203.07261.

[108] M. Schumann, L. Baudis, L. Bütikofer, A. Kish, and M. Selvi, *Dark matter sensitivity of multi-ton liquid xenon detectors*, *JCAP* **10** (2015) 016, [arXiv:1506.08309].

[109] **CTA** Collaboration, A. Acharyya et al., *Sensitivity of the Cherenkov Telescope Array to a dark matter signal from the Galactic centre*, *JCAP* **01** (2021) 057, [arXiv:2007.16129].

[110] H. Silverwood, C. Weniger, P. Scott, and G. Bertone, *A realistic assessment of the CTA sensitivity to dark matter annihilation*, *JCAP* **03** (2015) 055, [arXiv:1408.4131].

[111] V. Lefranc, E. Moulin, P. Panci, and J. Silk, *Prospects for Annihilating Dark Matter in the inner Galactic halo by the Cherenkov Telescope Array*, *Phys. Rev. D* **91** (2015), no. 12 122003, [arXiv:1502.05064].

[112] T. Han, Z. Liu, L.-T. Wang, and X. Wang, *WIMPs at High Energy Muon Colliders*, arXiv:2009.11287.

[113] T. Cohen, K. Murase, N. L. Rodd, B. R. Safdi, and Y. Soreq, *γ -ray Constraints on Decaying Dark Matter and Implications for IceCube*, *Phys. Rev. Lett.* **119** (2017), no. 2 021102, [arXiv:1612.05638].

[114] **PandaX** Collaboration, Y. Meng et al., *Dark Matter Search Results from the PandaX-4T Commissioning Run*, arXiv:2107.13438.

[115] H.-C. Cheng, B. A. Dobrescu, and K. T. Matchev, *Generic and chiral extensions of the supersymmetric standard model*, *Nucl. Phys. B* **543** (1999) 47–72, [hep-ph/9811316].

[116] J. L. Feng, T. Moroi, L. Randall, M. Strassler, and S.-f. Su, *Discovering supersymmetry at the Tevatron in wino LSP scenarios*, *Phys. Rev. Lett.* **83** (1999) 1731–1734, [hep-ph/9904250].

[117] T. Gherghetta, G. F. Giudice, and J. D. Wells, *Phenomenological consequences of supersymmetry with anomaly induced masses*, *Nucl. Phys. B* **559** (1999) 27–47, [hep-ph/9904378].

[118] M. Ibe, S. Matsumoto, and R. Sato, *Mass Splitting between Charged and Neutral Winos at Two-Loop Level*, *Phys. Lett. B* **721** (2013) 252–260, [arXiv:1212.5989].

[119] J. McKay and P. Scott, *Two-loop mass splittings in electroweak multiplets: winos and minimal dark matter*, *Phys. Rev. D* **97** (2018), no. 5 055049, [arXiv:1712.00968].

[120] M. Low and L.-T. Wang, *Neutralino dark matter at 14 TeV and 100 TeV*, *JHEP* **08** (2014) 161, [arXiv:1404.0682].

[121] M. Cirelli, F. Sala, and M. Taoso, *Wino-like Minimal Dark Matter and future colliders*, *JHEP* **10** (2014) 033, [arXiv:1407.7058]. [Erratum: JHEP 01, 041 (2015)].

[122] R. Capdevilla, F. Meloni, R. Simoniello, and J. Zurita, *Hunting wino and higgsino dark matter at the muon collider with disappearing tracks*, arXiv:2102.11292.

[123] L. Di Luzio, R. Gröber, J. F. Kamenik, and M. Nardecchia, *Accidental matter at the LHC*, *JHEP* **07** (2015) 074, [arXiv:1504.00359].

[124] S. Bottaro and D. Redigolo, *The dark matter unitarity bound at NLO*, arXiv:2305.01680.

[125] J. Bramante, P. J. Fox, G. D. Kribs, and A. Martin, *Inelastic frontier: Discovering dark matter at high recoil energy*, *Phys. Rev. D* **94** (2016), no. 11 115026, [arXiv:1608.02662].

[126] N. Song, S. Nagorny, and A. C. Vincent, *Pushing the frontier of WIMPy inelastic dark matter: Journey to the end of the periodic table*, *Phys. Rev. D* **104** (2021), no. 10 103032, [arXiv:2104.09517].

[127] B. J. Mount et al., *LUX-ZEPLIN (LZ) Technical Design Report*, arXiv:1703.09144.

[128] **XENON** Collaboration, E. Aprile et al., *Projected WIMP sensitivity of the XENONnT dark matter experiment*, *JCAP* **11** (2020) 031, [arXiv:2007.08796].

[129] J. Aalbers et al., *A Next-Generation Liquid Xenon Observatory for Dark Matter and Neutrino Physics*, arXiv:2203.02309.

[130] H. Al Ali et al., *The Muon Smasher's Guide*, arXiv:2103.14043.

[131] C. A. J. O'Hare, *New Definition of the Neutrino Floor for Direct Dark Matter Searches*, *Phys. Rev. Lett.* **127** (2021), no. 25 251802, [arXiv:2109.03116].

[132] M. W. Goodman and E. Witten, *Detectability of Certain Dark Matter Candidates*, *Phys. Rev. D* **31** (1985) 3059.

[133] **XENON** Collaboration, E. Aprile et al., *Dark Matter Search Results from a One Ton-Year Exposure of XENON1T*, *Phys. Rev. Lett.* **121** (2018), no. 11 111302, [arXiv:1805.12562].

[134] **PICO** Collaboration, C. Amole et al., *Dark matter search results from the PICO-60 CF_3I bubble chamber*, *Phys. Rev. D* **93** (2016), no. 5 052014, [arXiv:1510.07754].

[135] **CRESST** Collaboration, G. Angloher et al., *Results on light dark matter particles with a low-threshold CRESST-II detector*, *Eur. Phys. J. C* **76** (2016), no. 1 25, [arXiv:1509.01515].

[136] A. Münster et al., *Radiopurity of CaWO4 crystals for direct dark matter search with CRESST and EURECA*, *JCAP* **05** (2014) 018, [arXiv:1403.5114].

[137] J. W. Beeman et al., *New experimental limits on the alpha decays of lead isotopes*, *Eur. Phys. J. A* **49** (2013) 50, [arXiv:1212.2422].

[138] B. Lehnert, H. Ramani, M. Hult, G. Lutter, M. Pospelov, S. Rajendran, and K. Zuber, *Search for Dark Matter Induced Deexcitation of* $^{180}Ta^{m}$, *Phys. Rev. Lett.* **124** (2020), no. 18 181802, [arXiv:1911.07865].

[139] B. Broerman, M. Laubenstein, S. Nagorny, N. Song, and A. C. Vincent, *A search for rare and induced nuclear decays in hafnium*, *Nucl. Phys. A* **1012** (2021) 122212, [arXiv:2012.08339].

[140] P. Belli et al., *Search for α decay of naturally occurring osmium nuclides accompanied by γ quanta*, *Phys. Rev. C* **102** (2020), no. 2 024605, [arXiv:2009.01508].

[141] H. E. Haber and D. Wyler, *RADIATIVE NEUTRALINO DECAY*, *Nucl. Phys. B* **323** (1989) 267–310.

[142] J. Harz and K. Petraki, *Radiative bound-state formation in unbroken perturbative non-Abelian theories and implications for dark matter*, *JHEP* **07** (2018) 096, [arXiv:1805.01200].

[143] B. Ostdiek, *Constraining the minimal dark matter fiveplet with LHC searches*, **92** (Sept., 2015) 055008, [arXiv:1506.03445].

[144] M. Low and L.-T. Wang, *Neutralino dark matter at 100 tev*, arXiv:1404.0682v.

[145] European Strategy for Particle Physics Preparatory Group, *Physics Briefing Book*, arXiv:1910.11775. Physics Briefing Book - Input for the European Strategy for Particle Physics Update 2020.

[146] K. Harigaya, K. Ichikawa, A. Kundu, S. Matsumoto, and S. Shirai, *Indirect probe of electroweak-interacting particles at future lepton colliders*, *Journal of High Energy Physics* **9** (Sept., 2015) 105, [arXiv:1504.03402].

[147] L. Di Luzio, R. Gröber, and G. Panico, *Probing new electroweak states via precision measurements at the LHC and future colliders*, *JHEP* **01** (2019) 011, [arXiv:1810.10993].

[148] M. Boscolo, J.-P. Delahaye, and M. Palmer, *The future prospects of muon colliders and neutrino factories*, *Rev. Accel. Sci. Tech.* **10** (2019), no. 01 189–214, [arXiv:1808.01858].

[149] R. B. Palmer, *Muon colliders*, *Reviews of Accelerator Science and Technology* **07** (Jan, 2014) 137–159.

[150] International Muon Collider Design Study.

[151] N. Vignaroli, *Charged resonances and MDM bound states at a multi-TeV muon collider*, arXiv:2304.12362.

[152] S. Bottaro, A. Strumia, and N. Vignaroli, *Minimal Dark Matter bound states at future colliders*, *JHEP* **06** (2021) 143, [arXiv:2103.12766].

[153] P. J. Fox, R. Harnik, J. Kopp, and Y. Tsai, *LEP Shines Light on Dark Matter*, *Phys. Rev. D* **84** (2011) 014028, [arXiv:1103.0240].

[154] C. Bartels, M. Berggren, and J. List, *Characterising WIMPs at a future e^+e^- Linear Collider*, *Eur. Phys. J. C* **72** (2012) 2213, [arXiv:1206.6639].

[155] R. Franceschini and X. Zhao, *Going all the way in the search for WIMP dark matter at the muon collider through precision measurements*, arXiv:2212.11900.

[156] J. Alwall, M. Herquet, F. Maltoni, O. Mattelaer, and T. Stelzer, *MadGraph 5 : Going Beyond*, *JHEP* **06** (2011) 128, [arXiv:1106.0522].

[157] J. Alwall, R. Frederix, S. Frixione, V. Hirschi, F. Maltoni, O. Mattelaer, H. S. Shao, T. Stelzer, P. Torrielli, and M. Zaro, *The automated computation of tree-level and next-to-leading order differential cross sections, and their matching to parton shower simulations*, *JHEP* **07** (2014) 079, [arXiv:1405.0301].

[158] U. Schnoor, *Long-lived particle reconstruction at clic*, *Linear Collider Workshop 2019*.

[159] Erica Brondolin, *Disappearing tracks at CLIC*, *LLP workshop 2020*.

[160] **ATLAS** Collaboration, M. Aaboud et al., *Search for heavy charged long-lived particles in the ATLAS detector in 36.1 fb^{-1} of proton-proton collision data at $\sqrt{s} = 13$ TeV*, *Phys. Rev. D* **99** (2019), no. 9 092007, [arXiv:1902.01636].

[161] J. Billard, L. Strigari, and E. Figueroa-Feliciano, *Implication of neutrino backgrounds on the reach of next generation dark matter direct detection experiments*, *Phys. Rev. D* **89** (2014), no. 2 023524, [arXiv:1307.5458].

[162] J. Hisano, S. Matsumoto, M. M. Nojiri, and O. Saito, *Direct detection of the Wino and Higgsino-like neutralino dark matters at one-loop level*, *Phys. Rev. D* **71** (2005) 015007, [hep-ph/0407168].

[163] J. Hisano, K. Ishiwata, and N. Nagata, *A complete calculation for direct detection of Wino dark matter*, *Phys. Lett. B* **690** (2010) 311–315, [arXiv:1004.4090].

[164] M. Cirelli, E. Del Nobile, and P. Panci, *Tools for model-independent bounds in direct dark matter searches*, *JCAP* **10** (2013) 019, [arXiv:1307.5955].

[165] J. Hisano, K. Ishiwata, N. Nagata, and T. Takesako, *Direct Detection of Electroweak-Interacting Dark Matter*, *JHEP* **07** (2011) 005, [arXiv:1104.0228].

[166] J. Hisano, K. Ishiwata, and N. Nagata, *QCD Effects on Direct Detection of Wino Dark Matter*, *JHEP* **06** (2015) 097, [arXiv:1504.00915].

[167] **Flavour Lattice Averaging Group** Collaboration, S. Aoki et al., *FLAG Review 2019: Flavour Lattice Averaging Group (FLAG)*, *Eur. Phys. J. C* **80** (2020), no. 2 113, [arXiv:1902.08191].

[168] C. Alexandrou, V. Drach, K. Jansen, C. Kallidonis, and G. Koutsou, *Baryon spectrum with $N_f = 2 + 1 + 1$ twisted mass fermions*, *Phys. Rev. D* **90** (2014), no. 7 074501, [arXiv:1406.4310].

[169] **MILC** Collaboration, W. Freeman and D. Toussaint, *Intrinsic strangeness and charm of the nucleon using improved staggered fermions*, *Phys. Rev. D* **88** (2013) 054503, [arXiv:1204.3866].

[170] T. Katayose, S. Matsumoto, S. Shirai, and Y. Watanabe, *Thermal Real Scalar Triplet Dark Matter*, arXiv:2105.07650.

[171] M. Cirelli, T. Hambye, P. Panci, F. Sala, and M. Taoso, *Gamma ray tests of Minimal Dark Matter*, *JCAP* **10** (2015) 026, [arXiv:1507.05519].

[172] C. Garcia-Cely, A. Ibarra, A. S. Lamperstorfer, and M. H. G. Tytgat, *Gamma-rays from Heavy Minimal Dark Matter*, *JCAP* **10** (2015) 058, [arXiv:1507.05536].

[173] M. Cirelli, G. Corcella, A. Hektor, G. Hutsi, M. Kadastik, P. Panci, M. Raidal, F. Sala, and A. Strumia, *PPPC 4 DM ID: A Poor Particle Physicist Cookbook for Dark Matter Indirect Detection*, *JCAP* **03** (2011) 051, [arXiv:1012.4515]. [Erratum: JCAP 10, E01 (2012)].

[174] L. Rinchiuso, N. L. Rodd, I. Moult, E. Moulin, M. Baumgart, T. Cohen, T. R. Slatyer, I. W. Stewart, and V. Vaidya, *Hunting for Heavy Winos in the Galactic Center*, *Phys. Rev. D* **98** (2018), no. 12 123014, [arXiv:1808.04388].

[175] F. Iocco, M. Pato, and G. Bertone, *Evidence for dark matter in the inner Milky Way*, *Nature Phys.* **11** (2015) 245–248, [arXiv:1502.03821].

[176] C. Wegg, O. Gerhard, and M. Portail, *MOA-II Galactic microlensing constraints: the inner Milky Way has a low dark matter fraction and a near maximal disc*, *mnras* **463** (Nov., 2016) 557–570, [arXiv:1607.06462].

[177] M. Pato, F. Iocco, and G. Bertone, *Dynamical constraints on the dark matter distribution in the Milky Way*, *JCAP* **12** (2015) 001, [arXiv:1504.06324].

[178] Y. Huang, X. W. Liu, H. B. Yuan, M. S. Xiang, H. W. Zhang, B. Q. Chen, J. J. Ren, C. Wang, Y. Zhang, Y. H. Hou, Y. F. Wang, and Z. H. Cao, *The Milky Way's rotation curve out to 100 kpc and its constraint on the Galactic mass distribution*, *mnras* **463** (Dec., 2016) 2623–2639, [arXiv:1604.01216].

[179] V. Lefranc, G. A. Mamon, and P. Panci, *Prospects for annihilating Dark Matter towards Milky Way's dwarf galaxies by the Cherenkov Telescope Array*, *JCAP* **09** (2016) 021, [arXiv:1605.02793].

[180] P. Ullio and M. Valli, *A critical reassessment of particle Dark Matter limits from dwarf satellites*, *JCAP* **07** (2016) 025, [arXiv:1603.07721].

[181] K. Hayashi, K. Ichikawa, S. Matsumoto, M. Ibe, M. N. Ishigaki, and H. Sugai, *Dark matter annihilation and decay from non-spherical dark halos in galactic dwarf satellites*, *Mon. Not. Roy. Astron. Soc.* **461** (2016), no. 3 2914–2928, [arXiv:1603.08046].

[182] M. Baumgart, T. Cohen, I. Moult, N. L. Rodd, T. R. Slatyer, M. P. Solon, I. W. Stewart, and V. Vaidya, *Resummed Photon Spectra for WIMP Annihilation*, *JHEP* **03** (2018) 117, [arXiv:1712.07656].

[183] A. Hryczuk and R. Iengo, *The one-loop and Sommerfeld electroweak corrections to the Wino dark matter annihilation*, *JHEP* **01** (2012) 163, [arXiv:1111.2916]. [Erratum: JHEP 06, 137 (2012)].

[184] G. Ovanesyan, T. R. Slatyer, and I. W. Stewart, *Heavy Dark Matter Annihilation from Effective Field Theory*, *Phys. Rev. Lett.* **114** (2015), no. 21 211302, [arXiv:1409.8294].

[185] M. Baumgart, I. Z. Rothstein, and V. Vaidya, *Constraints on Galactic Wino Densities from Gamma Ray Lines*, *JHEP* **04** (2015) 106, [arXiv:1412.8698].

[186] M. Baumgart and V. Vaidya, *Semi-inclusive wino and higgsino annihilation to LL'*, *JHEP* **03** (2016) 213, [arXiv:1510.02470].

[187] G. Ovanesyan, N. L. Rodd, T. R. Slatyer, and I. W. Stewart, *One-loop correction to heavy dark matter annihilation*, *Phys. Rev. D* **95** (2017), no. 5 055001, [arXiv:1612.04814]. [Erratum: Phys.Rev.D 100, 119901 (2019)].

[188] **HESS** Collaboration, H. Abdalla et al., *Searches for gamma-ray lines and 'pure WIMP' spectra from Dark Matter annihilations in dwarf galaxies with H.E.S.S*, *JCAP* **11** (2018) 037, [arXiv:1810.00995].

[189] R. Mahbubani, M. Redi, and A. Tesi, *Indirect detection of composite asymmetric dark matter*, *Phys. Rev. D* **101** (2020), no. 10 103037, [arXiv:1908.00538].

[190] M. Farina, G. Panico, D. Pappadopulo, J. T. Ruderman, R. Torre, and A. Wulzer, *Energy helps accuracy: electroweak precision tests at hadron colliders*, *Phys. Lett. B* **772** (2017) 210–215, [arXiv:1609.08157].

[191] **CMS** Collaboration, A. Tumasyan et al., *Search for new physics in the lepton plus missing transverse momentum final state in proton-proton collisions at* $\sqrt{s}$ *= 13 TeV*, arXiv:2202.06075.

[192] A. Strumia, *Interpreting electroweak precision data including the W-mass CDF anomaly*, arXiv:2204.04191.

[193] S. Chen, A. Glioti, R. Rattazzi, L. Ricci, and A. Wulzer, *Learning from Radiation at a Very High Energy Lepton Collider*, arXiv:2202.10509.

[194] L. Lavoura and L.-F. Li, *Making the small oblique parameters large*, *Phys. Rev. D* **49** (1994) 1409–1416, [hep-ph/9309262].

[195] J. Fan, M. Reece, and L.-T. Wang, *Possible Futures of Electroweak Precision: ILC, FCC-ee, and CEPC*, *JHEP* **09** (2015) 196, [arXiv:1411.1054].

[196] D. Buttazzo, R. Franceschini, and A. Wulzer, *Two Paths Towards Precision at a Very High Energy Lepton Collider*, *JHEP* **05** (2021) 219, [arXiv:2012.11555].

[197] **CDF** Collaboration, T. Aaltonen et al., *High-precision measurement of the W boson mass with the CDF II detector*, *Science* **376** (2022), no. 6589 170–176.

[198] G. Panico, A. Pomarol, and M. Riembau, *EFT approach to the electron Electric Dipole Moment at the two-loop level*, *JHEP* **04** (2019) 090, [arXiv:1810.09413].

[199] C. Cesarotti, Q. Lu, Y. Nakai, A. Parikh, and M. Reece, *Interpreting the Electron EDM Constraint*, *JHEP* **05** (2019) 059, [arXiv:1810.07736].

[200] **ACME** Collaboration, V. Andreev et al., *Improved limit on the electric dipole moment of the electron*, *Nature* **562** (2018), no. 7727 355–360.

[201] Y. Cui, L. Randall, and B. Shuve, *A WIMPy Baryogenesis Miracle*, *JHEP* **04** (2012) 075, [arXiv:1112.2704].

[202] Y. Cui, *A Review of WIMP Baryogenesis Mechanisms*, *Mod. Phys. Lett. A* **30** (2015), no. 37 1530028, [arXiv:1510.04298].

[203] Jindariani, Sergo et al., *Promising Technologies and R&D Directions for the Future Muon Collider Detectors*, arXiv:2203.07224.

[204] R. Krall and M. Reece, *Last Electroweak WIMP Standing: Pseudo-Dirac Higgsino Status and Compact Stars as Future Probes*, *Chin. Phys. C* **42** (2018), no. 4 043105, [arXiv:1705.04843].

[205] Y. Kahn, G. Krnjaic, N. Tran, and A. Whitbeck, *M^3: a new muon missing momentum experiment to probe $(g-2)$ and dark matter at Fermilab*, *JHEP* **09** (2018) 153, [arXiv:1804.03144].

[206] H. Sieber, D. Banerjee, P. Crivelli, E. Depero, S. N. Gninenko, D. V. Kirpichnikov, M. M. Kirsanov, V. Poliakov, and L. Molina Bueno, *Prospects in the search for a new light Z' boson with the NA64μ experiment at the CERN SPS*, *Phys. Rev. D* **105** (2022), no. 5 052006, [arXiv:2110.15111].

[207] C. Cesarotti, S. Homiller, R. K. Mishra, and M. Reece, *Probing New Gauge Forces with a High-Energy Muon Beam Dump*, arXiv:2202.12302.

[208] B. Batell, N. Blinov, C. Hearty, and R. McGehee, *Exploring Dark Sector Portals with High Intensity Experiments*, in *2022 Snowmass Summer Study*, 7, 2022. arXiv:2207.06905.

[209] B. Batell et al., *Dark Sector Studies with Neutrino Beams*, in *2022 Snowmass Summer Study*, 7, 2022. arXiv:2207.06898.

[210] G. Krnjaic et al., *A Snowmass Whitepaper: Dark Matter Production at Intensity-Frontier Experiments*, arXiv:2207.00597.

[211] J. Berger et al., *Snowmass 2021 White Paper: Cosmogenic Dark Matter and Exotic Particle Searches in Neutrino Experiments*, in *2022 Snowmass Summer Study*, 7, 2022. arXiv:2207.02882.

[212] S. Gori et al., *Dark Sector Physics at High-Intensity Experiments*, arXiv:2209.04671.

[213] P. Coloma, L. W. Koerner, I. M. Shoemaker, and J. Yu, *Neutrino Frontier Topical Group Report (NF03): Physics Beyond the Standard Model*, arXiv:2209.10362.

[214] **MicroBooNE, LAr1-ND, ICARUS-WA104** Collaboration, M. Antonello et al., *A Proposal for a Three Detector Short-Baseline Neutrino Oscillation Program in the Fermilab Booster Neutrino Beam*, arXiv:1503.01520.

[215] **MicroBooNE** Collaboration, R. Acciarri et al., *Design and Construction of the MicroBooNE Detector*, *JINST* **12** (2017), no. 02 P02017, [arXiv:1612.05824].

[216] P. A. Machado, O. Palamara, and D. W. Schmitz, *The Short-Baseline Neutrino Program at Fermilab*, *Ann. Rev. Nucl. Part. Sci.* **69** (2019) 363–387, [arXiv:1903.04608].

[217] J. M. Berryman, A. de Gouvea, P. J. Fox, B. J. Kayser, K. J. Kelly, and J. L. Raaf, *Searches for Decays of New Particles in the DUNE Multi-Purpose Near Detector*, *JHEP* **02** (2020) 174, [arXiv:1912.07622].

[218] G. Chauhan, P. S. B. Dev, and X.-J. Xu, *Probing the ν_R-philic Z' at DUNE near detectors*, arXiv:2204.11876.

[219] B. Batell, J. Berger, and A. Ismail, *Probing the Higgs Portal at the Fermilab Short-Baseline Neutrino Experiments*, *Phys. Rev. D* **100** (2019), no. 11 115039, [arXiv:1909.11670].

[220] P. Ballett, M. Hostert, S. Pascoli, Y. F. Perez-Gonzalez, Z. Tabrizi, and R. Zukanovich Funchal, *Neutrino Trident Scattering at Near Detectors*, *JHEP* **01** (2019) 119, [arXiv:1807.10973].

[221] D. Curtin et al., *Long-Lived Particles at the Energy Frontier: The MATHUSLA Physics Case*, *Rept. Prog. Phys.* **82** (2019), no. 11 116201, [arXiv:1806.07396].

[222] J. Beacham et al., *Physics Beyond Colliders at CERN: Beyond the Standard Model Working Group Report*, *J. Phys. G* **47** (2020), no. 1 010501, [arXiv:1901.09966].

[223] **SHADOWS** Collaboration, M. Alviggi, S. Bachmann, W. Baldini, A. Balla, M. Biglietti, V. Büscher, A. Calcaterra, V. Cafaro, N. Charitonidis, A. Ceccucci, V. Cicero, P. Ciambrone, H. Danielsson, M. Dellapietra, A. DeRoeck, F. Duval, G. Felici, T. Ferber, L. Foggetta, M. Gatta, A. Gerbershagen, V. Giordano, S. Hansmann-Menzemer, P. Iengo, M. Iodice, K. Jakobs, M. Klute, K. Köneke, M. Koval, G. Lanfranchi, A. Laudrain, I. Lax, B. Leverington, P. Lichard, K. Massri, A. Montanari, R. Murphy, T. Napolitano, F. Neuhaus, L. Nevay, A. Paoloni, G. Papalino, U. Parzefall, S. Ritter, T. Rovelli, A. Saputi, B. Schmidt, M. Schott, H. Schultz-Coulon, G. Sekhniaidze, F. Stummer, G. Torromeo, N. Tosi, U. Uwer, M. vanDijk, A. Vannozzi, R. Wanke, C. Weiser, P. Wertelaers, and T. Zickler, *SHADOWS Letter of Intent*, tech. rep., CERN, Geneva, 2022.

[224] R. Essig et al., *Working Group Report: New Light Weakly Coupled Particles*, in *Community Summer Study 2013: Snowmass on the Mississippi*, 10, 2013. arXiv:1311.0029.

[225] J. Alexander et al., *Dark Sectors 2016 Workshop: Community Report*, 8, 2016. arXiv:1608.08632.

[226] B. Döbrich, J. Jaeckel, F. Kahlhoefer, A. Ringwald, and K. Schmidt-Hoberg, *ALPtraum: ALP production in proton beam dump experiments*, *JHEP* **02** (2016) 018, [arXiv:1512.03069].

[227] B. Döbrich, J. Jaeckel, and T. Spadaro, *Light in the beam dump - ALP production from decay photons in proton beam-dumps*, *JHEP* **05** (2019) 213, [arXiv:1904.02091]. [Erratum: JHEP 10, 046 (2020)].

[228] W. Altmannshofer, S. Gori, and D. J. Robinson, *Constraining axionlike particles from rare pion decays*, *Phys. Rev. D* **101** (2020), no. 7 075002, [arXiv:1909.00005].

[229] K. Asai, S. Iwamoto, Y. Sakaki, and D. Ueda, *New physics searches at the ILC positron and electron beam dumps*, *JHEP* **09** (2021) 183, [arXiv:2105.13768].

[230] E. Bertuzzo, A. L. Foguel, G. M. Salla, and R. Z. Funchal, *New limits on leptophilic ALPs and Majorons from ArgoNeuT*, arXiv:2202.12317.

[231] L. Harland-Lang, J. Jaeckel, and M. Spannowsky, *A fresh look at ALP searches in fixed target experiments*, *Phys. Lett. B* **793** (2019) 281–289, [arXiv:1902.04878].

[232] P. deNiverville, H.-S. Lee, and M.-S. Seo, *Implications of the dark axion portal for the muon g−2 , B factories, fixed target neutrino experiments, and beam dumps*, *Phys. Rev. D* **98** (2018), no. 11 115011, [arXiv:1806.00757].

[233] R. T. Co, S. Kumar, and Z. Liu, *Enhancing Searches for Heavy QCD Axions via Dimuon Final States*, arXiv:2210.02462.

[234] C. Arina, J. Hajer, and P. Klose, *Portal Effective Theories: A framework for the model independent description of light hidden sector interactions*, arXiv:2105.06477.

[235] L. Darmé, S. A. R. Ellis, and T. You, *Light Dark Sectors through the Fermion Portal*, *JHEP* **07** (2020) 053, [arXiv:2001.01490].

[236] E. Bertuzzo and M. Taoso, *Probing light dark scalars with future experiments*, *JHEP* **03** (2021) 272, [arXiv:2011.04735].

[237] A. Berlin, P. deNiverville, A. Ritz, P. Schuster, and N. Toro, *Sub-GeV dark matter production at fixed-target experiments*, *Phys. Rev. D* **102** (2020), no. 9 095011, [arXiv:2003.03379].

[238] A. Carmona, C. Scherb, and P. Schwaller, *Charming ALPs*, *JHEP* **08** (2021) 121, [arXiv:2101.07803].

[239] D. Barducci, E. Bertuzzo, M. Taoso, and C. Toni, *Probing right-handed neutrinos dipole operators*, arXiv:2209.13469.

[240] E. Bernreuther, K. Böse, T. Ferber, C. Hearty, F. Kahlhoefer, A. Morandini, and K. Schmidt-Hoberg, *Forecasting dark showers at Belle II*, arXiv:2203.08824.

[241] P. Schwaller, D. Stolarski, and A. Weiler, *Emerging Jets*, *JHEP* **05** (2015) 059, [arXiv:1502.05409].

[242] D. E. Kaplan, M. A. Luty, and K. M. Zurek, *Asymmetric Dark Matter*, *Phys. Rev. D* **79** (2009) 115016, [arXiv:0901.4117].

[243] R. Foot, H. Lew, and R. R. Volkas, *A Model with fundamental improper space-time symmetries*, *Phys. Lett. B* **272** (1991) 67–70.

[244] R. Foot, *Mirror dark matter: Cosmology, galaxy structure and direct detection*, *Int. J. Mod. Phys. A* **29** (2014) 1430013, [arXiv:1401.3965].

[245] Z. Chacko, H.-S. Goh, and R. Harnik, *The Twin Higgs: Natural electroweak breaking from mirror symmetry*, *Phys. Rev. Lett.* **96** (2006) 231802, [hep-ph/0506256].

[246] B. Batell, J. Berger, L. Darmé, and C. Frugiuele, *Inelastic dark matter at the Fermilab Short Baseline Neutrino Program*, *Phys. Rev. D* **104** (2021), no. 7 075026, [arXiv:2106.04584].

[247] P. deNiverville and C. Frugiuele, *Hunting sub-GeV dark matter with the NOνA near detector*, *Phys. Rev. D* **99** (2019), no. 5 051701, [arXiv:1807.06501].

[248] L. Buonocore, C. Frugiuele, and P. deNiverville, *Hunt for sub-GeV dark matter at neutrino facilities: A survey of past and present experiments*, *Phys. Rev. D* **102** (2020), no. 3 035006, [arXiv:1912.09346].

[249] P. deNiverville, M. Pospelov, and A. Ritz, *Observing a light dark matter beam with neutrino experiments*, *Phys. Rev. D* **84** (2011) 075020, [arXiv:1107.4580].

[250] B. Batell, P. deNiverville, D. McKeen, M. Pospelov, and A. Ritz, *Leptophobic dark matter at neutrino factories*, *Physical Review D* **90** (dec, 2014).

[251] B. Batell, M. Pospelov, and A. Ritz, *Exploring Portals to a Hidden Sector Through Fixed Targets*, *Phys. Rev. D* **80** (2009) 095024, [arXiv:0906.5614].

[252] P. deNiverville, C.-Y. Chen, M. Pospelov, and A. Ritz, *Light dark matter in neutrino beams: production modelling and scattering signatures at MiniBooNE, T2K and SHiP*, *Phys. Rev. D* **95** (2017), no. 3 035006, [arXiv:1609.01770].

[253] P. deNiverville, D. McKeen, and A. Ritz, *Signatures of sub-GeV dark matter beams at neutrino experiments*, *Phys. Rev. D* **86** (2012) 035022, [arXiv:1205.3499].

[254] D. Tucker-Smith and N. Weiner, *Inelastic dark matter*, *Phys. Rev. D* **64** (2001) 043502, [hep-ph/0101138].

[255] M. W. Winkler, *Decay and detection of a light scalar boson mixing with the Higgs boson*, *Phys. Rev. D* **99** (2019), no. 1 015018, [arXiv:1809.01876].

[256] P. Ilten, Y. Soreq, M. Williams, and W. Xue, *Serendipity in dark photon searches*, *JHEP* **06** (2018) 004, [arXiv:1801.04847].

[257] C. Baruch, P. Ilten, Y. Soreq, and M. Williams, *Axial vectors in DarkCast*, arXiv:2206.08563.

[258] B. R. Webber, *Average Multiplicities in Jets*, *Phys. Lett. B* **143** (1984) 501–504.

[259] C. Cesarotti, M. Reece, and M. J. Strassler, *Spheres To Jets: Tuning Event Shapes with 5d Simplified Models*, *JHEP* **05** (2021) 096, [arXiv:2009.08981].

[260] N. Blinov, E. Kowalczyk, and M. Wynne, *Axion-like particle searches at DarkQuest*, *JHEP* **02** (2022) 036, [arXiv:2112.09814].

[261] A. J. Buras, *Weak Hamiltonian, CP violation and rare decays*, in *Les Houches Summer School in Theoretical Physics, Session 68: Probing the Standard Model of Particle Interactions*, pp. 281–539, 6, 1998. hep-ph/9806471.

[262] T. Inami and C. S. Lim, *Effects of Superheavy Quarks and Leptons in Low-Energy Weak Processes k(L) —> mu anti-mu, K+ —> pi+ Neutrino anti-neutrino and K0 <—> anti-K0*, *Prog. Theor. Phys.* **65** (1981) 297. [Erratum: Prog.Theor.Phys. 65, 1772 (1981)].

[263] **SHiP** Collaboration, C. Ahdida et al., *Sensitivity of the SHiP experiment to Heavy Neutral Leptons*, *JHEP* **04** (2019) 077, [arXiv:1811.00930].

[264] J. L. Feng, I. Galon, F. Kling, and S. Trojanowski, *Dark Higgs bosons at the ForwArd Search ExpeRiment*, *Phys. Rev. D* **97** (2018), no. 5 055034, [arXiv:1710.09387].

[265] D. Gorbunov, I. Krasnov, Y. Kudenko, and S. Suvorov, *Heavy Neutral Leptons from kaon decays in the SHiP experiment*, *Phys. Lett. B* **810** (2020) 135817, [arXiv:2004.07974].

[266] I. Boiarska, K. Bondarenko, A. Boyarsky, V. Gorkavenko, M. Ovchynnikov, and A. Sokolenko, *Phenomenology of GeV-scale scalar portal*, *JHEP* **11** (2019) 162, [arXiv:1904.10447].

[267] W. Altmannshofer, J. A. Dror, and S. Gori, *New Insights Into Axion-Lepton Interactions*, arXiv:2209.00665.

[268] V. Barger, C.-W. Chiang, W.-Y. Keung, and D. Marfatia, *Constraint on parity-violating muonic forces*, *Phys. Rev. Lett.* **108** (2012) 081802, [arXiv:1109.6652].

[269] M. Hostert, K. Kaneta, and M. Pospelov, *Pair production of dark particles in meson decays*, *Phys. Rev. D* **102** (2020), no. 5 055016, [arXiv:2005.07102].

[270] **NA61/SHINE** Collaboration, A. Aduszkiewicz et al., *Measurement of ϕ meson production in $p+p$ interactions at 40, 80 and 158 GeV/c with the NA61/SHINE spectrometer at the CERN SPS*, *Eur. Phys. J. C* **80** (2020), no. 3 199, [arXiv:1908.04601].

[271] K. Kovarik et al., *nCTEQ15 - Global analysis of nuclear parton distributions with uncertainties in the CTEQ framework*, *Phys. Rev. D* **93** (2016), no. 8 085037, [arXiv:1509.00792].

[272] D. B. Clark, E. Godat, and F. I. Olness, *ManeParse : A Mathematica reader for Parton Distribution Functions*, *Comput. Phys. Commun.* **216** (2017) 126–137, [arXiv:1605.08012].

[273] S. Foroughi-Abari and A. Ritz, *Dark Sector Production via Proton Bremsstrahlung*, arXiv:2108.05900.

[274] M. Shifman, A. Vainshtein, and V. Zakharov, *Remarks on higgs-boson interactions with nucleons*, *Physics Letters B* **78** (1978), no. 4 443–446.

[275] T. Feuster and U. Mosel, *Photon- and meson-induced reactions on the nucleon*, *Physical Review C* **59** (Jan, 1999) 460491.

[276] A. S. Carroll et al., *Absorption Cross-Sections of $\pi^{\pm}$, $K^{\pm}$, p and $\bar{p}$ on Nuclei Between 60 GeV/c and 280 GeV/c*, *Phys. Lett. B* **80** (1979) 319–322.

[277] **SHiP** Collaboration, M. Anelli et al., *A facility to Search for Hidden Particles (SHiP) at the CERN SPS*, arXiv:1504.04956.

[278] **CHARM** Collaboration, F. Bergsma et al., *Search for Axion Like Particle Production in 400-GeV Proton - Copper Interactions*, *Phys. Lett. B* **157** (1985) 458–462.

[279] G. Marocco and S. Sarkar, *Blast from the past: Constraints on the dark sector from the BEBC WA66 beam dump experiment*, *SciPost Phys.* **10** (2021), no. 2 043, [arXiv:2011.08153].

[280] R. Barouki, G. Marocco, and S. Sarkar, *Blast from the past II: Constraints on heavy neutral leptons from the BEBC WA66 beam dump experiment*, arXiv:2208.00416.

[281] **MicroBooNE** Collaboration, P. Abratenko et al., *Search for a Higgs Portal Scalar Decaying to Electron-Positron Pairs in the MicroBooNE Detector*, *Phys. Rev. Lett.* **127** (2021), no. 15 151803, [arXiv:2106.00568].

[282] **MiniBooNE DM** Collaboration, A. A. Aguilar-Arevalo et al., *Dark Matter Search in Nucleon, Pion, and Electron Channels from a Proton Beam Dump with MiniBooNE*, *Phys. Rev. D* **98** (2018), no. 11 112004, [arXiv:1807.06137].

[283] **NOvA** Collaboration, P. P. Filip, *Hunting for Light Dark Matter with the NOvA Detector*, in *International Conference on Neutrinos and Dark Matter*, 2020.

[284] J. Bian, *Measurement of Neutrino-Electron Elastic Scattering at NOvA Near Detector*, in *Meeting of the APS Division of Particles and Fields*, 10, 2017. arXiv:1710.03428.

[285] **FASER** Collaboration, A. Ariga et al., *FASER's physics reach for long-lived particles*, *Phys. Rev. D* **99** (2019), no. 9 095011, [arXiv:1811.12522].

[286] **FASER** Collaboration, H. Abreu et al., *Detecting and Studying High-Energy Collider Neutrinos with FASER at the LHC*, *Eur. Phys. J. C* **80** (2020), no. 1 61, [arXiv:1908.02310].

[287] **FASER** Collaboration, H. Abreu et al., *First Direct Observation of Collider Neutrinos with FASER at the LHC*, arXiv:2303.14185.

[288] **SND@LHC** Collaboration, G. Acampora et al., *SND@LHC: The Scattering and Neutrino Detector at the LHC*, arXiv:2210.02784.

[289] L. A. Anchordoqui et al., *The Forward Physics Facility: Sites, experiments, and physics potential*, *Phys. Rept.* **968** (2022) 1–50, [arXiv:2109.10905].

[290] J. L. Feng, I. Galon, F. Kling, and S. Trojanowski, *ForwArd Search ExpeRiment at the LHC*, *Phys. Rev. D* **97** (2018), no. 3 035001, [arXiv:1708.09389].

[291] F. Kling and S. Trojanowski, *Heavy Neutral Leptons at FASER*, *Phys. Rev. D* **97** (2018), no. 9 095016, [arXiv:1801.08947].

[292] A. Berlin and F. Kling, *Inelastic Dark Matter at the LHC Lifetime Frontier: ATLAS, CMS, LHCb, CODEX-b, FASER, and MATHUSLA*, *Phys. Rev. D* **99** (2019), no. 1 015021, [arXiv:1810.01879].

[293] J. L. Feng, I. Galon, F. Kling, and S. Trojanowski, *Axionlike particles at FASER: The LHC as a photon beam dump*, *Phys. Rev. D* **98** (2018), no. 5 055021, [arXiv:1806.02348].

[294] A. Boyarsky, O. Mikulenko, M. Ovchynnikov, and L. Shchutska, *Searches for new physics at SND@LHC*, *JHEP* **03** (2022) 006, [arXiv:2104.09688].

[295] T. Kuwahara and S.-R. Yuan, *Dark Vector Mesons at LHC Forward Detector Searches*, arXiv:2303.03736.

[296] B. Batell, J. L. Feng, M. Fieg, A. Ismail, F. Kling, R. M. Abraham, and S. Trojanowski, *Hadrophilic dark sectors at the Forward Physics Facility*, *Phys. Rev. D* **105** (2022), no. 7 075001, [arXiv:2111.10343].

[297] B. Batell, J. L. Feng, and S. Trojanowski, *Detecting Dark Matter with Far-Forward Emulsion and Liquid Argon Detectors at the LHC*, *Phys. Rev. D* **103** (2021), no. 7 075023, [arXiv:2101.10338].

[298] **CHARM** Collaboration, J. Dorenbosch et al., *A search for decays of heavy neutrinos in the mass range 0.52.8 gev*, *Physics Letters B* **166** (1986), no. 4 473–478.

[299] S. N. Gninenko, *Constraints on sub-GeV hidden sector gauge bosons from a search for heavy neutrino decays*, *Phys. Lett. B* **713** (2012) 244–248, [arXiv:1204.3583].

[300] **DUNE** Collaboration, B. Abi et al., *Deep Underground Neutrino Experiment (DUNE), Far Detector Technical Design Report, Volume II: DUNE Physics*, arXiv:2002.03005.

[301] V. Brdar, B. Dutta, W. Jang, D. Kim, I. M. Shoemaker, Z. Tabrizi, A. Thompson, and J. Yu, *Axionlike Particles at Future Neutrino Experiments: Closing the Cosmological Triangle*, *Phys. Rev. Lett.* **126** (2021), no. 20 201801, [arXiv:2011.07054].

[302] K. J. Kelly, S. Kumar, and Z. Liu, *Heavy axion opportunities at the DUNE near detector*, *Phys. Rev. D* **103** (2021), no. 9 095002, [arXiv:2011.05995].

[303] R. Essig, R. Harnik, J. Kaplan, and N. Toro, *Discovering new light states at neutrino experiments*, *Physical Review D* **82** (dec, 2010).

[304] S. Foroughi-Abari and A. Ritz, *LSND constraints on the higgs portal*, *Physical Review D* **102** (aug, 2020).

[305] **LSND** Collaboration, C. Athanassopoulos et al., *Evidence for muon-neutrino —> electron-neutrino oscillations from pion decay in flight neutrinos*, *Phys. Rev. C* **58** (1998) 2489–2511, [nucl-ex/9706006].

[306] **LSND** Collaboration, A. Aguilar-Arevalo et al., *Evidence for neutrino oscillations from the observation of $\bar{\nu}_e$ appearance in a $\bar{\nu}_\mu$ beam*, *Phys. Rev. D* **64** (2001) 112007, [hep-ex/0104049].

[307] **NOvA** Collaboration, M. A. Acero et al., *Measurement of the ν_e-Nucleus Charged-Current Double-Differential Cross Section at $\langle E_\nu \rangle = 2.4$ GeV using NOvA*, arXiv:2206.10585.

[308] A. Bhattarai, V. Brdar, B. Dutta, W. Jang, D. Kim, I. M. Shoemaker, Z. Tabrizi, A. Thompson, and J. Yu, *BSM Targets at a Target-less DUNE*, arXiv:2206.06380.

[309] W. Altmannshofer, S. Gori, J. Martín-Albo, A. Sousa, and M. Wallbank, *Neutrino Tridents at DUNE*, *Phys. Rev. D* **100** (2019), no. 11 115029, [arXiv:1902.06765].

[310] Y. Gershtein, S. Knapen, and D. Redigolo, *Probing naturally light singlets with a displaced vertex trigger*, *Phys. Lett. B* **823** (2021) 136758, [arXiv:2012.07864].

[311] **ATLAS** Collaboration, M. Aaboud et al., *Search for dark matter and other new phenomena in events with an energetic jet and large missing transverse momentum using the ATLAS detector*, *JHEP* **01** (2018) 126, [arXiv:1711.03301].

[312] **ATLAS** Collaboration, M. Aaboud et al., *Search for long-lived particles produced in pp collisions at $\sqrt{s} = 13$ TeV that decay into displaced hadronic jets in the ATLAS muon spectrometer*, *Phys. Rev. D* **99** (2019), no. 5 052005, [arXiv:1811.07370].

[313] **ATLAS** Collaboration, G. Aad et al., *Search for long-lived neutral particles produced in pp collisions at $\sqrt{s} = 13$ TeV decaying into displaced hadronic jets in the ATLAS inner detector and muon spectrometer*, *Phys. Rev. D* **101** (2020), no. 5 052013, [arXiv:1911.12575].

[314] **ALEPH, DELPHI, L3, OPAL, SLD, LEP Electroweak Working Group, SLD Electroweak Group, SLD Heavy Flavour Group** Collaboration, S. Schael et al., *Precision electroweak measurements on the Z resonance*, *Phys. Rept.* **427** (2006) 257–454, [hep-ex/0509008].

[315] J. Blumlein et al., *Limits on neutral light scalar and pseudoscalar particles in a proton beam dump experiment*, *Z. Phys. C* **51** (1991) 341–350.

[316] J. Blumlein et al., *Limits on the mass of light (pseudo)scalar particles from Bethe-Heitler e+ e- and mu+ mu- pair production in a proton - iron beam dump experiment*, *Int. J. Mod. Phys. A* **7** (1992) 3835–3850.

[317] J. Blumlein and J. Brunner, *New Exclusion Limits for Dark Gauge Forces from Beam-Dump Data*, *Phys. Lett. B* **701** (2011) 155–159, [arXiv:1104.2747].

[318] J. Blümlein and J. Brunner, *New Exclusion Limits on Dark Gauge Forces from Proton Bremsstrahlung in Beam-Dump Data*, *Phys. Lett. B* **731** (2014) 320–326, [arXiv:1311.3870].

[319] G. Bernardi, G. Carugno, J. Chauveau, F. Dicarlo, M. Dris, J. Dumarchez, M. Ferro-Luzzi, J.-M. Levy, D. Lukas, J.-M. Perreau, Y. Pons, A.-M. Touchard, and F. Vannucci, *Search for neutrino decay*, *Physics Letters B* **166** (1986), no. 4 479–483.

[320] G. Bernardi, G. Carugno, J. Chauveau, F. Dicarlo, M. Dris, J. Dumarchez, M. Ferro-Luzzi, J.-M. Levy, D. Lukas, J.-M. Perreau, Y. Pons, A.-M. Touchard, and F. Vannucci, *Further limits on heavy neutrino couplings*, *Physics Letters B* **203** (1988), no. 3 332–334.

[321] S. N. Gninenko, *Stringent limits on the $\pi^0 \to \gamma X, X \to e + e-$ decay from neutrino experiments and constraints on new light gauge bosons*, *Phys. Rev. D* **85** (2012) 055027, [arXiv:1112.5438].

[322] D. Gorbunov, I. Krasnov, and S. Suvorov, *Constraints on light scalars from PS191 results*, *Phys. Lett. B* **820** (2021) 136524, [arXiv:2105.11102].

[323] C. N. Yang, *Selection rules for the dematerialization of a particle into two photons*, *Phys. Rev.* **77** (Jan, 1950) 242–245.

[324] L. D. Landau, *On the angular momentum of a system of two photons*, *Dokl. Akad. Nauk SSSR* **60** (1948), no. 2 207–209.

[325] **BaBar** Collaboration, J. P. Lees et al., *Search for $B \to K^{(*)}\nu\overline{\nu}$ and invisible quarkonium decays*, *Phys. Rev. D* **87** (2013), no. 11 112005, [arXiv:1303.7465].

[326] **Belle-II** Collaboration, F. Abudinén et al., *Search for $B+\to K+\nu\nu^{-}$ Decays Using an Inclusive Tagging Method at Belle II*, *Phys. Rev. Lett.* **127** (2021), no. 18 181802, [arXiv:2104.12624].

[327] **NA62** Collaboration, E. Cortina Gil et al., *Measurement of the very rare $K^+ \to \pi^+ \nu\overline{\nu}$ decay*, *JHEP* **06** (2021) 093, [arXiv:2103.15389].

[328] **BES** Collaboration, M. Ablikim et al., *Search for the invisible decay of J / psi in psi(2S) — pi+ pi- J / psi*, *Phys. Rev. Lett.* **100** (2008) 192001, [arXiv:0710.0039].

[329] F. Kling and S. Trojanowski, *Forward experiment sensitivity estimator for the LHC and future hadron colliders*, *Phys. Rev. D* **104** (2021), no. 3 035012, [arXiv:2105.07077].

[330] P. Ballett, T. Boschi, and S. Pascoli, *Heavy Neutral Leptons from low-scale seesaws at the DUNE Near Detector*, *JHEP* **03** (2020) 111, [arXiv:1905.00284].

[331] A. Caputo, H.-T. Janka, G. Raffelt, and E. Vitagliano, *Low-Energy Supernovae Severely Constrain Radiative Particle Decays*, *Phys. Rev. Lett.* **128** (2022), no. 22 221103, [arXiv:2201.09890].

[332] J. L. Feng et al., *The Forward Physics Facility at the High-Luminosity LHC*, arXiv:2203.05090.

[333] **Planck** Collaboration, N. Aghanim et al., *Planck 2018 results. VIII. Gravitational lensing*, *Astron. Astrophys.* **641** (2020) A8, [arXiv:1807.06210].

[334] M. M. Ivanov, *Effective Field Theory for Large Scale Structure*, arXiv:2212.08488.

[335] J. J. M. Carrasco, S. Foreman, D. Green, and L. Senatore, *The 2-loop matter power spectrum and the IR-safe integrand*, *JCAP* **07** (2014) 056, [arXiv:1304.4946].

[336] L. Senatore, *Bias in the Effective Field Theory of Large Scale Structures*, *JCAP* **11** (2015) 007, [arXiv:1406.7843].

[337] L. Senatore and M. Zaldarriaga, *Redshift Space Distortions in the Effective Field Theory of Large Scale Structures*, arXiv:1409.1225.

[338] A. Perko, L. Senatore, E. Jennings, and R. H. Wechsler, *Biased Tracers in Redshift Space in the EFT of Large-Scale Structure*, arXiv:1610.09321.

[339] M. Lewandowski, L. Senatore, F. Prada, C. Zhao, and C.-H. Chuang, *EFT of large scale structures in redshift space*, *Phys. Rev. D* **97** (2018), no. 6 063526, [arXiv:1512.06831].

[340] E. Pajer and M. Zaldarriaga, *On the Renormalization of the Effective Field Theory of Large Scale Structures*, *JCAP* **08** (2013) 037, [arXiv:1301.7182].

[341] L. Senatore and M. Zaldarriaga, *The IR-resummed Effective Field Theory of Large Scale Structures*, *JCAP* **02** (2015) 013, [arXiv:1404.5954].

[342] S. Bottaro, E. Castorina, M. Costa, D. Redigolo, and E. Salvioni, *Unveiling dark fifth forces with Large Scale Structures*, to appear.

[343] J. Lesgourgues, *The Cosmic Linear Anisotropy Solving System (CLASS) I: Overview*, arXiv:1104.2932.

[344] D. Blas, J. Lesgourgues, and T. Tram, *The Cosmic Linear Anisotropy Solving System (CLASS) II: Approximation schemes*, *JCAP* **07** (2011) 034, [arXiv:1104.2933].

[345] **Planck** Collaboration, N. Aghanim et al., *Planck 2018 results. V. CMB power spectra and likelihoods*, *Astron. Astrophys.* **641** (2020) A5, [arXiv:1907.12875].

[346] E. A. Kazin et al., *The WiggleZ Dark Energy Survey: improved distance measurements to $z = 1$ with reconstruction of the baryonic acoustic feature*, *Mon. Not. Roy. Astron. Soc.* **441** (2014), no. 4 3524–3542, [arXiv:1401.0358].

[347] F. Beutler, C. Blake, M. Colless, D. H. Jones, L. Staveley-Smith, L. Campbell, Q. Parker, W. Saunders, and F. Watson, *The 6dF Galaxy Survey: Baryon Acoustic Oscillations and the Local Hubble Constant*, *Mon. Not. Roy. Astron. Soc.* **416** (2011) 3017–3032, [arXiv:1106.3366].

[348] B. Audren, J. Lesgourgues, K. Benabed, and S. Prunet, *Conservative Constraints on Early Cosmology: an illustration of the Monte Python cosmological parameter inference code*, *JCAP* **1302** (2013) 001, [arXiv:1210.7183].

[349] T. Brinckmann and J. Lesgourgues, *MontePython 3: boosted MCMC sampler and other features*, *Phys. Dark Univ.* **24** (2019) 100260, [arXiv:1804.07261].

[350] F. Schmidt, *Effect of relative velocity and density perturbations between baryons and dark matter on the clustering of galaxies*, *Phys. Rev. D* **94** (2016), no. 6 063508, [arXiv:1602.09059].

[351] S.-F. Chen, E. Castorina, and M. White, *Biased Tracers of Two Fluids in the Lagrangian Picture*, *JCAP* **06** (2019) 006, [arXiv:1903.00437].

[352] V. Assassi, D. Baumann, D. Green, and M. Zaldarriaga, *Renormalized Halo Bias*, *JCAP* **08** (2014) 056, [arXiv:1402.5916].

[353] G. D'Amico, L. Senatore, and P. Zhang, *Limits on wCDM from the EFTofLSS with the PyBird code*, arXiv:2003.07956.

[354] N. Sailer, E. Castorina, S. Ferraro, and M. White, *Cosmology at high redshift — a probe of fundamental physics*, *JCAP* **12** (2021), no. 12 049, [arXiv:2106.09713].

[355] L. Amendola et al., *Cosmology and fundamental physics with the Euclid satellite*, *Living Rev. Rel.* **21** (2018), no. 1 2, [arXiv:1606.00180].

[356] **PUMA** Collaboration, A. Slosar et al., *Packed Ultra-wideband Mapping Array (PUMA): A Radio Telescope for Cosmology and Transients*, *Bull. Am. Astron. Soc.* **51** (2019) 53, [arXiv:1907.12559].

[357] D. J. Schlegel et al., *Astro2020 APC White Paper: The MegaMapper: a $z >$ 2 Spectroscopic Instrument for the Study of Inflation and Dark Energy*, *Bull. Am. Astron. Soc.* **51** (2019), no. 7 229, [arXiv:1907.11171].

[358] A. Oddo, E. Sefusatti, C. Porciani, P. Monaco, and A. G. Sánchez, *Toward a robust inference method for the galaxy bispectrum: likelihood function and model selection*, *JCAP* **03** (2020) 056, [arXiv:1908.01774].

[359] R. Angulo, M. Fasiello, L. Senatore, and Z. Vlah, *On the Statistics of Biased Tracers in the Effective Field Theory of Large Scale Structures*, *JCAP* **09** (2015) 029, [arXiv:1503.08826].

[360] G. D. Kribs and E. T. Neil, *Review of strongly-coupled composite dark matter models and lattice simulations*, *Int. J. Mod. Phys. A* **31** (2016), no. 22 1643004, [arXiv:1604.04627].

[361] T. Appelquist et al., *Stealth Dark Matter: Dark scalar baryons through the Higgs portal*, *Phys. Rev. D* **92** (2015), no. 7 075030, [arXiv:1503.04203].

[362] I. Baldes, M. Cirelli, P. Panci, K. Petraki, F. Sala, and M. Taoso, *Asymmetric dark matter: residual annihilations and self-interactions*, *SciPost Phys.* **4** (2018) 41.

[363] N. F. Bell, A. Melatos, and K. Petraki, *Realistic neutron star constraints on bosonic asymmetric dark matter*, *Phys. Rev. D* **87** (Jun, 2013) 123507.

[364] C. Kouvaris and P. Tinyakov, *Constraining Asymmetric Dark Matter through observations of compact stars*, *Phys. Rev. D* **83** (2011) 083512, [arXiv:1012.2039].

[365] M. L. Graesser, I. M. Shoemaker, and L. Vecchi, *Asymmetric WIMP dark matter*, *JHEP* **10** (2011) 110, [arXiv:1103.2771].

[366] S. J. Lonsdale and R. R. Volkas, *Comprehensive asymmetric dark matter model*, *Phys. Rev. D* **97** (2018), no. 10 103510, [arXiv:1801.05561].

[367] D. E. Kaplan, M. A. Luty, and K. M. Zurek, *Asymmetric dark matter*, *Phys. Rev. D* **79** (Jun, 2009) 115016.

[368] S. M. Barr, *Baryogenesis, sphalerons, and the cogeneration of dark matter*, *Phys. Rev. D* **44** (Nov, 1991) 3062–3066.

[369] M. Fukugita and T. Yanagida, *Baryogenesis Without Grand Unification*, *Phys. Lett. B* **174** (1986) 45–47.

[370] D. V. Nanopoulos and S. Weinberg, *Mechanisms for cosmological baryon production*, *Phys. Rev. D* **20** (Nov, 1979) 2484–2493.

[371] N. Haba and S. Matsumoto, *Baryogenesis from Dark Sector*, *Prog. Theor. Phys.* **125** (2011) 1311–1316, [arXiv:1008.2487].

[372] J. Shelton and K. M. Zurek, *Darkogenesis: A baryon asymmetry from the dark matter sector*, *Phys. Rev. D* **82** (2010) 123512, [arXiv:1008.1997].

[373] B. Dutta and J. Kumar, *Asymmetric dark matter from hidden sector baryogenesis*, *Physics Letters B* **699** (2011), no. 5 364–367.

[374] E. Hall, T. Konstandin, R. McGehee, and H. Murayama, *Asymmetric Matters from a Dark First-Order Phase Transition*, arXiv:1911.12342.

[375] R. Kitano and I. Low, *Dark matter from baryon asymmetry*, *Phys. Rev. D* **71** (Jan, 2005) 023510.

[376] S. Nussinov, *Technocosmology could a technibaryon excess provide a natural missing mass candidate?*, *Physics Letters B* **165** (1985), no. 1 55–58.

[377] S. Barr, R. Sekhar Chivukula, and E. Farhi, *Electroweak fermion number violation and the production of stable particles in the early universe*, *Physics Letters B* **241** (1990), no. 3 387–391.

[378] V. Kuzmin, V. Rubakov, and M. Shaposhnikov, *On anomalous electroweak baryon-number non-conservation in the early universe*, *Physics Letters B* **155** (1985), no. 1 36 – 42.

[379] S. B. Gudnason, C. Kouvaris, and F. Sannino, *Dark Matter from new Technicolor Theories*, *Phys. Rev. D* **74** (2006) 095008, [hep-ph/0608055].

[380] T. A. Ryttov and F. Sannino, *Ultra Minimal Technicolor and its Dark Matter TIMP*, *Phys. Rev. D* **78** (2008) 115010, [arXiv:0809.0713].

[381] M. T. Frandsen and F. Sannino, *iTIMP: isotriplet Technicolor Interacting Massive Particle as Dark Matter*, *Phys. Rev. D* **81** (2010) 097704, [arXiv:0911.1570].

[382] M. Y. Khlopov and C. Kouvaris, *Strong Interactive Massive Particles from a Strong Coupled Theory*, *Phys. Rev. D* **77** (2008) 065002, [arXiv:0710.2189].

[383] G. D. Kribs, T. S. Roy, J. Terning, and K. M. Zurek, *Quirky Composite Dark Matter*, *Phys. Rev. D* **81** (2010) 095001, [arXiv:0909.2034].

[384] M. Ibe, A. Kamada, S. Kobayashi, and W. Nakano, *Composite Asymmetric Dark Matter with a Dark Photon Portal*, *JHEP* **11** (2018) 203, [arXiv:1805.06876].

[385] M. Ibe, A. Kamada, S. Kobayashi, T. Kuwahara, and W. Nakano, *Ultraviolet Completion of a Composite Asymmetric Dark Matter Model with a Dark Photon Portal*, *JHEP* **03** (2019) 173, [arXiv:1811.10232].

[386] H. Fukuda, S. Matsumoto, and S. Mukhopadhyay, *Asymmetric dark matter in early Universe chemical equilibrium always leads to an antineutrino signal*, *Phys. Rev. D* **92** (2015), no. 1 013008, [arXiv:1411.4014].

[387] Y. Bai and P. Schwaller, *Scale of dark qcd*, *Phys. Rev. D* **89** (Mar, 2014) 063522.

[388] M. Blennow, B. Dasgupta, E. Fernandez-Martinez, and N. Rius, *Aidnogenesis via Leptogenesis and Dark Sphalerons*, *JHEP* **03** (2011) 014, [arXiv:1009.3159].

[389] D. S. M. Alves, S. R. Behbahani, P. Schuster, and J. G. Wacker, *Composite Inelastic Dark Matter*, *Phys. Lett. B* **692** (2010) 323–326, [arXiv:0903.3945].

[390] W. Detmold, M. McCullough, and A. Pochinsky, *Dark Nuclei I: Cosmology and Indirect Detection*, *Phys. Rev. D* **90** (2014), no. 11 115013, [arXiv:1406.2276].

[391] D. Spier Moreira Alves, S. R. Behbahani, P. Schuster, and J. G. Wacker, *The Cosmology of Composite Inelastic Dark Matter*, *JHEP* **06** (2010) 113, [arXiv:1003.4729].

[392] J. M. Cline, Z. Liu, G. D. Moore, and W. Xue, *Composite strongly interacting dark matter*, *Phys. Rev. D* **90** (Jul, 2014) 015023.

[393] G. Krnjaic and K. Sigurdson, *Big Bang Darkleosynthesis*, *Phys. Lett. B* **751** (2015) 464–468, [arXiv:1406.1171].

[394] M. Redi and A. Tesi, *Cosmological Production of Dark Nuclei*, *JHEP* **04** (2019) 108, [arXiv:1812.08784].

[395] E. Hardy, R. Lasenby, J. March-Russell, and S. M. West, *Big Bang Synthesis of Nuclear Dark Matter*, *JHEP* **06** (2015) 011, [arXiv:1411.3739].

[396] J. A. Harvey and M. S. Turner, *Cosmological baryon and lepton number in the presence of electroweak fermion-number violation*, *Phys. Rev. D* **42** (Nov, 1990) 3344–3349.

[397] A. Falkowski, J. T. Ruderman, and T. Volansky, *Asymmetric Dark Matter from Leptogenesis*, *JHEP* **05** (2011) 106, [arXiv:1101.4936].

[398] M. R. Buckley and L. Randall, *Xogenesis*, *JHEP* **09** (2011) 009, [arXiv:1009.0270].

[399] A. Mitridate, M. Redi, J. Smirnov, and A. Strumia, *Dark Matter as a weakly coupled Dark Baryon*, *JHEP* **10** (2017) 210, [arXiv:1707.05380].

[400] R. Contino, A. Mitridate, A. Podo, and M. Redi, *Gluequark Dark Matter*, *JHEP* **02** (2019) 187, [arXiv:1811.06975].

[401] A. Sakharov, *Violation of CP Invariance, C asymmetry, and baryon asymmetry of the universe*, *Sov. Phys. Usp.* **34** (1991), no. 5 392–393.

[402] P. Fileviez Perez and M. B. Wise, *Baryon Asymmetry and Dark Matter Through the Vector-Like Portal*, *JHEP* **05** (2013) 094, [arXiv:1303.1452].

[403] J. M. Cline, W. Huang, and G. D. Moore, *Challenges for models with composite states*, *Phys. Rev. D* **94** (2016), no. 5 055029, [arXiv:1607.07865].

[404] J. M. Arnold, B. Fornal, and M. B. Wise, *Simplified models with baryon number violation but no proton decay*, *Phys. Rev. D* **87** (Apr, 2013) 075004.

[405] A. Helset, C. Murgui, and M. B. Wise, *Simple models with both baryon and lepton number violation by two units*, arXiv:2104.03316.

[406] M. J. Ramsey-Musolf, G. White, and P. Winslow, *Color breaking baryogenesis*, *Physical Review D* **97** (Jun, 2018).

[407] R. Mahbubani, M. Redi, and A. Tesi, *Dark Nucleosynthesis: Cross-sections and Astrophysical Signals*, *JCAP* **02** (2021) 039, [arXiv:2007.07231].

[408] Y. Bai and B. A. Dobrescu, *Minimal $SU(3) \times SU(3)$ Symmetry Breaking Patterns*, *Phys. Rev. D* **97** (2018), no. 5 055024, [arXiv:1710.01456].

[409] E. W. Kolb and S. Wolfram, *Baryon Number Generation in the Early Universe*, *Nucl. Phys. B* **172** (1980) 224. [Erratum: Nucl.Phys.B 195, 542 (1982)].

[410] E. W. Kolb and M. S. Turner, *The Early Universe*, vol. 69. 1990.

[411] H. H. Patel, *Package-X: A Mathematica package for the analytic calculation of one-loop integrals*, *Comput. Phys. Commun.* **197** (2015) 276–290, [arXiv:1503.01469].

[412] H. H. Patel, *Package-X 2.0: A Mathematica package for the analytic calculation of one-loop integrals*, *Comput. Phys. Commun.* **218** (2017) 66–70, [arXiv:1612.00009].

[413] T. R. Slatyer, *Indirect Detection of Dark Matter*, in *Theoretical Advanced Study Institute in Elementary Particle Physics: Anticipating the Next Discoveries in Particle Physics*, pp. 297–353, 2018. arXiv:1710.05137.

[414] M. R. Buckley and S. Profumo, *Regenerating a symmetry in asymmetric dark matter*, *Phys. Rev. Lett.* **108** (Jan, 2012) 011301.

[415] M. Cirelli, P. Panci, G. Servant, and G. Zaharijas, *Consequences of DM/antiDM Oscillations for Asymmetric WIMP Dark Matter*, *JCAP* **03** (2012) 015, [arXiv:1110.3809].

[416] S. Tulin, H.-B. Yu, and K. M. Zurek, *Oscillating Asymmetric Dark Matter*, *JCAP* **05** (2012) 013, [arXiv:1202.0283].

[417] R. N. Mohapatra, *Neutron-Anti-Neutron Oscillation: Theory and Phenomenology*, *J. Phys. G* **36** (2009) 104006, [arXiv:0902.0834].

[418] Y. Cui and R. Sundrum, *Baryogenesis for weakly interacting massive particles*, *Phys. Rev. D* **87** (2013), no. 11 116013, [arXiv:1212.2973].

[419] S. J. Orfanidis and V. Rittenberg, *Nucleon-antinucleon annihilation into pions*, *Nucl. Phys. B* **59** (1973) 570–582.

[420] M. Ibe, S. Kobayashi, R. Nagai, and W. Nakano, *Oscillating composite asymmetric dark matter*, *Journal of High Energy Physics* **2020** (Jan, 2020).

[421] **H.E.S.S.** Collaboration, H. Abdallah et al., *Search for dark matter signals towards a selection of recently detected DES dwarf galaxy satellites of the Milky Way with H.E.S.S.*, *Phys. Rev. D* **102** (2020), no. 6 062001, [arXiv:2008.00688].

[422] P. Asadi, E. D. Kramer, E. Kuflik, G. W. Ridgway, T. R. Slatyer, and J. Smirnov, *Accidentally Asymmetric Dark Matter*, arXiv:2103.09822.

[423] T. Banks and N. Seiberg, *Symmetries and Strings in Field Theory and Gravity*, *Phys. Rev. D* **83** (2011) 084019, [arXiv:1011.5120].

[424] B. Audren, J. Lesgourgues, G. Mangano, P. D. Serpico, and T. Tram, *Strongest model-independent bound on the lifetime of Dark Matter*, *JCAP* **12** (2014) 028, [arXiv:1407.2418].

[425] E. Aubourg et al., *Cosmological implications of baryon acoustic oscillation measurements*, *Phys. Rev. D* **92** (2015), no. 12 123516, [arXiv:1411.1074].

[426] S. Ando and K. Ishiwata, *Constraints on decaying dark matter from the extragalactic gamma-ray background*, *JCAP* **05** (2015) 024, [arXiv:1502.02007].

[427] M. Cirelli, E. Moulin, P. Panci, P. D. Serpico, and A. Viana, *Gamma ray constraints on Decaying Dark Matter*, *Phys. Rev. D* **86** (2012) 083506, [arXiv:1205.5283].

[428] M. Cirelli, E. Del Nobile, and P. Panci, *Tools for model-independent bounds in direct dark matter searches*, *JCAP* **10** (2013) 019, [arXiv:1307.5955].

[429] M. Freytsis and Z. Ligeti, *On dark matter models with uniquely spin-dependent detection possibilities*, *Phys. Rev. D* **83** (2011) 115009, [arXiv:1012.5317].

[430] T. Binder, A. Filimonova, K. Petraki, and G. White, *Saha equilibrium for metastable bound states and dark matter freeze-out*, arXiv:2112.00042.

[431] N. Cabibbo and R. Gatto, *Electron Positron Colliding Beam Experiments*, *Phys. Rev.* **124** (1961) 1577–1595.

[432] N. Cabibbo, G. Karl, and L. Wolfenstein, *A New Unitarity Bound on e+ e- Annihilation*, *Phys. Lett. B* **51** (1974) 387–389.

[433] L. D. Landau, *Quantum Mechanics: Non-Relativistic Theory*, vol. v.3 of *Course of Theoretical Physics*. Butterworth-Heinemann, Oxford, 1991.

[434] M. Beneke, R. Szafron, and K. Urban, *Sommerfeld-corrected relic abundance of wino dark matter with NLO electroweak potentials*, *JHEP* **02** (2021) 020, [arXiv:2009.00640].

[435] S. Frixione, M. L. Mangano, P. Nason, and G. Ridolfi, *Improving the Weizsacker-Williams approximation in electron - proton collisions*, *Phys. Lett. B* **319** (1993) 339–345, [hep-ph/9310350].

[436] P. Masjuan, E. R. Arriola, and W. Broniowski, *Meson dominance of hadron form factors and large-N_c phenomenology*, *Phys. Rev. D* **87** (Jan, 2013) 014005.

[437] A. Ritz and S. Foroughi-Abari, *private communication*, .

[438] D. Gorbunov, A. Makarov, and I. Timiryasov, *Decaying light particles in the SHiP experiment: Signal rate estimates for hidden photons*, *Phys. Rev. D* **91** (2015), no. 3 035027, [arXiv:1411.4007].

[439] P. Ball and R. Zwicky, *New results on $B \to \pi, K, \eta$ decay formfactors from light-cone sum rules*, *Phys. Rev. D* **71** (2005) 014015, [hep-ph/0406232].

[440] N. Carrasco, P. Lami, V. Lubicz, L. Riggio, S. Simula, and C. Tarantino, *$K \to \pi$ semileptonic form factors with $N_f = 2 + 1 + 1$ twisted mass fermions*, *Phys. Rev. D* **93** (2016), no. 11 114512, [arXiv:1602.04113].

[441] P. Ball and R. Zwicky, *$B_{d,s} \to \rho, \omega, K^*, \phi$ decay form-factors from light-cone sum rules revisited*, *Phys. Rev. D* **71** (2005) 014029, [hep-ph/0412079].

[442] T. Hahn, *CUBA: A Library for multidimensional numerical integration*, *Comput. Phys. Commun.* **168** (2005) 78–95, [hep-ph/0404043].

[443] D. Egana-Ugrinovic, S. Homiller, and P. Meade, *Light Scalars and the Koto Anomaly*, *Phys. Rev. Lett.* **124** (2020), no. 19 191801, [arXiv:1911.10203].

[444] M. Tegmark, *Measuring cosmological parameters with galaxy surveys*, *Phys. Rev. Lett.* **79** (1997) 3806–3809, [astro-ph/9706198].

[445] S. Dodelson, *Modern Cosmology*. Academic Press, Amsterdam, 2003.

[446] G. Cowan, K. Cranmer, E. Gross, and O. Vitells, *Asymptotic formulae for likelihood-based tests of new physics*, *Eur. Phys. J. C* **71** (2011) 1554, [arXiv:1007.1727]. [Erratum: Eur.Phys.J.C 73, 2501 (2013)].

[447] L. Amendola, M. Pietroni, and M. Quartin, *Fisher matrix for the one-loop galaxy power spectrum: measuring expansion and growth rates without assuming a cosmological model*, *JCAP* **11** (2022) 023, [arXiv:2205.00569].